DYNAMICAL EQUILIBRATION AND TRANSPORT COEFFICIENTS OF STRONGLY INTERACTING MATTER

Dissertation
zur Erlangung des Doktorgrades
der Naturwissenschaften

vorgelegt beim Fachbereich Physik
der Johann Wolfgang Goethe-Universität
in Frankfurt am Main

von

Vitalii Ozvenchuk

aus Vinnytsya, Ukraine

Frankfurt am Main 2013
(D 30)

vom Fachbereich Physik der
Johann Wolfgang Goethe-Universität, Frankfurt am Main,
als Dissertation angenommen.

Dekan: Prof. Dr. Joachim Stroth

Gutachter: Prof. Dr. Elena Bratkovskaya

Datum der Disputation:

Zusammenfassung

In der vorliegenden Arbeit wurden mikroskopische Studien zur Äquilibrierung von partonischer und hadronischer Materie im Rahmen einer Nichtgleichgewichts-Transporttheorie durchgeführt, die sowohl hadronische als partonische Freiheitsgrade enthält und den Übergang zwischen beiden Phasen dynamisch beschreibt. Des Weiteren wurden die thermischen Eigenschaften des Gleichgewichtszustandes der stark wechselwirkenden Materie untersucht, insbesondere Fluktuationen in der Teilchenzahl wie auch höhere Momente von Observablen und deren Verhältnisse. Besonderes Interesse galt dabei den Transportkoeffizienten wie Scher- und Volumenviskosität sowie der elektrischen Leitfähigkeit.

Die Methode der Nichtgleichgewichts-Green'schen Funktionen - initiiert von Schwinger sowie Kadanoff und Baym - wurde vorgestellt um hochenergetische Kern-Kern Kollisionen zu beschreiben. Weiterhin wurde der Schwinger-Keldysh Formalismus benutzt um im Sinne einer Zweiteilchen-irreduziblen Näherung (2PI) die Dynamik von 'resummierten' Propagatoren und Kopplungen in konsistenter Weise zu beschreiben. Des Weiterhin wurden generalisierte Transportgleichungen auf der Basis der Kadanoff-Baym Gleichungen (in Phasenraumdarstellung) abgeleitet und ein Testteilchenverfahren zur Lösung dieser Gleichungen vorgestellt. Damit wurde der formale Rahmen der Parton-Hadron-String Dynamik (PHSD) abgesteckt.

Das PHSD Transportmodell wurde sodann für die Lösung der expliziten Fragestellungen in dieser Arbeit verwendet. Die 'Eingangsgrößen' des Modells wurden in Kapitel 3 aufgeführt. Weiterhin wurde aufgezeigt, dass das Transportmodell alle Phasen einer relativistischen Schwerionenkollision konsistent beschreibt, d.h. angefangen von den primären harten Stoßprozessen und der Bildung von 'Strings' zur Formierung einer partonischen Phase, den Wechselwirkungen in dieser Phase sowie die dynamische Beschreibung der Hadronisierung. Weiterhin enthält das Modell zudem die hadronischen Endzu-

standswechselwirkungen bis zum Ausfrieren der hadronischen Freiheitsgrade bei geringer Dichte.

Zur Beschreibung der partonischen Phase wurde das dynamische Quasiteilchen Modell (DQPM) zugrunde gelegt, welches die Eigenschaften der QCD Freiheitsgrade im Gleichgewicht über 'resummierte' Green'sche Funktionen mit endlicher spektraler Breite im Einklang mit Gitter-QCD Rechnungen spezifiziert. Dabei wurden die drei freien Parameter des Modells für die 'resummierte' Kopplung explizit an Gitter-QCD Resultate für die Zustandsgleichung im Gleichgewicht angepaßt. Ein weiteres Result des DQPM Modells entsteht durch Trennung von zeit- und raum-artigen Beiträgen zur Teilchendichte sowie zum Energie-Impuls Tensor, was zur Trennung von kinetischen und potentiellen Beiträgen zur Energiedichte führt. Ableitungen der potentiellen Energiedichte nach den zeitartigen Partonendichten liefern sodann Mean-Field Potentiale für die Partonen als auch (über zweite Ableitungen) die Stärke der effektiven Wechselwirkungen zwischen den Partonen. Dieses Modell erlaubte zudem auch Berechnungen bei endlichem chemischem Potential μ_q.

Das PHSD-Transport Modell ist ein nahezu universelles 'Werkzeug' zum Studium von Schwerionenreaktionen in einem weiten Energiebereich. Insbesondere wurden Kern-Kern Reaktionen von SIS bis RHIC Energien in Kapitel 4 vorgestellt. Hier sind die PHSD Resultate im Vergleich mit experimentellen Daten der NA49 Kollaboration für Pb+Pb Stöße im SIS Energiebereich vorgestellt worden. Es zeigte sich, dass die partonische Phase nur einen geringen Einfluß auf die longitudinalen Rapiditätsverteilungen der Hadronen hat, aber einen signifikanten Einfluß auf die transversalen Massenspektren von Kaonen aufgrund der partonischen Wechselwirkungen. Als deutlichster Effekt einer partonischen Phase wurde die erhöhte Produktion von Antibaryonen mit Strangeness herausgestellt, was auf eine Umverteilung der Quarks mit Antistrangeness in der Hadronisierung zurückgeführt werden konnte.

Die PHSD Resultate zeigten sich generell in recht guter Übereinstimmung mit den Daten für die transversalen Massenspektren und longitudinalen Rapiditätsverteilungen. Auch der kollektive elliptische Fluß v_2 wurde beschrieben für Au+Au Stöße bei $\sqrt{s} = 200$ GeV als Funktion der Zentralität und als Funktion des Transversalimpulses bis $p_T \simeq 1.5$ GeV. Ebenfalls lieferte das PHSD Modell näherungsweise eine Skalierung von $v_2(p_T)$ mit der Zahl der Konstituentenquarks in Übereinstimmung mit den experimentellen Daten der

STAR und PHENIX Kollaborationen. Nicht zuletzt beschreibt PHSD auch den kollektiven Fluß v_2 als Funktion der Laborenergie im Vergleich zu Daten von STAR im 'low Energy Beam Program' bei RHIC.

Die Dileptonenproduktion in In+In Reaktionen bei 158A GeV wurde ebenfalls im Rahmen des PHSD off-shell Modells berechnet unter Berücksichtigung einer Kollisionsverbreiterung der Vektormesonen, der Produktion in sekundären Kollisionen schwerer Mesonen sowie der Produktionskanäle in der partonischen QGP Phase, die mit den gleichen Freiheitsgraden berechnet wurden wie in der dynamischen Propagation im Transportmodell. Die Dileptonenspektren werden erfolgreich beschrieben im Vergleich mit den experimentellen Daten der NA60 Kollaboration unter Berücksichtigung der Kollisionsverbreiterung der Vektormesonen und Mitnahme der Strahlung aus dem partonischen Plasma wie Quark-Antiquark Annihilation, Quark-Annihilation mit Gluon Bremsstrahlung im Endzustand sowie Gluon-Compton Streuung.

In Kapitel 5 wurden sodann partonische Systeme etwas außerhalb vom Gleichgewicht in einer kubischen Box initialisiert und die Einstellung des Gleichgewichts (bei periodischen Randbedingungen) im PHSD untersucht. Es wurde explizit gezeigt, dass partonische Systeme oberhalb der kritischen Energiedichte von $\varepsilon_c \approx 0.5$ Gev/fm^3 ein kinetisches und chemisches Gleichgewicht erreichen. Ebenfalls zeigte sich die Zustandsgleichung im Gleichgewicht in guter Übereinstimmung mit dem DQPM und damit auch mit den Gitter-QCD Resultaten bei chemischem Potential $\mu_q = 0$. Es stellte sich überraschend heraus, dass der Strangeness-Freiheitsgrad lediglich auf Zeitskalen äquilibriert, die groß im Vergleich mit Reaktionszeiten von relativistischen Schwerionenstößen sind. Dieses Ergebnis scheint im Widerspruch zu den experimentellen Ergebnissen zu stehen, jedoch ist zu bemerken, dass die Zeitskalen aus den Box-Rechnungen nicht mit experimentellen Daten direkt konfrontiert werden dürfen, da die Anfangsbedingungen gänzlich verschieden sind.

Zusätzlich zur Einstellung des Gleichgewichts für die Mittelwerte von Observablen wurde die Dynamik von Fluktuationen von Observablen im und außerhalb vom Gleichgewicht untersucht. Für alle betrachteten Observablen wurde gefunden, dass $\tau_{\rm eq}$ kürzer ist für die Schwankungsgrößen als für die Mittelwerte. Dieses Verhalten ist besonders auffällig, wenn man alle Partonen betrachtet, aber weniger ausgeprägt für die Strangeness-Freiheitsgrade. Folglich können Fluktuationen von Observablen bereits die Gleichgewichtswerte

erreichen obwohl die Mittelwerte noch weit vom Gleichgewichtswert entfernt sind. Dieses Verhalten erinnert an Ergebnisse von Rechnungen auf der Basis der Kadanoff-Baym Gleichungen, in denen (Quanten-)Fluktuationen sich früh in der Zeit stabilisieren lange bevor ein kinetisches und/oder chemisches Gleichgewicht erreicht wird.

Die auf die Mittelwerte skalierten Varianzen in der Teilchenzahl diverser Partonen zeigen den Einfluß der Gesamtenergieerhaltung in der Box. Die Varianzen sind unterdrückt in der endlichen Box im Vergleich zu grokanonischen Rechnungen im thermodynamischen Limes. Weiterhin, durch Unterteilung der Box in kleinere Teilvolumina wurden die Fluktuationen als Funktion des Teilvolumens untersucht. Die skalierten Varianzen aller Observablen gehen für kleine Volumina über in den Limes einer Poisson-Verteilung mit $\omega = 1$. Dieses Verhalten ist auf den Einfluß globaler Erhaltungsgrößen zurückzuführen, die an Bedeutung verlieren, wenn nur ein kleines Teilsystem betrachtet wird. Nur wenn das Teilsystem mit der gesamten Box vergleichbar wird zeigt sich der nicht vernachlässigbare Einfluß der Erhaltungsgrößen auch im thermodynamischen Limes. Es konnte gezeigt werden, dass für Volumina größer als ≈ 5000 fm^3 der thermodynamische Limes rechnerisch annähernd erreicht wird. Die Analysen zu höheren Momenten der Verteilungen ('skewness, kurtosis') zeigten praktisch verschwindende Werte für diese Momente, die innerhalb der Statistik mit Resultaten der Gitter-QCD übereinstimmen.

Des Weiteren wurde das PHSD Transportmodell benutzt um Transportkoeffizienten für die hadronischen und partonischen Phasen zu ermitteln (Kapitel 6). Im PHSD sind diese Transportkoeffizienten nicht externe Eingabeparameter sondern dynamische Größen, die im Gleichgewicht als Funktion der Temperatur berechnet werden können ohne Einführung weiterer Annahmen oder Parameter. Es wurde hierzu der Kubo-Formalismus als auch die Relaxationszeit-Näherung untersucht um die Scherviskosität zu berechnen. Beide Methoden ergeben sehr ähnliche Resultate für das Verhältnis der Scherviskisität zur Entropiedichte $\eta(T)/s(T)$ mit einem Minimum in der Nähe der kritischen Temperatur T_c. Das Verhältnis erreicht das Resultat der störungstheoretischen QCD bei hohen Temperaturen. Unterhalb von T_c, d.h. in der hadronischen Phase, steigt das Verhältnis $\eta(T)/s(T)$ steil mit fallender Temperatur an, was auf die erheblich kleinere Anzahl an Freiheitsgraden (oder Entropiedichte) zurckzuführen ist. Die expliziten Resultate für $\eta(T)/s(T)$ sind weiterhin in erstaunlicher Übereinstimmung mit früheren Rechnungen im Rah-

men einer Virialentwicklung sowie mit Gitter-QCD Resultaten für den reinen Fall von Eichbosonen.

Die Resultate für die Volumenviskosität $\zeta(T)$ wurden in der Relaxationszeit-Näherung berechnet wobei besonderer Wert auf die Rolle der mittleren Felder für die Partonen gelegt wurde. Es zeigte sich, dass das Verhältnis von Volumenviskosität zur Entropiedichte $\zeta(T)/s(T)$ ein Maximum in der Nähe der kritischen Temperatur T_c hat bei Bercksichtigung der partonischen mittleren Felder. Diese Resultate für $\zeta(T)/s(T)$ sind konsistent mit Gitter-QCD Rechnungen. Weiterhin erlaubte der spezifische Soundkanal $(\eta + 3\zeta/4)(T)/s(T)$ einen weiteren Vergleich mit Gitter-QCD Resultaten, der ebenfalls positiv ausfiel. Letztendlich zeigt das Verhältnis der Viskositäten $\zeta(T)/\eta(T)$ ein ausgeprägtes Maximum in der Nähe von T_c, welches auf die Effekte der mittleren Felder für Partonen in PHSD und letztendlich auf die Erhöhung der resummierten Kopplung $g(T)$ nahe T_c zurückzuführen ist.

Zum Abschluß wurde die elektrische Leitfähigkeit $\sigma_0(T)$ hadronischer und partonischer Materie bei verschiedenen Temperaturen im Rahmen von PHSD Rechnungen in der Box berechnet. Das dimensionslose Verhältnis der Leitfähigkeit zur Temperatur $\sigma_0(T)/T$ steigt oberhalb von T_c nahezu linear mit der Temperatur bis 2.5 T_c und erreicht ein konstantes Plateau oberhalb von 5 T_c in den PHSD Rechnungen wie auch expliziten Berechnungen im Rahmen des DQPM in der Relaxationszeit-Näherung. In der hadronischen Phase, d.h. unterhalb von T_c, steigt das Verhältnis $\sigma_0(T)/T$ mit fallender Temperatur, da das System immer mehr einem System schwach wechselwirkender Pionen ähnelt, welches ein hohes Verhältnis von Ladungsquadrat zur Masse aufweist und eine längere Relaxationszeit als in der partonischen Phase.

Contents

Chapter 1

Introduction

One of the most intriguing open questions of modern physics is the phenomenon of confinement. From the phenomenological point of view, confinement can be defined as the nonobservability in nature of free quarks and gluons, which are in turn defined as the elementary particles carrying the quantum number of color. This textbook definition is tempting, because it is easily understandable even for nonspecialists. On the other hand, many of the specialists find that it lacks necessary precision and suggest alternative definitions, referring to the symmetries of the strong interaction or to the particular analytical properties of the gluon propagator in various gauges [1–6]. However, it is in the spirit of physics as a data-driven science that the ultimate proof for our understanding of confinement will follow an experimental confirmation of a phenomenological prediction. And in this respect we would like to point out here the connection between the quest for the understanding of confinement and that for the properties of the hot strongly interacting matter created in heavy-ion collisions.

Currently, Quantum Chromodynamics (QCD) is accepted as the theory of the strong interaction with quarks and gluons as elementary degrees of freedom [7, 8]. QCD explains a vast number of observations and as a part of the standard model of particle physics is one of the most meticulously tested theories. But there is no concluding proof so far that QCD is confining. For the first time, the quarks were introduced in the scope of the quark model [9], which implied the complex nature of the proton, neutron, and other hadrons. But the acceptance of this model was hindered by the fact that the particles with the quantum numbers of quarks (e.g., a fractional electric charge) were not discovered.

The way out was at first sight found in experiments on deep inelastic scattering (DIS), when it was possible with the help of electron scattering at very high energy to "kick out" single quarks from the proton. According to QCD, the confining interaction between two quarks becomes weak in the limit of high energy exchange—the asymptotic freedom property. This permits the successful use of perturbation theory (pQCD) for the description of DIS processes. Indeed, pQCD has proven to work with great precision for the description of partons (i.e., the proton constituents) in the DIS as well as other high-energy scattering processes at particle accelerators [7, 10, 11]. However, no partons are detected directly in these experiments. When quarks or gluons become separated from the parent proton or nucleon, as happens in such energetic collisions, a string of self-interacting gluons is pulled between them and at some point it is more energetically favorable to create new quark-antiquark pairs from the vacuum. As a result of this, when quarks are produced in particle accelerators, instead of the individual quarks, jets—or clusters—of many color-neutral particles (mesons and baryons) are detected. This process is a consequence of confinement; it is called hadronization, fragmentation, or string breaking and cannot be explained by perturbative methods.

The nonperturbative nature of the confining interaction makes the high-energy scattering processes unsuitable for its study. On the other hand, there is another domain, in which the hadronization, i.e., the transition between the partonic and hadronic degrees of freedom, can be explored. In the strongly interacting systems of high energy density, the interaction between quarks is screened in analogy to the Debye screening of the electromagnetic interaction in the ion-electron plasmas. As a consequence, the color charges move freely within the volume of such quark-gluon plasma (QGP), which is therefore called the deconfined state of matter. The confinement leads to the hadronization of quarks and gluons from the QGP into color-neutral hadronic particles and resonances. The onset of the hadronization in equilibrated matter is regulated by the external thermodynamical parameters of the system. In particular, one can define the critical temperature, T_c, and the critical quark chemical potential of the phase transition between the parton and hadron matter. Thus the study of parton-hadron matter in equilibrium at varying temperatures and chemical potentials is the theoretical laboratory for the investigation of the hadronization and confinement, for example, using lattice QCD (lQCD) calculations [12–15], quasiparticle models [16–22] or transport approaches [23–

29]. Let us note the importance of the equilibration assumption, which ensures that the response of the system to the perturbation reflects not the initial conditions or the system time evolution, but solely the underlying properties of the strong interaction.

The deconfined state of matter or QGP can be created experimentally in relativistic heavy-ion collisions. The phase transition to the QGP was reached at the Relativistic Heavy Ion Collider (RHIC) at Brookhaven [30–33], at the Large Hadron Collider (LHC) at CERN [34–37] and probably even in lower energy collisions at the Super Proton Synchrotron (SPS) [38, 39]. Various observables—from back-to-back jet suppression to the strong elliptic flow, to the melting of quarkonia, and to the enhancement of photon and dilepton emission—show that the created system does not show the properties of ordinary hadronic matter. One can conclude that the energy densities reached were high enough to dissolve the initial protons and neutrons into quarks and gluons. Moreover, the produced QGP shows features of a strongly interacting fluid unlike a weakly interacting parton gas [18, 40, 41].

Thus the key questions are now:

- Whether the created QGP reached equilibrium and which observables can test the degree of equilibration?

- How to use the available portfolio of measured data on the particle spectra, correlations, hard probe production to constrain the transport properties of the parton-hadron matter and of hadronization?

In particular, the current thesis focusses on the following questions:

- The microscopic study of the questions of thermalization and equilibration of confined and deconfined matter out of equilibrium within a nonequilibrium transport approach, incorporating both hadronic and partonic degrees of freedom and the dynamic phase transition.

- The study of the thermal properties of equilibrated strongly interacting matter, e.g., the particle number fluctuations (scaled variance, skewness, kurtosis) as well as the transport coefficients (shear and bulk viscosities, electric conductivity).

As the method for our investigation, we use the Parton-Hadron-String Dynamics (PHSD) off-shell transport approach [23–25], which is based on

generalized transport equations on the basis of the off-shell Kadanoff-Baym equations [42–44] for Green's functions in phase-space representation (in the first-order gradient expansion, beyond the quasiparticle approximation).

The thesis is organized as follows. The introduction to the transport theory and the derivation of generalized transport equations on the basis of the off-shell Kadanoff-Baym equations are presented in Chapter 2. In Chapter 3 we provide the detailed description of the PHSD transport approach. The PHSD results for rapidity distributions, transverse mass spectra, and collective flow for heavy-ion collisions at SPS and RHIC energies in comparison to the data from the various experimental collaborations are given in Chapter 4. The results for dilepton production in nucleus-nucleus collisions at top SPS energies within the PHSD are presented in Chapter 4, too. The microscopic study on dynamical equilibration of parton-hadron matter within a cubic box with periodic boundary conditions and the particle number fluctuations in equilibrium are discussed in Chapter 5. We then present in Chapter 6 the results on the transport properties of the parton-hadron matter in PHSD. In particular, the shear and bulk viscosities as well as the electric conductivity of parton-hadron matter are shown as a function of the temperature of the system and compared to available lQCD results. Finally, a summary and discussion are given in Chapter 7.

Chapter 2

Transport theory

Nonequilbrium many-body theory and quantum field theory have become major methods in nuclear physics, cosmology, particle physics as well as condensed matter physics. In particular, nonequilibrium Green's function techniques, initiated by Schwinger [45] and Kadanoff and Baym [42], are used to describe high-energy nuclear collisions [46, 47]. These methods allow to study the time evolution of a many-body quantum system. The one-particle Green's functions describes the one-particle quantities in a system, while the many-particle information about the system is contained in the self-energies in the Green's function equations of motion.

A powerful tool, which provides an appropriate basis for the formulation of the complex problems in the various areas of nonequilibrium quantum many-body physics, is the Schwinger-Keldysh [45, 48, 49] or closed time path (CTP) real-time Green's functions method. The resulting causal Dyson-Schwinger equation of motion for the one-particle Green's functions—the Kadanoff-Baym equations [42]—have served as the underlying scheme for treating various transport phenomena and deriving generalized transport equations. The introduction to the Green's function techniques as well as the derivation of the transport equations are presented in this Chapter.

2.1 Nonrelativistic quantum many-body systems

2.1.1 Basic definitions

A nonrelativistic quantum system of fermions or bosons is most conveniently described in terms of the second-quantized, Heisenberg representation, using particle-creation ($\hat{\psi}^\dagger(\mathbf{r},t)$) and annihilation ($\hat{\psi}(\mathbf{r},t)$) operators.

The density of particles at the point $(\mathbf{r},t)$ in this representation can be written as

$$\hat{n}(\mathbf{r},t) = \hat{\psi}^\dagger(\mathbf{r},t)\hat{\psi}(\mathbf{r},t) \tag{2.1}$$

and the operator for the total number of particles is defined by

$$\hat{N}(t) = \int d\mathbf{r}\ \hat{\psi}^\dagger(\mathbf{r},t)\hat{\psi}(\mathbf{r},t). \tag{2.2}$$

The total energy of a system of particles with mass m interacting through an instantaneous two-body potential $v(r)$ is given by

$$\begin{aligned}\hat{H}(t) \ &= \int d\mathbf{r}\ \hat{\psi}^\dagger(\mathbf{r},t)\left(-\frac{\nabla^2}{2m}\right)\hat{\psi}(\mathbf{r},t) \\ &+\frac{1}{2}\int d\mathbf{r}\ d\mathbf{r}'\ \hat{\psi}^\dagger(\mathbf{r},t)\hat{\psi}^\dagger(\mathbf{r}',t)v(|\mathbf{r}-\mathbf{r}'|)\hat{\psi}(\mathbf{r}',\mathbf{t})\hat{\psi}(\mathbf{r},\mathbf{t}).\end{aligned} \tag{2.3}$$

The equation of any operator $\hat{O}(t)$ in the Heisenberg representation is

$$i\frac{\partial\hat{O}(t)}{\partial t} = [\hat{O}(t),\hat{H}(t)] \tag{2.4}$$

and any time-dependent operator can be represented in the form

$$\hat{O}(t) = e^{i\hat{H}t}\hat{O}(0)e^{-i\hat{H}t}. \tag{2.5}$$

The field operators satisfy the commutation relations

$$\begin{aligned}\hat{\psi}(\mathbf{r},t)\hat{\psi}(\mathbf{r}',t) \mp \hat{\psi}(\mathbf{r}',t)\hat{\psi}(\mathbf{r},t) = 0, \\ \hat{\psi}^\dagger(\mathbf{r},t)\hat{\psi}^\dagger(\mathbf{r}',t) \mp \hat{\psi}^\dagger(\mathbf{r}',t)\hat{\psi}^\dagger(\mathbf{r},t) = 0, \\ \hat{\psi}(\mathbf{r},t)\hat{\psi}^\dagger(\mathbf{r}',t) \mp \hat{\psi}^\dagger(\mathbf{r}',t)\hat{\psi}^(\mathbf{r},t) = \delta(\mathbf{r}'-\mathbf{r}),\end{aligned} \tag{2.6}$$

where the upper sign refers to bosons and the lower sign refers to fermions. For fermions, $\hat{\psi}^2(\mathbf{r},t)=0$—an expression of the Pauli exclusion principle in space—it is impossible to find two identical fermions at the same point in space and time.

To describe the evolution of a many-body quantum system we may use the one-particle Green's function, which is a thermodynamic average of the product of the operators $\hat{\psi}(\mathbf{r}_1,t_1)$ and $\hat{\psi}^\dagger(\mathbf{r}_1',t_1')$ (the notation 1 means $\mathbf{r_1}t_1$ and $1'$ means $\mathbf{r_{1'}}t_{1'}$),

$$G(1,1')=\frac{1}{i}\langle T(\hat{\psi}(1)\hat{\psi}^\dagger(1'))\rangle, \tag{2.7}$$

and the two-particle Green's function, which is defined by

$$G_2(12,1'2')=\frac{1}{i^2}\langle T(\hat{\psi}(1)\hat{\psi}(2)\hat{\psi}^\dagger(2')\hat{\psi}^\dagger(1'))\rangle, \tag{2.8}$$

where T is the Wick time-ordering operation:

$$T(\hat{\psi}(1)\hat{\psi}^\dagger(1'))=\begin{cases}\hat{\psi}(1)\hat{\psi}^\dagger(1'), & \text{for} \quad t_1>t_{1'},\\ \pm\hat{\psi}^\dagger(1')\hat{\psi}(1), & \text{for} \quad t_1<t_{1'},\end{cases} \tag{2.9}$$

"$\pm$" stand for bosons (upper sign) and fermions (lower sign), respectively. In addition, we define the correlation functions

$$G^{>}(1,1')=\frac{1}{i}\langle\hat{\psi}(1)\hat{\psi}^\dagger(1')\rangle, \tag{2.10}$$

$$G^{<}(1,1')=\pm\frac{1}{i}\langle\hat{\psi}^\dagger(1')\hat{\psi}(1)\rangle. \tag{2.11}$$

These functions are known as the Wightman functions.

The Green's function (2.10) has a meaning of a density operator for a probe in the system (a particle added to the system with negligible perturbation to the system state). For $t_{1'}=t_1=t$, the r.h.s. of Eq. (2.11) represents the one-particle density matrix

$$\rho(\mathbf{r}_1,\mathbf{r}_{1'},t)=\langle\hat{\psi}^\dagger(\mathbf{r}_{1'},t)\hat{\psi}(\mathbf{r}_1,t)\rangle. \tag{2.12}$$

For example, the spatial density of particles, which is an expectation value of

the density operator (2.1), can be expressed as

$$n(\mathbf{r},t) = \langle \hat{n}(\mathbf{r},t) \rangle = \pm i G^{<}(\mathbf{r},t;\mathbf{r},t). \tag{2.13}$$

The Green's functions (2.10) and (2.11) in equilibrium satisfy the boundary condition

$$G^{<}(1,1')\Big|_{t_1=0} = \pm\, e^{\beta\mu}\; G^{>}(1,1')\Big|_{t_1=-i\beta}, \tag{2.14}$$

where $\beta = 1/T$ denotes the inverse temperature and μ stands for the chemical potential. We can define the same expression for the one-particle Green's function:

$$G(1,1')\Big|_{t_1=0} = \pm\, e^{\beta\mu}\; G(1,1')\Big|_{t_1=-i\beta}. \tag{2.15}$$

Because of the translational and rotational invariance of the Hamiltonian (2.3) in space and its translational invariance in time, $G^{>}$ and $G^{<}$ depend only on $|\mathbf{r_1} - \mathbf{r_1'}|$ and $t_1 - t_1'$. In terms of the difference variables, Eq. (2.14) becomes

$$G^{<}(\mathbf{r},t) = \pm\, e^{\beta\mu}\; G^{>}(\mathbf{r}, t - i\beta). \tag{2.16}$$

Let us now introduce the Fourier transforms of $G^{>}$ and $G^{<}$, which are defined by

$$\begin{aligned} G^{>}(\mathbf{p},\omega) &= i \int d\mathbf{r} \int_{-\infty}^{+\infty} dt\; e^{-i\mathbf{pr} + i\omega t}\; G^{>}(\mathbf{r},t), \\ G^{<}(\mathbf{p},\omega) &= \pm\, i \int d\mathbf{r} \int_{-\infty}^{+\infty} dt\; e^{-i\mathbf{pr} + i\omega t}\; G^{<}(\mathbf{r},t). \end{aligned} \tag{2.17}$$

In order to make $G^{>}(\mathbf{p},\omega)$ and $G^{<}(\mathbf{p},\omega)$ real nonnegative quantities—allowing for a probabilistic interpretation—the explicit factors of i and $\pm i$ have been included here. Then Eq. (2.14) can be written as

$$G^{<}(\mathbf{p},\omega) = e^{-\beta(\omega\,-\,\mu)}\; G^{>}(\mathbf{p},\omega). \tag{2.18}$$

It is useful to introduce the spectral function $A(\mathbf{p},\omega)$, which is defined by

$$A(\mathbf{p},\omega) = G^{>}(\mathbf{p},\omega) \mp G^{<}(\mathbf{p},\omega). \tag{2.19}$$

The boundary condition on G can be represented by

$$\begin{aligned} G^{>}(\mathbf{p},\omega) &= \left[1 \pm f(\omega)\right]\ A(\mathbf{p},\omega), \\ G^{<}(\mathbf{p},\omega) &= f(\omega)\ A(\mathbf{p},\omega), \end{aligned} \tag{2.20}$$

where $f(\omega)$ denotes the Fermi or Bose distribution.

When working with the ground state of a system, one usually deals with the chronological Green's function

$$iG^{c}(1,1') = \langle T^{c}(\hat{\psi}(1)\hat{\psi}^{\dagger}(1'))\rangle, \tag{2.21}$$

where T^{c} is the chronological-ordering operator. The chronological Green's function G^{c} is related to $G^{>}$ and $G^{<}$ by

$$G^{c}(1,1') = \Theta(t_1 - t_{1'})G^{>}(1,1') + \Theta(t_{1'} - t_1)G^{<}(1,1') \tag{2.22}$$

with

$$\Theta(t) = \begin{cases} 1, & \text{for} \quad t > 0, \\ 0, & \text{for} \quad t < 0. \end{cases} \tag{2.23}$$

The hermitian conjugate of Eq. (2.21) yields the antichronological Green's function

$$iG^{a}(1,1') = \langle T^{a}(\hat{\psi}(1)\hat{\psi}^{\dagger}(1'))\rangle, \tag{2.24}$$

where T^{a} is the antichronological-ordering operator. Similarly to Eq. (2.22), we have

$$G^{a}(1,1') = \Theta(t_1 - t_{1'})G^{<}(1,1') + \Theta(t_{1'} - t_1)G^{>}(1,1'). \tag{2.25}$$

The chronological (2.21) and antichronological (2.24) Green's functions possess propagator forms.

2.1.2 Equations of motion for the Green's function

Using the equation of motion (2.4) with the Hamiltonian (2.3) and commutation relations (2.6), we get

$$\left(i\frac{\partial}{\partial t} + \frac{\nabla^2}{2m}\right)\hat{\psi}(\mathbf{r}_1,t) = \int d\mathbf{r}_2\ v(\mathbf{r}_1 - \mathbf{r}_2)\hat{\psi}^{\dagger}(\mathbf{r}_2,t)\hat{\psi}(\mathbf{r}_2,t)\hat{\psi}(\mathbf{r}_1,t). \tag{2.26}$$

The equation of motion for the one-particle Green's function is derived from the equation of motion (2.26) for the annihilation operator $\hat{\psi}(1)$:

$$\begin{aligned}\frac{1}{i}\langle T\left[\left(i\frac{\partial}{\partial t_1}+\frac{\nabla_1^2}{2m}\right)\hat{\psi}(1)\hat{\psi}^\dagger(1')\right]\rangle \\ &= \pm\frac{1}{i}\int d\mathbf{r}_2\; v(\mathbf{r}_1-\mathbf{r}_2)\langle T\left(\hat{\psi}(1)\hat{\psi}(2)\hat{\psi}^\dagger(2^+)\hat{\psi}^\dagger(1')\right)\rangle\Big|_{t_2=t_1} \\ &= \pm i\int d\mathbf{r}_2\; v(\mathbf{r}_1-\mathbf{r}_2)G_2(12;1'2^+)\Big|_{t_2=t_1}. \qquad (2.27)\end{aligned}$$

The notation 2^+ denotes that the time argument of $\hat{\psi}^\dagger(2)$ must be chosen to be infinitesimally larger than the time arguments of the $\hat{\psi}$'s in order that the time ordering in G_2 reproduce the order of factors that appears in (2.26).

The commutation relation between spatial derivative and time-ordering operation is given by

$$\begin{aligned}\frac{\partial}{\partial t_1}\langle T\left(\hat{\psi}(1)\hat{\psi}^\dagger(1')\right)\rangle - \langle T\left(\frac{\partial}{\partial t_1}\hat{\psi}(1)\hat{\psi}^\dagger(1')\right)\rangle \\ &= \delta(t_1-t_{1'})\langle\left(\hat{\psi}(1)\hat{\psi}^\dagger(1')\mp\hat{\psi}^\dagger(1')\hat{\psi}(1)\right)\rangle \\ &= \delta(t_1-t_{1'})\;\delta(\mathbf{r}_1-\mathbf{r}_{1'})=\delta(1-1'). \qquad (2.28)\end{aligned}$$

Then we find that Eq. (2.27) becomes an equation of motion for G:

$$\left(i\frac{\partial}{\partial t_1}+\frac{\nabla_1^2}{2m}\right)G(1,1')=\delta(1-1')\pm i\int d\mathbf{r}_2\; v(\mathbf{r}_1-\mathbf{r}_2)G_2(12;1'2^+)\Big|_{t_2=t_1}. \quad (2.29)$$

Eq. (2.29) is a first-order differential equation in time and thus a single boundary condition is required to fix its solution precisely. The necessary boundary condition is Eq. (2.15).

2.1.3 The Hartree and Hartree-Fock approximations

To determine G for an interacting theory, i.e., when the potential $v \neq 0$, we must know the two-particle Green's function G_2 that appears in Eq. (2.29) and encodes the interaction. Approximations to G_2 can be done by the propagator interpretation of $G(1,1')$ and $G_2(12;1'2')$. The one-particle Green's function, $G(1,1')$, represents the propagation of a particle added to the medium at $1'$ and removed at 1. We can represent this by

$G(1,1') =$ 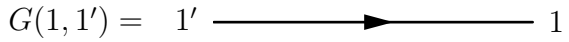

Note that the arrow represents propagation through the medium and not the vacuum. Accordingly, the two-particle Green's function, $G_2(12;1'2')$, which describes the propagation of two particles added to the medium at $1'$ and $2'$ and removed at 1 and 2, can be represented by

$G_2(12;1'2') =$ 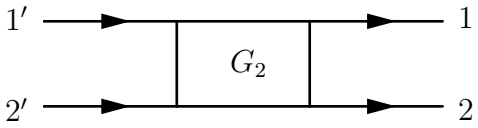

In general, the motion of the particles is correlated, however, in first approximation, we can neglect this correlation

$G_2(12;1'2') =$ 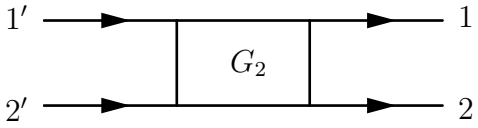

$\approx$ 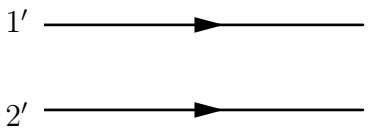

$= G(1,1')G(2,2')$

and then, with the redefinition (2.13), the equation of motion (2.29) becomes

$$\left(i\frac{\partial}{\partial t_1} + \frac{\nabla_1^2}{2m} - \int d\mathbf{r}_2\; v(\mathbf{r}_1 - \mathbf{r}_2)\langle n(\mathbf{r}_2)\rangle\right) G(1,1') = \delta(1-1'). \tag{2.30}$$

Eq. (2.30) is a Green's function form of the Hartree approximation. The potential field

$$U(\mathbf{r}_1) = \int d\mathbf{r}_2\; v(\mathbf{r}_1 - \mathbf{r}_2)\langle n(\mathbf{r}_2)\rangle \tag{2.31}$$

is called the self-consistent Hartree field or Hartree mean field and has the interpretation of the average field generated by all other particles in the system.

The Hartree approximation does not take into account the quantum statistics due to the identity of particles. We cannot distinguish processes, in which the particle added at $1'$ appears at 1 from processes in which it appears at 2, because the particles are identical. To include this possibility of exchange, we have to approximate $G_2(12;1'2')$ by

$G_2(12;1'2') =$ 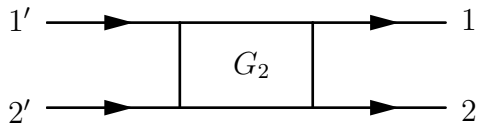

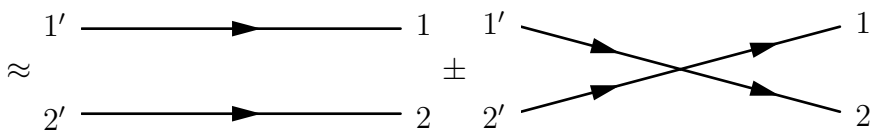

$$= G(1,1')G(2,2') \pm G(1,2')G(2,1'). \tag{2.32}$$

This approximation is called the Hartree-Fock approximation and the equation of motion (2.29) takes the form

$$\left(i\frac{\partial}{\partial t_1} + \frac{\nabla_1^2}{2m}\right) G(1,1') + \int d\mathbf{r}_2 \; \langle \mathbf{r}_1|U|\mathbf{r}_2\rangle G(2,1')\Big|_{t_2=t_1} = \delta(1-1'), \tag{2.33}$$

where the potential operator

$$\langle \mathbf{r}_1|U|\mathbf{r}_2\rangle = \delta(\mathbf{r}_1-\mathbf{r}_2)\int d\mathbf{r}_3 \; v(\mathbf{r}_1-\mathbf{r}_3)\langle n(\mathbf{r}_3)\rangle + iv(\mathbf{r}_1-\mathbf{r}_2)G^<(1,2)\Big|_{t_2=t_1} \tag{2.34}$$

has the interpretation of an average, self-consistent Hartree-Fock mean-field potential, which takes into account the (anti)symmetry of bosons (fermions). Note, however, that with the inclusion of the exchange term U becomes non-local in space.

2.1.4 The Born collision approximation

The Hartree and Hartree-Fock approximations predict an unphysical infinite lifetime for any state produced by adding a single particle to the system. The simplest process that can lead to a finite lifetime is the one in which two particles added at $1'$ and $2'$ and propagate to the spatial points $\bar{\mathbf{r}}_1$ and $\bar{\mathbf{r}}_2$. The interpretation is that at the time $\bar{t}_1$ the potential acts between the particles, scattering them. Then the particles propagate to the points 1 and 2, where they are removed from the system. We can represent the contribution of this process to G_2 by

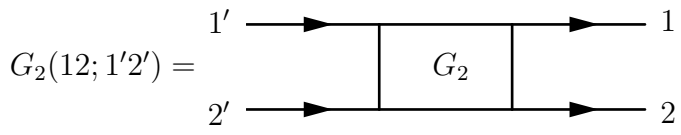

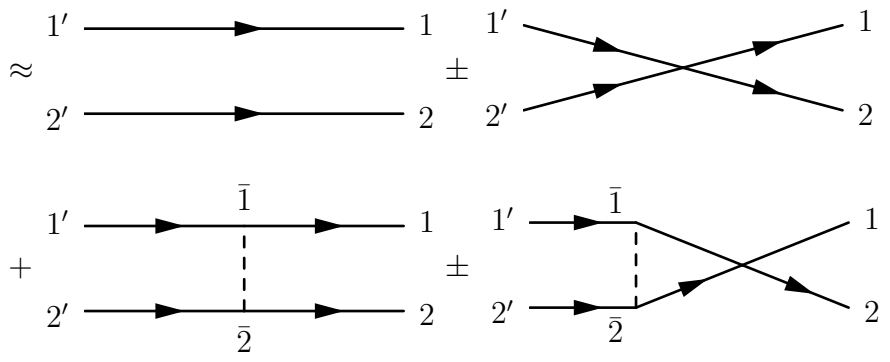

$$
\begin{aligned}
= \; & G(1,1')G(2,2') \pm G(1,2')G(2,1') \\
& + i\int_0^{-i\beta} d\bar{t}_1 d\bar{\mathbf{r}}_1 d\bar{\mathbf{r}}_2 \; v(\bar{\mathbf{r}}_1 - \bar{\mathbf{r}}_2)\Big[G(1,\bar{1})G(\bar{1},1')G(2,\bar{2})G(\bar{2},2') \\
& \pm G(2,\bar{1})G(\bar{1},1')G(1,\bar{2})G(\bar{2},2')\Big]\Big|_{\bar{t}_2 = \bar{t}_1}. \qquad (2.35)
\end{aligned}
$$

The approximation (2.35) for G_2 is called the Born scattering or collision approximation. Inserting (2.35) into the equation of motion (2.27) we end up with the following form for the Born scattering approximation

$$
\left[i\frac{\partial}{\partial t_1} + \frac{\nabla_1^2}{2m}\right] G(1,1') - \int_0^{-i\beta} d\bar{t}_1 d\bar{\mathbf{r}}_1 \; \Sigma(1,\bar{1})G(\bar{1},1') = \delta(1-1'), \quad 0 < it_{1(1')} < \beta, \qquad (2.36)
$$

where $\Sigma(1,1')$, which is called the self-energy, can be split into two parts,

$$
\Sigma(1,1') = \Sigma_{\mathrm{HF}}(1,1') + \Sigma_{\mathrm{C}}(1,1'). \qquad (2.37)
$$

The Hartree-Fock part is defined by

$$
\begin{aligned}
\Sigma_{\mathrm{HF}}(1,1') = \delta(t_1 - t_{1'})\Big[\delta(\mathbf{r}_1 - \mathbf{r}_{1'}) \int d\mathbf{r}_2 \; v(\mathbf{r}_1 - \mathbf{r}_2)\langle n(\mathbf{r}_2)\rangle \\
+ iv(\mathbf{r}_1 - \mathbf{r}_2)G^{<}(1,2)\Big|_{t_2 = t_1}\Big], \qquad (2.38)
\end{aligned}
$$

while the collision part of the self-energy in the Born scattering approximation is given by

$$
\begin{aligned}
\Sigma_{\mathrm{C}}(1,1') = \pm \, i^2 \int d\mathbf{r}_2 d\mathbf{r}_{2'} \; v(\mathbf{r}_1 - \mathbf{r}_2)v(\mathbf{r}_{1'} - \mathbf{r}_{2'}) \\
\times \Big[G(1,1')G(2,2')G(2',2) \pm G(1,2')G(2,1')G(2',2)\Big]\Big|_{t_2 = t_1, t_{2'} = t_{1'}} \qquad (2.39)
\end{aligned}
$$

The Fourier transform of the collisional part of the self-energy is

$$\begin{aligned}\Sigma_{\rm C}(\mathbf{p},t-t') = \pm\, i^2 \int \frac{d\mathbf{p}'}{(2\pi)^3}\frac{d\mathbf{p}}{(2\pi)^3}\frac{d\bar{\mathbf{p}}'}{(2\pi)^3} \\ \times\frac{1}{2}[v(\mathbf{p}-\bar{\mathbf{p}})\pm v(\mathbf{p}-\bar{\mathbf{p}}')]^2(2\pi)^3\delta(\mathbf{p}+\mathbf{p}'-\bar{\mathbf{p}}-\bar{\mathbf{p}}') \\ \times G(\mathbf{p}',t'-t)G(\bar{\mathbf{p}},t-t')G(\bar{\mathbf{p}}',t-t'). \qquad (2.40)\end{aligned}$$

The integrand in Eq. (2.40) describes processes, in which particles with momentum $\mathbf{p}$ and $\mathbf{p}'$ scatter into states with momentum $\bar{\mathbf{p}}$ and $\bar{\mathbf{p}}'$ as well as the inverse processes. The delta function represents the conservation of momentum, while $(1/2)[v(\mathbf{p}-\bar{\mathbf{p}})\pm v(\mathbf{p}-\bar{\mathbf{p}}')]^2$ represents the first Born approximation collision cross section with (anti)symmetrization included.

The self-energy (2.39) is composed of two analytic functions:

$$\Sigma_{\rm C}(\mathbf{p},t-t') = \begin{cases}\Sigma^{>}(\mathbf{p},t-t')\ , & \text{for} \quad it > it'\ , \\ \Sigma^{<}(\mathbf{p},t-t')\ , & \text{for} \quad it < it'\ ,\end{cases} \qquad (2.41)$$

where, in analogy to Eq. (2.40),

$$\begin{aligned}\Sigma^{>}(\mathbf{p},t-t') &= \int ...\ G^{<}(\mathbf{p}',t'-t)G^{>}(\bar{\mathbf{p}},t-t')G^{>}(\bar{\mathbf{p}}',t-t') \\ \Sigma^{<}(\mathbf{p},t-t') &= \int ...\ G^{>}(\mathbf{p}',t'-t)G^{<}(\bar{\mathbf{p}},t-t')G^{<}(\bar{\mathbf{p}}',t-t').\end{aligned} \qquad (2.42)$$

According to Eq. (2.17) the functions $\Sigma^{>}$ and $\Sigma^{<}$ can be represented as

$$\begin{aligned}\Sigma^{>}(\mathbf{p},t) &= \int_{-\infty}^{\infty}\frac{d\omega}{2\pi i}\ \Sigma^{>}(\mathbf{p},\omega)e^{-i\omega t}, \\ \Sigma^{<}(\mathbf{p},t) &= \pm\int_{-\infty}^{\infty}\frac{d\omega}{2\pi i}\ \Sigma^{<}(\mathbf{p},\omega)e^{-i\omega t}.\end{aligned} \qquad (2.43)$$

The collisional part of the self-energy satisfies the same boundary condition (2.15) as G. Thus, for $0 < it_{1'} < \beta$,

$$\Sigma_{\rm C}(1,1')\Big|_{t_1=0} = \pm\, e^{\beta\mu}\ \Sigma_{\rm C}(1,1')\Big|_{t_1=-i\beta}. \qquad (2.44)$$

Therefore $\Sigma^{>}(\mathbf{p},\omega)$ and $\Sigma^{<}(\mathbf{p},\omega)$ are related in the same way as $G^{>}(\mathbf{p},\omega)$ and $G<(\mathbf{p},\omega)$. Thus

$$\Gamma(\mathbf{p},\omega) = \Sigma^{>}(\mathbf{p},\omega) + \Sigma^{<}(\mathbf{p},\omega) \tag{2.45}$$

and in analogy with Eq. (2.20),

$$\begin{aligned} \Sigma^{>}(\mathbf{p},\omega) &= \Gamma(\mathbf{p},\omega)\big[1 \pm f(\omega)\big], \\ \Sigma^{<}(\mathbf{p},\omega) &= \Gamma(\mathbf{p},\omega) f(\omega). \end{aligned} \tag{2.46}$$

In general, $\Gamma(\mathbf{p},\omega)$ depends on the frequency ω. However, if this is a slowly varying function of the frequency, we can associate Γ to the lifetime of the single-particle excited state with momentum $\mathbf{p}$.

The spectral function, $A(\mathbf{p},\omega)$, and width, $\Gamma(\mathbf{p},\omega)$, are connected by the dispersion relation

$$A(\mathbf{p},\omega) = \frac{\Gamma(\mathbf{p},\omega)}{\Big[\omega - E(\mathbf{p}) - \mathrm{Re}\Sigma_{\mathrm{C}}(\mathbf{p},\omega)\Big]^2 + \left[\dfrac{\Gamma(\mathbf{p},\omega)}{2}\right]^2}, \tag{2.47}$$

where $\mathrm{Re}\Sigma_{\mathrm{C}}(\mathbf{p},\omega)$ can be interpreted as the average energy gained by a particle with momentum $\mathbf{p}$ due to its correlations with all the other particles in the system.

2.2 Nonequilibrium quantum field theory

The recapitulation of the relativistic quantum many-body theory in this Section is based closely on Ref. [50] in order to have a consistency in concepts and definitions with Chapter 3.

2.2.1 The Schwinger-Keldysh formalism

The starting point of the Schwinger-Keldysh formalism [45,48,49] (also known as the closed time path formalism or in-in formalism) is the observation that not only scattering amplitudes allow for a representation in terms of path integrals but also the time evolution of expectation values of operators. In this formalism all quantities are given on a special real-time contour with the time argument running from $-\infty$ to t on the chronological branch $(+)$ and returning from t to $-\infty$ on the antichronological branch $(-)$. It is important

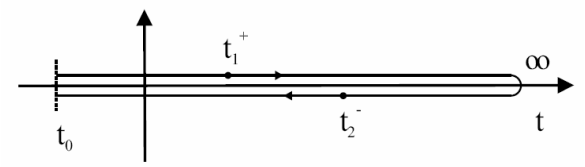

Figure 2.1: The closed time contour in the Schwinger-Keldysh formalism. The figure is taken from Ref. [50].

to remember that the two branches of integration are independent such that in the Heisenberg picture operators are path ordered and not time ordered.

In case of systems prepared at time t_0, this value is (instead of $-\infty$) the start and end point of real-time contour (cf. Fig. 2.1). In particular, the path ordered Green's functions (in case of real scalar fields $\phi(x)$) are defined as

$$\begin{aligned} G(x,y) &= \langle T^P(\phi(x)\phi(y))\rangle \\ &= \Theta^P(x_0-y_0)\langle(\phi(x)\phi(y))\rangle + \Theta^P(y_0-x_0)\langle(\phi(y)\phi(x))\rangle, \end{aligned} \tag{2.48}$$

where the operator T^P orders the field operators according to the position of their arguments on the real-time path as accomplished by the path step-function Θ^P. The expectation value in Eq. (2.48) is taken with respect to some initially given density matrix ρ_0, which is constant in time, while the operators in the Heisenberg picture contain the entire time dependence of the nonequilibrium system and can be represented as in Eq. (2.5), i.e.,

$$\hat{O}(t) = e^{i\hat{H}(t-t_0)}\hat{O}(0)e^{-i\hat{H}(t-t_0)}. \tag{2.49}$$

Self-consistent equations of motion for these Green's functions can be obtained with help of the two-particle irreducible (2PI) effective action $\Gamma[G]$, which is given by

$$\Gamma[G] = \Gamma^0 + \frac{i}{2}[\ln(1-\odot_p G_0 \odot_p \Sigma) + \odot_p G \odot_p \Sigma] + \Phi[G] \tag{2.50}$$

in case of vanishing vacuum expectation value $\langle 0|\phi(x)|0\rangle = 0$. In Eq. (2.50) Γ^0 depends only on free Green's functions and its treated as a constant, while the symbols $\odot_p$ represent convolution integrals over the closed time path in Fig. 2.1. The functional Φ is the sum of all closed 2PI diagrams built up by

full propagators G; it determines the self-energies by functional variation as

$$\Sigma(x,y) = 2i\frac{\delta\Phi}{\delta G(y,x)}. \tag{2.51}$$

From the effective action (2.50) the equations of motion for the Green's function are determined by the stationary condition

$$\delta\Gamma/\delta G = 0, \tag{2.52}$$

giving the Dyson-Schwinger equation for the full path-ordered Green's function as

$$G(x,y)^{-1} = G_0(x,y)^{-1} - \Sigma(x,y). \tag{2.53}$$

As in case of quantum mechanics, the evaluation of operators in quantum field theory then leads to path-ordered expectation values. This leads to the fact that the Dyson series of time-dependent perturbation theory does not only involve the time-ordered Green's functions, but also the anti-time-ordered and unordered ones. In line with the position of the coordinates on the contour there exist four different two-point functions

$$\begin{aligned} iG^c(x,y) &= iG^{++}(x,y) = \langle T^c\{\phi(x)\phi(y)\}\rangle, \\ iG^<(x,y) &= iG^{+-}(x,y) = \langle\{\phi(y)\phi(x)\}\rangle, \\ iG^>(x,y) &= iG^{-+}(x,y) = \langle\{\phi(x)\phi(y)\}\rangle, \\ iG^a(x,y) &= iG^{--}(x,y) = \langle T^a\{\phi(x)\phi(y)\}\rangle. \end{aligned} \tag{2.54}$$

Here $T^c(T^a)$ represent the (anti-)time-ordering operators in case of both arguments lying on the (anti-)chronological branch of the real-time contour. These four functions are not independent of each other. In particular, the chronological (2.21) and antichronological (2.24) Green's functions, G^c and G^a, are build up by the Wightman functions (2.10) and (2.11), $G^>$ and $G^<$.

2.2.2 The Kadanoff-Baym equations

By using the stationary condition for the action (2.52) and resolving the time structure in the Dyson-Schwinger equation (2.53) we obtain the Kadanoff-

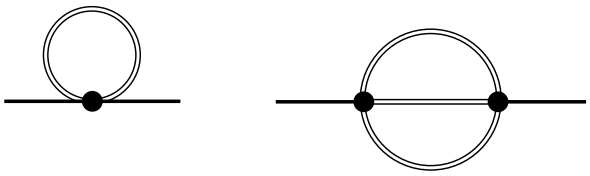

Figure 2.2: Self-energies of the Kadanoff-Baym equation: tadpole self-energy (l.h.s.) and sunset self-energy (r.h.s.). Since the lines represent full Green's functions the self-energies are self-consistent with the external coordinates indicated by full dots. The figure is taken from Ref. [50].

Baym equations for the time evolution of the Wightman functions [43, 51, 52]:

$$\begin{aligned}
-[\partial_\mu^x \partial_x^\mu + m^2] G^{\lessgtr}(x,y) &= \Sigma^\delta(x) G^{\lessgtr}(x,y) \\
&+ \int_{t_0}^{x_0} dz_0 \int d^d z \; [\Sigma^>(x,z) - \Sigma^<(x,z)] G^{\lessgtr}(z,y) \\
&- \int_{t_0}^{y_0} dz_0 \int d^d z \; \Sigma^{\lessgtr}(x,z) [G^>(z,y) - G^<(z,y)], \\
-[\partial_\mu^y \partial_y^\mu + m^2] G^{\lessgtr}(x,y) &= \Sigma^\delta(y) G^{\lessgtr}(x,y) \\
&+ \int_{t_0}^{x_0} dz_0 \int d^d z \; [G^>(x,z) - G^<(x,z)] \Sigma^{\lessgtr}(z,y) \\
&- \int_{t_0}^{y_0} dz_0 \int d^d z \; G^{\lessgtr}(x,z) [\Sigma^>(z,y) - \Sigma^<(z,y)],
\end{aligned} \tag{2.55}$$

where d denotes the spatial dimension of the problem. The path-ordered self-energy in Eq. (2.55) has been divided into a local contribution Σ^δ and a nonlocal one, which can be expressed—analogously to the Green's functions (2.48)—by a sum over path Θ functions. The self-energy entering the Dyson-Schwinger equation (2.53) is written as

$$\begin{aligned}
\Sigma(x,y) = \Sigma^\delta(x) \delta_p^{(d+1)}(x-y) + \Theta_p(x_0 - y_0) \Sigma^>(x,y) \\
+ \Theta_p(y_0 - x_0) \Sigma^<(x,y).
\end{aligned} \tag{2.56}$$

The scalar ϕ^4-theory can be considered here as an example for a fully relativistic field theory. Within the three-loop approximation for the 2PI effective action one gets two different self-energies: In leading order of the coupling con-

stant only the local tadpole diagram (l.h.s. of Fig. 2.2) contributes and leads to the generation of an effective mass for the field quanta. This self-energy (in coordinate space) is given by

$$\Sigma^{\delta}(x) = \frac{\lambda}{2} i G^{<}(x,x) \tag{2.57}$$

and is local in space and time. In next order in the coupling constant (i.e., λ^2) the nonlocal sunset self-energy (r.h.s. of Fig. 2.2) enters the time evolution as

$$\Sigma^{\lessgtr}(x,y) = -\frac{\lambda^2}{6} G^{\lessgtr}(x,y) G^{\lessgtr}(x,y) G^{\lessgtr}(x,y) \tag{2.58}$$

$$\Rightarrow \Sigma^{\lessgtr}(x,y) = -\frac{\lambda^2}{6} \left[G^{\lessgtr}(x,y)\right]^3 . \tag{2.59}$$

Thus the Kadanoff-Baym equation (2.55) in our case includes the influence of a mean field on the particle propagation—generated by the tadpole diagram—as well as scattering processes as inherent in the sunset diagram.

The Kadanoff-Baym equation describes the full quantum nonequilibrium time evolution on the two-point level for a system prepared at an initial time t_0, i.e., when higher-order correlations are discarded. The causal structure of this initial value problem is obvious since the time integrations are performed over the past up to the actual time x_0 (or y_0, respectively) and do not extend to the future.

Furthermore, also linear combinations of the Green's functions in single-time representation are of interest. The retarded Green's function G^R and the advanced Green's function G^A are given as

$$\begin{aligned} G^R(x,y) &= \Theta(x_0 - y_0)[G^{>}(x,y) - G^{<}(x,y)] \\ &= \Theta(x_0 - y_0)\langle [\phi(x)\phi(y)]_- \rangle \\ &= G^c(x,y) - G^{<}(x,y) = G^{>}(x,y) - G^a(x,y), \end{aligned} \tag{2.60}$$

$$\begin{aligned} G^A(x,y) &= -\Theta(y_0 - x_0)[G^{>}(x,y) - G^{<}(x,y)] \\ &= -\Theta(y_0 - x_0)\langle [\phi(x)\phi(x)]_- \rangle \\ &= G^c(x,y) - G^{>}(x,y) = G^{<}(x,y) - G^a(x,y). \end{aligned} \tag{2.61}$$

These Green's functions contain exclusively spectral, but no statistical information of the system. Their time evolution is determined by Dyson-Schwinger

equations and given by

$$-[\partial_\mu^x \partial_x^\mu + m^2 + \Sigma^\delta(x)]G^{R/A}(x,y) = \delta^{(d+1)}(x-y) + \int d^{d+1}z\ \Sigma^{R/A}(x,z)G^{R/A}(z,y), \quad (2.62)$$

where the retarded and advanced self-energies, Σ^R and Σ^A, can be defined via $\Sigma^>$ and $\Sigma^<$ similar to the Green's functions.

2.2.3 Generalized transport equations

For the derivation of generalized transport equations let us start by rewriting the Kadanoff-Baym equation (2.55) for the Wightman functions in coordinate space ($x_1 = (t_1, \mathbf{x_1}), x_2 = (t_2, \mathbf{x_2})$) as

$$[\partial_\mu^{x_1} \partial_{x_1}^\mu + m^2 + \Sigma^\delta(x_1)]iG^{\lessgtr}(x_1,x_2) = iI_1^{\lessgtr}(x_1,x_2). \quad (2.63)$$

The collision terms on the r.h.s. of Eq. (2.63) are given in $D = d+1$ space-time dimensions by convolution integrals over coordinate space self-energies and Green's functions:

$$I_1^{\lessgtr}(x_1,x_2) = -\int_{t_0}^{t_1} d^D z\ [\Sigma^>(x_1,z) - \Sigma^<(x_1,z)]G^{\lessgtr}(z,x_2) + \int_{t_0}^{t_2} d^D z\ \Sigma^{\lessgtr}(x_1,z)[G^>(z,x_2) - G^<(z,x_2)], \quad (2.64)$$

where Σ^δ is the local (non-dissipative) part of the path self-energy, while $\Sigma^{\lessgtr}$ stand for the nonlocal collisional self-energy contributions. In Eq. (2.64) the integration boundaries are exclusively given for the time coordinates, while the integration over the spatial coordinates extends over the whole spatial volume from $-\infty$ to $+\infty$ in d dimensions.

Since transport theories are formulated in phase space one changes to the Wigner representation via Fourier transformation with respect to the rapidly varying ("intrinsic") relative coordinate $\Delta x = x_1 - x_2$ and treats the system evolution in terms of the ("macroscopic") mean space-time coordinate $x = (x_1 + x_2)/2$ and the four-momentum $p = (p_0, \mathbf{p})$. The functions in Wigner

space are obtained as

$$\bar{F}(p,x) = \int_{-\infty}^{\infty} d^D\Delta x e^{i\Delta x_\mu p^\mu} F(x_1 = x + \Delta x/2, x_2 = x - \Delta x/2). \tag{2.65}$$

A convolution integral in D dimensions as appearing in Eq. (2.64) (for arbitrary functions F, G),

$$H(x_1,x_2) = \int_{-\infty}^{\infty} d^D z\ F(x_1,z)G(z,x_2) \tag{2.66}$$

transforms as

$$\begin{aligned}\bar{H}(p,x) &= \int_{-\infty}^{\infty} d^D\Delta x\ e^{i\Delta x_\mu p^\mu} H(x_1,x_2)\\ &= \Delta x e^{i\Delta x_\mu p^\mu} \Delta x e^{i\Delta x_\mu p^\mu} \int_{-\infty}^{\infty} d^D z\ F(x_1,z)G(z,x_2)\\ &= e^{i(1/2)(\partial_p^\mu \partial_\mu^{x'} - \partial_x^\mu \partial_\mu^{p'})} \left[\bar{F}(p,x)\bar{G}(p',x')\right]\Big|_{x'=x,p'=p}. \end{aligned}\tag{2.67}$$

In accordance with the standard assumption of transport theory we assume that all functions only smoothly evolve in the mean space-time coordinates and thus restrict to first-order derivatives. All terms proportional to second- or higher-order derivatives in the mean space-time coordinates (also mixed ones) will be neglected here. Thus the Wigner transformed convolution integrals (2.66) are given in first-order gradient expansion by,

$$\bar{H}(p,x) = \bar{F}(p,x)\bar{G}(p,x) + i\frac{1}{2}\{\bar{F}(p,x),\bar{G}(p,x)\} + O(\partial_x^2), \tag{2.68}$$

where the relativistic generalization of the Poisson bracket is defined as

$$\{\bar{F}(p,x),\bar{G}(p,x)\} = \partial_\mu^p \bar{F}(p,x)\partial_x^\mu \bar{G}(p,x) - \partial_\mu^x \bar{F}(p,x)\partial_p^\mu \bar{G}(p,x). \tag{2.69}$$

As a next step, we rewrite the memory terms in the collision integrals (2.64) such that the time integrations extend from $-\infty$ to $+\infty$. In this respect we consider the initial time $t_0 = -\infty$, whereas the upper time boundaries t_1 and

t_2 are taken into account by $\Theta-$functions, i.e.,

$$\begin{aligned} I_1^{\lessgtr}(x_1,x_2) &= -\int_{-\infty}^{\infty} d^D x'\ \Theta(t_1-t')[\Sigma^{>}(x_1,x')-\Sigma^{<}(x_1,x']G^{\lessgtr}(x',x_2) \\ &+ \int_{-\infty}^{\infty} d^D x'\ \Sigma^{\lessgtr}(x_1,x')\Theta(t_2-t')[G^{>}(x',x_2)-G^{<}(x',x_2)] \\ &= -\int_{-\infty}^{\infty} d^D x' \left[\Sigma^R(x_1,x')G^{\lessgtr}(x',x_2)+\Sigma^{\lessgtr}(x_1,x')G^A(x',x_2)\right] \end{aligned} \tag{2.70}$$

We now perform a first-order gradient expansion of the Wigner transformed Kadanoff-Baym equation using Eq. (2.70) for the memory integrals. Then we separate the real and the imaginary parts in the resulting equation, which have to be satisfied independently. At the end of this procedure one obtains a generalized transport equation [42, 47, 53–58]:

$$\underbrace{2p^\mu\partial_\mu^x i\bar{G}^{\lessgtr}-\{\mathrm{Re}\bar{\Sigma}^R,i\bar{G}^{\lessgtr}\}}_{\{\bar{M},i\bar{G}^{\lessgtr}\}} -\{i\bar{\Sigma}^{\lessgtr},\mathrm{Re}\bar{G}^R\}=i\bar{\Sigma}^{<}i\bar{G}^{>}-i\bar{\Sigma}^{>}i\bar{G}^{<}. \tag{2.71}$$

One additionally obtains a generalized mass-shell equation

$$\underbrace{[p^2-m^2-\mathrm{Re}\bar{\Sigma}^R]}_{\bar{M}}\,i\bar{G}^{\lessgtr}=i\bar{\Sigma}^{\lessgtr}\mathrm{Re}\bar{G}^R+\frac{1}{4}\{i\bar{\Sigma}^{>},i\bar{G}^{<}\}-\frac{1}{4}\{i\bar{\Sigma}^{<},i\bar{G}^{>}\} \tag{2.72}$$

with the mass function

$$\bar{M}=p^2-m^2-\mathrm{Re}\bar{\Sigma}^R. \tag{2.73}$$

In the transport equation (2.71) one recognizes on the l.h.s. the drift term $p^\mu\partial_\mu^x i\bar{G}^{\lessgtr}$ as well as the Vlasov term with the real part of the retarded self-energy $\mathrm{Re}\bar{\Sigma}^R$. On the other hand, the r.h.s. of Eq. (2.71) represents the collision term with its typical "gain and loss" structure. Thus the interaction between the degrees of freedom is incorporated into the mean-field and collision terms as in the Vlasov-Boltzmann "standard" transport approach [59]. In contrast, in the off-shell transport there is an additional term $-\{i\bar{\Sigma}^{\lessgtr},\mathrm{Re}\bar{G}^R\}$, which is denoted as the back-flow term and is responsible for the proper off-shell propagation. It vanishes in the on-shell quasiparticle limit. Note, however, that the self-energies $\bar{\Sigma}$ fully determine the dynamics of the Green's functions for

given initial conditions.

We, further on, represent Eqs. (2.71) and (2.72) in terms of real quantities by the decomposition of the retarded and advanced Green's functions and self-energies as

$$\bar{G}^{R/A} = \mathrm{Re}\bar{G}^{R} \pm i\mathrm{Im}\bar{G}^{R} = \mathrm{Re}\bar{G}^{R} \mp i\bar{A}/2, \tag{2.74}$$

$$\bar{A} = \mp 2\mathrm{Im}\bar{G}^{R/A}, \tag{2.75}$$

$$\bar{\Sigma}^{R/A} = \mathrm{Re}\bar{\Sigma}^{R} \pm i\mathrm{Im}\bar{\Sigma}^{R} = \mathrm{Re}\bar{\Sigma}^{R} \mp i\bar{\Gamma}/2, \tag{2.76}$$

$$\bar{\Gamma} = \mp 2\mathrm{Im}\bar{\Sigma}^{R/A}. \tag{2.77}$$

We note that in Wigner space the real parts of the retarded and advanced Green's functions and self-energies are equal, while the imaginary parts have opposite sign and are proportional to the spectral function $\bar{A}$ and to the width $\bar{\Gamma}$, respectively.

With the redefinitions (2.74)–(2.77) one obtains two algebraic relations for the spectral function $\bar{A}$ and the real part of the retarded Green's function, $\mathrm{Re}\bar{G}^{R}$, in terms of the width $\bar{\Gamma}$ and the real part of the retarded self-energy, $\mathrm{Re}\bar{\Sigma}^{R}$, as [47, 50, 53]

$$\left[p_0^2 - \mathbf{p}^2 - m^2 - \mathrm{Re}\bar{\Sigma}^{R}\right] \mathrm{Re}\bar{G}^{R} = 1 + \frac{1}{4}\bar{\Gamma}\bar{A}, \tag{2.78}$$

$$\left[p_0^2 - \mathbf{p}^2 - m^2 - \mathrm{Re}\bar{\Sigma}^{R}\right] \bar{A} = \bar{\Gamma}\mathrm{Re}\bar{G}^{R}. \tag{2.79}$$

Note that all terms with first-order gradients have disappeared in Eqs. (2.78) and (2.79). A first consequence of Eq. (2.79) is a direct relation between the real and the imaginary parts of the retarded, advanced Green's function, which reads (for $\bar{\Gamma} \neq 0$)

$$\mathrm{Re}\bar{G}^{R} = \frac{p_0^2 - \mathbf{p}^2 - m^2 - \mathrm{Re}\bar{\Sigma}^{R}}{\bar{\Gamma}}\bar{A}. \tag{2.80}$$

Inserting Eq. (2.80) in Eq. (2.78) we end up with the following result for the spectral function and the real part of the retarded Green's function:

$$\bar{A} = \frac{\bar{\Gamma}}{\left[p_0^2 - \mathbf{p}^2 - m^2 - \mathrm{Re}\bar{\Sigma}^{R}\right]^2 + \bar{\Gamma}^2/4}, \tag{2.81}$$

$$\mathrm{Re}\bar{G}^{R} = \frac{\left[p_0^2 - \mathbf{p}^2 - m^2 - \mathrm{Re}\bar{\Sigma}^{R}\right]}{\left[p_0^2 - \mathbf{p}^2 - m^2 - \mathrm{Re}\bar{\Sigma}^{R}\right]^2 + \bar{\Gamma}^2/4}. \tag{2.82}$$

The spectral function (2.81) shows a typical Breit-Wigner shape with energy- and momentum-dependent self-energy terms. Although the above equations are purely algebraic solutions and contain no derivative terms, they are valid up to the first order in the gradients.

In addition, subtraction of the real parts and adding up the imaginary parts lead to the time-evolution equations

$$p^\mu \partial_\mu^x \bar{A} = \frac{1}{2}\left\{\mathrm{Re}\bar{\Sigma}^R, \bar{A}\right\} + \frac{1}{2}\left\{\bar{\Gamma}, \mathrm{Re}\bar{G}^R\right\}, \tag{2.83}$$

$$p^\mu \partial_\mu^x \mathrm{Re}\bar{G}^R = \frac{1}{2}\left\{\mathrm{Re}\bar{\Sigma}^R, \mathrm{Re}\bar{G}^R\right\} - \frac{1}{8}\left\{\bar{\Gamma}, \bar{A}\right\}. \tag{2.84}$$

The Poisson bracket containing the mass function $\bar{M}$ leads to the well-known drift operator $p^\mu \partial_\mu^x \bar{F}$ (for an arbitrary function $\bar{F}$), i.e.,

$$\{\bar{M}, \bar{F}\} = \{p_0^2 - \mathbf{p}^2 - m^2 - \mathrm{Re}\bar{\Sigma}^R, \bar{F}\} = 2p^\mu \partial_\mu^x \bar{F} - \{\mathrm{Re}\bar{\Sigma}^R, \bar{F}\} \tag{2.85}$$

such that the first-order equations (2.83) and (2.84) can be written in a more comprehensive form as

$$\{\bar{M}, \bar{A}\} = \{\bar{\Gamma}, \mathrm{Re}\bar{G}^R\}, \tag{2.86}$$

$$\{\bar{M}, \mathrm{Re}\bar{G}^R\} = -\frac{1}{4}\{\bar{\Gamma}, \bar{A}\}. \tag{2.87}$$

When inserting Eqs. (2.81) and (2.82) we find that these first-order time-evolution equations are solved by the algebraic expressions. In this case the following relations hold:

$$\{\bar{M}, \bar{A}\} = \{\bar{\Gamma}, \mathrm{Re}\bar{G}^R\} = \{\bar{M}, \bar{\Gamma}\}\frac{\bar{M}^2 - \bar{\Gamma}^2/4}{[\bar{M}^2 + \bar{\Gamma}^2/4]^2}, \tag{2.88}$$

$$\{\bar{M}, \mathrm{Re}\bar{G}^R\} = -\frac{1}{4}\{\bar{\Gamma}, \bar{A}\} = \{\bar{M}, \bar{\Gamma}\}\frac{\bar{M}\bar{\Gamma}/2}{[\bar{M}^2 + \bar{\Gamma}^2/4]^2}. \tag{2.89}$$

Thus we have derived the proper structure of the spectral function (2.81) within the first-order gradient (or semiclassical) approximation. Together with the explicit form for the real part of the retarded Green's function (2.82) we now have fixed the dynamics of spectral properties, which is consistent up to first order in the gradients.

In order to evaluate the $\{i\bar{\Sigma}^<, \mathrm{Re}\bar{G}^R\}$-term on the l.h.s. of Eq. (2.71) it is useful to introduce distribution functions and self-energies as (cf. Eqs. (2.20)

and (2.46))

$$i\bar{G}^<(p,x) = \bar{N}(p,x)\bar{A}(p,x), \quad i\bar{G}^>(p,x) = [1+\bar{N}(p,x)]\bar{A}(p,x), \quad (2.90)$$
$$i\bar{\Sigma}^<(p,x) = \bar{N}^\Sigma(p,x)\bar{\Gamma}(p,x), \quad i\bar{\Sigma}^>(p,x) = [1+\bar{N}^\Sigma(p,x)]\bar{\Gamma}(p,x). \quad (2.91)$$

In equilibrium the distribution function with respect to the Green's functions $\bar{N}$ and the self-energies $\bar{N}^\Sigma$ are given as Bose functions in the energy p_0 at given temperature. They thus are equal in equilibrium, but in general might differ out of equilibrium. Following the argumentation of Botermans and Malfliet [55] the distribution functions $\bar{N}$ and $\bar{N}^\Sigma$ in Eqs. (2.90) and (2.91) should be identical within the second term of the l.h.s. of Eq. (2.71) in order to obtain a consistent first-order gradient expansion. In order to demonstrate their argument we write

$$i\bar{\Sigma}^< = \bar{N}\bar{\Gamma} + \bar{K}, \quad (2.92)$$

where the "correction" term

$$\bar{K} = \bar{\Gamma}(\bar{N}^\Sigma - \bar{N}) = (i\bar{\Sigma}^< i\bar{G}^> - i\bar{\Sigma}^> i\bar{G}^<)\bar{A}^{-1} \quad (2.93)$$

is proportional to the collision term of the generalized transport equation (2.71), which itself is already of first order in gradients. Thus, whenever a distribution function $\bar{N}^\Sigma$ appears within a Poisson bracket, the difference term $(\bar{N}^\Sigma - \bar{N})$ becomes of second order in the gradients and should be neglected. As a consequence $\bar{N}^\Sigma$ can be replaced by $\bar{N}$ and thus the self-energy $\bar{\Sigma}^\lessgtr$ by $\bar{G}^\lessgtr\bar{\Gamma}/\bar{A}$ in the Poisson bracket term $\{\bar{\Sigma}^\lessgtr, \mathrm{Re}\bar{G}^R\}$. The generalized transport equation (2.71) then can be written in shorthand notation as

$$\frac{1}{2}\bar{A}\bar{\Gamma}\left[\{\bar{M}, i\bar{G}^<\} - \frac{1}{\bar{\Gamma}}\{\bar{\Gamma}, \bar{M}i\bar{G}^<\}\right] = i\bar{\Sigma}^< i\bar{G}^> - i\bar{\Sigma}^> i\bar{G}^< \quad (2.94)$$

with the mass function $\bar{M}$ (3.2). Numerically, the off-shell transport equation (2.94) can be solved by employing a generalized testparticle ansatz for the real quantity $i\bar{G}^<(x,p)$, which will be discussed in Sec. 2.2.4.

2.2.4 Testparticle representation

To obtain an approximate solution to the transport equation (2.94) we use a testparticle ansatz for the Green's function $G^<$, more specifically for the real and positive quantity $F(x,p)$, which represents the probability to find a

particle in a given phase-space cell,

$$F(x,p) = \bar{A}(p)N(x,p) = iG^<(x,p) \\ \sim \sum_{i=1}^{N} \delta^{(3)}[\mathbf{x} - \mathbf{x}_i(t)]\delta^{(3)}[\mathbf{p} - \mathbf{p}_i(t)]\delta[p_0 - \varepsilon_i(t)]. \tag{2.95}$$

The testparticle method was applied to the generalized transport equation first in Ref. [53]. In the most general case (where self-energies depend on four-momentum p, time t and the spatial coordinates $\mathbf{x}$) the equations of motion for the testparticles become (cf. Ref. [47])

$$\frac{d\mathbf{x}}{dt} = \frac{1}{1-C_{(i)}}\frac{1}{2\varepsilon_i}\left[2\mathbf{p}_i + \boldsymbol{\nabla}_{p_i}\mathrm{Re}\Sigma^R_{(i)} + \frac{\varepsilon_i^2 - \mathbf{p}_i^2 - M_0^2 - \mathrm{Re}\Sigma^R_{(i)}}{\Gamma_{(i)}}\boldsymbol{\nabla}_{p_i}\Gamma_{(i)}\right], \tag{2.96}$$

$$\frac{d\mathbf{p}}{dt} = \frac{1}{1-C_{(i)}}\frac{1}{2\varepsilon_i}\left[\boldsymbol{\nabla}_{x_i}\mathrm{Re}\Sigma^R_{(i)} + \frac{\varepsilon_i^2 - \mathbf{p}_i^2 - M_0^2 - \mathrm{Re}\Sigma^R_{(i)}}{\Gamma_{(i)}}\boldsymbol{\nabla}_{x_i}\Gamma_{(i)}\right], \tag{2.97}$$

$$\frac{d\varepsilon_i}{dt} = \frac{1}{1-C_{(i)}}\frac{1}{2\varepsilon_i}\left[\frac{\partial\mathrm{Re}\Sigma^R_{(i)}}{\partial t} + \frac{\varepsilon_i^2 - \mathbf{p}_i^2 - M_0^2 - \mathrm{Re}\Sigma^R_{(i)}}{\Gamma_{(i)}}\frac{\partial\Gamma_{(i)}}{\partial t}\right], \tag{2.98}$$

where the notation $F_{(i)}$ implies that the function is taken at the coordinates of the testparticle, i.e., $F_{(i)} \equiv F(t, \mathbf{x}_i(t), \mathbf{p}_i(t), \varepsilon_i(t))$. The quantity $C_{(i)}$, which contains the energy derivatives of the retarded self-energy, is defined as

$$C_{(i)} = \frac{1}{2\varepsilon_i}\left[\frac{\partial\mathrm{Re}\Sigma^R_{(i)}}{\partial\varepsilon_i} + \frac{\varepsilon_i^2 - \mathbf{p}_i^2 - M_0^2 - \mathrm{Re}\Sigma^R_{(i)}}{\Gamma_{(i)}}\frac{\partial\Gamma_{(i)}}{\partial\varepsilon_i}\right]. \tag{2.99}$$

It yields a shift of the system time t to the "eigentime" of particle i defined by $\bar{t} = t/(1 - C_{(i)})$. Then the derivatives with respect to the "eigentime", i.e., $d\mathbf{x}_i/d\bar{t}_i$, $d\mathbf{p}_i/d\bar{t}_i$, and $d\varepsilon_i/d\bar{t}_i$ emerge without the renormalization factor, $(1-C_{(i)})^{-1}$, for each testparticle i when neglecting higher-order time derivatives in line with the semiclassical approximation scheme.

When self-energies only depend on space-time coordinates, i.e., $\mathrm{Re}\Sigma^R_{(i)}(x,p) = \mathrm{Re}\Sigma^R_{(i)}(x)$, and the width vanishes, $\Gamma_{(i)} = 0$, we obtain directly the familiar equations of motion in the quasiparticle approximation assuming quasiparticles states with an effective mass squared, $M_0^2 + \mathrm{Re}\Sigma^R_{(i)}(x)$, and a spectral function, which is proportional to a δ-function. This limit has been used in transport theories [60–62] although its applicability should be restricted to low collision rates.

In case of a momentum-independent width $\Gamma(x)$ we take $M^2 = p^2 - \mathrm{Re}\Sigma^R$

as an independent variable instead of p_0, which then fixes the energy (for given $\mathbf{p}$ and M) to

$$p_0^2 = \mathbf{p}^2 + M^2 + \mathrm{Re}\Sigma^R(x, \mathbf{p}). \tag{2.100}$$

Then Eq. (2.98) can be written as

$$\frac{d\Delta M_i^2}{dt} = \frac{\Delta M_i^2}{\Gamma_{(i)}} \frac{d\Gamma_{(i)}}{dt} \qquad \Leftrightarrow \qquad \frac{d}{dt} \ln\left(\frac{\Delta M_i^2}{\Gamma_{(i)}}\right) = 0 \tag{2.101}$$

for the time evolution of the testparticle i in the invariant mass squared, with $\Delta M_i^2 = M_i^2 - M_0^2$.

2.2.5 Collision terms

The collision term of the Kadanoff-Baym equation can only be worked out in more detail by giving explicit approximations for $\Sigma^<$ and $\Sigma^>$. A corresponding collision term can be formulated in full analogy to Refs. [63, 64], e.g., from Dirac-Brueckner theory following detailed balance as

$$\begin{aligned} I_{coll}(x, \mathbf{p}, M^2)A = {} & \mathrm{Tr}_2\mathrm{Tr}_3\mathrm{Tr}_4 A(x, \mathbf{p}, M^2)A(x, \mathbf{p}_2, M_2^2)A(x, \mathbf{p}_3, M_3^2)A(x, \mathbf{p}_4, M_4^2) \\ & \times |T[(\mathbf{p}, M^2) + (\mathbf{p}_2, M_2^2) \to (\mathbf{p}_3, M_3^2) + (\mathbf{p}_4, M_4^2)]|_{a,s}^2 \delta^{(4)}(p + p_2 - p_3 - p_4) \\ & \times \left[N_{x\mathbf{p}_3 M_3^2} N_{x\mathbf{p}_4 M_4^2} \bar{f}_{x\mathbf{p}M^2} \bar{f}_{x\mathbf{p}_2 M_2^2} - N_{x\mathbf{p}M^2} N_{x\mathbf{p}_2 M_2^2} \bar{f}_{x\mathbf{p}_3 M_3^2} \bar{f}_{x\mathbf{p}_4 M_4^2} \right] \end{aligned} \tag{2.102}$$

with

$$\bar{f}_{x\mathbf{p}M^2} = 1 + \eta N_{x\mathbf{p}M^2} \tag{2.103}$$

and $\eta = \pm 1$ for bosons (upper sign) and fermions (lower sign), respectively. The indices a, s stand for the (anti)symmetric matrix element of the in-medium scattering amplitude T in case of bosons (fermions). In Eq. (2.102) the trace over particles 2, 3, 4 reads explicitly for fermions

$$\mathrm{Tr}_2 = \sum_{\sigma_2, \tau_2} \frac{1}{(2\pi)^4} \int d^3\mathbf{p}_2 \frac{dM_2^2}{2\sqrt{\mathbf{p}_2^2 + M_2^2}}, \tag{2.104}$$

where σ_2, τ_2 denote spin and isospin of particle 2. In case of bosons we have

$$\mathrm{Tr}_2 = \sum_{\sigma_2, \tau_2} \frac{1}{(2\pi)^4} \int d^3\mathbf{p}_2 \frac{dp_{0,2}^2}{2}, \tag{2.105}$$

since here the spectral function A_B is normalized as

$$\int \frac{dp_0^2}{4\pi} A_B(x,p) = 1, \tag{2.106}$$

whereas for fermions we have

$$\int \frac{dp_0}{2\pi} A_F(x,p) = 1. \tag{2.107}$$

Neglecting the "gain-term" in Eq. (2.102) one recognizes that the collisional width of the particle in the rest frame is given by

$$\begin{aligned}\Gamma_{coll}(x,\mathbf{p},M^2) = \mathrm{Tr}_2\mathrm{Tr}_3\mathrm{Tr}_4 |T\left[(\mathbf{p},M^2)+(\mathbf{p}_2,M_2^2)\to(\mathbf{p}_3,M_3^2)+(\mathbf{p}_4,M_4^2)\right]|^2_{a,s} \\ \times A(x,\mathbf{p}_2,M_2^2)A(x,\mathbf{p}_3,M_3^2)A(x,\mathbf{p}_4,M_4^2)\delta^{(4)}(p+p_2-p_3-p_4) \\ \times N_{x\mathbf{p}_2M_2^2}\bar{f}_{x\mathbf{p}_3M_3^2}\bar{f}_{x\mathbf{p}_4M_4^2},\end{aligned} \tag{2.108}$$

where—as in Eq. (2.102)—local on-shell processes are assumed for the transitions $p+p_2 \to p_3+p_4$. We note that the extension of Eq. (2.102) to inelastic scattering processes (e.g., $NN \to N\Delta$, etc.) is straightforward when exchanging the elastic transition amplitude T by the corresponding inelastic one and taking care of Pauli-blocking or Bose-enhancement factors for the particles in the final state.

For particles of infinite lifetime in vacuum—such as protons—the collisional width (2.108) has to be identified with twice the imaginary part of the self-energy. Thus the transport approach determines the particle spectral function via Eq. (2.108) for all particles if the in-medium transition amplitudes T are known in their full off-shell dependence. Since this information is not available for configurations of hot and dense matter, a couple of assumptions and numerical approximation schemes have to be invoked in actual applications—such as the PHSD transport approach—for the investigations within this work.

2.3 Summary

In this Chapter we have recalled the basic definitions of the Green's function techniques in nonequilibrium many-body theory. The Hartree and Hartree-Fock approximations as well as the Born collision approximation in a non-relativistic quantum many-body systems have been presented as first- and

second-order approximations. Based on the Schwinger-Keldysh formalism and on the two-particle irreducible (2PI) approach we have extended the nonequilibrium Green's function techniques to relativistic systems for "resummed" propagators and couplings. The derivation of Kadanoff-Baym equations and the generalized transport equations were shown, too. Furthermore, in order to obtain an approximate solution to the resulting transport equation (in first-order gradient expansion) we have presented the generalized expressions for testparticle equations of motion in 8-dimensional phase space. Finally, we have given the collision term of the Kadanoff-Baym equation in momentum representation.

Chapter 3

The Parton-Hadron-String Dynamics Transport Approach

The Parton-Hadron-String Dynamics (PHSD) approach is a microscopic covariant transport model [23–25], which is in line with generalized transport equations on the basis of the off-shell Kadanoff-Baym equations [42–44] for Green's functions in phase-space representation (in the first-order gradient expansion, beyond the quasiparticle approximation) (cf. Sec. 2.2). The approach consistently describes the full evolution of a relativistic heavy-ion collision from the initial hard scatterings and string formation through the dynamical deconfinement phase transition to the strongly interacting quark-gluon plasma (sQGP) as well as hadronization and the subsequent interactions in the expanding hadronic phase. In the hadronic sector PHSD is equivalent to the Hadron-String-Dynamics (HSD) transport approach [63,65] that has been used for the description of pA and AA collisions from GSI heavy-ion synchrotron (SIS) to RHIC energies in the past.

In particular, PHSD incorporates off-shell dynamics for partons and hadrons. In the off-shell transport description, the hadron and parton spectral functions change dynamically during the propagation through the medium and—in case of hadrons—evolve toward the on-shell spectral function in vacuum if the system expands in the course of heavy-ion collisions. As demonstrated in [47,53,66] the off-shell dynamics is important for hadronic resonances with a rather long lifetime in vacuum but strongly decreasing lifetime in the nuclear medium (especially ω and ϕ mesons) and also proves vital for the correct description of dilepton decays of ρ mesons with masses close to the two-pion decay threshold.

3.1 Explicit equations for fermions

The generalized transport equations are implemented in PHSD in the integral forms (2.71) and (2.72) by using the following representation for the self-energies. In case of fermions—such as baryons or quarks—the real part of the self-energy $\mathrm{Re}\bar{\Sigma}^R$ is separated into different Lorentz structures of scalar and vector type:

$$\mathrm{Re}\bar{\Sigma}^R = 2\omega(U_h^S(x,p) + \gamma_\mu U_h^\mu(x,p)) \tag{3.1}$$

for each fermion species h. The mass function for fermions is then

$$M_h(p,x) = \Pi_0^2 - \mathbf{\Pi}^2 - m_h^{*2} \ , \tag{3.2}$$

with the effective mass and four-momentum given by

$$m_h^*(x,p) = m_h + U_h^S(x,p) \ , \tag{3.3}$$

$$\Pi^\mu(x,p) = p^\mu - U_h^\mu(x,p) \ , \tag{3.4}$$

where m_h stands for the bare (vacuum) mass. After inserting Eq. (3.2) into the generalized transport equation (2.71), the covariant off-shell transport theory emerges. It is formally written as a coupled set of transport equations for the phase-space distributions $N_h(x,p)$ ($x=(t,\mathbf{r})$, $p=(\omega,\mathbf{p})$) of fermion h with a spectral function $A_h(x,p)$ (using $i\bar{G}_h^<(x,p) = N_h(x,p)A_h(x,p)$), i.e.,

$$\begin{aligned}
&\left(\Pi_\mu - \Pi_\nu \partial_\mu^p U_h^\nu - m_h^* \partial_\mu^p U_h^S\right) \partial_x^\mu N_h(x,p) A_h(x,p) \\
&\qquad + \left(\Pi_\nu \partial_\mu^x U_h^\nu + m_h^* \partial_\mu^x U_h^S\right) \partial_p^\mu N_h(x,p) A_h(x,p) - \{i\bar{\Sigma}^<, \mathrm{Re}\bar{G}^R\} \\
&= (2\pi)^4 \sum_{h_2 h_3 h_4} \mathrm{tr}_2 \mathrm{tr}_3 \mathrm{tr}_4 [T^\dagger T]_{12\to 34} \\
&\quad \times \delta^4(\Pi + \Pi_2 - \Pi_3 - \Pi_4) A_h(x,p) A_{h_2}(x,p_2) A_{h_3}(x,p_3) A_{h_4}(x,p_4) \\
&\quad \times \left[N_{h_3}(x,p_3) N_{h_4}(x,p_4) \bar{f}_h(x,p) \bar{f}_{h_2}(x,p_2) - N_h(x,p) N_{h_2}(x,p_2) \bar{f}_{h_3}(x,p_3) \bar{f}_{h_4}(x,p_4)\right]
\end{aligned} \tag{3.5}$$

with

$$\bar{f}_h(x,p) = 1 - N_h(x,p)$$

and

$$\mathrm{tr}_n = \int \frac{d^4 p_n}{(2\pi)^4}.$$

Here $\partial^x_\mu \equiv (\partial_t, \nabla_\mathbf{r})$ and $\partial^p_\mu \equiv (\partial_\omega, \nabla_\mathbf{p})$ ($\mu = 0, 1, 2, 3$). The factor $|T^\dagger T|$ stands for the in-medium transition matrix element (squared) for the binary reaction $1 + 2 \to 3 + 4$, which has to be known also off the mass shell. The back-flow term in (3.5) is given by

$$-\{i\bar{\Sigma}^<, \mathrm{Re}\bar{G}^R\} \approx \partial^\mu_p \left(\frac{M_h(x,p)}{M_h(x,p)^2 + \Gamma_h(x,p)^2/4} \right) \partial^x_\mu \left[N_h(x,p)\Gamma_h(x,p) \right] - \partial^x_\mu \left(\frac{M_h(x,p)}{M_h(x,p)^2 + \Gamma_h(x,p)^2/4} \right) \partial^\mu_p \left[N_h(x,p)\Gamma_h(x,p) \right]. \quad (3.6)$$

As pointed out before, this expression stands for the off-shell evolution, which vanishes in the on-shell limit or when the spectral function $A_h(x,p)$ does not change its shape during the propagation through the medium, i.e., for $\nabla_\mathbf{r}\Gamma(x,p) = 0$ and $\nabla_\mathbf{p}\Gamma(x,p) = 0$. We recall that the transport equations (3.5) have been the basis for the off-shell HSD transport approach for the baryon and antibaryon dynamics [63] before they were applied also to the quark and gluon dynamics within the PHSD transport.

In order to specify the dynamics of partons one has to evaluate/specify the related self-energies for quarks and antiquarks as well as gluons that enter the spectral functions (2.81) and retarded Green's functions (2.82). This task has been carried out within a dynamical quasiparticle model, which will be presented in Sec. 3.2 (following Ref. [50]).

3.2 The Dynamical Quasiparticle Model

The basis of the partonic phase description in PHSD is the dynamical quasiparticle model (DQPM) [16, 17, 50, 67, 68], which describes QCD properties in terms of single-particle Green's functions (in the sense of a two-particle irreducible (2PI) approach) and has been matched to reproduce lQCD results—including the partonic equation of state—in thermodynamic equilibrium. The DQPM allows for a simple and transparent interpretation of thermodynamic quantities, as will be demonstrated below, and correlators—measured on the lattice—by means of effective strongly interacting partonic quasiparticles with broad spectral functions. The essential quantities in the DQPM are the "resummed" single-particle propagators $\bar{G}_q$, $\bar{G}_{\bar{q}}$, and $\bar{G}_g$.

We stress that a nonvanishing width $\bar{\Gamma}$ (2.77) in the partonic spectral function is the main difference between the DQPM and conventional quasiparticle

models [19–22, 69]. Its influence on the collision dynamics is essentially seen in the correlation functions. E.g., in the stationary limit, the correlation involving the off-diagonal elements of the energy-momentum tensor T^{kl} define the shear viscosity η of the medium [18]. In Sec. 6.1 we will show that a sizable width is mandatory to obtain a small ratio of the shear viscosity to entropy density, η/s [70], which results in a roughly hydrodynamical evolution of the partonic system in PHSD [23]. The finite width leads to two-particle correlations, which are taken into account in PHSD by means of the generalized off-shell transport equations (cf. Sec. 2.2.3) that go beyond the mean-field and Boltzmann approximations.

3.2.1 Quasiparticle properties and thermodynamics of the DQPM from lattice QCD

The DQPM was first introduced by Peshier and Cassing [18, 67, 68]. The model assumes that the degrees of freedom of QCD at high temperatures are interacting massive quasiparticles—quarks, antiquarks, and gluons—with broad spectral functions.

Let us start with the entropy density in the quasiparticle limit [67, 71–74]

$$\begin{aligned} s^{dqp} &= d_q \int \frac{d\omega}{2\pi}\frac{d^3p}{(2\pi)^3}\frac{\partial n_F((\omega-\mu_q)/T)}{\partial T}(\mathrm{Im}\ln(-S_q^{-1}) + \mathrm{Im}\Sigma_q\,\mathrm{Re}S_q) \\ &- d_{\bar q} \int \frac{d\omega}{2\pi}\frac{d^3p}{(2\pi)^3}\frac{\partial n_F((\omega+\mu_q)/T)}{\partial T}(\mathrm{Im}\ln(-S_{\bar q}^{-1}) + \mathrm{Im}\Sigma_{\bar q}\,\mathrm{Re}S_{\bar q}) \\ &- d_g \int \frac{d\omega}{2\pi}\frac{d^3p}{(2\pi)^3}\frac{\partial n_B}{\partial T}(\mathrm{Im}\ln(-\Delta^{-1}) + \mathrm{Im}\Pi\,\mathrm{Re}\Delta), \end{aligned} \tag{3.7}$$

where n_F and n_B denote the Fermi and Bose distributions, respectively, and μ_q stands for the quark chemical potential, while $S_q = (p^2 - \Sigma_q)^{-1}$, $S_{\bar q} = (p^2 - \Sigma_{\bar q})^{-1}$, and $\Delta = (p^2 - \Pi)^{-1}$, with $p^2 = \omega^2 - \mathbf{p}^2$, denote scalar quasiparticle propagators of quarks q, antiquarks $\bar q$, and gluons g. The number of gluonic degrees of freedom is $d_g = 16$, while the fermion degrees of freedom amount to $d_q = d_{\bar q} = 2N_cN_f = 18$ in case of three flavors ($N_f = 3$). The quasiparticle limit here means the assumption that the spectral functions of particles have a single (well-defined) peak. The accuracy of this approximation can be judged by the size of the ratio Γ/M. In Eq. (3.7) $\Sigma = \Sigma_q \approx \Sigma_{\bar q}$ and Π stand for the quasiparticle self-energies.

For simplicity of presentation we consider here scalar quasiparticles, for

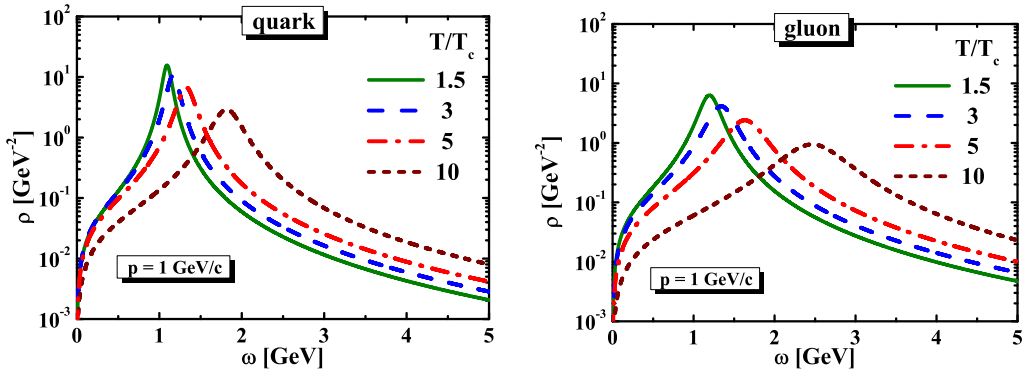

(a) (b)

Figure 3.1: The partonic spectral functions as functions of energy ω at given momentum $|\mathbf{p}| = 1$ GeV and for different temperatures, $T/T_c = 1.5$ (solid green lines), $T/T_c = 3$ (dashed blue lines), $T/T_c = 5$ (dash-dotted red lines), and $T/T_c = 10$ (short-dashed burgundy lines). (a) quarks and antiquarks; (b) gluons.

which the propagator Δ as well as the quasiparticle self-energy Π are considered as Lorentz scalars, however, keep in mind that in PHSD these quantities for quarks, antiquarks, and gluons are Lorentz tensors. The "dressed" propagators may be calculated in a nonpertubative framework. An alternative procedure is to employ an ansatz with a Lorentzian spectral function and to fit the few parameters to results from lQCD,

$$\begin{aligned} \bar{A}_j = \rho_j(\omega, \mathbf{p}) &= \frac{\Gamma_j}{E_j}\left(\frac{1}{(\omega - E_j)^2 + \Gamma_j^2} - \frac{1}{(\omega + E_j)^2 + \Gamma_j^2}\right) \\ &= \frac{4\omega\Gamma_j}{(\omega^2 - \mathbf{p}^2 - M_j^2)^2 + 4\Gamma_j^2\omega^2}, \end{aligned} \tag{3.8}$$

separately for quarks, antiquarks, and gluons ($j = q, \bar{q}, g$), with the notation $E_j^2(\mathbf{p}^2) = \mathbf{p}^2 + M_j^2 - \Gamma_j^2$. We may identify (cf. Sec. 2.2.3)

$$\mathrm{Re}\bar{\Sigma}_j^R = M_j^2, \qquad \bar{\Gamma}_j = 2\omega\Gamma_j. \tag{3.9}$$

Note that $\bar{\Gamma}$ in Eq. (3.9) corresponds to Γ in Chapter 2. The spectral function (3.8) is antisymmetric in ω and normalized as

$$\int_{-\infty}^{\infty} \frac{d\omega}{2\pi}\, \omega\rho_j(\omega, \mathbf{p}) = \int_{0}^{\infty} \frac{d\omega}{2\pi}\, 2\omega\rho_j(\omega, \mathbf{p}) = 1. \tag{3.10}$$

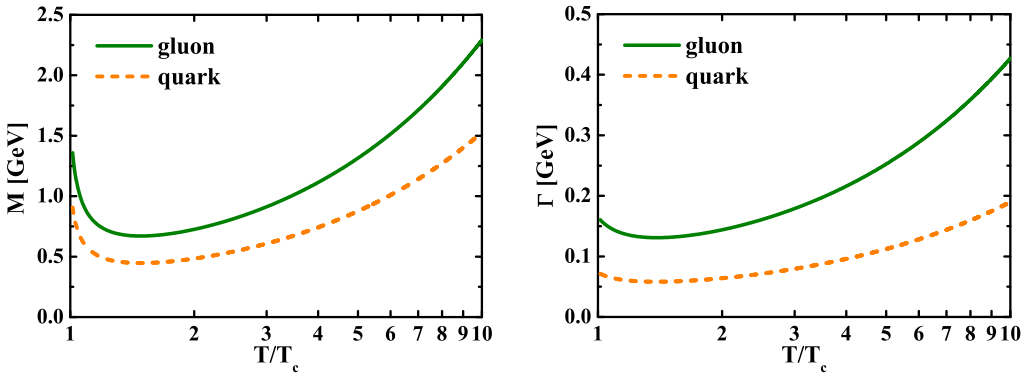

(a) (b)

Figure 3.2: The quasiparticle properties of quarks and antiquarks (short-dashed orange lines) and of gluons (solid green lines) as functions of the scaled temperature T/T_c ($T_c = 0.158$ GeV) (at $\mu_q = 0$). (a) mass; (b) width.

In Fig. 3.1 the fermionic (l.h.s.) and gluonic (r.h.s.) spectral functions at various values for the temperature, $T/T_c = 1.5$, 3, 5, 10, are shown (for the parameters fitted to lQCD).

The functional form of the parton quasiparticle mass is chosen to coincide with that of the perturbative thermal mass in the asymptotic high-momentum (high-temperature) regime, i.e., for quarks (antiquarks)

$$M^2_{q(\bar{q})}(T) = \frac{N_c^2 - 1}{8N_c} g^2 \left(T^2 + \frac{\mu_q^2}{\pi^2} \right), \tag{3.11}$$

and for gluons

$$M^2_g(T) = \frac{g^2}{6} \left(\left(N_c + \frac{1}{2} N_f \right) T^2 + \frac{N_c}{2} \sum_q \frac{\mu_q^2}{\pi^2} \right), \tag{3.12}$$

where the running coupling constant (squared) for $T > T_c$ is approximated by

$$g^2(T/T_c) = \frac{48\pi^2}{(11N_c - 2N_f) \ln[\lambda^2 (T/T_c - T_s/T_c)^2]}, \tag{3.13}$$

In Eqs. (3.11)–(3.13), $N_c = 3$ stands for the number of colors, T_c is the critical temperature, while $N_f(=3)$ denotes the number of flavors.

The effective quarks, antiquarks, and gluons in the DQPM have finite

widths, which for $\mu_q = 0$ are approximated by

$$\Gamma_{q(\bar{q})}(T) = \frac{1}{3}\frac{N_c^2 - 1}{2N_c}\frac{g^2 T}{8\pi}\ln\left(\frac{2c}{g^2} + 1\right), \tag{3.14}$$

$$\Gamma_g(T) = \frac{1}{3}N_c\frac{g^2 T}{8\pi}\ln\left(\frac{2c}{g^2} + 1\right), \tag{3.15}$$

where c is related to a magnetic cutoff. We stress here that the DQPM assumes $\Gamma_j = \text{const}(\omega)$. Also, the decomposition of the total width Γ_j into the collisional width (due to elastic and inelastic collisions) and the decay width is not addressed in the DQPM. This question will be discussed in Sec. 5.2. Note that for $\mu_q = 0$ the DQPM gives

$$M_{q(\bar{q})} = \frac{2}{3}M_g, \quad \Gamma_{q(\bar{q})} = \frac{4}{9}\Gamma_g \tag{3.16}$$

and reflects the ratio of the Casimir eigenvalues in color space. The temperature dependence (for $T > T_c$) for masses and widths of quasiparticles at $\mu_q = 0$ are displayed in Fig. 3.2.

From the expressions (3.11)–(3.16) one can see that at high temperature, $T \to \infty$, the masses and the interaction strength of the quasiparticles in the DQPM are approaching the one-loop perturbative QCD results.

After the real and imaginary parts of the propagators Δ and S (cf. Sec. 2.2.3) are determined by Eqs. (3.8)–(3.16) as functions of temperature, the entropy density (3.7) can be evaluated numerically and compared to lQCD results in order to extract the values for λ, T_c, T_s, and c.

With the resulting entropy density $s(T)$, we can calculate also the other thermodynamic quantities, such as the pressure P and the energy density ε, from the thermodynamic relations (for $\mu_q = 0$),

$$s(T) = \frac{\partial P}{\partial T}, \tag{3.17}$$

$$\varepsilon(T) = Ts - P \tag{3.18}$$

as well as the interaction measure

$$W(T) = \varepsilon(T) - 3P(T) = Ts - 4P \tag{3.19}$$

that vanishes for massless and noninteracting degrees of freedom.

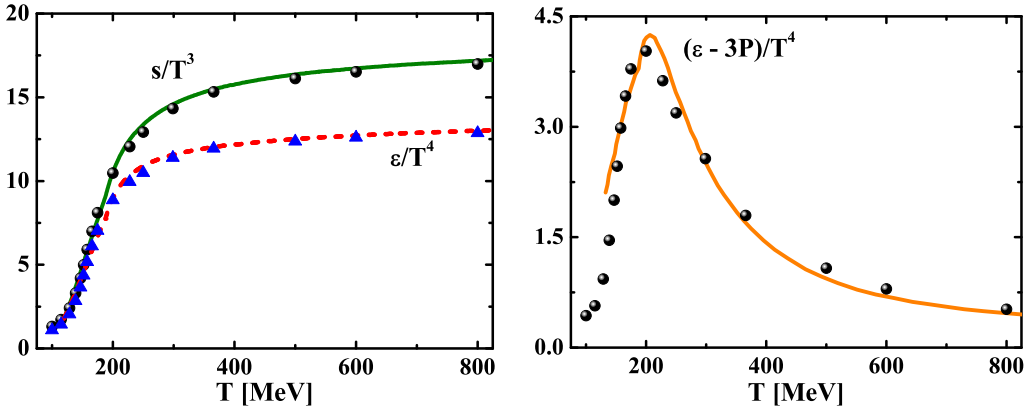

(a) (b)

Figure 3.3: The thermodynamic quantities as functions of temperature from the DQPM and corresponding lQCD results from Refs. [75, 76] (black dots and blue triangles). (a) the scaled entropy density $s(T)/T^3$ (solid green line) and scaled energy density $\varepsilon(T)/T^4$ (short-dashed red line); (b) the dimensionless interaction measure $(\varepsilon - 3P)/T^4$ (solid orange line).

After a direct comparison of the resulting entropy density $s(T)$ and energy density $\varepsilon(T)$ from the DQPM with lQCD results from Refs. [75, 76], which is presented in Fig. 3.3(a) (both results have been divided by T^3 and T^4, respectively), the parameters were fixed to: $T_c = 0.158$ GeV, $T_s/T_c = 0.56$, $\lambda = 2.42$, and $c = 14.4$. The dimensionless interaction measure $(\varepsilon - 3P)/T^4$ is presented in Fig. 3.3(b). The DQPM is thermodynamically consistent and represents a two-particle irreducible (2PI) approximation to hot QCD, once the free parameters in Eqs. (3.13)–(3.15) are fitted to lQCD results.

The results for the strong coupling constant for $T > T_c$, which in the DQPM is given by

$$\alpha_s(T/T_c) = \frac{g^2(T/T_c)}{4\pi} = \frac{12\pi}{(11N_c - 2N_f)\ln[\lambda^2(T/T_c - T_s/T_c)^2]}, \tag{3.20}$$

are presented in Fig. 3.4. For comparison, we show on the same plot the lQCD results for pure $SU_c(3)$ gauge theory ($N_f = 0$) from Ref. [77].

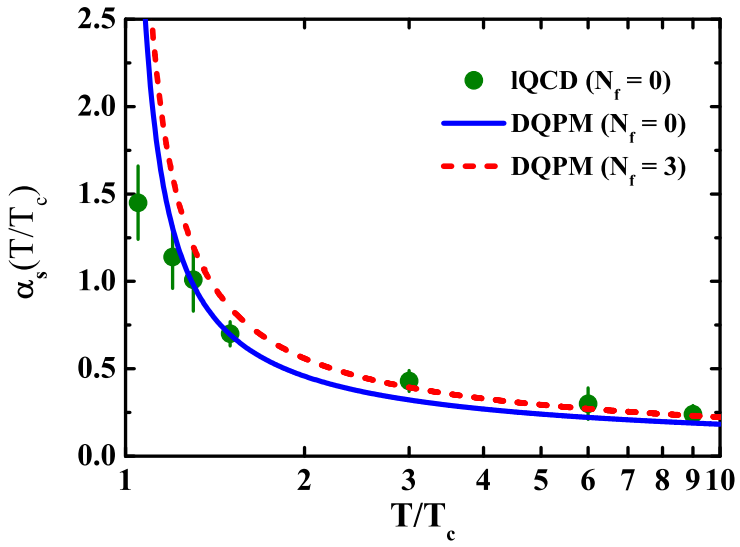

Figure 3.4: The results for the strong coupling, α_s, as a function of temperature from the DQPM for $N_f = 0$ (solid blue line) and for $N_f = 3$ (short-dashed red line) in comparison to the lQCD data from Ref. [77] (green dots).

3.2.2 Timelike and spacelike quantities

For the further description of the DQPM let us introduce the shorthand notations (following Ref. [50])

$$\begin{aligned}
\hat{\mathrm{Tr}}_q^{\pm} \ldots &= d_q \int \frac{d\omega}{2\pi}\frac{d^3p}{(2\pi)^3} 2\omega\rho_q(\omega,\mathbf{p})\Theta(\omega)n_F[(\omega-\mu_q)/T]\Theta(\pm p^2)\ldots, \\
\hat{\mathrm{Tr}}_{\bar{q}}^{\pm} \ldots &= d_{\bar{q}} \int \frac{d\omega}{2\pi}\frac{d^3p}{(2\pi)^3} 2\omega\rho_{\bar{q}}(\omega,\mathbf{p})\Theta(\omega)n_F[(\omega+\mu_q)/T]\Theta(\pm p^2)\ldots, \\
\hat{\mathrm{Tr}}_g^{\pm} \ldots &= d_g \int \frac{d\omega}{2\pi}\frac{d^3p}{(2\pi)^3} 2\omega\rho_g(\omega,\mathbf{p})\Theta(\omega)n_B(\omega/T)\Theta(\pm p^2)\ldots,
\end{aligned} \tag{3.21}$$

with $p^2 = \omega^2 - \mathbf{p}^2$ denoting the invariant mass squared, the spectral functions, $\rho_j(\omega,\mathbf{p})$, $(j = q,\bar{q},g)$, are taken in Lorentzian form (3.8), n_F and n_B are the Fermi and Bose distributions, respectively. The $\Theta(\pm p^2)$ function in Eq. (3.21) separates timelike $(+)$ quantities from spacelike $(-)$ quantities.

Following the notations (3.21), the "quasiparticle densities" are defined (in equilibrium) by

$$N_q^{\pm}(T) = \hat{\mathrm{Tr}}_q^{\pm} 1, \qquad N_{\bar{q}}^{\pm}(T) = \hat{\mathrm{Tr}}_{\bar{q}}^{\pm} 1, \qquad N_g^{\pm}(T) = \hat{\mathrm{Tr}}_g^{\pm} 1. \tag{3.22}$$

Note that only the timelike integrals over space have a particle number inter-

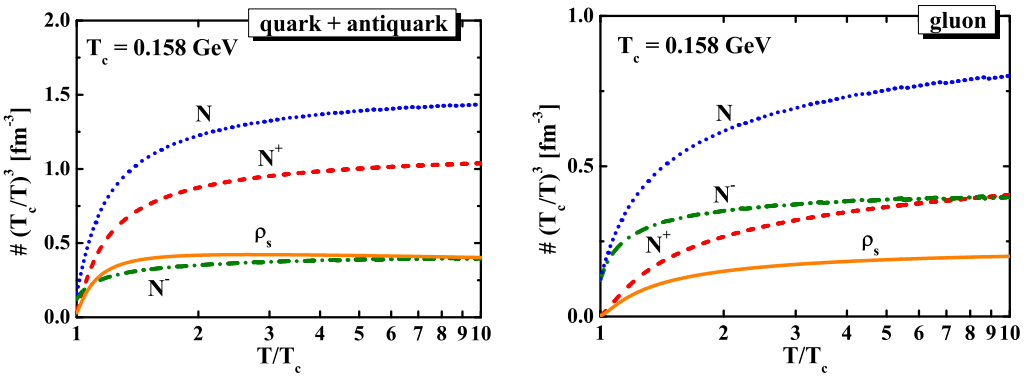

(a) (b)

Figure 3.5: The different "densities" (3.22) as well as the scalar densities (3.24) (at $\mu_q = 0$). The solid orange lines represent the scalar densities ρ_s, the short-dashed red lines—the timelike densities N^+, the dash-dotted green lines—the spacelike densities N^-, and the short-dotted blue lines are the sum $N = N^+ + N^-$ as functions of T/T_c. All densities are multiplied by the dimensionless factor $(T_c/T)^3$. (a) quarks and antiquarks; (b) gluons.

pretation, i.e., the parton density ρ_p is given as

$$\rho_p(T) = N_q^+ + N_{\bar{q}}^+ + N_g^+. \tag{3.23}$$

Scalar densities for quarks, antiquarks, and gluons are defined by integrating in the timelike sector

$$\rho_q^s(T) = \hat{\mathrm{Tr}}_q^+\left(\frac{\sqrt{p^2}}{\omega}\right), \quad \rho_{\bar{q}}^s(T) = \hat{\mathrm{Tr}}_{\bar{q}}^+\left(\frac{\sqrt{p^2}}{\omega}\right), \quad \rho_g^s(T) = \hat{\mathrm{Tr}}_g^+\left(\frac{\sqrt{p^2}}{\omega}\right). \tag{3.24}$$

The results for the different "densities" are presented in Fig. 3.5 for quarks and antiquarks (l.h.s.) and for gluons (r.h.s.).

Our further studies in the thesis mostly will be focussed on the PHSD simulations in a cubic box with periodic boundary conditions and it is useful to introduce the vector density ρ_v as

$$\rho_v(T) = N_q^+ + N_{\bar{q}}^+ + 2N_g^+, \tag{3.25}$$

because the total energy in the box, which can be expressed as a function of the vector density, will be conserved during the time evolution without running into numerical instabilities. One can use the timelike vector density as an independent variable, instead of the temperature T and chemical potential μ_q.

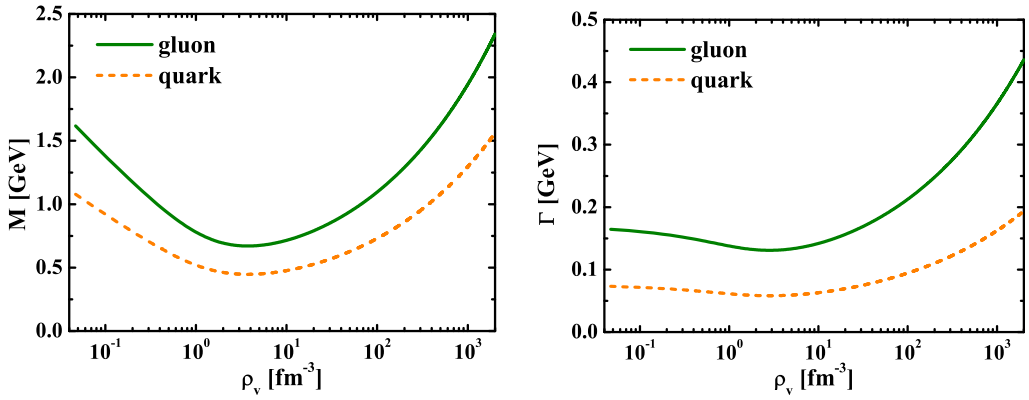

(a) (b)

Figure 3.6: The quasiparticle properties of quarks and antiquarks (short-dashed orange lines) and of gluons (solid green lines) as functions of the vector density ρ_v (at $\mu_q = 0$). (a) mass; (b) width.

This is useful for the numerical realization, because the quasiparticle properties are varying smoothly with ρ_v, while they depend on high powers of T. For example, the quasiparticle masses (3.11) and (3.12) as well as widths (3.14) and (3.15) are shown in Fig. 3.6 as functions of the vector density ρ_v.

We, furthermore, separate the spacelike and timelike components for the energy densities

$$T^{\pm}_{00,q}(T) = \hat{\mathrm{Tr}}^{\pm}_{q}\omega, \qquad T^{\pm}_{00,\bar{q}}(T) = \hat{\mathrm{Tr}}^{\pm}_{\bar{q}}\omega, \qquad T^{\pm}_{00,g}(T) = \hat{\mathrm{Tr}}^{\pm}_{g}\omega. \tag{3.26}$$

The spacelike parts of the energy densities are related to the potential energy densities (or interaction energy), while the timelike fractions are the quark, antiquark, and gluon quasiparticle energy densities, which propagate within the lightcone. The results for the quasiparticle energy densities of different components (at $\mu_q = 0$) are shown in Fig. 3.7 for quarks and antiquarks (l.h.s.) and for gluons (r.h.s.).

Summing up the timelike and spacelike contributions for quarks, antiquarks, and gluons we obtain the total energy density T^{00},

$$T^{00} = T^{+}_{00,q} + T^{+}_{00,\bar{q}} + T^{+}_{00,g} + T^{-}_{00,q} + T^{-}_{00,\bar{q}} + T^{-}_{00,g} \tag{3.27}$$

and the potential energy density V (only spacelike parts),

$$V = T^{-}_{00,q} + T^{-}_{00,\bar{q}} + T^{-}_{00,g}. \tag{3.28}$$

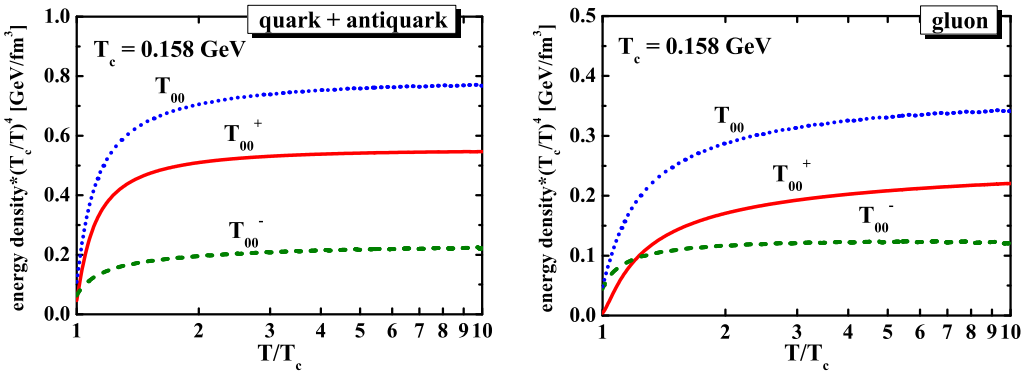

(a) (b)

Figure 3.7: The spacelike energy density T_{00}^{-} (short-dashed green lines), the timelike energy density T_{00}^{+} (solid red lines), and their sum $T_{00} = T_{00}^{-} + T_{00}^{+}$ (short-dotted blue lines) as functions of T/T_c. All densities are multiplied by the dimensionless factor $(T_c/T)^4$. (a) quarks and antiquarks; (b) gluons.

In Fig. 3.8(a) the dimensionless total energy density T^{00}/T^4 and the dimensionless potential energy density V/T^4 are presented as functions of temperature T. The quantity T^{00} practically coincides with the energy density ε (3.18) obtained from the thermodynamic relations. Small differences ($\approx$5%) relate to the systematic uncertainties in our study. The ratio of the potential V to total T^{00} energy density is displayed in Fig. 3.8(b). The ratio $V/T^{00} \approx 0.33$ holds for a very wide range of temperatures T.

3.2.3 Self-energies and effective interactions of quasiparticles

The spacelike quasiparticles cannot be propagated in transport approaches without violating causality and/or Lorentz invariance. It means that self-energies and scatterings of quasiparticles can be defined only for the timelike sector. However, as was discussed above, the spacelike part of the total energy density is interpreted as the partonic potential energy density (3.28).

It is useful to separate the potential energy density V into three parts: a pure fermionic interaction density V'_{qq}, a pure gluonic interaction density V'_{gg}, and a gluon-fermion interaction density V'_{gq}

$$V = V'_{qq} + V'_{gg} + V'_{gq} \tag{3.29}$$

and to add half of the interaction density V'_{gq} to the fermion and gluon parts

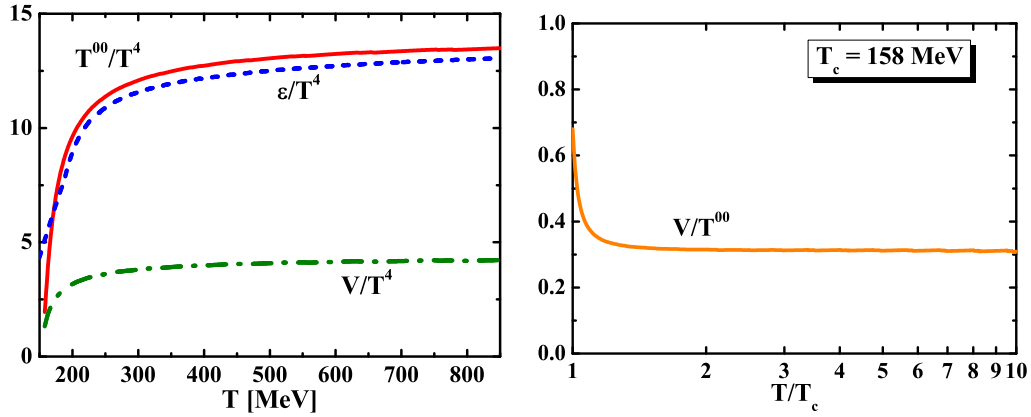

(a) (b)

Figure 3.8: (a) The scaled total quasiparticle energy density T^{00}/T^4 (solid red line), the scaled potential quasiparticle energy density V/T^4 (dash-dotted green line), and the DQPM results for ε/T^4 (short-dashed blue line) obtained from the thermodynamic relations as functions of temperature T; (b) The ratio of the total to potential quasiparticle energy density (solid orange line) as a function of temperature T.

separately, e.g.,

$$T^-_{00,g} = V'_{gg} + 0.5V'_{gq}, \qquad T^-_{00,q} + T^-_{00,\bar{q}} = V'_{qq} + 0.5V'_{gq}. \tag{3.30}$$

Let us introduce the quantity $\lambda(\rho_v)$ as a function of the vector density ρ_v (3.25)

$$\lambda(\rho_v) = \frac{V'_{qq} - V'_{gg}}{T^-_{00,q} + T^-_{00,\bar{q}} + T^-_{00,g}}. \tag{3.31}$$

Using the ansatz

$$V'_{qq} + V'_{gg} = (1-\xi)V, \tag{3.32}$$

we end up with the following expressions for the different interaction densities

$$V'_{gg} = 0.5(1-\xi-\lambda)V, \quad V'_{qq} = 0.5(1-\xi+\lambda)V, \quad V'_{gq} = \xi V, \tag{3.33}$$

but still with the unknown fraction ξ for the gluon-fermion interaction density V'_{gq}.

Mean-field potentials for quarks (including antiquarks), $U_q(\rho_v)$, and for

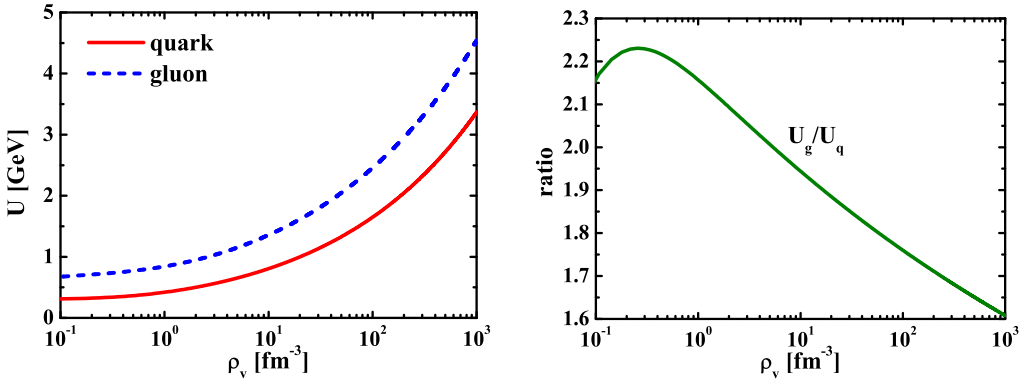

(a) (b)

Figure 3.9: (a) The mean-field potentials $U_q(\rho_v)$ for quarks—including antiquarks—(solid red line) and $U_q(\rho_v)$ for gluons (short-dashed blue line) as functions of the vector density ρ_v; (b) The ratio U_g/U_q (solid green line) as a function of the vector density ρ_v.

gluons, $U_g(\rho_v)$, can be determined as (cf. Refs. [16, 17, 78–80])

$$U_q(\rho_v) = \frac{\partial(V'_{qq} + V'_{gq})}{\partial(N_q^+ + N_{\bar{q}}^+)}, \qquad U_g(\rho_v) = \frac{\partial(V'_{gg} + V'_{gq})}{\partial N_g^+}, \tag{3.34}$$

which after inserting Eq. (3.33) gives

$$\begin{aligned} U_q(\rho_v) &= \frac{1}{2}\frac{\partial(1+\lambda+\xi)V}{\partial\rho_v}\frac{\partial\rho_v}{\partial(N_q^+ + N_{\bar{q}}^+)}, \\ U_g(\rho_v) &= \frac{1}{2}\frac{\partial(1-\lambda+\xi)V}{\partial\rho_v}\frac{\partial\rho_v}{\partial(N_g^+)}. \end{aligned} \tag{3.35}$$

Note that $\xi = \xi(\rho_p)$ is here taken to be a constant. In order to define the fraction of the interaction density, ξ, one has to fix this fraction in comparison to the gluon mean-field from Ref. [17], where the pure gluonic sector has be evaluated in the same way. As a result we obtain $\xi \approx 0.3$.

The results for mean-field potentials $U_q(\rho_v)$ and $U_g(\rho_v)$ are shown in Fig. 3.9(a). The ratio $U_g/U_q \approx 1.9$ holds, as can be seen in Fig. 3.9(b), for a very wide range of vector densities ρ_v within 10% accuracy.

The second derivatives of the potential energy density, V, relate to the

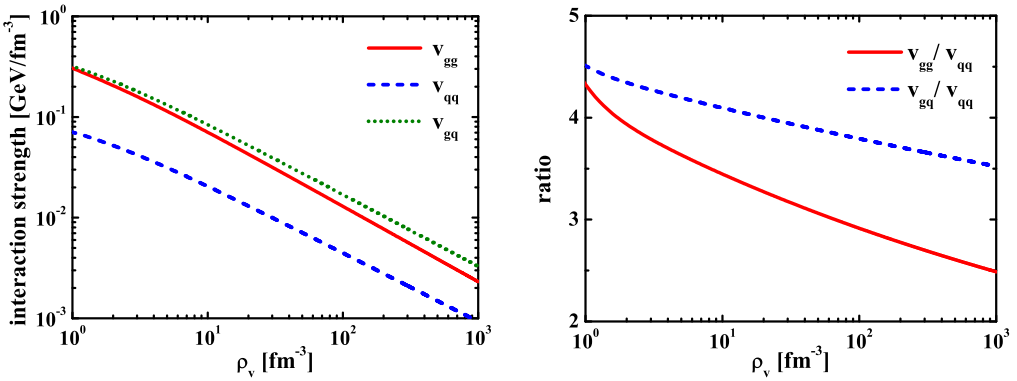

(a) (b)

Figure 3.10: (a) The effective gluon-gluon v_{gg} (solid red line), quark-quark v_{qq} (short-dashed blue line), and gluon-quark v_{gq} (short-dotted green line) interaction from the DQPM for $\xi = 0.3$ (see text) as functions of the vector density ρ_v; (b) The ratios v_{gg}/v_{qq} (solid red line) and v_{gq}/v_{qq} (short-dashed blue line) as a function of the vector density ρ_v.

effective fermion-fermion, gluon-fermion, and gluon-gluon interactions as

$$
\begin{aligned}
v_{qq}(\rho_v) &= \frac{\partial^2 V'_{qq}}{\partial(N_q^+ + N_{\bar{q}}^+)^2} \approx \frac{1}{2}\frac{\partial^2(1-\xi+\lambda)V}{\partial\rho_v^2}\left(\frac{\partial\rho_v}{\partial(N_q^+ + N_{\bar{q}}^+)}\right)^2, \\
v_{gq}(\rho_v) &= \frac{\partial^2 V'_{gq}}{\partial(N_q^+ + N_{\bar{q}}^+)\partial N_g^+} \approx \frac{\partial^2(\xi V)}{\partial\rho_v^2}\left(\frac{\partial\rho_v}{\partial(N_q^+ + N_{\bar{q}}^+)}\right)\left(\frac{\partial\rho_v}{\partial N_g^+}\right), \\
v_{gg}(\rho_v) &= \frac{\partial^2 V'_{gg}}{\partial(N_g^{+2}} \approx \frac{1}{2}\frac{\partial^2(1-\xi-\lambda)V}{\partial\rho_v^2}\left(\frac{\partial\rho_v}{\partial N_g^+}\right)^2.
\end{aligned}
\tag{3.36}
$$

The actual results for the effective interactions (3.36) are displayed in Fig. 3.10(a) and for the ratios v_{gg}/v_{qq} and v_{gq}/v_{qq} – in Fig. 3.10(b).

3.2.4 The scaling hypothesis

The extension of the DQPM to finite quark chemical potential μ_q is more delicate since a guidance by lQCD is presently very limited. In case of the DQPM the quasiparticle widths $\Gamma(T, \mu_q)$ have to be known in the (T, μ_q) plane.

In hard thermal loop (HTL) approaches [81,82] the damping of a hard quark (or gluon) does not depend on the quark chemical potential explicitly [83] and one might use Eqs. (3.14) and (3.15) for the quasiparticle widths also at finite μ_q. However, HTL approaches assume small couplings g^2 and should be applied at sufficiently high temperature, only. The lQCD calculations [84] suggest that

the ratio of pressure to energy density P/ε is approximately independent on quark chemical potential μ_q as a function of energy density ε. Accordingly, the functional dependence of the quasiparticle width Γ in the (T, μ_q) plane has to be modeled in line with "lattice phenomenology".

For three light flavors ($q = u, d, s$) and for all equal chemical potentials ($\mu_u = \mu_d = \mu_s = \mu$) Eqs. (3.11) and (3.12) show that the effective quark and gluon masses are functions of

$$T^{*2} = T^2 + \frac{\mu^2}{\pi^2}. \tag{3.37}$$

A straightforward extension of the DQPM for the running coupling (squared) (3.13) is to consider the running coupling as a function of $T^*/T_c(\mu)$ with a μ-dependent critical temperature,

$$T_c(\mu) \approx T_c(0) \left(1 - 0.09 \frac{\mu^2}{T_c(0)^2}\right). \tag{3.38}$$

The coefficient in front of the μ^2-dependent part can be compared to lQCD calculations at finite (but small) quark chemical potential μ, which gives 0.07(3) [85]. If the partonic widths are assumed to have the forms (3.14) and (3.15) than one has to expect an approximate scaling of the DQPM results,

$$\Gamma_{q(\bar{q})}(T, \mu) = \frac{1}{3} \frac{N_c^2 - 1}{2N_c} \frac{g^2(T^*/T_c(\mu))}{4\pi} T \ln\left(\frac{2c}{g^2(T^*/T_c(\mu))} + 1\right), \tag{3.39}$$

$$\Gamma_g(T, \mu) = \frac{1}{3} N_c \frac{g^2(T^*/T_c(\mu))}{4\pi} T \ln\left(\frac{2c}{g^2(T^*/T_c(\mu))} + 1\right), \tag{3.40}$$

where $g^2(T/T_c)$ has been replaced by $g^2(T^*/T_c(\mu))$.

The results for the quasiparticle masses and widths as functions of $T^*/T_c(\mu)$ within the scaling hypothesis (3.38)–(3.40) are presented in Fig. 3.11. Furthermore, the quantities M/T stay about the same as functions of the scaled temperature $T^*/T_c(\mu)$ for various quark chemical potentials.

The more interesting question is how the energy density T^{00} (3.27) and the vector density ρ_v (3.25) change with quark chemical potential in the DQPM. This information is provided in Fig. 3.12, where the l.h.s. shows the energy density T^{00} (3.27) (scaled in terms of $T_{c0} = T_c(\mu = 0)$) as a function of the scaled temperature $T^*/T_c(\mu)$. The energy density ε is seen to scale well with $(T/T_{c0})^4$ as a function of the scaled temperature for $T^*/T_c(\mu) > 5$, however,

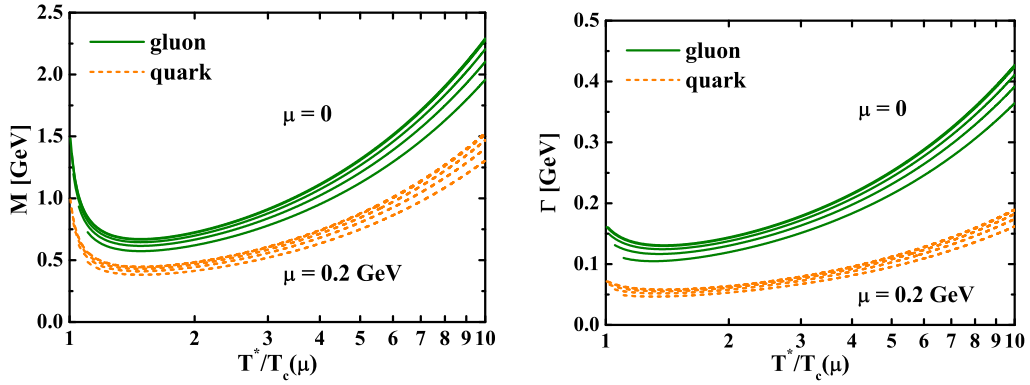

(a) (b)

Figure 3.11: The quasiparticle properties of quarks and antiquarks (short-dashed orange lines) and of gluons (solid green lines) as functions of the scaled temperature $T^*/T_c(\mu)$ for various quark chemical potentials $\mu_q = \mu$ from $\mu = 0$ to $\mu = 0.2$ GeV in steps of 0.05 GeV. (a) mass; (b) width.

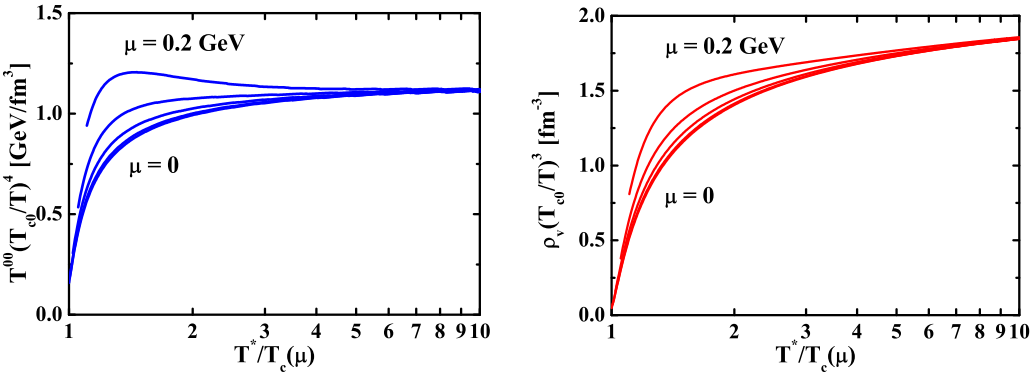

(a) (b)

Figure 3.12: (a) The energy density $T^{00}(3.27)$ (solid blue lines) and (b) the vector density ρ_v (3.25) (solid red lines) as functions of the scaled temperature $T^*/T_c(\mu)$ for $N_f = 3$ for quark chemical potentials μ from 0 to 0.2 GeV in steps of 0.05 GeV. Note that the energy density T^{00} is scaled by the dimensionless factor $(T_{c0}/T)^4$, while the parton density is scaled by the factor $(T_{c0}/T)^3$.

increases with μ close to the phase boundary. Note that a quark chemical potential of 0.2 GeV corresponds to a baryon chemical potential of $\mu_B = 3\mu = 0.6$ GeV, which is already substantial and the validity of Eq. (3.38) becomes questionable.

The r.h.s. of Fig. 3.12 shows the vector density ρ_v as a function of the scaled temperature $(T^*/T_c(\mu))$ (multiplied by $(T_{c0}/T)^3$) for quark chemical potentials from $\mu = 0$ to $\mu = 0.2$ GeV in steps of 0.05 GeV. The scaled vector density increases with μ. One should recall, that a tri-critical endpoint might be expected for $\mu_B = 3\mu \approx 0.4$ GeV [86], which corresponds to $\mu \approx 0.13$ GeV. The explicit change in the vector density ρ_v as well as in the energy density T^{00} with μ stays very moderate.

3.3 Dynamical hadronization

The hadronization, i.e., the transition from partonic to hadronic degrees of freedom, is described in PHSD by covariant transition rates for the fusion of quark-antiquark pairs to mesonic resonances or three quarks (antiquarks) to baryonic states [23, 24], e.g., for $q + \bar{q}$ fusion to a meson m of four-momentum $p = (\omega, \mathbf{p})$ at space-time point $x = (t, \mathbf{x})$:

$$\begin{aligned}\frac{dN_m(x,p)}{d^4x d^4p} &= Tr_q Tr_{\bar{q}}\ \delta^4(p - p_q - p_{\bar{q}})\delta^4\left(\frac{x_q + x_{\bar{q}}}{2} - x\right) \\ &\times \omega_q \rho_q(p_q)\omega_{\bar{q}}\rho_{\bar{q}}(p_{\bar{q}})|v_{q\bar{q}}|^2 W_m\left(x_q - x_{\bar{q}}, \frac{p_q - p_{\bar{q}}}{2}\right) \\ &\times N_q(x_q, p_q) N_{\bar{q}}(x_{\bar{q}}, p_{\bar{q}})\delta(\text{flavor}, \text{color}). \end{aligned} \tag{3.41}$$

In Eq. (3.41) we have introduced the shorthand operator notation

$$Tr_j\ ... = \sum_j \int d^4x_j \int \frac{d^4p_j}{(2\pi)^4} \ldots, \tag{3.42}$$

where $\sum_j$ denotes a summation over discrete quantum numbers (spin, flavor, and color); $N_j(x,p)$ is the phase-space density of parton j at space-time position x and four-momentum p. In Eq. (3.41) δ(flavor, color) stands symbolically for the conservation of flavor quantum numbers as well as color neutrality of the formed hadron m, which can be viewed as a color dipole or "pre-hadron." Furthermore, $v_{q\bar{q}}(\rho_p)$ is the effective quark-antiquark interaction from the DQPM (3.36) as a function of the local vector density ρ_v (3.25) (or energy density)

and $W_m(x,p)$ is the dimensionless phase-space distribution of the formed pre-hadron, i.e.,

$$W_m(\xi, p_\xi) = \exp\left(\frac{\xi^2}{2b^2}\right) \exp\left[2b^2\left(p_\xi^2 - \frac{(M_q - M_{\bar{q}})^2}{4}\right)\right], \tag{3.43}$$

with $\xi = x_1 - x_2 = x_q - x_{\bar{q}}$ and $p_\xi = (p_1 - p_2)/2 = (p_q - p_{\bar{q}})/2$. The width parameter b has been fixed by $\sqrt{\langle r^2 \rangle} = b = 0.66$ fm (in the rest frame), which corresponds to an average rms radius of mesons. We note that the expression (3.43) corresponds to the limit of independent harmonic oscillator states and that the final hadron-formation rates are approximately independent of the parameter b within reasonable variations. By construction the quantity (3.43) is Lorentz invariant; in the limit of instantaneous "hadron formation," i.e., $\xi^0 = 0$, it provides a Gaussian dropping in the relative distance squared, $(\mathbf{r}_1 - \mathbf{r}_2)^2$. The four-momentum dependence reads explicitly (except for a factor 1/2)

$$(E_1 - E_2)^2 - (\mathbf{p}_1 - \mathbf{p}_2)^2 - (M_1 - M_2)^2 \leq 0 \tag{3.44}$$

and leads to a negative argument of the second exponential in Eq. (3.43) favoring the fusion of partons with low relative momenta $p_q - p_{\bar{q}} = p_1 - p_2$.

Note that due to the off-shell nature of both partons and hadrons, the hadronization process obeys all conservation laws (i.e., four-momentum conservation and flavor current conservation) in each event, detailed balance relations, and an increase in the total entropy S in case of a rapidly expanding system. The physics behind Eq. (3.41) is that the inverse reaction, i.e., the dissolution of hadronic states to quark-antiquark pairs (in case of mesons), at low energy density is inhibited by the huge masses of the partonic quasiparticles according to the DQPM. Vice versa, the resonant q-$\bar{q}$ pairs have a large phase space to decay to several 0^- octet mesons. We recall that the transition matrix element becomes huge below the critical energy density.

If the system is initialized by an ensemble of partons, but the energy density in the system is below the critical energy density ($\varepsilon_c \approx 0.5$ GeV/fm^3), the evolution proceeds through the dynamical phase transition and ends up in an ensemble of hadrons. In Fig. 3.13 we show the results of the PHSD calculations for the system initialized in a cubic box with periodic boundary conditions by quarks, antiquarks, and gluons at $\mu_q = 0$ and $\varepsilon = 0.35$ GeV/fm^3 (the details of the box calculations will be addressed in Chapter 5). The numbers of partons (solid red line) and hadrons (dashed blue line) are shown as functions of time.

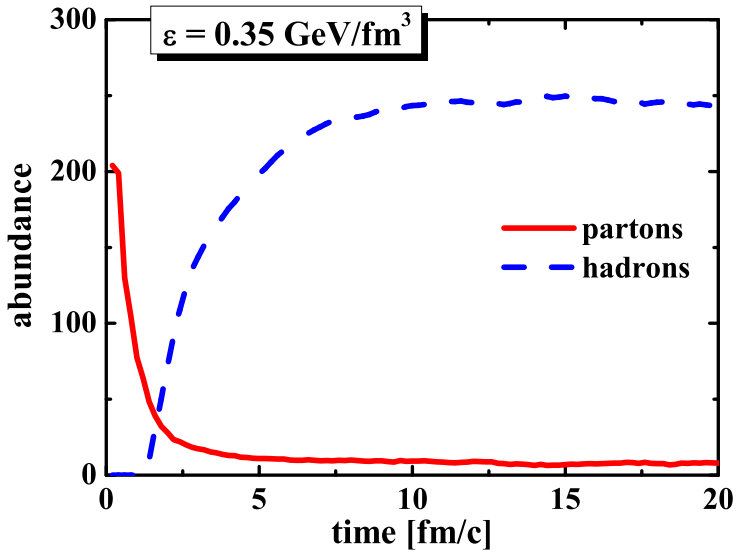

Figure 3.13: PHSD calculations for the system initialized by quarks and gluons at $\mu_q = 0$ and $\varepsilon = 0.35$ GeV/fm^3. The numbers of partons (solid red line) and hadrons (dashed blue line) are shown as functions of time.

We observe that the transition from partonic to hadronic degrees of freedom is complete after about 9 fm/c. A small nonvanishing fraction of partons remains due to local fluctuations of the energy density from cell to cell.

3.4 Summary

In this Chapter we have specified in more detail the ingredients of PHSD. In particular, we have presented the generalized transport equations for fermions, which are implemented in PHSD. To evaluate the self-energies for quarks and antiquarks as well as gluons—that enter the spectral functions and retarded Green's functions—we have recapitulated the DQPM, which describes QCD properties in terms of single-particle Green's functions and has been matched to reproduce lQCD results.

An ansatz with a Lorentzian spectral function as an alternative procedure to calculate the "dressed" propagators in a nonperturbative framework—by fitting the few parameters to results from lQCD—has been presented in this Chapter. Employing this ansatz, we have shown that the DQPM is the thermodynamically consistent model which is well in line with lQCD thermodynamics.

We have provided another implication of the DQPM by separating timelike and spacelike quantities for particle densities, energy densities, etc. By taking

derivatives of the potential energy densities with respect to the timelike gluon and fermion densities we have obtained mean-field potentials for quarks, antiquarks, and gluons as functions of the vector density ρ_v, which enters instead of thermodynamical Lagrange parameters T and μ_q. Second derivatives w.r.t. the gluon and/or fermion densities then define effective interactions between quarks, antiquarks, and gluons.

An extension of the DQPM to finite quark chemical potentials has been presented, too. The energy density, T^{00}, and the vector density, ρ_v, are found to increase slightly with μ_q close to T_c.

Furthermore, we have presented the basic equations for the transition from partons to hadrons and vice versa, i.e., the dynamical hadronization in PHSD that incorporates all conservation laws, detailed balance relations, and leads to an increase in total entropy in case of a rapidly expanding system.

Chapter 4

PHSD results for heavy-ion collisions

The PHSD transport approach was applied to nucleus-nucleus collisions from SPS to RHIC energies in order to explore the spacetime regions of partonic matter. The actual implementations of PHSD for heavy-ion collisions have been presented in detail in Refs. [24, 25, 87]. The comparison to the data allows us to control the implementation of the microscopic description of the QGP and the dynamical hadronization in PHSD before we proceed to the novel results on the properties of strongly interacting matter in Chapters 5 and 6.

In this Chapter we compare the PHSD results to the experimental data for heavy-ion collisions from SPS to RHIC energies as well as to related transport approaches. In Sec. 4.1 we present the results for rapidity distributions, transverse mass spectra, and elliptic flow for heavy-ion collisions at SPS energies in comparison to the data from the experimental collaborations. Then in Sec. 4.2 we provide the same comparison for heavy-ion collisions at RHIC energies. We also present in Sec. 4.3 the dilepton production from the partonic and hadronic sources within PHSD in nucleus-nucleus collisions at the top SPS energy in comparison to the data from the NA60 Collaboration. Finally, a summary is given in Sec. 4.4.

4.1 Application to nucleus-nucleus collisions at SPS energies

In this Section we employ the PHSD approach to nucleus-nucleus collisions at moderate relativistic energies. It is of interest, how the PHSD approach compares to the HSD model [63, 65] (without explicit partonic degrees of freedom) as well as to the experimental data. In Fig. 4.1 we display the transverse mass spectra of π^-, K^+, and K^- mesons for 7% central Pb+Pb collisions at 40 and 80A GeV and 5% central collisions at 158A GeV in comparison to the data of the NA49 Collaboration [88, 89]. Here the slope of the π^- spectra is

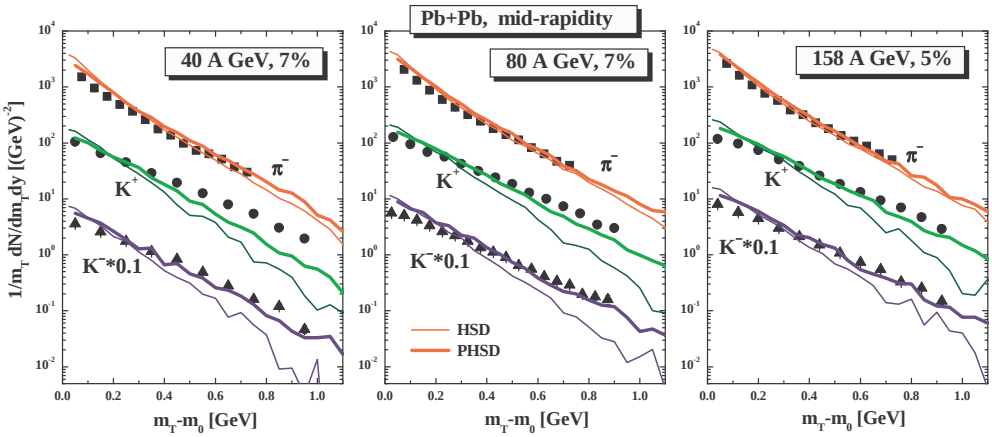

Figure 4.1: The π^-(orange), K^+(green) and K^-(violet) transverse mass spectra for central Pb+Pb collisions at 40, 80, and 158A GeV from PHSD (thick solid lines) in comparison to the distributions from HSD (thin solid lines) and the experimental data from the NA49 Collaboration [88, 89] (black symbols). The figure is taken from Refs. [24, 90].

only slightly enhanced in PHSD (thick solid lines) relative to HSD (thin solid lines), which demonstrates that the pion transverse motion shows no sizeable sensitivity to the partonic phase. However, the $K^\pm$ transverse mass spectra are substantially hardened with respect to the HSD calculations at all bombarding energies—i.e., PHSD is more in line with the data—and thus suggests that partonic effects are better visible in the strangeness degrees of freedom. The hardening of the kaon spectra can be traced back to parton-parton scattering as well as a larger collective acceleration of partons in the transverse direction due to the presence of the repulsive mean fields for partons. The enhancement of the spectral slope for the kaons and antikaons in PHSD due to collective partonic flow shows up much clearer for the kaons due to their

significantly larger mass (relative to pions). We recall that in Ref. [91] the underestimation of the $K^{\pm}$ slope by HSD (and also UrQMD) had been suggested to be a signature for missing partonic degrees of freedom; the present PHSD calculations support this early suggestion. Moreover, the PHSD calculations for RHIC energies (cf. Sec. 4.2) show a very similar trend – the inverse slope increases by including the partonic phase.

The strange antibaryon sector is of further interest since here the HSD calculations have always underestimated the yield [92]. Our detailed studies in Ref. [24] show that the HSD and PHSD calculations both give a reasonable description of the $\Lambda + \Sigma^0$ yield of the NA49 Collaboration [93]; both models underestimate the NA57 data [94, 95] by about 30%. An even larger discrepancy in the data from the NA49 and NA57 Collaborations is seen for $(\bar{\Lambda}+\bar{\Sigma}^0)/N_{wound}$. The PHSD calculations give results, which are in between the NA49 data and the NA57 data, whereas the HSD underestimates the $(\bar{\Lambda}+\bar{\Sigma}^0)$ midrapidity yield at all centralities. Both results are presented in Fig. 4.2.

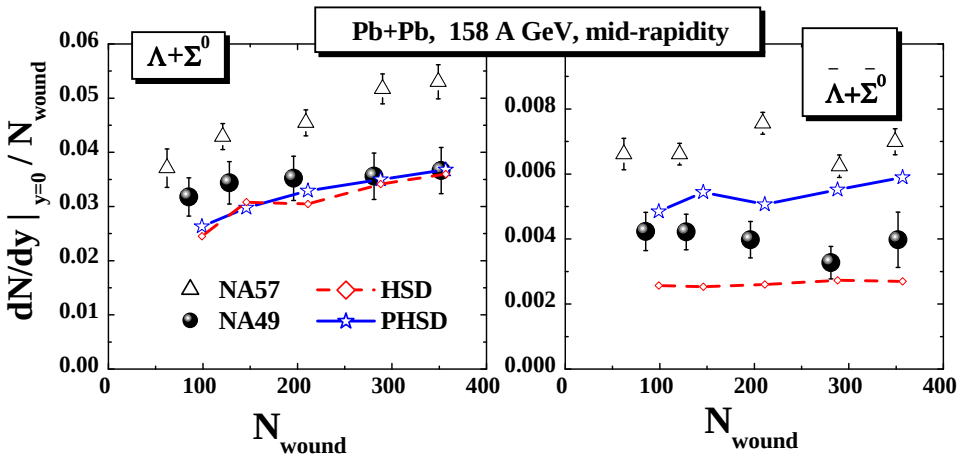

Figure 4.2: The multiplicities of $(\Lambda + \Sigma^0)/N_{wound}$ (l.h.s.) and $(\bar{\Lambda} + \bar{\Sigma}^0)/N_{wound}$ (r.h.s.) as functions of the number of wounded nucleons N_{wound} for Pb+Pb collisions at 158A GeV at midrapidity from PHSD (solid blue lines) and HSD (dashed-dotted red lines) in comparison to the experimental data from the NA57 Collaboration [94, 95] (open triangles) and the NA49 Collaboration [93] (solid dots). The HSD and PHSD calculations have an error of about 5−10% due to limited statistics. The figure is taken from Refs. [24, 90].

The latter results suggest that the partonic phase does not show up explicitly in an enhanced production of strangeness (or, in particular, strange mesons and baryons), but leads to a different redistribution of antistrange quarks between mesons and antibaryons. In fact, as demonstrated in Ref. [24], we find

no sizeable differences in the double strange baryons from HSD and PHSD—in a good agreement with the NA49 data—but observe a large enhancement in the double strange antibaryons from PHSD relative to HSD.

4.2 Application to nucleus-nucleus collisions at RHIC energies

In this Section we continue the comparison of the PHSD transport approach to the experimental data for heavy-ion collisions at RHIC energies as well as to the corresponding HSD results (for more details we refer the reader to Ref. [25]). We start with rapidity spectra from PHSD (solid red lines) for

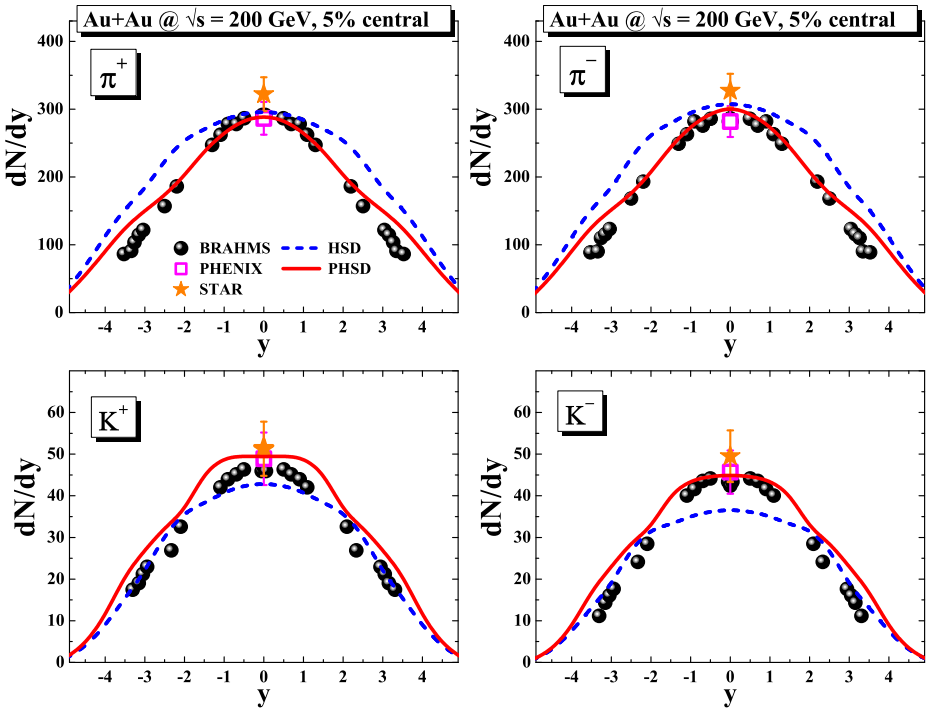

Figure 4.3: The rapidity distribution of π^+ (upper part, l.h.s.), K^+ (lower part, l.h.s.), π^- (upper part, r.h.s.), and K^- (lower part, r.h.s.) for 5% central Au+Au collisions at $\sqrt{s} = 200$ GeV from PHSD (solid red lines) in comparison to the distribution from HSD (dashed blue lines) and to the experimental data from the PNENIX, STAR, and BRAHMS Collaborations (symbols) [30–32]. The figure is taken from Refs. [25, 90].

charged pions and kaons in 5% central Au+Au collisions at $\sqrt{s} = 200$ GeV, which are compared in Fig. 4.3 to the data from the PHENIX, STAR, and BRAHMS Collaborations [30–32] as well as to results from HSD (dashed blue

lines). We find the rapidity distributions of the charged mesons to be slightly narrower in PHSD than those from HSD and actually closer to the experimental data. Also note that there is slightly more production of $K^{\pm}$ mesons in PHSD than in HSD, while the number of charged pions is slightly lower. The actual deviations between the PHSD and HSD spectra are not dramatic, but more clearly visible than at SPS energies (cf. Ref. [24]). Nevertheless, it becomes clear from Fig. 4.3 that the energy transfer in the nucleus-nucleus collision from initial nucleons to produced hadrons—reflected dominantly in the light meson spectra—is rather accurately described by PHSD. Fig. 4.3 also demonstrates that the longitudinal motion is well understood within the PHSD approach.

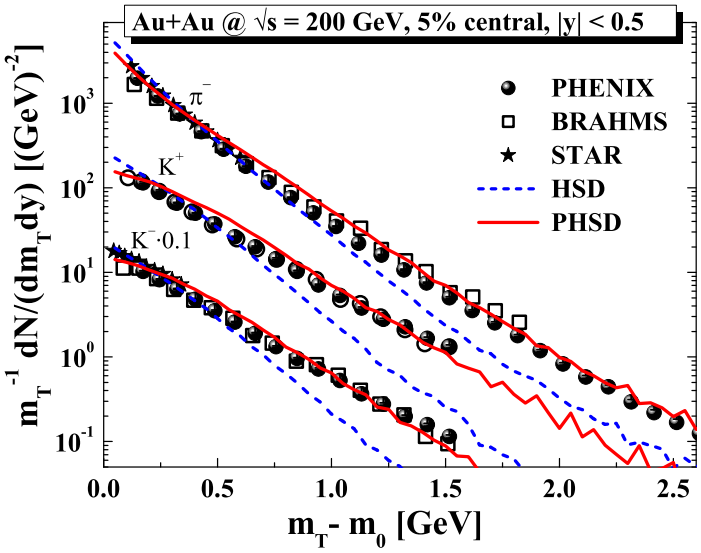

Figure 4.4: The π^-, K^+ and K^- transverse mass spectra for 5% central Au+Au collisions at $\sqrt{s} = 200$ GeV from PHSD (solid red lines) in comparison to the distributions from HSD (dashed blue lines) and to the experimental data from the PHENIX, STAR, and BRAHMS Collaborations (symbols) [30–32] at midrapidity. The figure is taken from Refs. [25, 90].

Independent information on the active degrees of freedom is provided by transverse mass spectra of the hadrons, especially in a central collisions. The actual results for RHIC energies are displayed in Fig. 4.4 where we show the transverse mass spectra of π^-, K^+ and K^- mesons for 5% central Au+Au collisions at $\sqrt{s} = 200$ GeV in comparison to the data from the PHENIX, STAR, and BRAHMS Collaborations [30–32]. Here the slope of the π^- spectra is slightly enhanced in PHSD (solid red lines) relative to HSD (dashed blue

lines), which demonstrates that the pion transverse mass spectra also show some sensitivity to the partonic phase (contrary to the SPS energy regime). The $K^{\pm}$ transverse mass spectra are substantially hardened with respect to the HSD calculations—i.e., PHSD is more in line with the data—and thus suggest that partonic effects are better visible in the strangeness degrees of freedom. The hardening of the kaon spectra can be traced back to parton-parton scattering as well as a larger collective acceleration of partons in the transverse direction due to the presence of the repulsive mean fields for partons. The enhancement of the spectral slopes for kaons and antikaons in PHSD due to collective partonic flow shows up much clearer for the kaons due to their significantly larger mass (relative to pions).

The transverse mass spectra for protons at midrapidity from HSD and PHSD in comparison to the experimental data from the PHENIX Collaboration [31] are shown in Fig. 4.5. Here the HSD spectrum (dashed blue line)

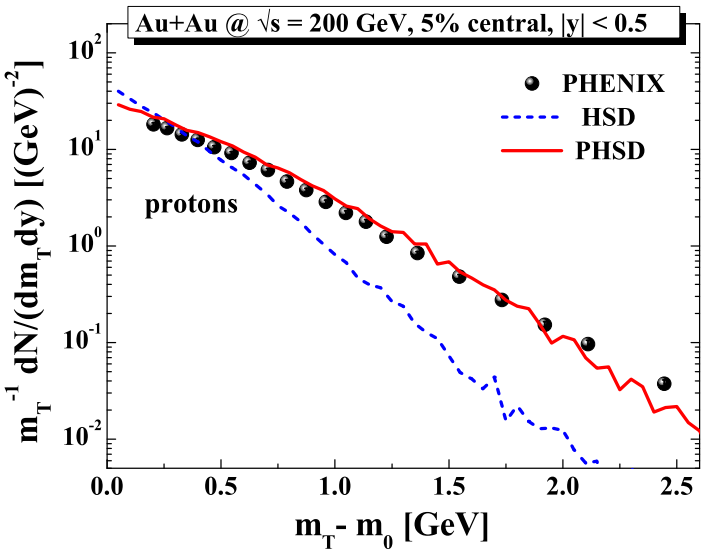

Figure 4.5: The proton transverse mass spectra for 5% central Au+Au collisions at $\sqrt{s} = 200$ GeV from PHSD (solid red line) in comparison to the distribution from HSD (dashed blue line) and to the experimental data from the PHENIX Collaboration (black dots) [31] at midrapidity. The figure is taken from Ref. [25].

severely underestimates the slope of the data from Ref. [31], whereas the PHSD spectrum (solid red line) is fairly in line. These differences are so dramatic, because in HSD the protons at midrapidity dominantly stem from initial string decays and are not allowed to rescatter during their formation time of $\gamma_L \tau_0$,

where γ_L denotes the Lorentz factor and $\tau_0 = 0.8$ fm/c is the default formation time for hadrons in HSD [63, 96]. On the other hand, in PHSD the dominant source of protons (and also the other baryons and antibaryons) at midrapidity is the fusion of three quarks from the partonic phase. Since the partonic degrees of freedom interact strongly the protons pick up the momenta from the fusing partons and thus show a sizeable harder slope in the transverse mass spectrum.

Of additional interest are the collective properties of the strongly interacting system, which are explored experimentally via the elliptic flow

$$v_2(p_T, y) = \left\langle (p_x^2 - p_y^2)/(p_x^2 + p_y^2) \right\rangle |_{p_T, y} \tag{4.1}$$

of hadrons as a function of centrality, rapidity y, transverse momentum p_T or transverse kinetic energy per participating quarks and antiquarks, and collision energy $\sqrt{s}$. We note that the reaction plane in PHSD is given by the $x - z$ plane with the z-axis in beam direction.

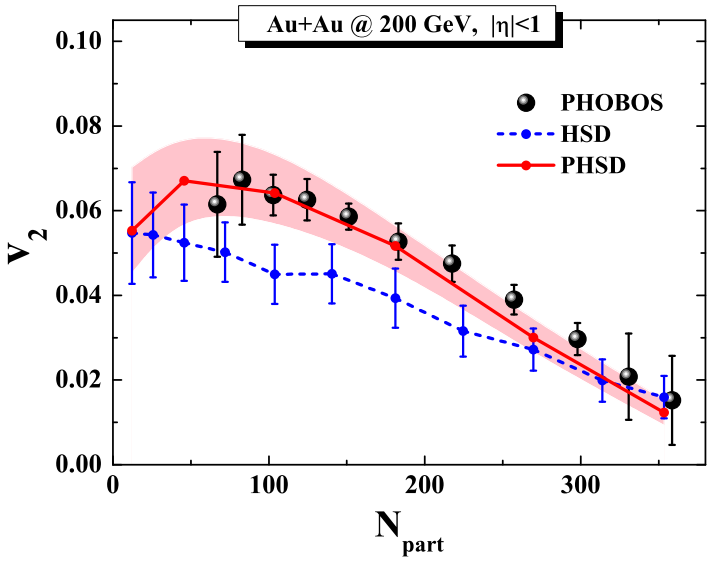

Figure 4.6: The elliptic flow v_2 for Au+Au collisions at $\sqrt{s} = 200$ GeV as a function of centrality measured by the number of participating nucleons N_{part}. The solid red line stands for the results from PHSD, whereas the dashed blue line represents the results from HSD (from Ref. [97]). The data are taken from the PHOBOS Collaboration (black dots) [33] and correspond to momentum integrated events in the pseudo-rapidity window $|\eta| \leq 1$ for charged particles. The shaded band signals the statistical uncertainties of the PHSD calculations. The figure is taken from Refs. [25, 90].

We start in Fig. 4.6 with the elliptic flow v_2 (for Au+Au collisions at the top RHIC energy) as a function of centrality of the reaction measured by the number of participating nucleons N_{part}. The solid red line stands for the results from PHSD, which is compared to the data for charged particles from the PHOBOS Collaboration [33]. The dashed blue line refers to the corresponding results for v_2 from HSD, which is taken from Ref. [97]. The momentum integrated results in the pseudo-rapidity window $|\eta| \leq 1$ from PHSD compare well to the data from Ref. [33], whereas the HSD results clearly underestimate the elliptic flow as pointed out before in Ref. [97]. The relative enhancement of v_2 in PHSD with respect to HSD can be traced back to the high interaction rate in the partonic phase and again to the repulsive mean fields for partons.

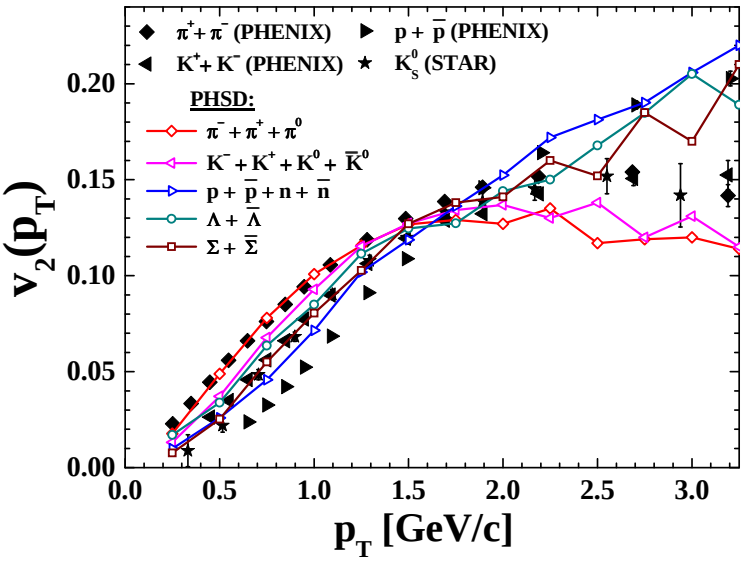

Figure 4.7: The hadron elliptic flow v_2 for inclusive Au+Au collisions as a function of the transverse momentum p_T for different hadrons in comparison to the experimental data from the STAR [98, 99] and PHENIX Collaborations [100] within the same rapidity cuts. The figure is taken from Refs. [25, 90].

Fig. 4.7 shows the final hadron v_2 versus the transverse momentum p_T for different particle species in comparison to the experimental data from the STAR [98, 99] and PHENIX Collaborations [100]. We observe a mass separation in p_T as well as a separation in mesons and baryons for $p_T > 2$ GeV roughly in line with data. The elliptic flow of mesons is slightly underestimated for $p_T > 2$ GeV in PHSD, which is opposite to ideal hydrodynamics, which overestimates v_2 at high transverse momenta. On the other hand, the proton (and antiproton) elliptic flow is slightly overestimated at low transverse

momenta $p_T < 1.5$ GeV.

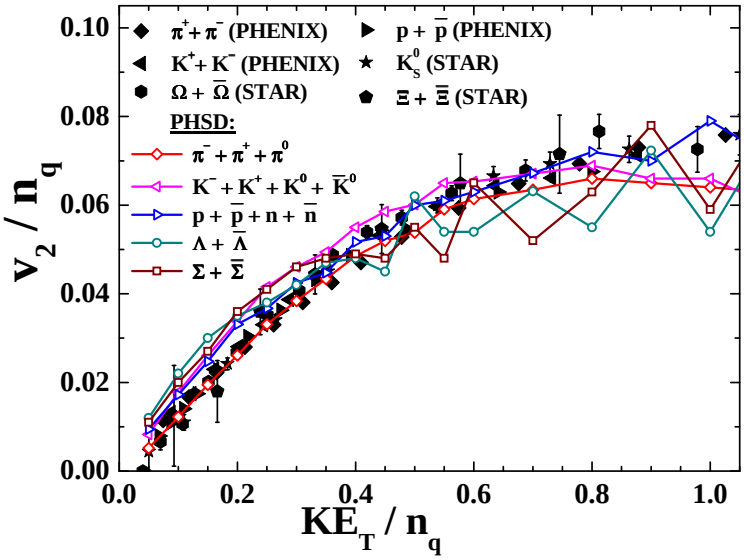

Figure 4.8: The elliptic flow v_2—scaled by the number of constituent quarks n_q—versus the transverse kinetic energy (4.2) divided by n_q for different hadron species in comparison to the experimental data from the STAR [98, 99] and PHENIX Collaborations [100]. The figure is taken from Refs. [25, 90].

A further test of the PHSD approach is provided by the "constituent quark number scaling" of the elliptic flow v_2, which has been observed experimentally in central Au+Au collisions at RHIC [100, 101]. In this respect we plot v_2/n_q versus the transverse kinetic energy per constituent parton,

$$KE_T = \frac{m_T - m}{n_q}, \tag{4.2}$$

with m_T and m denoting the transverse mass and actual hadron mass, respectively. For mesons we have $n_q = 2$ and for baryons/antibaryons $n_q = 3$. The results for the scaled elliptic flow are shown in Fig. 4.8 in comparison to the experimental data from the STAR [98, 99] and PHENIX Collaborations [100] for different hadrons and suggest an approximate scaling. For $KE_T > 0.5$ GeV there is a tendency to underestimate the experimental measurements for Λ, Σ, $\bar{\Lambda}$, $\bar{\Sigma}$ baryons, which we attribute to an underestimation of interaction terms in PHSD for high momentum hadrons. In this respect we recall that the momentum independence of the quasiparticle width Γ and mass M is presently a rough approximation and has to be refined.

We directly continue with the results for elliptic flow as a function of collision energy from PHSD in comparison to the various transport approaches

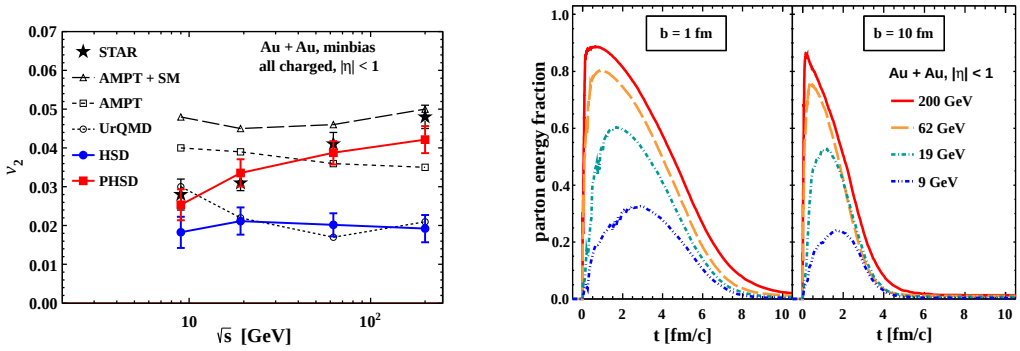

(a) (b)

Figure 4.9: (a) The average elliptic flow v_2 of charged particles at midrapidity for minimum bias collisions at $\sqrt{s} = 9.2$, 19.6, 62.4, and 200 GeV (black stars) is taken from the data compilation of Ref. [102]. The corresponding results from different models are compared to the data and explained in more detail in the text. (b) Evolution of the parton fraction of the total energy density at midrapidity (from PHSD) for different collision energies at impact parameters $b = 1$ fm and 10 fm. The figure is taken from Refs. [87, 103].

and to the available experimental data.

Note that at high bombarding energies the longitudinal size of the Lorentz contracted nuclei becomes negligible compared to its transverse size. The forward shadowing effect then becomes negligible and the elliptic flow fully develops in-plane, leading to a positive value of the average flow v_2 since no shadowing from spectators takes place. In Fig. 4.9(a) the experimental v_2 data compilation for the transient energy range is compared to the results from various models: PHSD, HSD as well as from UrQMD [26, 27] and AMPT [29]. The centrality selection is the same for the data and the various models.

We find from Fig. 4.9 that the interactions between the minijet partons in the AMPT model indeed increase the elliptic flow significantly as compared to the hadronic models UrQMD and HSD. An additional inclusion of interactions between partons in the AMPT-SM model gives rise to another 20% of v_2 bringing it into agreement (for AMPT-SM) with the data at the maximal collision energy. So, both versions of the AMPT model indicate the importance of partonic contributions to the observed elliptic flow v_2 but do not reproduce its growth with $\sqrt{s}$. We address this result to the partonic equation of state (EoS) employed which corresponds to a massless and noninteracting relativistic gas of particles. This EoS deviates severely from the results of lQCD calculations for temperatures below 2-3 T_c. Accordingly, the degrees of freedom are

propagated without self-energies and a parton spectral function.

The PHSD approach incorporates the latter medium effects in line with a lQCD equation of state and also includes a dynamical hadronization scheme based on covariant transition rates (cf. Chapter 3). The elliptic flow v_2 from PHSD (red line) agrees with the experimental data from the STAR Collaboration and clearly shows an increase with bombarding energy.

An explanation for the increase in v_2 with collision energy is provided in Fig. 4.9(b) where the partonic fraction of the energy density is shown with respect to the total energy at midrapidity. The main contribution to the elliptic flow is coming from an initial partonic stage at high $\sqrt{s}$. The fusion of partons to hadrons or, inversely, the melting of hadrons to partonic quasiparticles occurs when the local energy density is about $\varepsilon \approx 0.5$ GeV/fm^3. As follows from Fig. 4.9(b), the parton fraction of the total energy goes down substantially with decreasing bombarding energy while the duration of the partonic phase is roughly the same. The maximal fraction reached is the same in central and peripheral collisions but the parton evolution time is shorter in peripheral collisions. We point out in addition that the increase of v_2 in PHSD relative to HSD is partly due to the higher interaction rates in the partonic medium because of a lower ratio of η/s for partonic degrees of freedom at energy densities above the critical energy density than for hadronic media below the critical energy density (cf. Sec. 6.1).

4.3 Dilepton production in nucleus-nucleus collisions within PHSD

The PHSD transport approach [23–25], which incorporates the relevant off-shell dynamics of vector mesons and the explicit partonic phase in the early hot and dense reaction region as well as the dynamics of hadronization, allows for a microscopic study of various dilepton production channels out of equilibrium. This off-shell transport approach is particularly suitable for this investigation, because it incorporates various scenarios for the modification of vector mesons in a hot and dense medium, seen experimentally in the enhanced production of lepton pairs in the invariant mass range $0.3 \leqslant M \leqslant 0.7$ GeV. In this Section, we calculate dilepton production from the partonic and hadronic sources within PHSD by including the multimeson channels and the partonic channels besides the usual hadron decay channels. By treating in the same

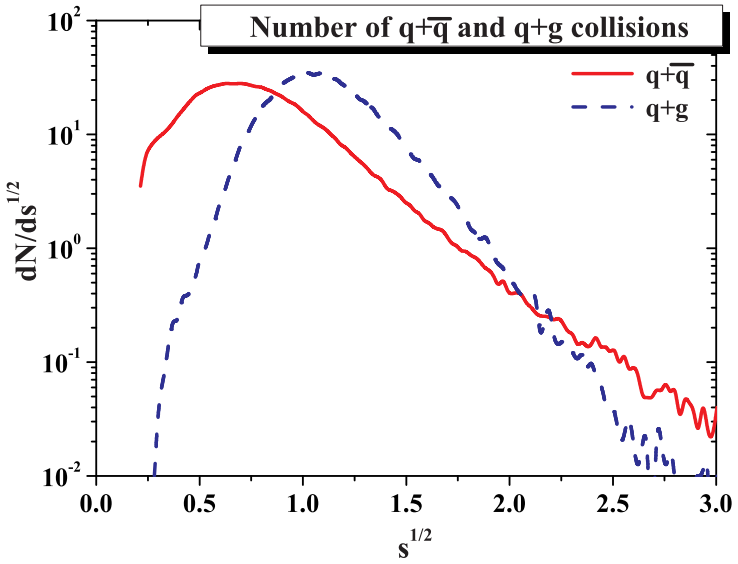

Figure 4.10: Number of parton collisions per event in a central In+In reaction at an incident energy of 158A GeV versus the $\sqrt{s}$ of the elementary partonic collision as simulated in PHSD; the number of $q + \bar{q}$ collisions is given by the solid red line, the number of $q + g$ collisions is given by the dashed blue line.

microscopic transport framework both partonic and hadronic phases of the collision system, we are aiming to determine the relative importance of different dilepton production mechanisms and to point out the regions in phase space, where partonic channels are dominant.

For an illustration of the quark and gluon interactions in a heavy-ion collision as generated in PHSD, we show in Fig. 4.10 the number of $q+\bar{q}$ (solid red line) and $q + g$ (dashed blue line) collisions that can create dilepton pairs per event in a central In+In reaction at an incident energy of 158A GeV versus the invariant energy $\sqrt{s}$ of the elementary partonic collision. One can see that the tails of the collision distributions calculated in the PHSD transport are almost exponential, thus close to thermal. On the other hand, the collisions at very low $\sqrt{s}$ are suppressed. This "threshold effect" is due to the finite masses of the dynamical quarks, antiquarks, and gluons (cf. Eqs. (3.11) and (3.12)). Additionally, one notices that the threshold is not sharp because of the rather broad spectral functions (3.8) (and therefore broad mass distributions) of colliding partons.

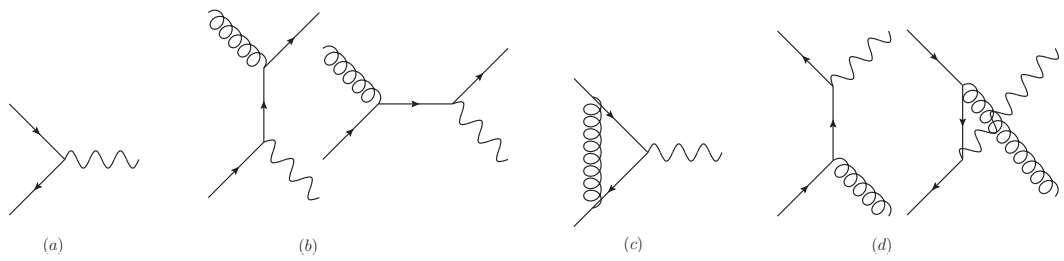

Figure 4.11: Diagrams contributing to the dilepton production from the QGP: (a) Drell-Yan mechanism, (b) gluon-Compton scattering (GCS), (c) vertex correction, (d) gluon Bremsstrahlung (NLODY), where virtual photons (wavy lines) split into lepton pairs, spiral lines denote gluons, arrows denote quarks. In each diagram the time runs from left to right.

4.3.1 Partonic and hadronic sources of dileptons in PHSD

In the scope of the one- and two-particle interactions, dilepton radiation by the constituents of the strongly interacting QGP proceeds via the elementary processes illustrated in Figs. 4.11 and 4.12: the basic Born $q + \bar{q}$ annihilation mechanism, gluon-Compton scattering ($q+g \to \gamma^* + q$ and $\bar{q}+g \to \gamma^* + \bar{q}$), and quark + antiquark annihilation with gluon bremsstrahlung in the final state ($q+\bar{q} \to g+\gamma^*$), virtual quark decay ($q \to q+g+\gamma^*$), and virtual gluon decay ($g \to q+\bar{q}+\gamma^*$). In the on-shell approximation one uses pQCD cross sections for the processes listed above. However, in the strongly interacting QGP the gluon and quark propagators differ significantly from the noninteracting propagators. Accordingly, the cross sections for dilepton production in the partonic channels have been calculated in Refs. [104–106] in the DQPM model.

The importance of finite mass corrections to the pertubartive cross sections has been stressed in Refs. [104–106]. It was shown that the finite quark and gluon masses can modify the magnitude as well as the M dependence and p_T dependence of the cross sections compared to the perturbative results for massless partons (cf. Figs. 3 and 4 of Refs. [104–106]). The modification are large at lower M^2 and at the edges of the phase space. It was shown that the most prominent effect of the quark masses on the dimuon production cross sections in the Born mechanism ($q + \bar{q} \to \gamma^*$) was a sharp threshold value for the invariant mass of dilepton pair $M_{min} = m_1 + m_2$. On the other hand, the finite masses of the quark and antiquark produce additional higher-twist corrections to the cross section, which decrease with increasing M^2, so that the

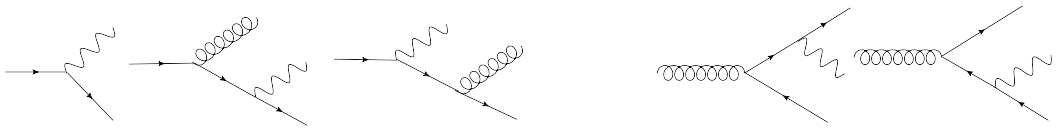

Figure 4.12: Diagrams contributing to the dilepton production by virtual quasiparticles in addition to the ones presented in Fig. 4.11. Left-hand side: the decay of a virtual quark; Right-hand side: the decay of a virtual gluon. Virtual photons (wavy lines) split into lepton pairs, spiral lines denote gluons, arrows denote quarks.

off-shell cross sections approach the leading twist—on-shell—result in the limit of high dilepton masses. In Fig. 4 of Refs. [104–106], an analogous comparison for the $2 \to 2$ process $q + \bar{q} \to \gamma^* + g$ was shown by plotting the off-shell (i.e., with finite masses for the quarks and gluons) cross section for the quark annihilation with gluon bremsstrahlung in the final state at various values of the quark and gluon off-shellnesses (masses) and the corresponding on-shell result. As found in Refs. [104–106], the maximum pair mass shifts to a lower value (in order to produce a massive gluon in the final state). For the rest of the M values, the effect of the quark and gluon masses is about 50%. For $m_{q/g} \to 0$, the cross section approaches the leading twist pQCD result.

The question of the effect of a finite parton width—which parametrizes the effect of their interaction rate and correlation, including multiple scattering—on dilepton rates in heavy-ion collisions was addressed in Refs. [104–106] by convoluting the off-shell cross sections with phenomenological spectral functions $A(m_q)$ and $A(m_g)$ for the quarks and gluons in the QGP and with parton distributions in a heavy-ion collision similar to those of Fig. 4.10. The finite width of the quasiparticles was found to have a sizable effect on the dilepton production rates. In particular, the threshold of the Drell-Yan contribution was washed out. Also, the shape and magnitude of the $2 \to 2$ processes ($q + \bar{q} \to g + \gamma^*$ and $q + g \to q + \gamma^*$) were modified. We further observed that the contribution of the gluon Compton process $q + g \to q + \gamma^*$ to the rates was small compared to that of $q + \bar{q}$ annihilations.

We have implemented the cross sections obtained in Refs. [104–106] into the PHSD transport approach in the following way: Whenever the quark-antiquark, quark-gluon and antiquark-gluon collisions occur in the course of the Monte Carlo simulation of the partonic phase, a dilepton pair can be produced according to the off-shell cross sections [104–106], which depend, in

addition to the virtualities of the partons involved, on the energy density in the local cell, in which the collision takes place. The local energy density governs the widths of the quark and gluon spectral functions as well as the strong coupling (cf. Eqs. (3.13)–(3.15)). Numerically, one finds from a PHSD simulation of a heavy-ion collision at SPS energies that the running coupling α_S in the partonic phase is often of order $O(1)$ and thus the contribution of the higher-order Bremsstrahlung diagram is compatible in magnitude to the Born term.

In the hadronic sector, PHSD is equivalent to the HSD transport approach [63,65]. The implementation of the hadronic decays into dileptons (π-, η-, η'-, ω-, Δ-, a_1-Dalitz, $\rho \to l^+l^-$, $\omega \to l^+l^-$, $\phi \to l^+l^-$) in HSD (and PHSD) has been described in detail in Refs. [66, 107]. For the treatment of the leptonic decays of open charm mesons and charmonia we refer to Refs. [108–110]. In Ref. [111] the hadronic sources for dilepton production have been extended to include secondary multimeson interactions by incorporating the channels $\pi\omega \to l^+l^-$, $\pi a_1 \to l^+l^-$, and $\rho\rho \to l^+l^-$.[1]

4.3.2 In-medium modification of vector mesons

While the properties of hadrons are rather well-known in free space (embedded in the nonperturbative QCD vacuum), the masses and lifetimes of hadrons in a baryonic and/or mesonic environment are subject of current research that aims at achieving a better understanding of the strong interaction and the nature of confinement. For example, a broadening of the vector mesons can be understood as a shortening of the lifetime of the vector mesons ρ, ω, and ϕ in the medium. In this context the modification of hadron properties in nuclear matter are of fundamental interest (cf. Refs. [112–118]), since QCD sum rules [114, 115, 119] as well as QCD inspired effective Lagrangian models [112, 113, 116, 120–123] predict significant changes, e.g., in the properties of the vector mesons (ρ, ω, and ϕ) with the nuclear density ρ_N and/or temperature T [63, 124–126].

A modification of the properties of vector mesons in the nuclear medium was first seen experimentally in the enhanced production of lepton pairs above known sources in nucleus-nucleus collisions at SPS energies [127–132]. As proposed in Refs. [133,134], the observed enhancement in the invariant mass range

[1] The author has contributed to this study by calculating the additional multimeson dilepton channels [111] (cf. Appendix A).

$0.3 \leqslant M \leqslant 0.7$ GeV might be due to a shift of the ρ-meson mass following the Brown-Rho scaling [112,113] or the Hatsuda-Lee sum rule prediction [114]. The microscopic transport studies in Refs. [65,135,136] for these systems have given support for this interpretation. On the other hand, more conventional approaches that describe a melting of the ρ meson in the medium due to the strong hadronic coupling (along the lines of Refs. [120–123]) have also been found to be compatible with the early data from the CERES Collaboration [124, 135, 137–139]. This ambiguous situation has been clarified to some extent in 2006 by the NA60 Collaboration because the invariant mass spectra for $\mu^+\mu^-$ pairs from In+In collisions at 158A GeV favored the "melting" scenario [38,140–142]. Also, the later data from the CERES Collaboration (with enhanced mass resolution) [143–146] showed a preference for the "melting ρ" picture.

The various models, which predict a change of the hadronic spectral functions in the (hot and dense) nuclear medium, may be classified into two different categories: (i) a broadening of the spectral function or (ii) a mass shift of the vector mesons with density and/or temperature. In view of many-body dynamics, both modifications should be studied simultaneously as well [147]. Thus we explore three possible scenarios with respect to the low-mass dilepton spectrum, which essentially addresses all possible properties of the ρ meson: (1) a broadening of the ρ spectral function, (2) a mass shift, and (3) a broadening plus a mass shift.

We incorporate the effect of collisional broadening of the vector-meson spectral functions (as in Refs. [148–150]), by using for the vector meson width:

$$\Gamma^*_V(M, |\mathbf{p}|, \rho_N) = \Gamma_V(M) + \Gamma_{\rm coll}(M, |\mathbf{p}|, \rho_N). \tag{4.3}$$

Here $\Gamma_V(M)$ is the total width of the vector mesons ($V = \rho, \omega$) in the vacuum. The collisional width in Eq. (4.3) is approximated as

$$\Gamma_{\rm coll}(M, |\mathbf{p}|, \rho_N) = \gamma \rho_N \langle v \sigma^{\rm tot}_{VN} \rangle \approx \alpha_{\rm coll} \frac{\rho_N}{\rho_0}. \tag{4.4}$$

Here $v = |\mathbf{p}|/E$, $\mathbf{p}$, and E are the velocity, three-momentum, and energy of the vector meson in the rest frame of the nucleon current and $\gamma^2 = 1/(1-v^2)$. Furthermore, ρ_N is the nuclear density and $\sigma^{\rm tot}_{VN}$ is the meson-nucleon total cross section.

To simplify the actual calculations for dilepton production, the coefficient

$\alpha_{\rm coll}$ has been extracted in the PHSD transport calculations from the vector-meson collision rate in In+In reactions at 158A GeV as a function of the density ρ_N. In case of the ρ meson the collision rate is dominated by the absorption channels $\rho N \to \pi N$ or $\rho N \to \Delta\pi \to \pi\pi N$. Also the reactions $\rho + \pi \leftrightarrow a_1$ are incorporated. The numerical results for $\Gamma_{\rm coll}(\rho_N)$ then have been divided by ρ_N/ρ_0 to fix the coefficient $\alpha_{\rm coll}$ in Eq. (4.4). We obtain $\alpha_{\rm coll} \approx 150$ MeV for the ρ mesons and $\alpha_{\rm coll} \approx 70$ MeV for the ω mesons, which are consistent with those of Ref. [151]. In this way the average effects of collisional broadening are incorporated in accordance with the transport calculations and allow for an explicit representation of the vector-meson spectral functions versus the nuclear density as demonstrated in Ref. [66].

To explore the observable consequences of vector-meson mass shifts at finite nuclear density, the in-medium vector-meson pole masses are modeled (optionally) according to the Hatsuda-Lee sum rule prediction [114] or the Brown-Rho scaling [112, 113] as

$$M_0^*(\rho_N) = \frac{M_0}{(1 + \alpha\rho_N/\rho_0)}, \tag{4.5}$$

where ρ_N is the nuclear density at the resonance decay position $\mathbf{r}$, $\rho_0 = 0.16$ fm^{-3} is the normal nuclear density and $\alpha \simeq 0.16$ for the ρ meson and $\alpha \simeq 0.12$ for the ω meson [151]. The parametrization (4.5) may be employed also at much higher collision energies and one does not have to introduce a cutoff density in order to avoid negative pole masses. Note that Eq. (4.5) is uniquely fixed by the "customary" expression $M_0^*(\rho_N) \approx M_0(1 - \alpha\rho_N/\rho_0)$ in the low-density regime.

The spectral function of the vector meson V for the mass M at baryon density ρ_N is taken in the Breit-Wigner form:

$$A_V(M, \rho_N) = C_1 \frac{2}{\pi} \frac{M^2 \Gamma_V^*(M, \rho_N)}{(M^2 - M_0^{*2}(\rho_N))^2 + (M\Gamma_V^*(M, \rho_N))^2}. \tag{4.6}$$

The factor C_1 is fixed by the normalization condition for arbitrary ρ_N:

$$\int_{M_{\rm min}}^{M_{\rm lim}} A_V(M, \rho_N)\, dM = 1, \tag{4.7}$$

where $M_{lim} = 2$ GeV is chosen as an upper limit for the numerical integration. The lower limit for the vacuum spectral function corresponds to the two-pion decay, $M_{\rm min} = 2m_\pi$, whereas for the in-medium collisional broadening case

$M_{\rm min} = 2m_e \to 0$, with m_e denoting the electron mass. M_0^* is the pole mass of the vector-meson spectral function, which is $M_0^*(\rho_N = 0) = M_0$ in vacuum, but may be shifted in the medium for the dropping mass scenario according to Eq. (4.5). The resulting spectral functions for the ρ and ω mesons are displayed in Fig. 2 of Ref. [66].

With increasing nuclear density ρ_N elastic and inelastic interactions of the vector mesons shift strength to low invariant masses. In the "collisional broadening" scenario we find a dominant enhancement of strength below the pole mass for the ρ meson while the ω-meson spectral function is drastically enhanced in the low- and high-mass region with density (on expense of the pole-mass regime). In the "dropping mass + collisional broadening" scenario both vector mesons dominantly show a shift of strength to low invariant masses with increasing ρ_N. Qualitatively similar pictures are obtained for the ϕ meson but quantitatively smaller effects are seen due to the lower effect of mass shifts and a substantially reduced ϕN cross section which is a consequence of the $s\bar{s}$ substructure of the ϕ meson.

4.3.3 Results and comparison to data

Let us first recall that the bulk properties of heavy-ion reactions at the top SPS energy, such as the number of charged particles, as well as their rapidity, p_T and transverse energy distributions, are rather well described by PHSD; we refer to Sec. 4.1 for an extended comparison to the data.

Previously, by employing the HSD approach to the low-mass dilepton production in relativistic heavy-ion collisions, it was shown in Ref. [107] that the NA60 Collaboration data for the invariant mass spectra of $\mu^+\mu^-$ pairs from In+In collisions at 158A GeV favored the melting ρ scenario [38,140–142]. Also the data from the CERES Collaboration [143–146] showed a preference for the melting ρ picture. For other vector mesons (ω, ϕ), the effects are relatively small, because, due to their much longer lifetimes, ω and ϕ decay predominantly outside the medium after regaining the vacuum properties.

As we see in Fig. 4.13, the current calculation in the PHSD approach confirms the earlier finding in the hadronic model that the NA60 data favor the scenario of the in-medium broadening of vector mesons. A comparison of the transport calculations to the data of the NA60 Collaborations points towards a melting of the ρ meson at high densities, i.e., a broadening of the vector meson's spectral function in line with the findings by Rapp [152]. No

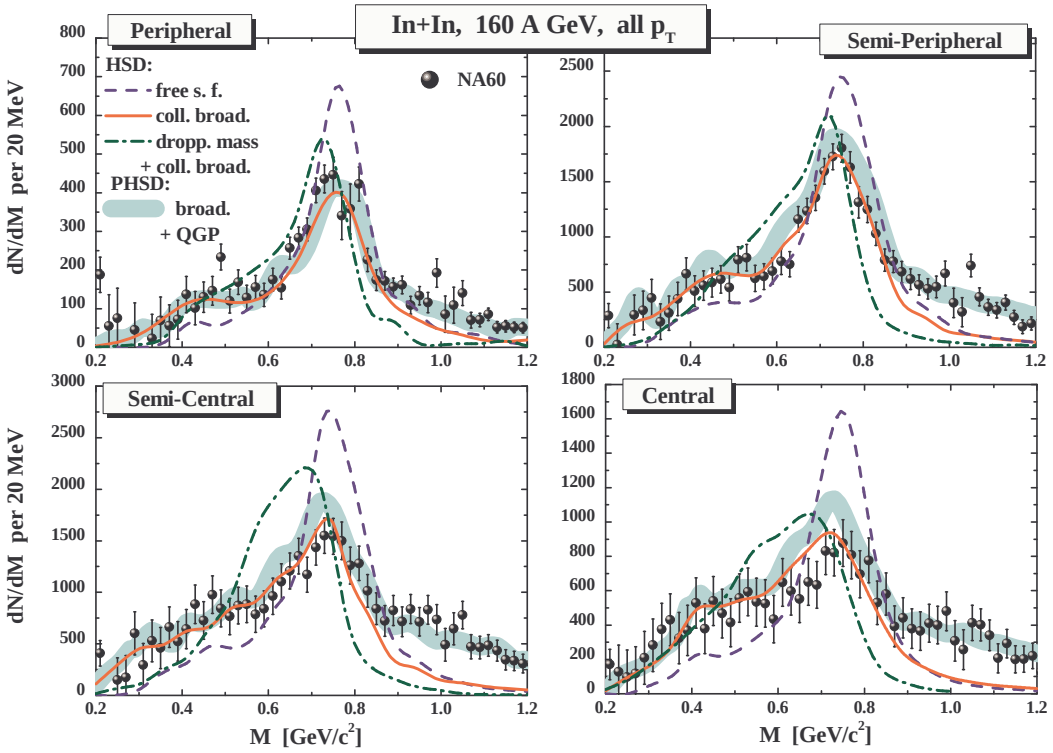

Figure 4.13: The HSD results for the mass differential dilepton spectra from In + In collisions at 158A GeV in comparison to the excess mass spectrum from the NA60 Collaboration (black dots) [38, 140–142]. The actual NA60 acceptance filter and mass resolution have been incorporated. The solid lines show the HSD results for a scenario including the collisional broadening of the ρ meson, whereas the dashed lines correspond to calculations with "free" ρ spectral functions for reference. The dash-dotted lines represent the HSD calculations for the dropping mass + collisional broadening model. The wide (light blue) bands represent the PHSD results incorporating direct dilepton radiation from the QGP in addition to a broadened ρ meson.

pronounced mass shift of the vector mesons is visible in the data. On the other hand, a closer inspection of Fig. 4.13 shows that the conventional hadronic sources do not match the measured yield at invariant masses above about 1 GeV, while the yield at masses close to 1 GeV is reproduced by taking into account the dilepton production channels in the QGP.

The NA60 Collaboration has published acceptance corrected data with subtracted charm contribution [153]. In Fig. 4.14 we present PHSD results for the dilepton spectrum excess over the known hadronic sources as produced in In+In reactions at 158A GeV compared to the acceptance-corrected data. We find here that the spectrum at invariant masses in the vicinity of the ρ peak

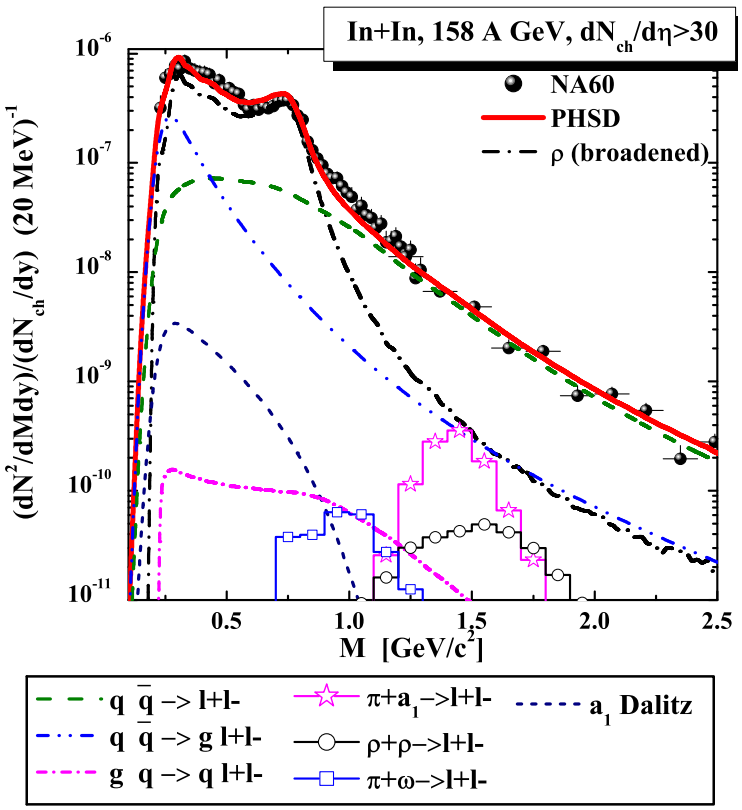

Figure 4.14: Acceptance-corrected mass spectra of excess dimuons from In+In at 158A GeV integrated over p_T in $0.2 < p_T < 2.4$ GeV from PHSD compared to the data of the NA60 Collaboration [153]. The dash-dotted black line shows the dilepton yield from the in-medium ρ with a broadened spectral function, the dashed blue line presents the yield from the $q + \bar{q}$ annihilation, the dash-dot-dotted light blue line gives the contribution of the gluon Bremsstrahlung process ($q\bar{q} \to gl^+l^-$), while the solid red line is the sum of all contributions. For the description of the other lines, which correspond to the nondominant channels, we refer to the figure legend.

is well reproduced by the ρ meson yield, if a broadening of the meson spectral function in the medium is assumed, while the partonic sources account for the yield at high masses.

One can conclude from Fig. 4.14 that the measured spectrum for $M >$ 1 GeV is dominated by the partonic sources. Indeed, the domination of the radiation from the QGP over the hadronic sources in PHSD is related to a rather long—of the order or 3 fm/c—evolution in the partonic phase (in coexistence with the spacetime separated hadronic phase) on one hand, cf. Fig. 10 of Ref. [24], and the rather high initial energy densities created in the collision on the other hand, cf. Fig. 6 of Ref. [109].

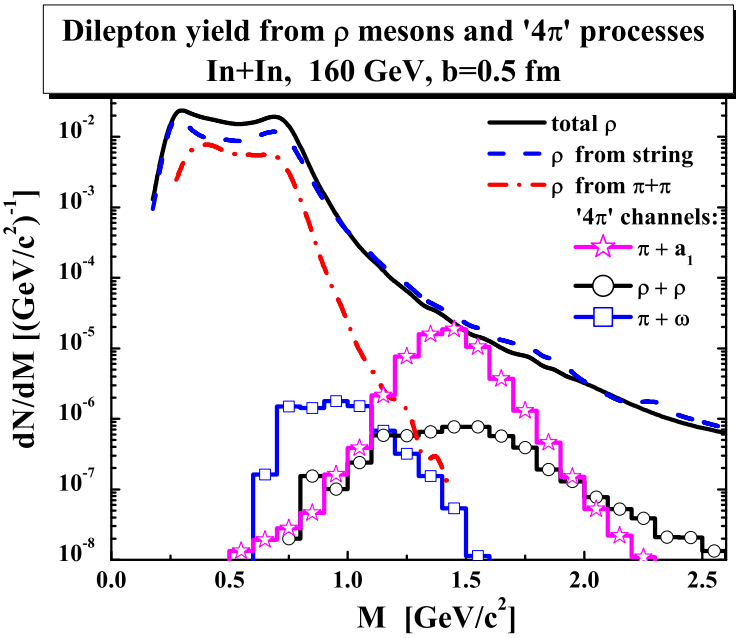

Figure 4.15: Dilepton radiation from ρ mesons of different origins in PHSD from central In+In collisions at 158A GeV compared to the contributions from the 4π processes (a_1+π, π+ω, ρ+ρ). The direct ρ mesons produced in mesonic and baryonic strings are given by the dashed blue line and the thermal ρ mesons produced in $\pi+\pi$ annihilations by the dash-dotted red line. The contributions of the 4π processes are shown by the lines with symbols: the $\pi + a_1 \to l^+l^-$ process is displayed by the magenta line with stars, $\pi + w \to l^+l^-$ by the blue line with squares and $\rho + \rho \to l^+l^-$ by the black line with circles.

In addition, we find from Fig. 4.14 that in PHSD the partonic sources have a considerable contribution to the dilepton yield at $M < 0.6$ GeV. The yield from the two-to-two process $q + \bar{q} \to g + l^+l^-$ is especially important close to the threshold (≈ 0.211 GeV). This conclusion from the microscopic calculation is in qualitative agreement with the conclusion of an early (more schematic) investigation in Ref. [154].

To elucidate the relative importance of the different hadronic sources of the excess dileptons in heavy-ion collisions at the top SPS energy, we show in Fig. 4.15 the channel decomposition of the main hadronic contributions to the dilepton rates in central In+In collisions at 158A GeV integrated over rapidity and p_T. In particular, the dilepton yield from the decays of the ρ mesons (solid black line) is dominantly composed of two channels: the direct ρ mesons produced in mesonic and baryonic strings (dashed blue line) and the thermal ρ mesons produced in $\pi+\pi$ annihilations (dash-dotted red line). For comparison, the contributions of the 4π processes are shown by the lines with symbols: the

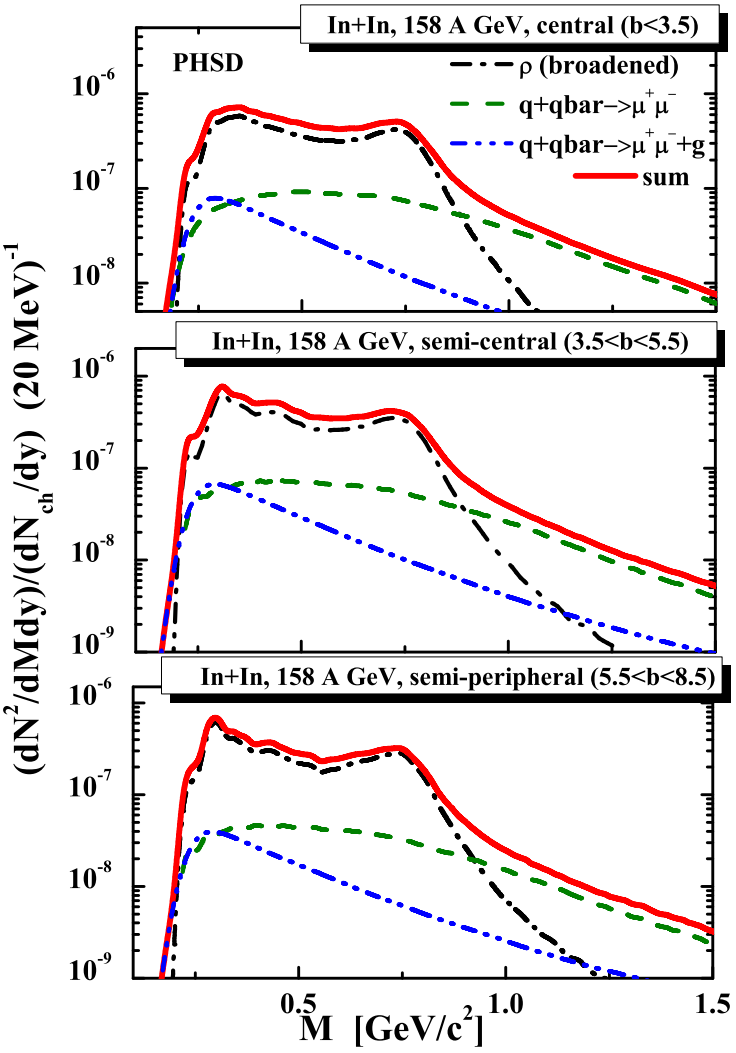

Figure 4.16: Mass spectra of excess dimuons from In+In at 158A GeV for $0.2 < p_T < 2.4$ GeV and $3 < \eta < 4.2$ from PHSD for different centrality bins. The dash-dotted black, dashed green, and solid red lines show, respectively, the dilepton yield from the in-medium ρ meson with a broadened spectral function, the dilepton yield from the $q + \bar{q}$ annihilation and the sum of them.

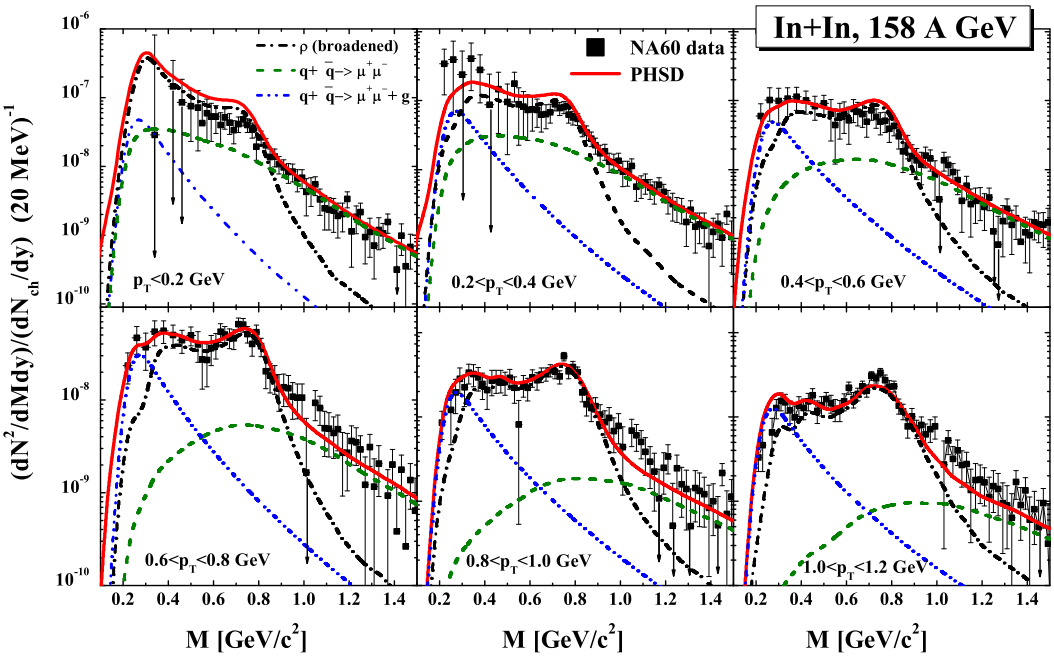

Figure 4.17: Acceptance-corrected mass spectra of excess dimuons from In+In collisions at 158A GeV for different transverse momentum bins from PHSD compared to the data of the NA60 Collaboration [38, 140–142, 153]. The dash-dotted black, dashed green and dash-dot-dotted blue, and solid red lines show, respectively, the dilepton yield from the in-medium ρ meson with a broadened spectral function, the dilepton yield from $q + \bar{q}$ and the sum of them.

$\pi + a_1 \to l^+l^-$ process is displayed by the magenta line with stars, $\pi + w \to l^+l^-$ by the blue line with squares and $\rho + \rho \to l^+l^-$ by the black line with circles. We find that the dilepton yield from the decays of the thermal ρ mesons falls exponentially at high masses. The contributions from the 4π processes start dominating over the yield from the thermal ρ-meson decays at $M \approx 1$ GeV. We further confirm in PHSD that at $M > 1$ GeV the contribution of the $\pi + a_1$ process is the highest among the secondary mesonic sources of dileptons, as was first noted by the authors of Ref. [155]. On the other hand, in contrast to the thermal ρ mesons, the direct ρ mesons produced in the string decays (following the initial hard collisions) exhibit a power-law tail at masses above 1 GeV and, consequently, dominate the overall dilepton spectrum of hadronic origin for $M > 1$ GeV. Note that the sizable contribution of direct ρ mesons is due to the large "corona" in In+In collisions at SPS energies.

Next we investigate the centrality dependance of the dilepton production in heavy-ion collisions at SPS energies. In Fig. 4.16 we present the mass spectra of excess dimuons from In+In at 158A GeV for $0.2 < p_T < 2.4$ GeV and

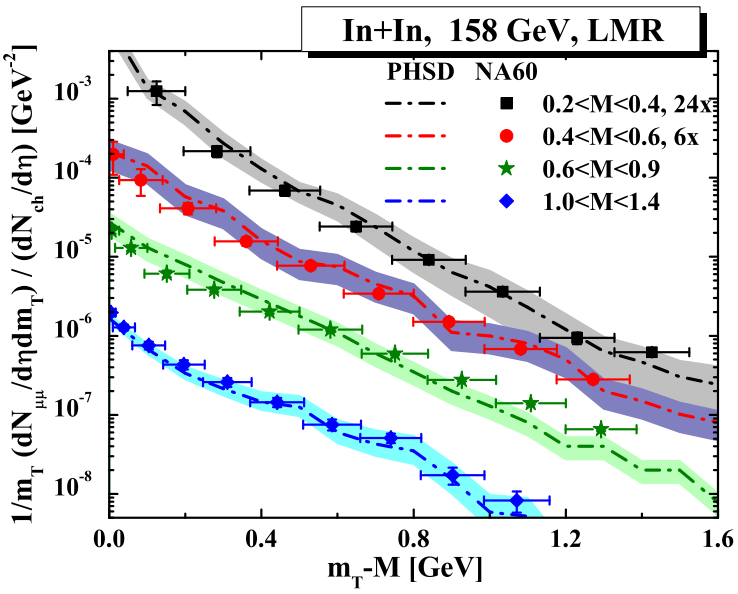

Figure 4.18: Transverse mass spectra of dileptons for In+In at 158A GeV in PHSD (dash-dotted lines) compared to the data of the NA60 Collaboration (symbols) [38, 140–142, 153].

$3 < \eta < 4.2$ from PHSD for different centrality bins. The dash-dotted black, dashed green, and solid red lines show, respectively, the dilepton yield from the in-medium ρ meson with a broadened spectral function, the dilepton yield from the $q+\bar{q}$ annihilation and the sum of them. We have chosen the following centrality classes: central collisions (impact parameter 0.5 fm$< b <$ 3.5 fm), semicentral (3.5 fm$< b <$ 5.5 fm), and semiperipheral ($5.5 < b <$ 8.5 fm). The predictions in Fig. 4.16 can be verified/falsified in the future by a direct comparison to the data as the latter become available.

The NA60 Collaboration has accessed the information on the transverse-momentum dependence of dilepton production by measuring the dilepton yield in different bins of p_T. In Fig. 4.17 we show the mass spectra of excess dimuons from In+In at 158A GeV for different transverse momentum bins from PHSD compared to the data of the NA60 Collaboration [38, 140–142, 153]. The dash-dotted black, dashed green and dash-dot-dotted blue, and solid red lines show, respectively, the dilepton yield from the in-medium ρ meson with a broadened spectral function, the dilepton yield from the $q + \bar{q}$ annihilation, and the sum of them. One observes a generally good agreement with the data.

In Fig. 4.18, transverse mass spectra of dileptons for In+In at 158 AGeV in PHSD are compared to the data of the NA60 Collaboration for the four mass bins. The comparison of the mass dependence of the slope parameter

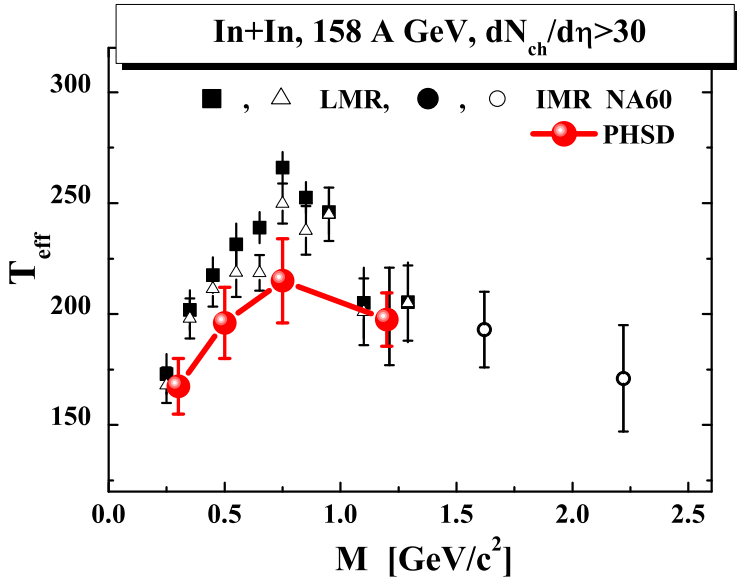

Figure 4.19: The inverse slope parameter T_{eff} of the dimuon yield from In+In at 158A GeV as a function of the dimuon invariant mass in PHSD (red dots) compared to the data of the NA60 Collaboration (black symbols) [38, 140–142, 153].

evolution in PHSD and the data is shown explicitly in Fig. 4.19. Including partonic dilepton sources allows us to reproduce in PHSD the m_T spectra (cf. Fig. 4.18) as well as the finding of the NA60 Collaboration [38, 140–142, 153] that the effective temperature of dileptons (slope parameters) in the intermediate-mass range is lower than that of the dileptons in the mass bin $0.6 < M < 1$ GeV, which is dominated by hadronic sources (cf. Fig. 4.19). The softening of the transverse mass spectrum with growing invariant mass implies that the partonic channels occur dominantly before the collective radial flow has developed. Also, the fact that the slope in the lowest-mass bin and the highest one are approximately equal—both in the data and in PHSD—can be traced back to the two windows of the mass spectrum that in our picture are influenced by the radiation from the sQGP: $M = 2M_\mu - 0.6$ GeV and $M > 1$ GeV. A detailed look at the PHSD results shows that in total we still slightly underestimate the slope parameter T_{eff} in the ρ-mass region which might be due to missing partonic initial-state effects or an underestimation of flow in the initial phase of the reaction.

4.4 Summary

In this Chapter we have addressed relativistic collisions of Pb+Pb as well as of In+In (in case of dilepton production) at SPS energies and Au+Au collisions at RHIC energies in the PHSD approach which includes explicit partonic degrees of freedom as well as dynamical local transition rates from partons to hadrons (3.41). We have found that even central collisions at the top SPS energy show a large fraction of non-partonic, i.e., hadronic or string-like matter, which can be viewed as a "hadronic corona" [156]. On the other hand—studying in detail Pb+Pb reactions at SPS energies in comparison to the data [24]—it is found that the partonic phase has only a very low impact on the longitudinal rapidity distributions of hadrons, but a sizeable influence on the transverse-mass distribution of final kaons due to the partonic interactions. The most pronounced effect is seen on the production of multi-strange antibaryons due to a slightly enhanced $s\bar{s}$ pair production in the partonic phase from massive timelike gluon decay and a more abundant formation of strange antibaryons in the hadronization process.

At RHIC energies the PHSD calculations show also a good reproduction of the hadron transverse mass and rapidity spectra. Furthermore, the elliptic flow v_2 is well reproduced for Au+Au reactions at $\sqrt{s} = 200$ GeV as a function of centrality as well as of transverse momenta up to $p_T \simeq 1.5$ GeV. Due to the local transition rates from partons to hadrons (3.41) the PHSD approach also gives an approximate quark number scaling of the elliptic flow as found experimentally by the STAR and PHENIX Collaborations. The elliptic flow v_2 as a function of the collision energy in comparison to the available experimental data as well as to the various transport approach is presented, too.

Furthermore, we have studied the dilepton production in In+In collisions at 158A GeV within the PHSD off-shell transport approach including a collisional broadening of vector mesons, microscopic secondary multimeson channels and the strongly interacting QGP radiation, which is described by the interactions of dynamical quasiparticles in line with the degrees of freedom propagated in the transport approach. A comparison to the data of the NA60 Collaboration shows that the dilepton yield is well described by including the collisional broadening of vector mesons, while simultaneously accounting for the electromagnetic radiation of the strongly coupled QGP via off-shell quark-antiquark annihilation, quark annihilation with gluon Bremsstrahlung and the gluon-Compton scattering mechanisms. Furthermore, the spectra in the intermediate

mass range ($1 \leq M \leq 2.5$ GeV) are found to be dominated by quark-antiquark annihilation in the nonperturbative QGP. Also, the observed softening of the transverse mass spectra at intermediate masses ($1 \leq M \leq 2.5$ GeV) is approximately reproduced.

In view of the successful description of single-particle spectra, collective flow v_2 as well as electromagnetic radiation in nucleus-nucleus collisions from lower SPS to top RHIC energies we infer that the cross sections implemented into PHSD are compatible with experimental observations.

Chapter 5

Dynamical equilibration of strongly interacting matter

In the first milliseconds after the "big bang" our entire universe existed in the QGP state. Whereas the early "big bang" of the universe most likely evolved through steps of kinetic and chemical equilibrium, the laboratory "tiny bangs" proceed through phase-space configurations that initially are far from an equilibrium phase and then evolve by fast expansion. On the other hand, many observables from strongly interacting systems are dominated by many-body phase space such that spectra and abundances look "thermal." It is thus tempting to characterize the experimental observables by global thermodynamical quantities such as "temperature," chemical potentials or entropy [157–165]. We note that the use of macroscopic models such as hydrodynamics [166–169] employs as a basic assumption the concept of local thermal and chemical equilibrium in the infinite-volume limit, although by introducing different chemical potentials one may treat chemical off-equilibrium also in hydrodynamics. The crucial question, however, of how and on what time scales thermodynamic equilibrium can be achieved is presently a matter of debate. Thus nonequilibrium approaches have been used in the past to address the problem of time scales associated with global or local equilibration [60, 170–179]. Another question is the influence of finite-size effects on fluctuation observables and the possibility of relating experimental observations in relativistic heavy-ion collisions to the theoretical predictions obtained in the thermodynamic limit. Therefore, a thorough microscopic study of the questions of thermalization and equilibration of confined and deconfined matter within a nonequilibrium transport approach, incorporating both hadronic and partonic degrees of freedom and

the dynamic phase transition, is mandatory.

This Chapter is dedicated to the study of the thermalization and equilibration of confined and deconfined matter, which is a main task of this thesis. The presentation is organized as follows. In Sec. 5.1 we provide the initialization procedure of the box with periodic boundary conditions. Then in Sec. 5.2 we define the effective cross sections for each of the various partonic channels, while in Sec. 5.3 we present the actual results on the chemical equilibration of the partonic matter in PHSD. In Sec. 5.4 we investigate the properties of the partonic matter in chemical and kinetic equilibrium and compare the particle properties in equilibrium with the DQPM, which has been developed to describe the thermodynamics of lQCD. In Sec. 5.5 we study (within the dynamical approach) the parton properties at finite quark chemical potential μ_q, while in Sec. 5.6 higher moments of parton distributions and the equilibration of fluctuation observables as well as the size of fluctuations in equilibrium are investigated. We then show in Sec. 5.7 the time scales for the relaxation of fluctuation observables in comparison to the time scales for the equilibration of the average values of the observables. Finally, a summary of this Chapter is presented in Sec. 5.8[1].

5.1 Initialization of the box with periodic boundary conditions

We simulate the "infinite" matter within a cubic box with periodic boundary conditions at various values for the quark density (or chemical potential) and energy density. The system is initialized out of equilibrium and approaches kinetic and chemical equilibrium during its evolution by PHSD. We are not investigating here configurations far from equilibrium, such as, e.g., the result of initial hard scatterings in a heavy-ion collision. Instead, we study here configurations which are reasonably close to equilibrium because in this case the approach to equilibrium will have universal characteristics that will not depend on the precise choice of the initial state (cf. Fig. 5.12 and its description). Let us describe our initial state in detail:

- The size of the box is fixed to 9^3 fm^3 for most of the following calculations. However, we will study also larger box sizes in order to determine whether

[1]Note that most of the results of this Chapter have been published in Refs. [180–182] by the author.

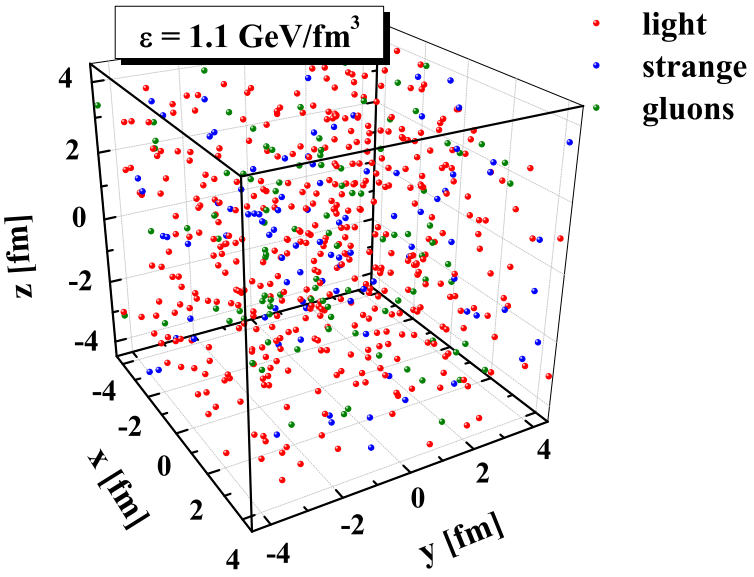

Figure 5.1: The initial distributions of light (red dots) and strange (blue dots) quarks and antiquarks as well as of gluons (green dots) in coordinate space for a system at $\varepsilon = 1.1$ GeV/fm^3.

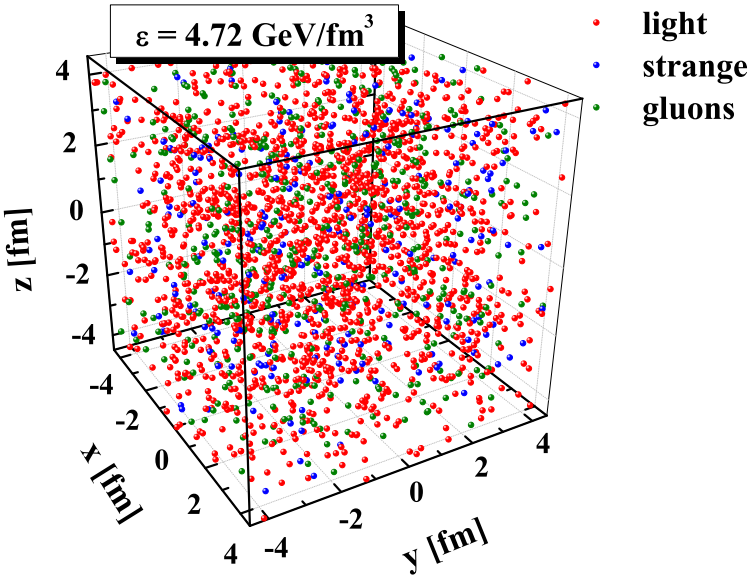

Figure 5.2: The initial distributions of light (red dots) and strange (blue dots) quarks and antiquarks as well as of gluons (green dots) in coordinate space for a system at $\varepsilon = 4.72$ GeV/fm^3.

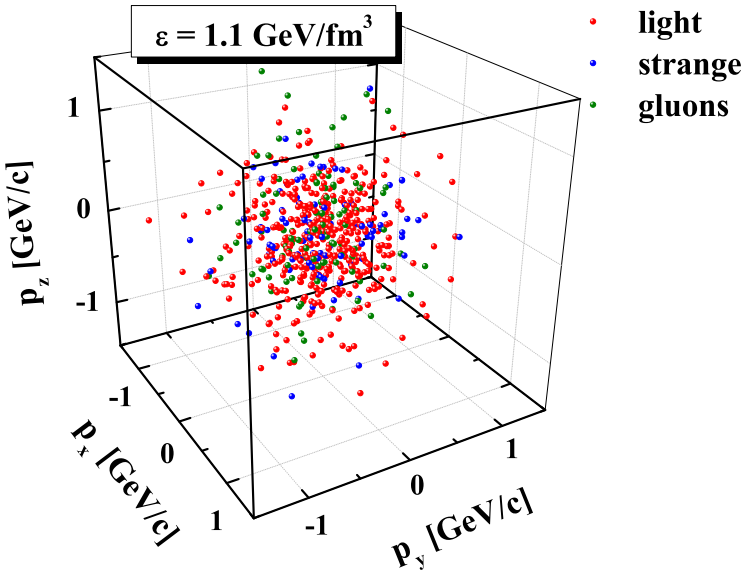

Figure 5.3: The initial distributions of light (red dots) and strange (blue dots) quarks and antiquarks as well as of gluons (green dots) in momentum space for a system at $\varepsilon = 1.1$ GeV/fm^3.

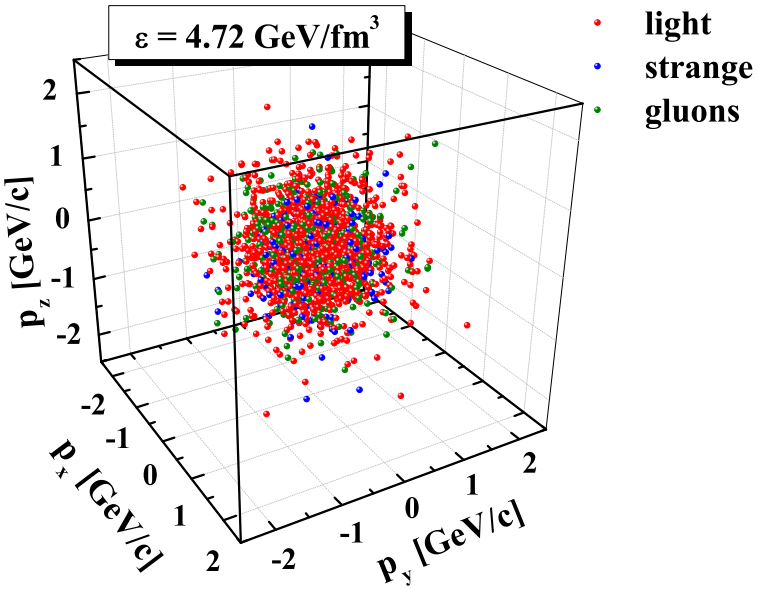

Figure 5.4: The initial distributions of light (red dots) and strange (blue dots) quarks and antiquarks as well as of gluons (green dots) in momentum space for a system at $\varepsilon = 4.72$ GeV/fm^3.

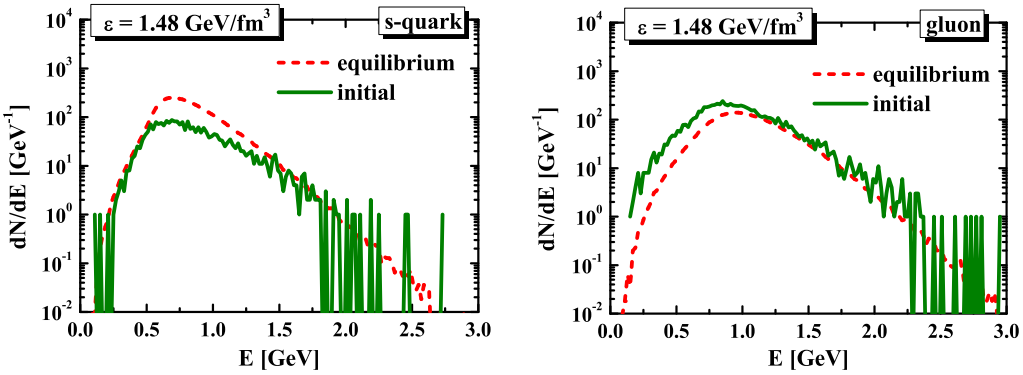

(a) (b)

Figure 5.5: The initial energy distributions (solid green lines) in comparison to the equilibrium energy distributions (short-dashed red lines) for a system at $\varepsilon = 1.48$ GeV/fm^3. (a) s quarks; (b) gluons.

the thermodynamic limit is approximately reached, in particular, when addressing the fluctuation measures.

- The initialization is done by populating the box with light (u and d) and strange (s) quarks, antiquarks, and gluons.

- The initial space coordinates for the quarks, antiquarks, and gluons are chosen at random within the finite box as shown in Figs. 5.1 and 5.2 for different energy densities. As an example, we present the initial distributions of partons in momentum space in Figs. 5.3 and 5.4 for $\varepsilon = 1.1$ and 4.72 GeV/fm^3.

- The system is initialized close to kinetic but out of chemical equilibrium. The initial momentum distributions and abundances of partons are given by the thermal distributions

$$f(\omega, \mathbf{p}) = C_i p^2 \omega \rho_i(\omega, \mathbf{p}) n_{\mathrm{F(B)}}(\omega/T_{\mathrm{in}}) \,, \tag{5.1}$$

where $\rho_i(\omega, \mathbf{p})$ are the spectral functions (with $i = q, \bar{q}, g$) and $n_{\mathrm{B(F)}}(\omega/T_{\mathrm{in}})$ are the Bose (Fermi) distributions with a "temperature" parameter T_{in}, which should not be misidentified with the final temperature T, which will be characteristic for the energy distributions of the particles after the thermalization. The latter, "true" temperature T is well defined for the final, thermalized state, and in Sec. 5.4 it will be extracted from the final particle spectra by fitting their high-energy tails. We will use

this extracted final temperature T to study the equation of state of the partonic matter in PHSD in Sec. 5.4. On the other hand, the value of the "temperature" parameter $T_{\rm in}$ of the initial energy-momentum distributions and the numbers of partons (determined by the coefficients C_i) just define the total energy of the system (and in equilibrium the quark chemical potentials). We show in Fig. 5.5 the initial (solid green lines) energy distributions of the strange quarks (l.h.s) and gluons (r.h.s.) in comparison to the equilibrium (short-dashed red lines) energy distributions. As can be seen in Fig. 5.5, the slopes of the initial and equilibrium distributions are slightly different (the "initial" and final temperatures differ from each other).

- The system is initialized far from chemical equilibrium due to the initial suppression of the strange quarks and antiquarks. In the initial state the ratio of the number of s quarks to the number of u quarks and to the number of d quarks is taken as 1:3:3 such that the strangeness is clearly undersaturated initially. However, we expect that in the chemically equilibrated state the ratio of strange quarks to the number of light (u or d) quarks is governed by the thermodynamics ratios according to their masses.

- The spectral properties (pole masses and the widths) of the quarks, antiquarks, and gluons are initially taken in the simple Lorentzian form (3.8) with two parameters for each parton type (M, Γ). Note that in the DQPM model one also assumes Lorentzian shapes for the parton spectral functions; however, we choose to start the system evolution not from the explicit DQPM equilibrium spectral functions. For this purpose we deliberately employ an average value for the pole mass parameter in the spectral function of the strange quark at initialization (i.e., we choose $M_s = M_u = M_d$). The other parameters (M_u, M_d, M_g, Γ_i) are initially as in the DQPM. The spectral functions of partons then evolve dynamically in time and in the final state may deviate noticeably from the initial ones. We will see in the results of Sec. 5.4 that indeed in the final thermalized state the dynamical gluon spectral functions deviate from the Lorentzian input and thus are not described properly by the DQPM ansatz. On the other hand, the pole mass of the strange quark dynamically reaches the "correct" value in equilibrium. We stress here

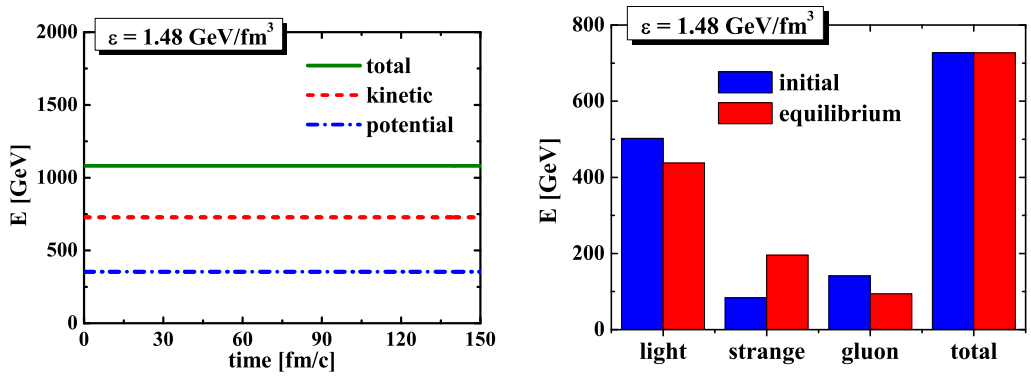

(a) (b)

Figure 5.6: (a) The time evolution of the total (solid green line), kinetic (short-dashed red line), and potential (short-dash-dotted blue line) energies for a system at $\varepsilon = 1.48$ GeV/fm^3; (b) The ratio between the initial (blue columns) and equilibrium (red columns) kinetic energies for a system at $\varepsilon = 1.48$ GeV/fm^3, which is stored in different parton species, separately.

the importance of using off-shell transport for our studies. Only in case of the generalized transport propagation we can study the evolution of the spectral functions!

- The dynamical quarks, antiquarks, and gluons within PHSD interact also via the mean fields. Note that the potential energy of this interaction is taken into account at initialization, so that it contributes to the total energy density. The strength of the quark and gluon potential energy in PHSD is given by the spacelike part of the 00-components of the energy momentum tensor T^{00} as in the DQPM (cf. Sec. 3.2.2). We present in Fig. 5.6 (l.h.s) the time evolution of the total (solid green line), kinetic (short-dashed red line), and potential (short-dash-dotted blue line) energies. The r.h.s. of Fig. 5.6 shows the ratio between the initial (blue columns) and equilibrium (red columns) kinetic energies, which is stored in different parton species, separately. As can be seen in Fig. 5.6 (l.h.s.), the total energy is conserved in our simulations and the ratio of the potential to total energy ≈ 0.33 holds for the whole time evolution (cf. Fig. 3.8(b)).

5.2 Reaction rates and effective cross sections

In this Section we present the effective cross sections for each of the various partonic channels as a function of energy density ε; these cross sections determine the partial widths of the dynamical quasiparticles as well as the various interaction rates. This analysis is important, because, although the DQPM provides the basis for the description of the strongly interacting quark-gluon system in PHSD in equilibrium, the dynamical transport approach (i.e., PHSD) goes beyond the DQPM in simulating hadronic and partonic systems also out of equilibrium. For the microscopic transport calculations the partial widths of the microscopic scattering and decay channels have to be known, while the DQPM provides only the total widths of the dynamical quasiparticles that have been fixed by lQCD calculations as described in Sec. 3.2. Furthermore, the explicit shape of the partonic spectral functions—taken as Lorentzians in the DQPM (3.8)—will depend on the decomposition of the interactions into particular channels within the coupled-channel dynamics of PHSD.

In order to fix the partial cross sections for the interactions between the dynamical quarks and gluons (as functions of energy density ε) we perform the PHSD calculations in a cubic finite box with periodic boundary conditions—simulating "infinite" hadronic or partonic matter (cf. Sec. 5.1). In this particular case the derivatives of the retarded self-energies with respect to space vanish in Eq. (3.5) such that we essentially deal with the parton dynamics due to the collision terms in Eq. (3.5).

The following (quasi)elastic interactions among quarks, antiquarks, and gluons $(q, \bar{q}, g)$ are implemented in PHSD:

$$q(m_1) + q(m_2) \rightarrow q(m_3) + q(m_4), \tag{5.2}$$

$$q + \bar{q} \rightarrow q + \bar{q}, \tag{5.3}$$

$$\bar{q} + \bar{q} \rightarrow \bar{q} + \bar{q}, \tag{5.4}$$

$$g + q \rightarrow g + q, \tag{5.5}$$

$$g + \bar{q} \rightarrow g + \bar{q}, \tag{5.6}$$

$$g + g \rightarrow g + g. \tag{5.7}$$

The (quasi)elastic processes (5.2)–(5.7) play a crucial role for the thermalization in PHSD due to the possibility to change the masses of interacting partons in the final state as shown in Eq. (5.2).

The flavor exchange of partons is possible only within the inelastic interactions in PHSD, which are:

$$g \leftrightarrow q + \bar{q}, \tag{5.8}$$

$$g \leftrightarrow g + g, \tag{5.9}$$

$$g + g \leftrightarrow q + \bar{q}. \tag{5.10}$$

The inelastic interactions (5.8)–(5.10) are the basic processes for the chemical equilibration in PHSD; however, the inelastic processes in Eqs. (5.9) and (5.10) are strongly suppressed (<1%) kinematically in PHSD due to the large masses of gluons.

We recall that for binary channels we have explicit formulae for the partial widths, e.g. (from the collision term in Eq. (3.5)),

$$\begin{aligned}\Gamma^{elastic}(p_1) = & \sum_{2,3,4} tr_2 tr_3 tr_4 |T^\dagger T|^2_{1+2\to 3+4} \\ & \times A_{h_2}(p_2) A_{h_3}(p_3) A_{h_4}(p_4) N_{h_2}(p_2) \bar{f}_{h_3}(p_3) \bar{f}_{h_4}(p_4) \\ & \times (2\pi)^4 \delta^4(P_1 + P_2 - P_3 - P_4),\end{aligned} \tag{5.11}$$

where h_i is an index, which can be equal to "q_i", "$\bar{q}_i$" or "g", ($q_i = u, d, s$). Since we study partons at high temperature the fermion blocking terms can be neglected, i.e., approximated by $\bar{f} = 1$, and one ends up with

$$\begin{aligned}\Gamma^{elastic}(p_1) = & \sum_{2,3,4} tr_2 \; |T^\dagger T|^2_{1+2\to 3+4} \\ & \times A_{h_2}(p_2) N_{h_2}(p_2) R_2(p_1 + p_2; M_3, M_4),\end{aligned} \tag{5.12}$$

where the four-momenta of particle 4 are fixed by energy-momentum conservation and R_2 stands for the two-body phase-space integral (cf. Ref. [183]). We recall that the squared matrix element times the two-body phase-space integral defines a binary cross section σ times a kinematic factor, i.e.,

$$\sum_{3,4} |T^\dagger T|^2_{1+2\to 3+4} \; R_2(p_3 + p_4) \; = 4 E_1 E_2 v_{rel} \sigma, \tag{5.13}$$

with the relativistic relative velocity for initial invariant energy squared, s, given by

$$v_{rel} = \sqrt{(s - M_1^2 - M_2^2)^2 - 4 M_1^2 M_2^2}/(2 E_1 E_2) \; . \tag{5.14}$$

In Eq. (5.13) $\sum_{3,4}$ stands for a summation over discrete final channels.

If the cross section σ is essentially independent of the momenta, which should hold for low-energy binary scattering, we may write Eq. (5.12) as

$$\Gamma^{elastic}(p_1) = \langle v_{12}\sigma\rangle \tilde{N}_2 \ , \tag{5.15}$$

which corresponds to the Boltzmann limit relating the collision rate to the average velocity between the colliding partners (in the center-of-mass frame) and the cross section for scattering as well as the density $\tilde{N}_2$ (summed over the discrete quantum numbers of particle 2). We employ these relations in determining the effective elastic cross sections between partons in PHSD. Note that the total number of collisions between particles of type 1 and 2 are obtained from Eq. (5.15) (in our case) by multiplication with the volume V and the particle density $\tilde{N}_1$, i.e.,

$$\frac{dN_{12}^{coll}}{dt} = V\langle v_{12}\sigma\rangle \tilde{N}_1 \tilde{N}_2 \ . \tag{5.16}$$

Both the number of collisions between the individual particle species per time as well as their densities are easily accessible in the transport approach.

The cross section for gluon formation from flavor-neutral $q + \bar{q}$ interactions in the color octet channel is calculated by the resonant cross section at invariant energy squared, $s = (p_q + p_{\bar{q}})^2$,

$$\sigma_{q\bar{q}\to g}(s, \varepsilon, M_q, M_{\bar{q}}) = \frac{2}{4} \frac{4\pi s \Gamma_g^2(\varepsilon)}{\left[s - M_g^2(\varepsilon)\right]^2 + s\Gamma_g^2(\varepsilon)} \frac{1}{P_{rel}^2}, \tag{5.17}$$

with

$$P_{rel}^2 = \frac{\left[s - (M_q + M_{\bar{q}}^2\right] \left[s - (M_q - M_{\bar{q}})^2\right]}{4s} \ , \tag{5.18}$$

while the factor 2/4 corresponds to the ratio of final to initial spins (assuming two transverse degrees of freedom for the gluon in line with the DQPM). Note that formula (5.17) provides an off-shell cross section which depends on the four-momenta of the incoming quark and antiquark as well as on the spectral properties of the gluon. We recall that in the actual simulation the quark and antiquark masses are distributed according to the spectral function (3.8) and their three-momenta vary in a broad range roughly in line with thermal Boltzmann distributions.

We point out that the iteration of the coupled equations has been performed

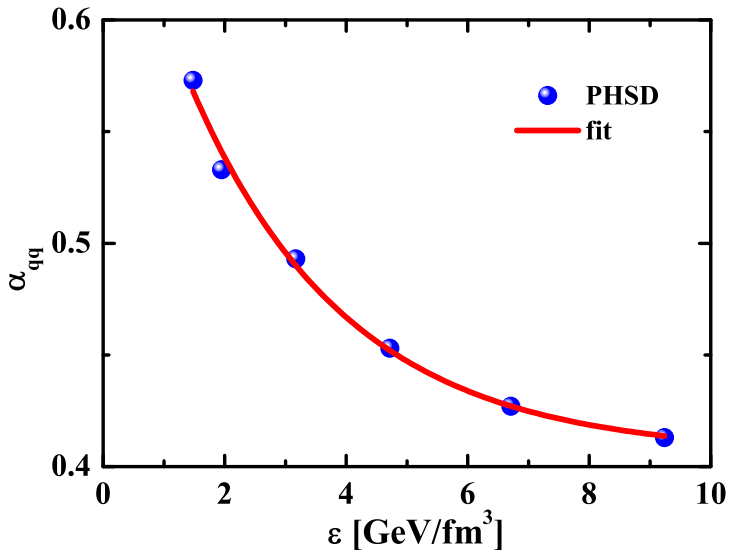

Figure 5.7: The energy-density dependence of the coefficient α_{qq} extracted from the PHSD simulations in the box (blue dots) and the corresponding fit (solid red line) (5.21).

with the additional boundary conditions

$$\sigma_{gq(qg)} = \frac{4}{9}\sigma_{gg}(\varepsilon), \quad \sigma_{qq} = \alpha_{qq}(\varepsilon)\sigma_{gg}(\varepsilon) \tag{5.19}$$

as suggested by lQCD, which roughly follows a scaling with the color Casimir operators. This is also reflected in the DQPM ansatz (3.16). We mention that this scaling might be violated and require a further independent parameter, which, however, presently cannot be fixed appropriately by lQCD calculations. The function $\alpha_{qq}(\varepsilon)$ has to be determined by the iteration procedure until self-consistency has been reached for each value of the energy density ε. Note that for $\mu_q = 0$ we have identical phase-space distributions for quarks and antiquarks and also identical interaction rates, which simplifies substantially the iteration process. Additionally, we assume that the elastic scattering process is isotropic.

The numerical results of the self-consistent determination of the cross sections and widths can be parametrized in the following form (with the cross sections given in fm^2):

$$\sigma_{gg}(\varepsilon) \approx 7.6e^{-\varepsilon/0.8} + 106.2e^{-\varepsilon/0.2} + 1.7e^{-\varepsilon/3.7} + 0.3, \tag{5.20}$$

where ε is given in units of GeV/fm^3. The solution of the coupled equations

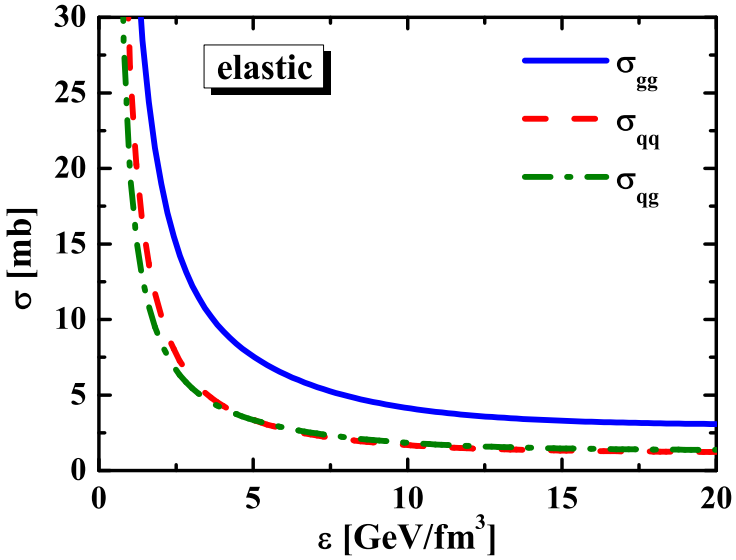

Figure 5.8: The gluon-gluon (solid blue line), quark(antiquark)-quark(antiquark) (dashed red line), and quark(antiquark)-gluon or gluon-quark(antiquark) (dash-dotted green line) elastic cross sections as functions of the energy density.

then give the coefficient

$$\alpha_{qq}(\varepsilon) \approx 0.3\ e^{-\varepsilon/2.6} + 0.4\ . \tag{5.21}$$

This fit is shown in comparison to the numerical results of the iteration in Fig. 5.7. Accordingly, the expressions for the partonic elastic scatterings may be parametrized as

$$\sigma_{gq(qg)} = \frac{4}{9}\sigma_{gg}(\varepsilon), \quad \sigma_{qq} \approx (0.3\ e^{-\varepsilon/2.6} + 0.4)\sigma_{gg}(\varepsilon). \tag{5.22}$$

In Fig. 5.8 we display the resulting gluon-gluon (solid blue line), quark-quark (dashed red line), and quark-gluon (dash-dotted green line) elastic cross sections as functions of the energy density. Note that these cross sections are moderate at high energy density and typically in the order of 2–3 mb but become large close to the critical energy density. This behavior basically reflects the infrared enhancement of the strong coupling (3.13) around T_c and implies that partons "see each other" at distances of about 1 fm (and even more) in the vicinity of the phase transition. The physics interpretation is that color singlet $q\bar{q}$ pairs form "rotating strings" whereas qq or $(\bar{q}\bar{q})$ pairs form resonant (and colored) diquark (antidiquark) states that may fuse with another quark

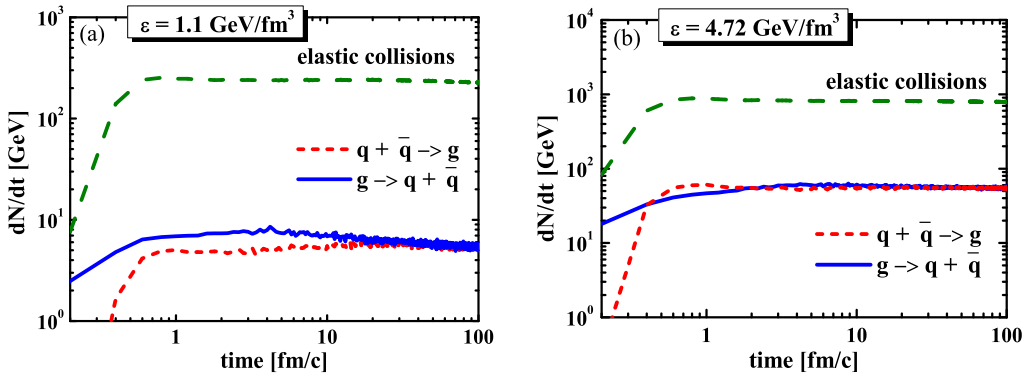

Figure 5.9: The reaction rates for elastic parton scattering (dashed green lines), gluon splitting (solid blue lines), and flavor-neutral $q\bar{q}$ fusion (short-dashed red lines) as functions of time for systems at different energy densities initially slightly out-of equilibrium. (a) $\varepsilon = 1.1$ GeV/fm^3; (b) $\varepsilon = 4.72$ GeV/fm^3.

(or antiquark) to form baryonic resonances.

Although the cross sections (5.22) have been extracted for $\mu_q = 0$ in thermal equilibrium we may adopt the same cross sections also out of equilibrium and for $\mu_q \neq 0$ in the PHSD transport approach. This appears legitimate for phase-space configurations slightly out of equilibrium as well as for moderate μ_q.

5.3 Chemical and thermal equilibration

In this Section we present the results on chemical and kinetic equilibration of strongly interacting matter within PHSD. In the course of the subsequent transport evolution of the system by PHSD, the numbers of gluons, quarks, and antiquarks change dynamically through inelastic and elastic collisions to equilibrium values. We observe in Fig. 5.9 that after about 20 fm/c (for ε = 1.1 GeV/fm^3) or 3 fm/c (for ε = 4.72 GeV/fm^3) the reactions rates are practically constant and obey detailed balance for gluon splitting and $q\bar{q}$ fusion. In Fig. 5.9 the reaction rates for elastic parton scattering (dashed green lines), gluon splitting (solid blue lines), and flavor-neutral $q\bar{q}$ fusion (short-dashed red lines) are presented as functions of time at energy densities of 1.1 and 4.72 GeV/fm^3. We find that the rate of inelastic collisions relative to the elastic rate is larger at higher energy density; this is due to a larger gluon fraction with increasing energy density (or temperature) since gluons are more suppressed at low temperature due to their larger mass difference relative to the quarks.

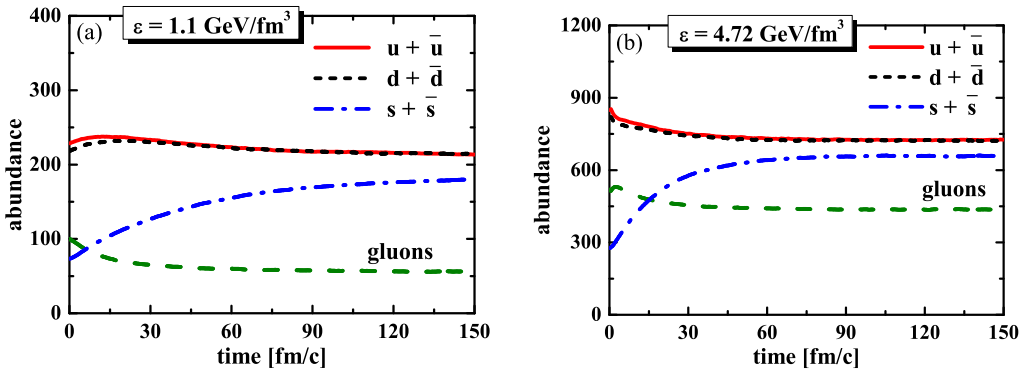

(a) (b)

Figure 5.10: Abundances of the u (solid red lines), d (short-dashed black lines), and s (dash-dotted blue lines) quarks + antiquarks and gluons (dashed green lines) as functions of time for systems at different energy densities. (a) $\varepsilon = 1.1$ GeV/fm^3; (b) $\varepsilon = 4.72$ GeV/fm^3.

Nevertheless, it is worth mentioning that the elastic scattering between partons dominates in PHSD.

A sign for chemical equilibration is the stabilization of the numbers of partons of the different species in time for $t \to \infty$. In Fig. 5.10 we show the particle abundances of u, d, and s quarks+antiquarks (solid red, short-dashed black, and dash-dotted blue lines, respectively) and gluons (dashed green lines) for systems at energy densities of 1.1 and 4.72 GeV/fm^3, which are above the critical energy density (as in the previous figure). We note in Sec. 5.1 that energy conservation within PHSD holds with an accuracy better than 10^{-3} in these cases, which is a necessary requirement for our study. The slow increase of the total number of strange quarks and antiquarks during the time evolution reflects long equilibration times through inelastic processes involving strange partons. These time scales are significantly larger than typical reaction times of nucleus-nucleus collisions at SPS or RHIC energies. Note, however, that the rapidity and transverse momentum spectra of strange hadrons are well described by PHSD from lower SPS to top RHIC energies (cf. Chapter 4).

These findings appear to be in contradiction; however, the time scales from the box calculations cannot directly be applied to nucleus-nucleus collisions since the initial conditions are very different. The initial state in the box is chosen close to thermal parton equilibrium. This suppresses the production of strange quark-antiquark pairs due to kinematics or available energy. The strangeness production in A+A collisions occurs mainly in the early stage of

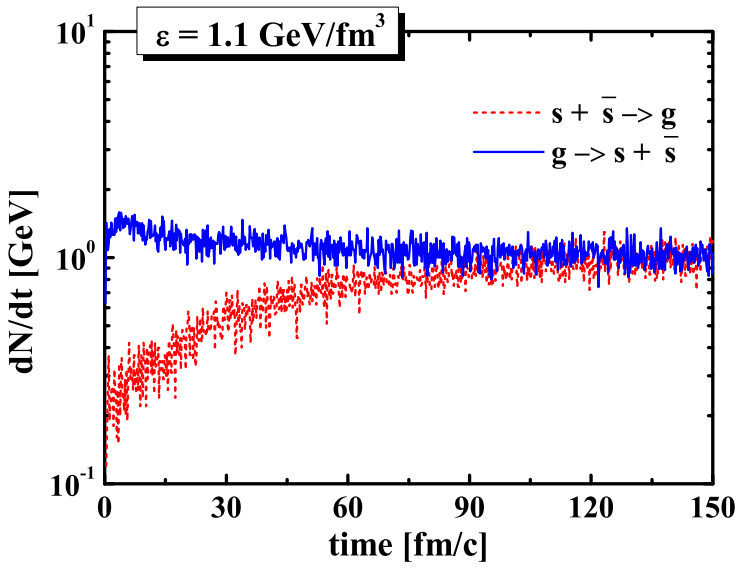

Figure 5.11: The reactions rates for gluon splitting to pairs of strange quarks and antiquarks (solid blue line) and flavor-neutral $s\bar{s}$ fusion (short-dashed red line) as functions of time for a system at an energy density of 1.1 GeV/fm^3.

A+A reactions where the system is rather far away from local thermal equilibrium and kinematical (energy) constraints are subleading, i.e., particle collisions with large center-of-mass energies take place. These energies are much larger than those in local thermal equilibrium, which makes the strangeness production more effective in A+A collisions and leads to lower strangeness equilibration times. Note that these arguments are supported by the calculations also in HSD, where both colliding and produced particles are hadrons, which happens at Alternating Gradient Synchrotron (AGS) and lower SPS energies, as well as in PHSD, where the degrees of freedom are quarks and gluons (at top SPS, RHIC, and LHC energies).

In Fig. 5.11 we present the time evolution of the reaction rates for gluon splitting to pairs of strange quarks and antiquarks (solid blue line) and $s\bar{s}$ fusion (short-dashed red line) for a system at an energy density of 1.1 GeV/fm^3 with the s and $\bar{s}$ quarks initially suppressed by a factor of 3 with respect to the light quarks. Accordingly, the initial rate for $s + \bar{s} \to g$ is suppressed by about a factor of 9 and a large time for chemical equilibration is observed again.

The results, shown in Figs. 5.9–5.11, correspond to the initial ratios between u, d, and s quarks (and antiquarks) taken as

$$u : d : s = 3 : 3 : 1.$$

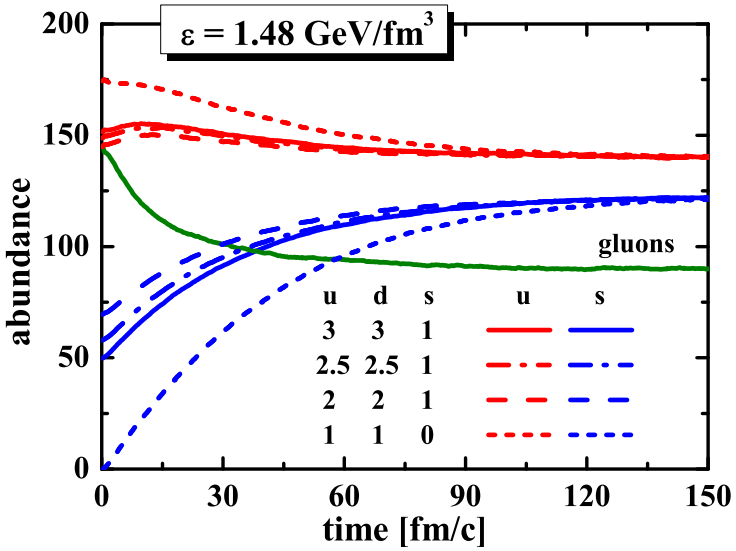

Figure 5.12: Abundances of the u, s quarks and gluons as functions of time for systems at $\varepsilon = 1.48$ GeV/fm^3 with the different initial flavor ratios $u:d:s = 3:3:1$ (solid lines), $u:d:s = 2.5:2.5:1$ (dash-dotted lines), $u:d:s = 2:2:1$ (dashed lines) and $u:d:s = 1:1:0$ (short-dashed lines).

We now vary the initial flavor decomposition and see if the system approaches the same final state (at constant energy density). In Fig. 5.12 we show the particle abundances of the u, and s quarks and gluons as functions of time for systems populated with the different initial flavor ratios: $u:d:s = 3:3:1$ (solid lines), $u:d:s = 2.5:2.5:1$ (dash-dotted lines), $u:d:s = 2:2:1$ (dashed lines), and $u:d:s = 1:1:0$ (short-dashed lines) while preserving the same energy density of the system $\varepsilon = 1.48$ GeV/fm^3 in all cases. One can see that the equilibrium values of the parton numbers for different flavors do not depend on the initial flavor ratios. This implies that our calculations are stable with respect to the different initializations, confirming that the system does reach equilibrium in our microscopic PHSD calculations. Since the equilibrium state is well defined by the PHSD calculations at each energy density (e.g., for times $t > 120$ fm/c), we may now proceed to study further properties of the system in dynamical equilibrium.

5.4 PHSD equilibrium calculations in comparison to the DQPM

To compare the particle properties in the equilibrated dynamical model and in the DQPM, which has been developed to describe QCD in equilibrium, we calculate dynamically the different parton spectral functions. Let us consider the scalar parton density function ρ_s (3.24) defined (in equilibrium) by

$$\begin{aligned}\rho_s\,(T) = d_g \int_0^\infty \frac{d\omega}{2\pi} \int \frac{d^3p}{(2\pi)^3}\; 2\sqrt{p^2}\; \rho_g(\omega,\mathbf{p}) n_B(\omega/T)\Theta(p^2) \\ + d_{q(\bar{q})} \int_0^\infty \frac{d\omega}{2\pi} \int \frac{d^3p}{(2\pi)^3}\; 2\sqrt{p^2}\; \rho_{q(\bar{q})}(\omega,\mathbf{p}) \\ \times \{n_F[(\omega-\mu_q)/T] + n_F[(\omega+\mu_q)/T]\}\Theta(p^2), \end{aligned} \tag{5.23}$$

where n_B and n_F denote the Bose and Fermi distributions, respectively, while μ_q stands for the quark chemical potential. Here the scalar parton density is summed over gluons, quarks, and antiquarks. We recall that the number of gluonic degrees of freedom is $d_g = 16$, while the fermion degrees of freedom amount to $d_q = d_{\bar{q}} = 2N_cN_f = 18$ in case of three flavors ($N_f = 3$). The function $\Theta(p^2)$ (with $p^2 = \omega^2 - \mathbf{p^2}$) projects on timelike four-momenta since only this fraction of the four-momentum distribution can be propagated within the light cone. In Eq. (5.23) the parton spectral functions ρ_j (with $j = q, \bar{q}, g$) are no longer δ-functions in invariant mass squared but taken as in Eq. (3.8).

Then the total number of timelike gluons g (quarks q or antiquarks $\bar{q}$) in equilibrium (for $\mu_q = 0$) is given by the vector densities in thermodynamic equilibrium multiplied by the volume V:

$$N_{g(q,\bar{q})} = V d_{g(q,\bar{q})} \int_0^\infty \frac{d\omega}{2\pi} \int \frac{d^3p}{(2\pi)^3}\; 2\omega\; \rho_{g(q,\bar{q})}(\omega,\mathbf{p}) n_{B(F)}(\omega/T)\Theta(p^2). \tag{5.24}$$

Note that for the scalar densities the integrand is the invariant mass divided by the energy ω $\left(\sqrt{p^2}/\omega\right)$, while for the vector densities the integrand is simply 1. For the energy spectrum we have

$$\frac{dN_{g(q,\bar{q})}}{d\omega} = \frac{V d_{g(q,\bar{q})}}{2\pi} \int \frac{d^3p}{(2\pi)^3}\; 2\omega\; \rho_{g(q,\bar{q})}(\omega,\mathbf{p}) n_{B(F)}(\omega/T)\Theta(p^2). \tag{5.25}$$

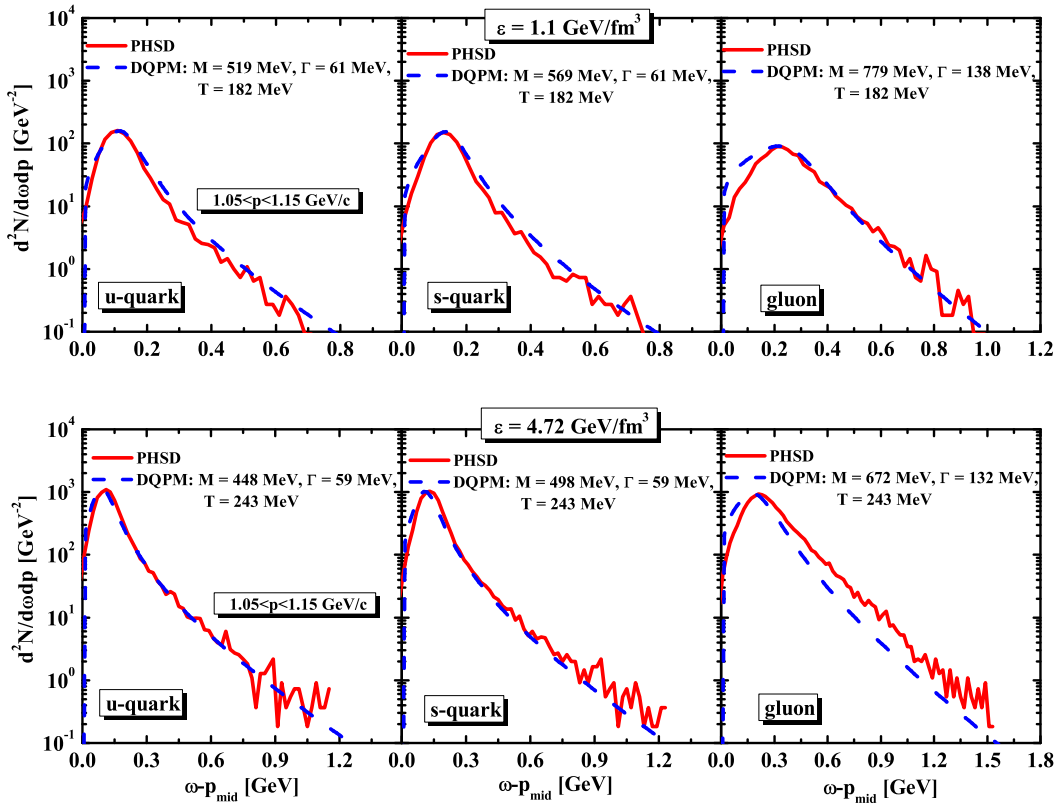

Figure 5.13: The spectra of the u and s quarks and gluons in equilibrium for different energy densities from the PHSD simulations (solid red lines) in comparison to the DQPM model (dashed blue lines).

By choosing the momenta of the partons in the (narrow) interval $|\mathbf{p}| \in [p_-, p_+]$, the energy spectrum is given by

$$\left.\frac{dN_{g(q,\bar{q})}}{d\omega}\right|_{|\mathbf{p}|\in[p_-,p_+]} = \frac{V d_{g(q,\bar{q})}}{2\pi^3}(p_+ - p_-)|p_{mid}|^2\omega\ \rho_{g(q,\bar{q})}(\omega, p_{mid}) n_{B(F)}(\omega/T), \tag{5.26}$$

where $p_{mid} = (p_+ - p_-)/2$ is the average momentum in the bin.

In the transport approach we can construct the distribution of partons with given energy and momentum as

$$\frac{d^2N_{g(q,\bar{q})}}{d\omega dp} = \frac{1}{p_+ - p_-}\left.\frac{dN_{g(q,\bar{q})}}{d\omega}\right|_{|\mathbf{p}|\in[p_-,p_+]}, \tag{5.27}$$

which can be easily evaluated within the PHSD simulations in the box. Its

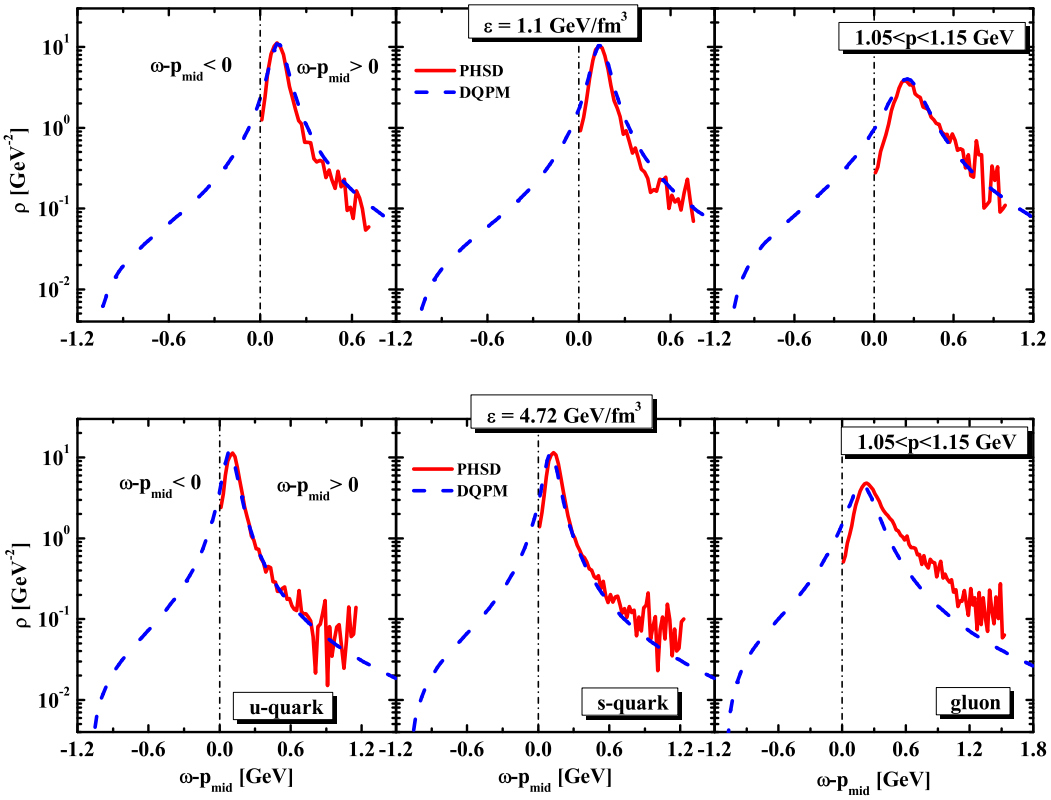

Figure 5.14: The spectral functions of the u and s quarks and gluons in equilibrium from the PHSD simulations (solid red lines) for different energy densities in comparison to the DQPM model (dashed blue lines).

counterpart within the DQPM model is

$$\frac{d^2N_{g(q,\bar{q})}}{d\omega dp} = \frac{V d_{g(q,\bar{q})}}{2\pi^3} p^2_{mid}\ \omega\rho_{g(q,\bar{q})}(\omega, p_{mid}) n_{B(F)}. \tag{5.28}$$

In Fig. 5.13, we show $d^2N/d\omega dp$ for u and s quarks and gluons obtained by the PHSD simulations (red solid lines) of "infinite" partonic systems at energy densities of 1.1 and 4.72 GeV/fm^3. For comparison, we present on the same plots the DQPM assumptions (dashed blue lines) for the respective distributions. One can see that the DQPM distributions are in good agreement with the dynamical calculations within PHSD for all quarks but deviate from the simulations at high energy density for gluons. We will return to this apparent deviation below.

Due to the off-shell dynamics in PHSD (cf. Sec. 2.2.3) we have also access to the dynamical spectral functions in and out of equilibrium. Here we focus on the equilibrium state. Accordingly, we can compare the spectral functions

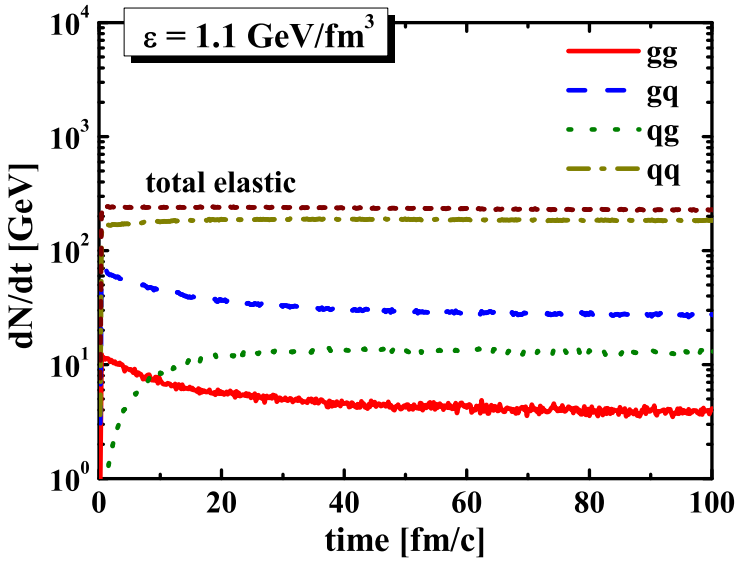

Figure 5.15: The total reaction rate for parton elastic scattering (short-dashed burgundy line) and separately the reaction rates for gluon-gluon (solid red line), gluon-quark (dashed blue line), quark-gluon (dotted green line), and quark-quark (dash-dotted dark yellow line) elastic scatterings as functions of time for the system at $\varepsilon = 1.1$ GeV/fm^3.

of partons within the PHSD simulations in the box and with the DQPM assumption for the spectral functions (3.8). Using the expression for the energy spectrum (5.26), we get

$$\rho_{g(q,\bar{q})} = \frac{2\pi^3}{V d_{g(q,\bar{q})}} \frac{1}{|p_{mid}|^2 \omega} \frac{n^{-1}_{B(F)}}{p_+ - p_-} \frac{dN_{g(q,\bar{q})}}{d\omega}\bigg|_{|\mathbf{p}|\in[p_-,p_+]} . \tag{5.29}$$

In Fig. 5.14 we show the dynamical spectral functions $\rho(\omega)$ for u and s quarks and gluons as obtained by the PHSD simulations (red solid lines) for "infinite" partonic systems—at energy densities of 1.1 and 4.72 GeV/fm^3—and the DQPM assumptions (dashed blue lines) for the spectral functions (3.8) at the corresponding energy densities of the system.

We find that the dynamical spectral functions of quarks and gluons are generally fairly well described by the DQPM form (3.8). However, there is a slight deviation visible at high energy density, especially for gluons. This deviation explains the difference between the dynamical results and the DQPM in Fig. 5.13. The origin of the deviation can be traced back to the inelastic collisions of $q\bar{q}$ pairs forming gluons in Eq. (5.17) in dense systems. The reactions favor the high-mass part of the gluon spectral function and predominantly populate

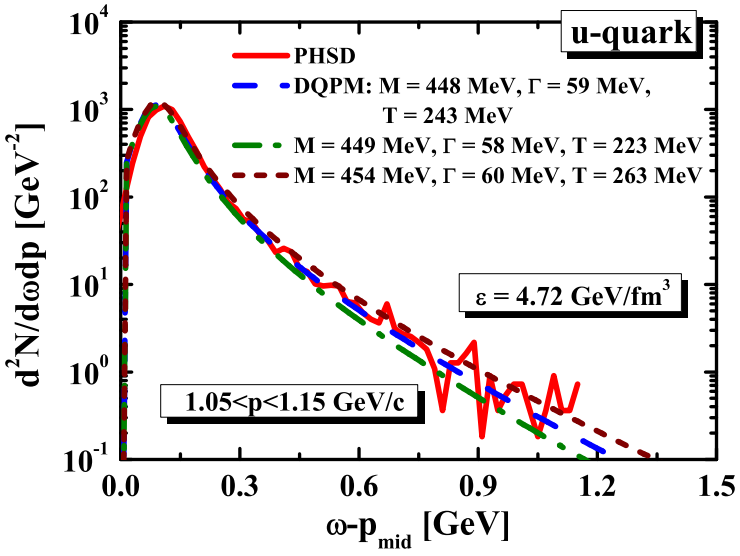

Figure 5.16: The spectrum of u quarks in equilibrium obtained by the PHSD simulations (red solid line) for systems at energy density 4.72 GeV/fm^3 in comparison to the thermal distributions with different temperatures: $T = 243$ MeV (dashed blue line), $T = 223$ MeV (dash-dotted green line), and $T = 263$ MeV (short-dashed burgundy line).

dynamically the right-hand side from the gluon pole mass since the sum of the pole masses of quarks and antiquarks is larger than the pole mass of the gluon (cf. Eq. (3.16)). Indeed, let us recall that the inelastic collisions are more important at higher energy densities (cf. Fig. 5.9). Moreover, from Fig. 5.15 we see that the elastic scattering rate of gluons is lower than that of quarks. Therefore, the inelastic interaction contributes considerably to the shape of the spectral function of gluons at high energy density, while it is not so important for the quarks at $\varepsilon = 1.1$ GeV/fm^3. In the DQPM it is assumed that the width in the spectral function is independent of the mass, which indeed is found to be a good approximation if elastic scatterings dominate (as in case of the quarks and antiquarks). However, the inelastic interaction of partons in PHSD is dominated by the resonant gluon formation, which dynamically generates a mass-dependent width for the gluon spectral function. This dynamical effect in the gluon width is not incorporated in the DQPM assumption (3.8). Accordingly, the PHSD simulations for systems in equilibrium supersede the DQPM assumptions but well reproduce the DQPM assumptions in the fermionic sector.

Note that the calculations of $d^2N/d\omega dp$ in PHSD in the box in the final, equilibrated state allows us to extract the temperature of the "infinite" par-

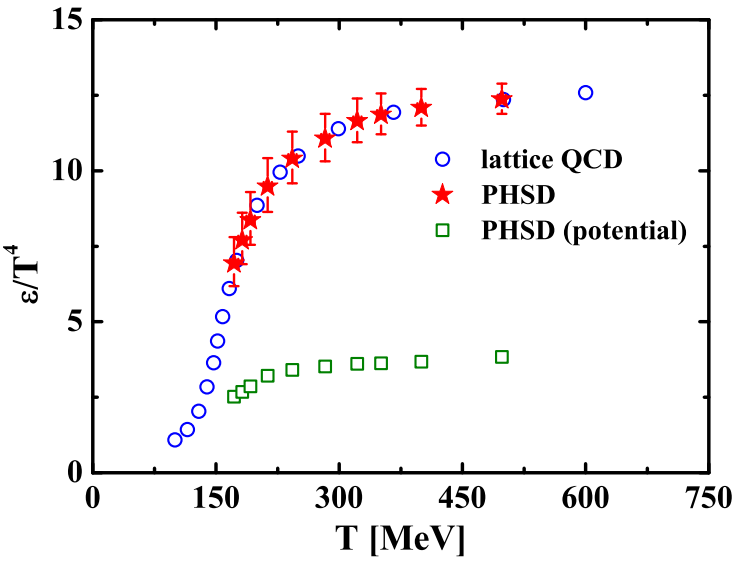

Figure 5.17: The scaled energy density ε/T^4 (red stars) and the potential energy fraction of the scaled energy density (green open squares) extracted from the PHSD calculations in the box in comparison to the lQCD data from Refs. [75, 76] (blue open circles).

ton matter. We obtain the final temperature by fitting the parton spectrum obtained by the PHSD simulations with the product of the Bose (Fermi) distribution and a Lorentzian spectral function (cf. Eq. (5.28)). In Fig. 5.16, we show the spectrum of u quarks from the PHSD simulations (solid red line) for a system at energy density 4.72 GeV/fm^3 in comparison to the fit with different temperatures: $T = 243$ MeV (dashed blue line), $T = 223$ MeV (dash-dotted green line), and $T = 263$ MeV (short-dashed burgundy line). All three curves were normalized to coincide at the peak of the spectral function. One can see that the high-momentum behavior of the distribution is governed by the temperature and that the temperature $T = 243$ MeV gives the best fit at the energy density of 4.72 GeV/fm^3. We note that the same procedure is repeated for each particle species and each value of the energy density.

The question of whether the equation of state from the PHSD in equilibrium compares reasonably with the lattice data from Refs. [75, 76] can now be answered. To this end we present in Fig. 5.17 the equation of state extracted from the PHSD calculations in the box (red stars) in comparison to the respective results from the Wuppertal-Budapest group [75, 76] (blue open circles) as functions of the temperature T. We also show the potential energy contribution to the equation of state extracted from the PHSD calculations

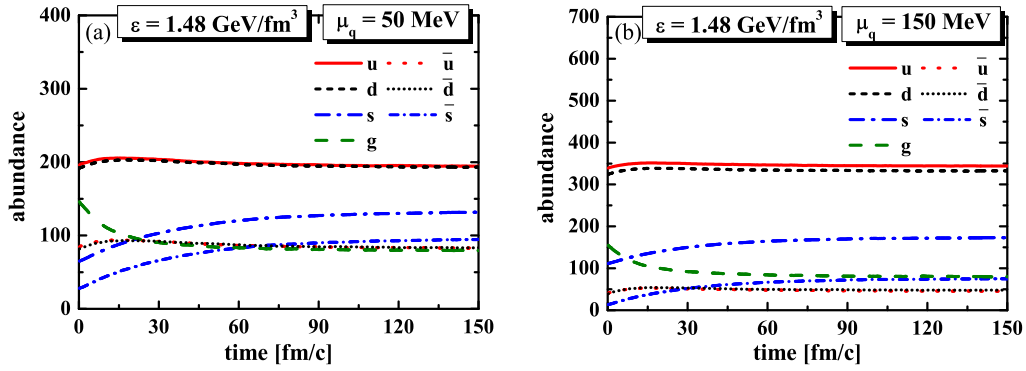

(a) (b)

Figure 5.18: Abundances of u, d, and s quarks (solid red lines, short-dashed black lines, and dash-dotted blue lines, respectively) and $\bar{u}$, $\bar{d}$, and $\bar{s}$ antiquarks (dotted red lines, short-dotted black lines, and short-dash-dotted blue lines, respectively) and gluons (dashed green lines) as functions of time for systems at $\varepsilon = 1.48$ GeV/fm^3 and at different quark chemical potentials: (a) $\mu_q = 50$ MeV; (b) $\mu_q = 150$ MeV.

in the box (green open squares) that is equivalent to the DQPM potential energy density. We find that the equation of state implemented in PHSD is well in agreement with the DQPM and the lQCD results. This finding implies that PHSD dynamically describes systems of quarks, antiquarks, and gluons in equilibrium that have the same properties as explicit QCD calculations on the lattice.

5.5 Finite quark chemical potentials

We have seen in Sec. 5.4 that the dynamical calculations within PHSD reproduce equilibrium properties of QCD matter as seen in lQCD calculations at $\mu_q = 0$. Let us now proceed further and study within the dynamical approach the quark and gluon properties at finite quark chemical potential μ_q (cf. Sec. 3.2.4), which are currently not yet well established in lQCD calculations.

In Fig. 5.18 we present the particle abundances of u, d, and s quarks (solid red, short-dashed black, and dash-dotted blue lines, respectively), $\bar{u}$, $\bar{d}$, and $\bar{s}$ antiquarks (dotted red, short-dotted black, and short-dash-dotted blue lines, respectively) and gluons (dashed green lines) as functions of time for systems at $\varepsilon = 1.48$ GeV/fm^3 and at quark chemical potentials μ_q of 50 and 150 MeV. Again chemical equilibrium is achieved for large times but now the abundances of quarks and antiquarks differ considerable (especially for $\mu_q = 150$ MeV). A

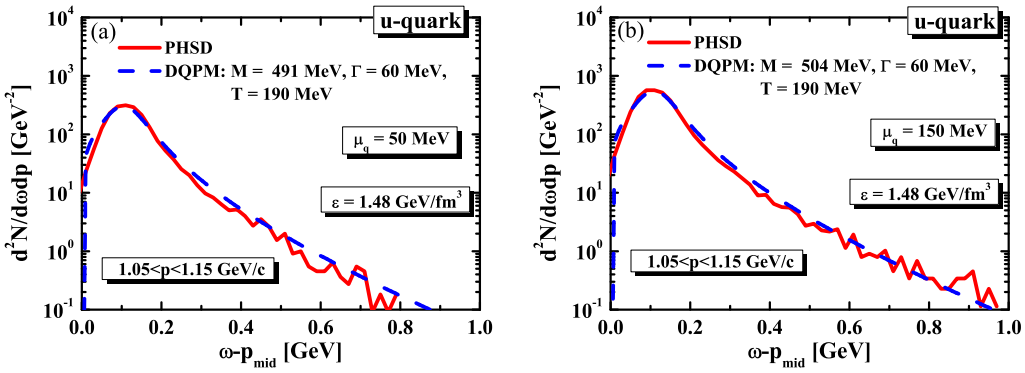

(a) (b)

Figure 5.19: The spectrum of u quarks in equilibrium as obtained by the PHSD simulations in the box (solid red lines) in comparison to the DQPM model (blue dashed lines) for systems at an energy density of 1.48 GeV/fm^3 at different quark chemical potentials: (a) $\mu_q = 50$ MeV; (b) $\mu_q = 150$ MeV.

closer inspection also shows that the strangeness equilibration proceeds slower since the amount of flavor-neutral $q\bar{q}$ pairs decreases with increasing μ_q. Note that the gluon abundance in the equilibrium stage does not depend on the initialization.

The phase boundary $T_c(\mu_q)$ in the DQPM (and PHSD) is defined by demanding that the phase transition happens at the same critical energy density ε_c for all μ_q. The prediction of Fig. 5.18 might in future be compared to lQCD calculations at finite μ_q.

In Fig. 5.19 we show $d^2N/d\omega dp$ for u quarks obtained by the PHSD simulations (solid red lines) of "infinite" partonic systems at $\varepsilon = 1.48$ GeV/fm^3 and at quark chemical potentials of 50 and 150 MeV. For comparison, we present on the same plots the DQPM assumptions (blue dashed lines) for the respective distributions. The agreement is fairly good since the inelastic channels are further suppressed with increasing μ_q. Note that in the present version the DQPM and PHSD treat the quark-hadron transition as a smooth crossover at all μ_q. There are, however, some physical arguments in favor of a first-order phase transition at large μ_q and for the existence of a critical endpoint for the first-order transition line in the T-μ_q plane. Presently, we are not able to calculate the properties of a quark-gluon system close to a critical endpoint. It is also not yet clear whether such an endpoint exists.

5.6 Particle number fluctuations

In this Section we address higher moments of parton distributions in the sQGP within the PHSD approach and study the equilibration of fluctuation observables as well as the size of fluctuations in equilibrium. We recall that various fluctuation observables have been addressed theoretically within lQCD [184–187] as well as within effective models [188–193]. Furthermore, some of these observables have been studied experimentally by the various collaborations at SPS and RHIC. Most of these have been evaluated in the HSD approach including the individual detector acceptance and experimental biases. For a recent review we refer the reader to Ref. [194] (and references cited therein). The evaluation of the various fluctuations in PHSD (in analogy to HSD) is straightforward and in this Section performed for $\mu_q = 0$.

5.6.1 Scaled variance

We start with the scaled variance

$$\omega = \frac{\sigma^2}{\mu}, \tag{5.30}$$

where μ is the mean value of the observable x averaged over N events,

$$\mu = \frac{1}{N}\sum_{i=1}^{N} x_i, \tag{5.31}$$

and σ^2 is the sample variance given by

$$\sigma^2 = \frac{1}{N-1}\sum_{i=1}^{N}(x_i - \mu)^2. \tag{5.32}$$

The standard error of the scaled variance ω is given by

$$\begin{aligned} \Delta\omega &= \sqrt{\left(\frac{\partial\omega}{\partial\mu}\right)^2 (\Delta\mu)^2 + \left(\frac{\partial\omega}{\partial(\sigma^2)}\right)^2 [\Delta(\sigma^2)]^2} \\ &= \sqrt{\left(-\frac{\sigma^2}{\mu^2}\right)^2 (\Delta\mu)^2 + \left(\frac{1}{\mu}\right)^2 [\Delta(\sigma^2)]^2}, \end{aligned} \tag{5.33}$$

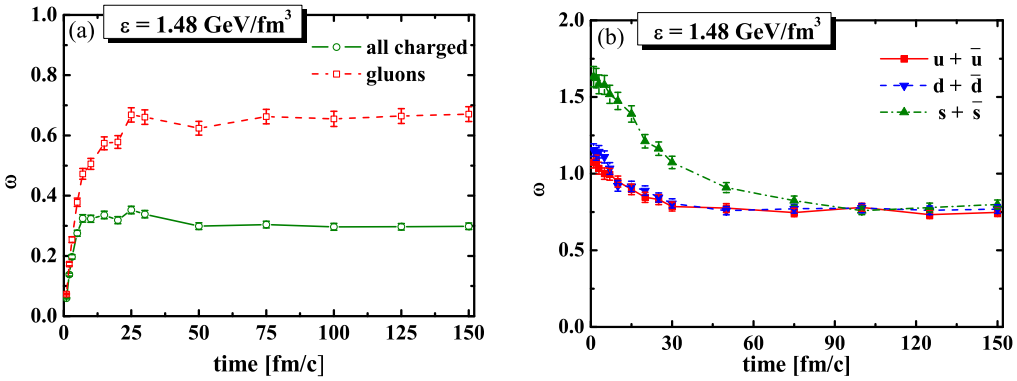

(a) (b)

Figure 5.20: The scaled variance as functions of time for a system at $\varepsilon = 1.48$ GeV/fm^3 for (a) all charged particles (green open circles) and gluons (red open squares) and (b) different quark flavors: u (red squares), d (blue down triangles), and s (green up triangles) quarks + antiquarks.

where

$$\Delta\mu = \frac{\sigma}{\sqrt{N}}, \tag{5.34}$$

$$\Delta(\sigma^2) = \sqrt{\frac{1}{N}\left(m_4 - \frac{N-3}{N-1}\sigma^4\right)}, \tag{5.35}$$

and m_4 is the fourth central moment,

$$m_4 = \frac{1}{N}\sum_{i=1}^{N}(x_i - \mu)^4. \tag{5.36}$$

In Fig. 5.20 we show the scaled variances ω for particle number fluctuations as functions of time for the quarks+antiquarks of all flavors (green open circles), for separate quark flavors—u (red squares), d (blue down triangles), and s (green up triangles)—and for gluons (red open squares), for a system at an energy density of 1.48 GeV/fm^3. The same results are presented in Fig. 5.21 for a system at $\varepsilon = 4.72$ GeV/fm^3. Note that in the grand canonical ensemble, i.e., for an equilibrium system with constant temperature (due to the presence of a thermostat) and with thermal fluctuations of the total system energy, one would expect $\omega \approx 1$ for all particle number fluctuations. On the other hand, for an isolated statistical system the global energy conservation for the microcanonical ensemble leads to a suppression of the particle number fluctuations and thus to $\omega < 1$ (see Refs. [195–198] for more details). As seen from Figs. 5.20 and 5.21 the equilibrium values of ω are smaller than 1. This can be

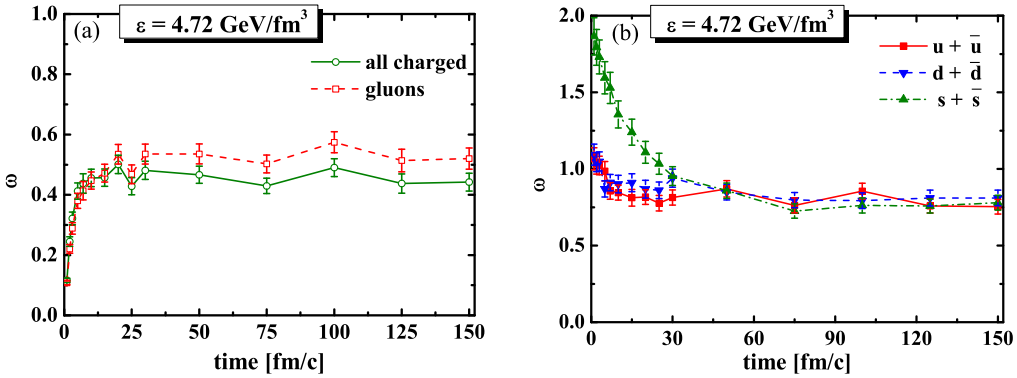

(a) (b)

Figure 5.21: The scaled variance as functions of time for a system at $\varepsilon = 4.72$ GeV/fm^3 for (a) all charged particles (green open circles) and gluons (red open squares) and (b) different quark flavors: u (red squares), d (blue down triangles), and s (green up triangles) quarks + antiquarks.

interpreted as a consequence of the total energy conservation, which is fixed more strictly (but still numerically not exactly) in our PHSD box calculations than that in the grand canonical ensemble. In a mixture of different particle species the influence of the global energy conservation on particle number fluctuations is different for different species in the mixture. The suppression effects are stronger for those species that contain larger fractions of the total system energy. The scaled variance of all charged particles (i.e., quarks plus antiquarks of all flavors) is lower than that of gluons or of a single quark flavor. This reflects the larger energy fraction stored in all quarks. For illustration, we show in Fig. 5.22 the total energy of partons (dash-dotted green lines), the energy of all charged partons (solid red lines), and the energy of gluons (dashed blue lines) as functions of time for systems at energy densities of 1.48 and 4.72 GeV/fm^3. We observe that the scaled variances reach a plateau in time for all observables and energy densities. The scaled fluctuations in the gluon number are more pronounced at $\varepsilon = 1.48$ GeV/fm^3 since the fraction of the gluon energy is quite small at this energy density. The difference with respect to the scaled variance of all charged partons decreases with energy due to the higher relative fraction of the gluon energy, as discussed before. Due to the initially lower abundance (thus smaller energy fraction) of strange quarks the respective scaled variance is initially larger but reaches the same asymptotic value as the light quarks in the course of the time evolution. Accordingly, the fluctuations in the fermion number are flavor blind in equilibrium.

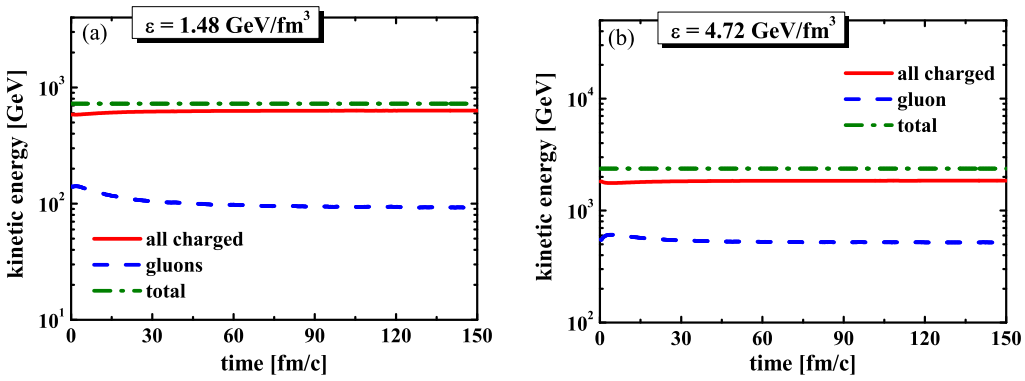

(a) (b)

Figure 5.22: The total kinetic energy of partons (dash-dotted green lines), the kinetic energy of all charged partons (solid red lines), and the kinetic energy of gluons (dashed blue lines) as functions of time for systems at different energy densities: (a) $\varepsilon = 1.48$ GeV/fm^3; (b) $\varepsilon = 4.72$ GeV/fm^3.

It is interesting to study the scaled variance for a cell inside the box as a function of the cell volume. This can easily be achieved by subdividing the total volume $V = 9^3$ fm^3 in different subvolumes V_n of equal size and evaluating the scaled variance in each subvolume. Finally an average over the n subvolumes V_n is performed. In Fig. 5.23 we present the scaled variance as functions of $n = V/V_n$ in the box for all charged particles (red open circles) and gluons (blue open squares) and for different quarks flavors [u (red open squares), d (blue open circles), and s (green open triangles) quarks + antiquarks] for systems at energy densities of 1.48 and 4.72 GeV/fm^3, respectively. The inserts show the observables for larger box sizes by up to about a factor of 8 ($n \approx 0.15$) in order to explore the thermodynamic limit. Indeed, our calculations demonstrate that the scaled variances no longer change (within statistics) when increasing the volume of the box by up to about an order of magnitude, thus approaching the thermodynamic limit. We recall that $\omega = 1$ for a Poissonian distribution (dash-dotted black lines). The impact of total energy conservation in the box volume V is relaxed in the subvolume V_n. This influence becomes weaker for $n \gg 1$, i.e., $V_n \ll V$. Therefore, in the subvolume V_n the energy fluctuates and these fluctuations behave as in the grand canonical ensemble for $n \gg 1$. The remaining part of the box plays—in this limit—the role of a thermostat for the cell V_n. This explains the behavior $\omega \cong 1$ for all scaled variances at large n as seen in Fig. 5.23. Such a behavior can be also expected from the "law of rare events": the scaled variances for all observables approach the Poissonian

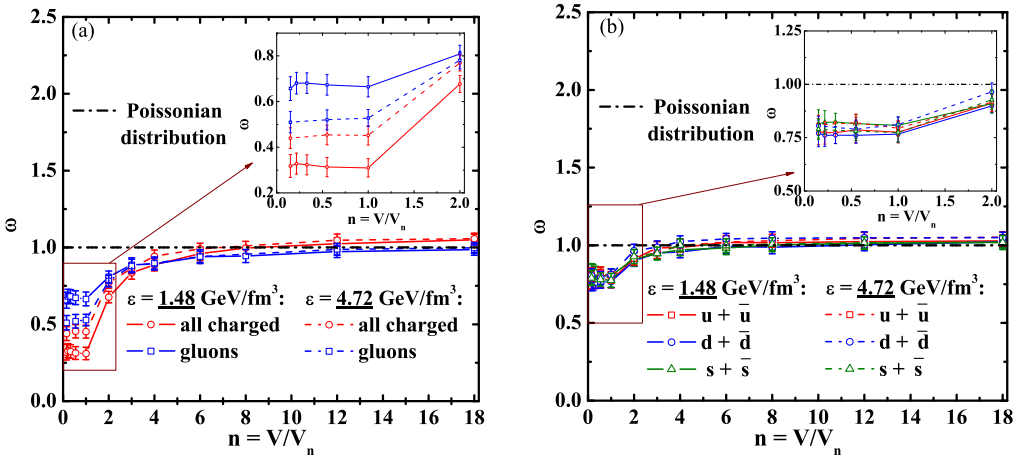

(a) (b)

Figure 5.23: The scaled variances in equilibrium (at $t > 120$ fm/c) as functions of relative system size $n = V/V_n$ at energy densities of 1.48 and 4.72 GeV/fm^3, where V is the default box volume and V_n is the subsystem volume for (a) all charged particles (red open circles) and gluons (blue open squares) and (b) different quark flavors: u (red open squares), d (blue open circles), and s (green open triangles) quarks + antiquarks. Note that $n = 1$ corresponds to a subsystem volume $V_1 = V \equiv 9^3 = 729$ fm^3; $n = 10$ stands for $V_{10} = 72.9$ fm^3; while $n = 0.2$ means a system of volume $V_{0.2} = 5 \times 729 = 3645$ fm^3, which is larger than our default box size V.

limit when one considers only a tiny fraction of all particles in the system.

This observation raises a new question concerning the event-by-event fluctuations in nucleus-nucleus collisions within a viscous hydrodynamical approach. The basic requirement of this approach is that the local cell size—in which a possibly chemical and kinetic equilibrium is achieved—is small compared to the macroscopic dimension of the system; in particular, the gradients in the energy density should be small. In each cell then equilibrium values for averages as well as fluctuations of observables should be considered within the grand canonical treatment. Thus, the influence of the conservation laws (both energy-momentum and charge conservation) gets lost. However, the influence of the global conservation laws on fluctuation observables is by no means negligible even in the thermodynamical limit, if the detector would accept an essential fraction of all particles.

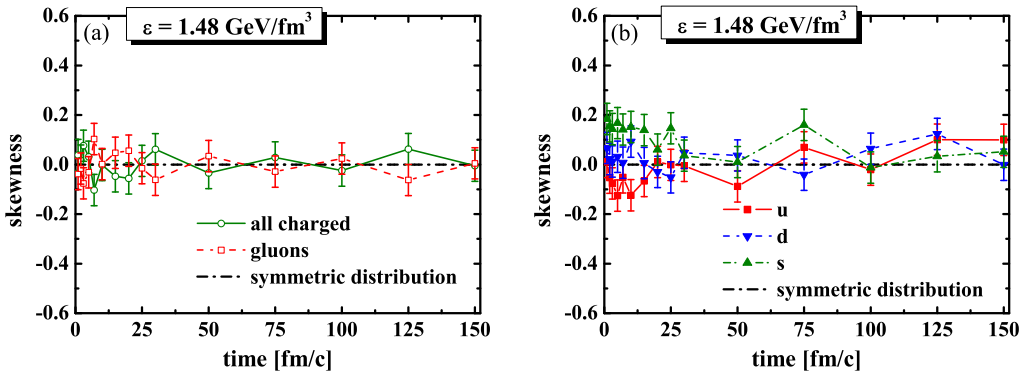

(a) (b)

Figure 5.24: The skewness as a function of time for a system at $\varepsilon = 1.48$ GeV/fm^3 for (a) all charged particles (green open circles) and gluons (red open squares) and (b) different quarks flavors: u (red squares), d (blue down triangles), and s (green up triangles) quarks.

5.6.2 Skewness

The skewness characterizes the asymmetry of the distribution function with respect to its average value. If the bulk of the data are at the left and the right tail is stretched out, then the distribution is skewed right or positively skewed; if the peak is toward the right and the left tail is more pronounced, then the distribution is skewed left or negatively skewed. The definition of skewness is as follows:

$$g_1 = \frac{m_3}{m_2^{3/2}} = \frac{m_3}{\sigma^3}, \tag{5.37}$$

where m_2 and m_3 are the second (variance) and third central moments, respectively, with

$$m_3 = \frac{1}{N}\sum_{i=1}^{N}(x_i - \mu)^3. \tag{5.38}$$

The skewness of a sample is given by

$$G_1 = \frac{\sqrt{N(N-1)}}{N-2} g_1, \tag{5.39}$$

and its standard error is

$$\Delta G_1 = \sqrt{\frac{6N(N-1)}{(N-2)(N+1)(N+3)}}. \tag{5.40}$$

In Fig. 5.24 we show the skewness as functions of time for all charged particles (green open circles) and gluons (red open squares) and for different quarks flavors [u (red squares), d (blue down triangles), and s (green up triangles) quarks] for a system at $\varepsilon = 1.48$ GeV/fm^3. Note that the skewness is equal to zero for symmetric distributions (dash-dotted black lines). We find that in our case the skewness of the number of all charged particles tends to be antisymmetric to the skewness of the number of gluons, but both are compatible with zero for the present accuracy of the calculations. We only show the results for a single energy density since our findings are independent of the energy density.

5.6.3 Kurtosis

The height and sharpness of the distribution peak relative to a number is called kurtosis. Higher values of kurtosis indicate a higher, sharper peak; lower values of kurtosis indicate a lower, less distinct peak. The kurtosis is defined as

$$\beta_2 = \frac{m_4}{m_2^2} = \frac{m_4}{\sigma^4}, \tag{5.41}$$

where m_4 is determined by Eq. (5.36). It is equal to 3 for a normal distribution, so often the excess kurtosis is presented which characterizes the deviation from a normal distribution,

$$g_2 = \beta_2 - 3. \tag{5.42}$$

The sample excess kurtosis then is defined by

$$G_2 = \frac{N-1}{(N-2)(N-3)}[(N+1)g_2 + 6]. \tag{5.43}$$

The standard error of the kurtosis is given by

$$\Delta G_2 = 2\Delta G_1 \sqrt{\frac{N^2-1}{(N-3)(N+5)}}, \tag{5.44}$$

where ΔG_1 is determined by Eq. (5.40).

In Fig. 5.25 we present the excess kurtosis as functions of time for all charged particles (green open circles) and gluons (red open squares) and for different quarks flavors [u (red squares), d (blue down triangles), and s (green up triangles) quarks] for a system at an energy density of 1.48 GeV/fm^3. Note

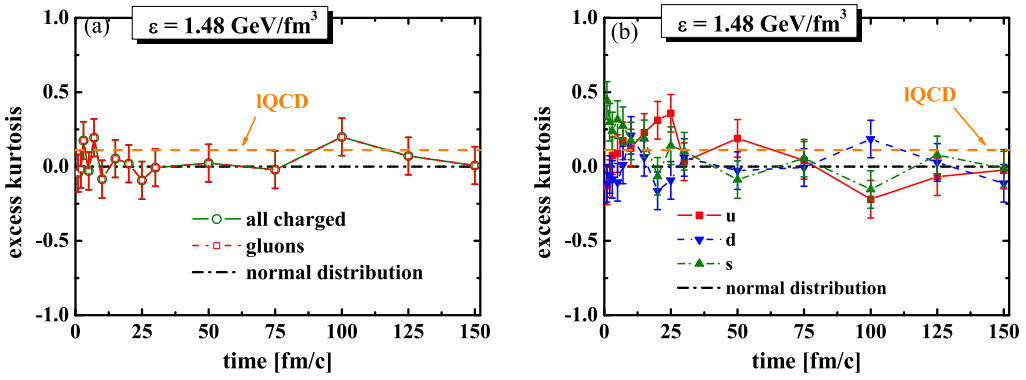

(a) (b)

Figure 5.25: The excess kurtosis as a function of time for a system at an energy density of 1.48 GeV/fm^3 and the corresponding lQCD results (dashed orange lines) from Ref. [186] for (a) all charged particles (green open circles) and gluons (red open squares) and (b) different quarks flavors: u (red squares), d (blue down triangles), and s (green up triangles) quarks.

that the excess kurtosis is equal to zero for normal distributions (dash-dotted black lines). The lQCD results from Ref. [186] are nonzero and shown by the dashed orange lines. We find that in our case the excess kurtosis of the number of all charged particles is equal to the excess kurtosis of the number of gluons. However, within statistical errors, the excess kurtosis is compatible with zero as well as with the lQCD results from Ref. [186] for gluons and charged particles. This finding holds for all energy densities considered.

5.7 Equilibration times

An inspection of the time evolution of the scaled variances in Figs. 5.20 and 5.21 shows that the equilibration of the various scaled variances occurs on time scales that are shorter than the time scales for the equilibration of the average values of the observables. In order to quantify this observation we fit the explicit time dependence of the abundances and scaled variances by the function

$$O_t = O_{t=0} + (O_{t\to\infty} - O_{t=0}) \left(1 - e^{-t/\tau_{eq}}\right), \tag{5.45}$$

which defines a characteristic equilibration time τ_{eq}. The results of our fits for different observables and energy densities are summarized in Table 5.1. For all particle species and energy densities, the equilibration time τ_{eq} is found to be shorter for the scaled variances than for the average values. This is

Particle type	Equilibration times τ_{eq} fm/c			
	$\varepsilon = 1.48$ GeV/fm^3		$\varepsilon = 4.72$ GeV/fm^3	
	abundance	ω	abundance	ω
$u + \bar{u}$	43	16	21	6
$d + \bar{d}$	45	14	21	5
$s + \bar{s}$	35	28	19	17
gluons	18	5	18	4
all charged	18	3	18	2

Table 5.1: Equilibration times for the abundances and the scaled variances for the different particle species and two values of the energy density.

most pronounced when considering all charged partons but less distinct for strange quarks. Accordingly, scaled variances may achieve an equilibrium, even if the average values of an observable are still out of equilibrium. This finding is reminiscent of strongly interacting quantum systems evaluated on the basis of Kadanoff-Baym equations in Refs. [43,44], where quantum fluctuations stabilize early in time, i.e., long before a kinetic or chemical equilibrium is achieved.

5.8 Summary

In this Chapter we have employed the PHSD off-shell transport approach to study systems slightly out of equilibrium as well as in equilibrium in a finite box with periodic boundary conditions, thus simulating "infinite" matter.

We have demonstrated explicitly that partonic systems at energy densities ε, above the critical energy density $\varepsilon_c \approx 0.5$ Gev/fm^3, achieve kinetic and chemical equilibrium in time. Furthermore, the energy density of the partonic system at fixed temperature and quark chemical potential for $\mu_q = 0$ is well in line with the lQCD calculations in equilibrium.

In addition to equilibration phenomena of average values for observables such as particle number or charged particle number we have studied the dynamics of fluctuation observables in and out of equilibrium. For all observables the equilibration time τ_{eq} is found to be shorter for the scaled variances than for the average values. This is most pronounced when considering all charged partons but less distinct for strange quarks. Accordingly, scaled variances may achieve an equilibrium even if the average values of an observable are still out of equilibrium.

The scaled variances for the fluctuations in the numbers of different partons in the box show an influence of total energy conservation. We have observed a suppression of the parton number fluctuations in comparison to the fluctuations in the grand canonical ensemble. Furthermore, by dividing the box into several cells we have calculated the scaled variances of different observables in the cell as functions of the cell size. The scaled variances for all observables approach the Poissonian limit with $\omega = 1$ when the cell volume is much smaller than that of the box. This observation indicates that global conservation laws (for energy-momentum and charges) are not important when one detects only a small fraction from all particles in the system. However, if the fraction of the accepted particles is comparable to that in the whole system, the influence of global conservation laws on fluctuation observables is not negligible even in the thermodynamic limit. We have shown, furthermore, that the scaled variances no longer depend on the size of the box when increasing it up to about an order of magnitude up to $\sim$5000 fm^3. Accordingly, the continuum limit has approximately been reached in the calculations.

Our analysis of the skewness and kurtosis gives practically vanishing values for these observables in time and especially in equilibrium within the limited statistics achieved. We mention that our results within statistics are also compatible with the lQCD results from Ref. [186].

Chapter 6

Transport coefficients of strongly interacting matter

Ultrarelativistic heavy-ion collisions at RHIC and LHC energies have produced a new state of matter, the QGP, for a couple of fm/c. The produced QGP shows shows features of a strongly interacting fluid unlike a weakly interacting parton gas [18, 40, 41]. Large values of the observed azimuthal asymmetry of charged particles in momentum space, i.e., the elliptic flow v_2 [98–101, 199], could quantitatively be well described by hydrodynamics up to transverse momenta on the order of 1.5 GeV [200–204]. A perfect fluid has been defined as having a zero shear viscosity η; yet semiclassical arguments have been given suggesting that the shear viscosity cannot be arbitrarily small [205]. Indeed, the lower bound for the shear viscosity to entropy density ratio $\eta/s = 1/4\pi$ was conjectured by Kovtun-Son-Starinets (KSS) [206, 207] for infinitely coupled supersymmetric Yang-Mills gauge theory based on the AdS/CFT duality conjecture. On the basis of holographically dual computations [208], also for the bulk viscosity of strongly coupled gauge theory plasmas, a lower bound was conjectured: $\zeta/\eta \geqslant 2(1/3 - c_s^2)$, where c_s is the speed of sound. Empirically, relativistic viscous hydrodynamic calculations—using the Israel-Stewart framework—require a very small but finite η/s of $0.08 - 0.24$ in order to reproduce the RHIC elliptic flow v_2 data [209–212]. The main uncertainty in these estimates results from the equation of state and the initial conditions employed in the hydrodynamical calculations as well as in the temperature dependence of $\eta/s(T)$.

Thus not only the absolute values of the shear and bulk viscosities are of great interest but also the temperature dependence of these coefficients, which

is expected to be quite strong. There is evidence from atomic and molecular systems that η/s should have a minimum in the vicinity of the phase transition or—in case of strong interactions at vanishing chemical potential—of the rapid crossover between hadronic matter and the QGP [70, 213, 214]. Furthermore, it is argued that the ratio of the bulk viscosity to entropy density ζ/s should have a maximum close to T_c—as suggested by lQCD—and might even diverge in case of a second-order phase transition [215–221]. Such a peak in the bulk viscosity can lead to instabilities in viscous hydrodynamics simulations for heavy-ion collisions and possibly to clusterization effects [222].

Shear and bulk viscosities of strongly interacting systems have been evaluated within different approaches. Calculations have been performed at high temperatures, where perturbation theory can be applied [223–225], as well as at extremely low temperatures [225–227]. First results for shear and bulk viscosities obtained within lQCD simulations above the critical temperature of pure gluon matter have been presented in [228–231]. There are several methods for the calculation of shear and bulk viscosities for strongly interacting systems: the Relaxation Time Approximation (RTA) [232], the Chapmann-Enskog (CE) method [233] and the Green-Kubo approach [234–236]. The RTA method has been used to calculate the viscosity [188, 205, 219, 220, 237–240] as well as the Green-Kubo approach [18, 241–245] for both hadronic and partonic matter providing a rough picture of the transport properties of strongly interacting matter.

This Chapter is dedicated to the study of the transport coefficients of strongly interacting matter within PHSD. In this approach the transport coefficients do not enter as external parameters but are generic properties of the degrees of freedom under consideration and can be calculated for systems in equilibrium as a function of temperature explicitly without incorporating any additional parameters. Furthermore, the PHSD approach allows to evaluate the transport coefficients within the partonic as well as within the hadronic phase on the same footing. Since PHSD yields a reasonable description of hadronic, collective and electromagnetic observables from heavy-ion collisions in a wide energy range (cf. Chapter 4), we may deduce the size and temperature dependence of the transport coefficients.[1]

[1]Note that most of the results of this Chapter have been published in Refs [246–248] by the author.

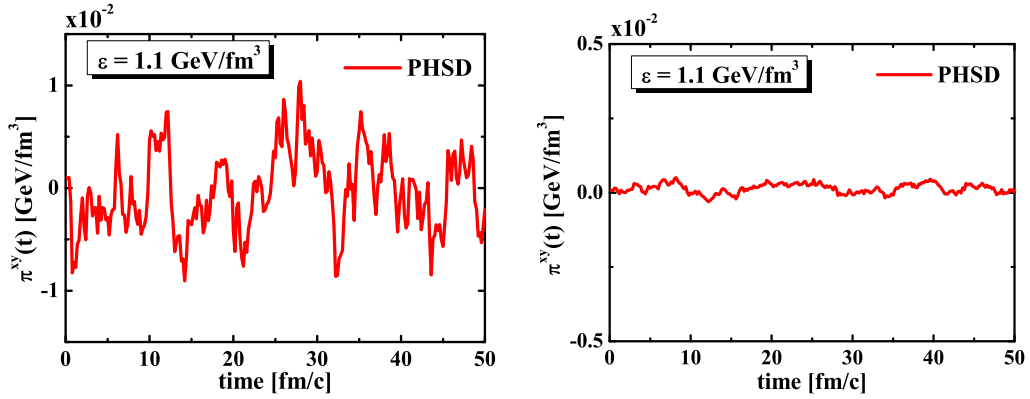

(a) (b)

Figure 6.1: The shear component of the energy-momentum tensor as a function of time for a system at an energy density of 1.1 GeV/fm^3 from the PHSD simulations. (a) 1 event; (b) 500 events.

6.1 Shear and bulk viscosities

In this Section we calculate the shear and bulk viscosities as a function of temperature (or energy density) within PHSD employing the Green-Kubo formalism and the relaxation time approximation for comparison.

6.1.1 The Kubo formalism

The Kubo formalism relates linear transport coefficients such as heat conductivity, shear and bulk viscosities to nonequilibrium correlations of the corresponding dissipative fluxes and treats dissipative fluxes as perturbations to local thermal equilibrium [234–236]. The Green-Kubo formula for the shear viscosity η is as follows [249]:

$$\eta = \frac{1}{T}\int d^3r \int_0^\infty dt \langle \pi^{xy}(\mathbf{0},0)\pi^{xy}(\mathbf{r},t)\rangle, \tag{6.1}$$

where T is the temperature of the system and $\langle ... \rangle$ denotes the ensemble average in thermal equilibrium. In Eq. (6.1) π^{xy} is the shear component (non-diagonal spacial part) of the energy-momentum tensor $\pi^{\mu\nu}$:

$$\pi^{xy}(\mathbf{r},t) \equiv T^{xy}(\mathbf{r},t) = \int \frac{d^3p}{(2\pi)^3}\frac{p^x p^y}{E} f(\mathbf{r},\mathbf{p};t), \tag{6.2}$$

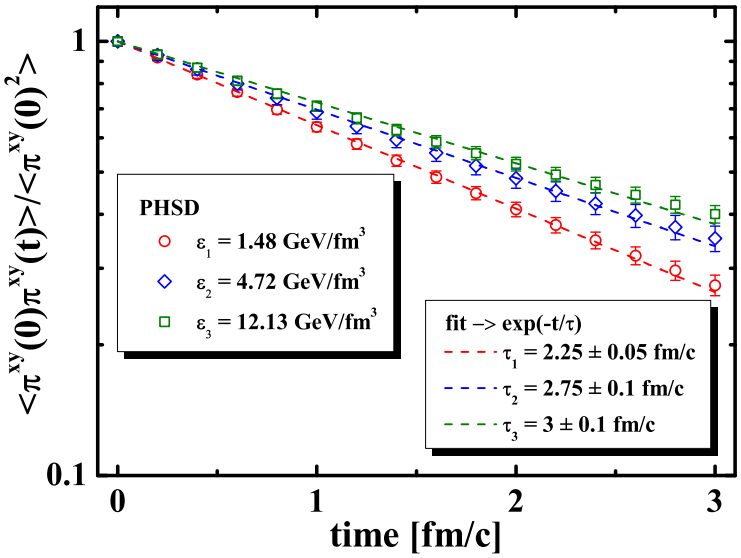

Figure 6.2: The correlation functions $\langle \pi^{xy}(0)\pi^{xy}(t)\rangle$, which are normalized by $\langle \pi^{xy}(0)^2\rangle$, as a function of time from the PHSD simulations in the box (open symbols) for systems at different energy densities. The corresponding exponential fits are given by dashed lines; the extracted relaxation times τ are given, too.

where the scalar mean-field U_s (from PHSD) enters in the energy $E = \sqrt{\mathbf{p}^2 + U_s^2}$. In Fig. 6.1 we present the shear component of the energy-momentum tensor as a function of time from the PHSD simulations in the box.

In our numerical simulation—within the testparticles representation—the volume averaged shear component of the energy momentum tensor can be written as

$$\pi^{xy}(t) = \frac{1}{V}\sum_{i=1}^{N}\frac{p_i^x p_i^y}{E_i}, \tag{6.3}$$

where V is the volume of the system and the sum is over all particles in the box at time t. Note that the scalar mean-field contribution U_s only enters via the energy E. Taking into account that point particles are uniformly distributed in our box (implying $\pi^{xy}(\mathbf{r},t) = \pi^{xy}(t)$)), we can simplify the Kubo formula for the shear viscosity to

$$\eta = \frac{V}{T}\int_0^\infty dt \langle \pi^{xy}(0)\pi^{xy}(t)\rangle. \tag{6.4}$$

The correlation functions $\langle \pi^{xy}(0)\pi^{xy}(t)\rangle$ are empirically found to decay almost

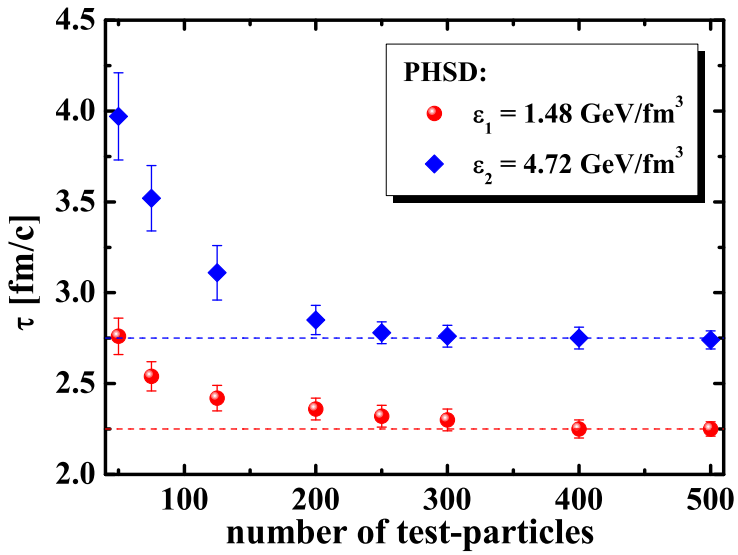

Figure 6.3: The relaxation time τ as a function of the number of test-particles obtained by the PHSD simulations in the box (symbols) for systems at different energies density. The dashed lines provide the convergent values for the relaxation time τ.

exponentially in time

$$\left\langle \pi^{xy}(0)\pi^{xy}(t)\right\rangle = \left\langle \pi^{xy}(0)\pi^{xy}(0)\right\rangle \, e^{-t/\tau} \tag{6.5}$$

as shown in Fig. 6.2, where τ are the respective relaxation times. Finally, we end up with the Green-Kubo formula for the shear viscosity:

$$\eta = \frac{V}{T}\left\langle \pi^{xy}(0)^2\right\rangle \tau, \tag{6.6}$$

which we use to extract the shear viscosity from the PHSD simulations in the box at given energy density. Note that the temperature T is uniquely related to the energy density $\varepsilon(T)$ in PHSD (in thermodynamic equilibrium).

We check the numeric stability of the method by plotting the respective relaxation times τ, extracted from the PHSD simulations in the box, as a function of the number of testparticles in Fig. 6.3. The results for the relaxation time τ converge for $N_{test} \geqslant 400$ independent of the energy density. In this study, we use a high amount of microcanonical simulations in the ensemble average ($N_{test} = 500$), which leads to reliable (within statistical error bars) results.

We also note that our numerical results for η do not depend on the volume

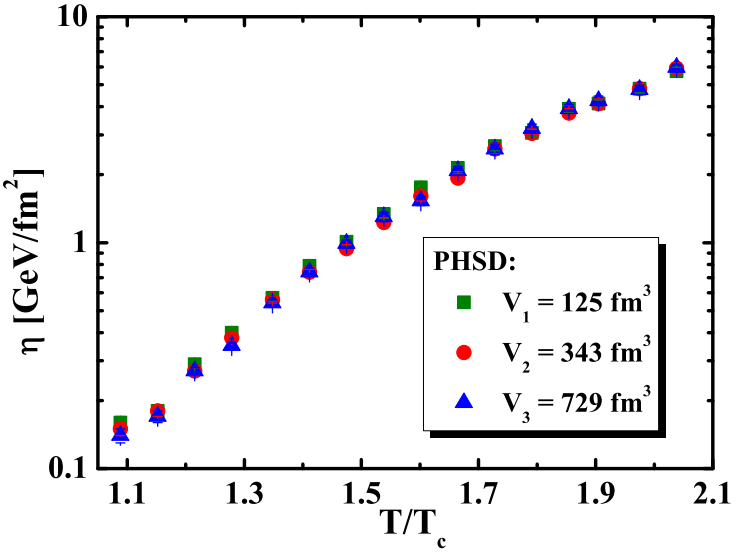

Figure 6.4: The shear viscosity η as a function of temperature from the PHSD simulations in the box for various volumes of the box: $V = 125$ GeV/fm^3 (green squares), $V = 343$ GeV/fm^3 (red circles) and $V = 729$ GeV/fm^3 (blue triangles).

V of the box within reasonable variations by factors of 6 as shown in Fig. 6.4.

6.1.2 The relaxation time approximation

The starting hypothesis of the relaxation time approximation (RTA) is that the collision integral can be approximated by

$$C[f] = -\frac{f - f^{eq}}{\tau}, \tag{6.7}$$

where τ is the relaxation time. In this approach it has been shown that the shear and bulk viscosities (without mean-field or potential effects) can be written as [250–252]:

$$\eta = \frac{1}{15T}\sum_a \int \frac{d^3p}{(2\pi)^3}\frac{|\mathbf{p}|^4}{E_a^2}\tau_a(E_a) f_a^{eq}(E_a/T), \tag{6.8}$$

$$\zeta = \frac{1}{9T}\sum_a \int \frac{d^3p}{(2\pi)^3}\frac{\tau_a(E_a)}{E_a^2}\left[(1-3v_s^2)E_a^2 - m_a^2\right]^2 f_a^{eq}(E_a/T), \tag{6.9}$$

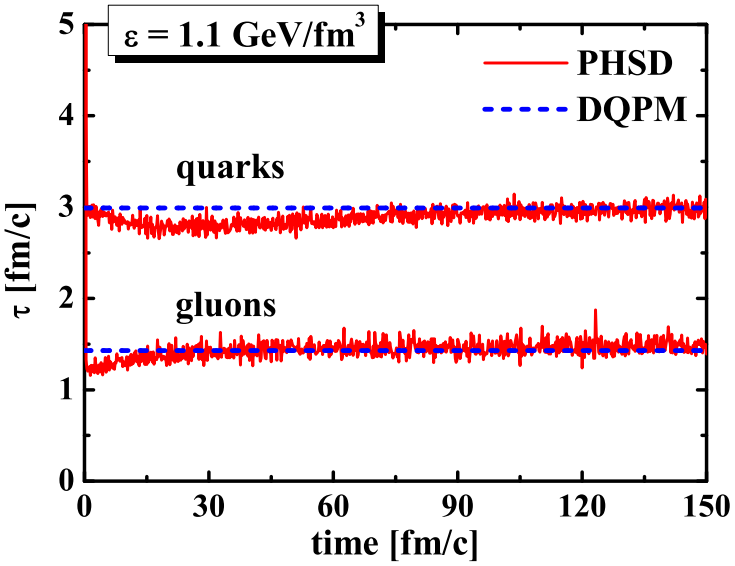

Figure 6.5: The relaxation time τ of partons as a function of time extracted from the PHSD simulations in the box (solid red lines) in comparison to the DQPM (short-dashed blue lines) for a system at $\varepsilon = 1.1$ GeV/fm^3.

where the sum is over particles of different type a (in our case, $a = q, \bar{q}, g$). In the PHSD transport approach the relaxation time is given by:

$$\tau_a(T) = \Gamma_a^{-1}(T), \tag{6.10}$$

where $\Gamma_a(T)$ is the width of particles of type $a = q, \bar{q}, g$ as defined by Eqs. (3.14) and (3.15). In Fig. 6.5 we present the relaxation time of partons extracted from the PHSD simulations in the box in comparison to the DQPM. In our numerical simulation—within the testparticle representation—the volume averaged shear and bulk viscosities are given by the following expressions:

$$\eta = \frac{1}{15TV} \sum_{i=1}^{N} \frac{|\mathbf{p}_i|^4}{E_i^2} \Gamma_i^{-1}, \tag{6.11}$$

$$\zeta = \frac{1}{9TV} \sum_{i=1}^{N} \frac{\Gamma_i^{-1}}{E_i^2} \left[(1 - 3v_s^2)E_i^2 - m_i^2\right]^2, \tag{6.12}$$

where the speed of sound $v_s = v_s(T)$ is taken from lQCD [75,253] or the DQPM, alternatively. Note that $v_s(T)$ from both approaches is practically identical since it is governed by the DQPM, which reproduces the lQCD pressure and energy density.

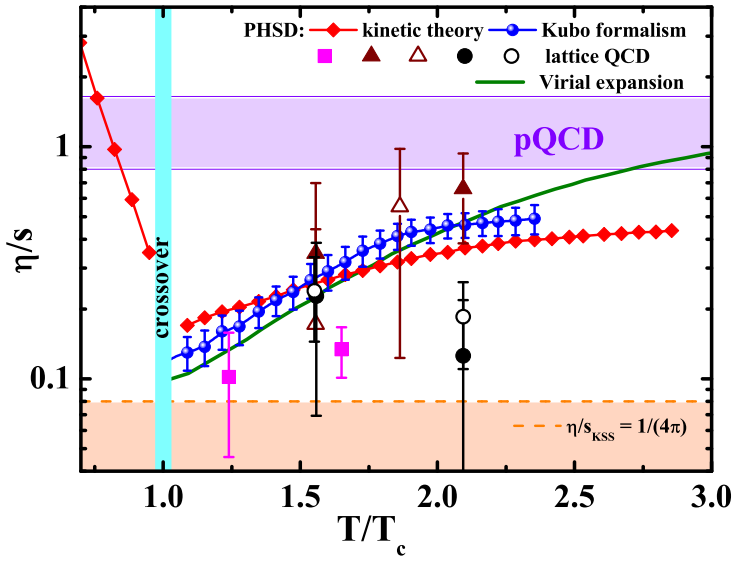

Figure 6.6: The shear viscosity to entropy density ratio η/s as a function of temperature of the system obtained by the PHSD simulations using different methods: the relaxation-time approximation (red line+diamonds) and the Kubo formalism (blue line+dots). The other symbols denote lQCD data for pure $SU_c(3)$ gauge theory from [228] (magenta squares), from [230] (open and full triangles), and from [231] (black open and full circles). The orange dashed line demonstrates the Kovtun-Son-Starinets bound [206, 207] $(\eta/s)_{KSS} = 1/(4\pi)$. For comparison, the results from the virial expansion approach (green line) [70] are shown as a function of temperature, too.

6.1.3 Results for the shear viscosity

In Fig. 6.6 we present the shear viscosity to entropy density ratio η/s as a function of temperature T of the system extracted from the PHSD simulations in the box, where the viscosity was extracted employing the relaxation time approximation (red line+diamonds) and the Kubo formalism (blue line+dots). We find that these approaches give roughly the same η/s as a function of temperature within error bars. For comparison, the results from the virial expansion approach [70] are given by the green line as well as lQCD data for pure $SU_c(3)$ gauge theory. The results for $T < T_c$ stem from PHSD in the relaxation-time framework and rapidly rise with decreasing temperature. This is mainly because of a strong decrease of the entropy density, $s \to 0$ for $T \to 0$ as $e^{-m_\pi/T}$.

The behavior of the specific shear viscosity with temperature in the PHSD is in agreement with the results of the SHMC-HQB approach [239, 240, 254], where the partonic phase is described in the heavy-quark bag model. However,

we obtain considerably lower values for the shear viscosity, in particular in the partonic phase. The low viscosity of the quark-gluon matter in the PHSD is caused by the stronger interaction between the degrees of freedom and is supported by the successful description of experimental data on the collective flow in heavy-ion collisions within PHSD [23, 87, 255] (cf. Chapter 4).

At $T < T_c$, the PHSD results for the viscosity of the hadronic matter at vanishing quark chemical potential $\mu_q = 0$ qualitatively agree with the calculations in Refs. [256–259]. On the other hand, let us note that the results for the hadronic phase here have to be extended to finite μ_q before applications to realistic heavy-ion collisions can be performed.

6.1.4 Mean-field or potential effects

We recall that partonic mean-fields affect the bulk viscosity but not the shear viscosity (except for a contribution in the energy E in the denominator). According to Refs. [237, 252], the expression for the bulk viscosity with potential effects reads

$$\zeta = \frac{1}{T}\sum_a \int \frac{d^3p}{(2\pi)^3}\frac{\tau_a(E_a)}{E_a^2} f_a^{eq}(E_a/T)\Big[\Big(\frac{1}{3}-v_s^2\Big)|\mathbf{p}|^2 - v_s^2\Big(m_a^2 - T^2\frac{dm_a^2}{dT^2}\Big)\Big]^2. \tag{6.13}$$

In the numerical simulation the volume averaged bulk viscosity (including the mean-field effects from PHSD) is evaluated as

$$\zeta = \frac{1}{TV}\sum_{i=1}^{N} \frac{\Gamma_i^{-1}}{E_i^2}\Big[\Big(\frac{1}{3}-v_s^2\Big)|\mathbf{p}|^2 - v_s^2\Big(m_i^2 - T^2\frac{dm_i^2}{dT^2}\Big)\Big]^2. \tag{6.14}$$

By using the DQPM expressions for the masses of quarks and gluons (for $\mu_q = 0$)

$$m_q^2(T/T_c) = \frac{1}{3}g^2(T/T_c)T^2, \quad m_g^2(T/T_c) = \frac{3}{4}g^2(T/T_c)T^2$$

we can calculate the derivatives w.r.t. T^2. Thus all quantities in Eq. (6.14) are uniquely determined within PHSD. We recall that the DQPM description of thermodynamic properties of lQCD results as well as its implementation in PHSD give practically the same results (cf. Sec.3.2 and Sec. 5.4). The derivation of partonic mean fields as well as their values can be found in Sec. 3.2.3.

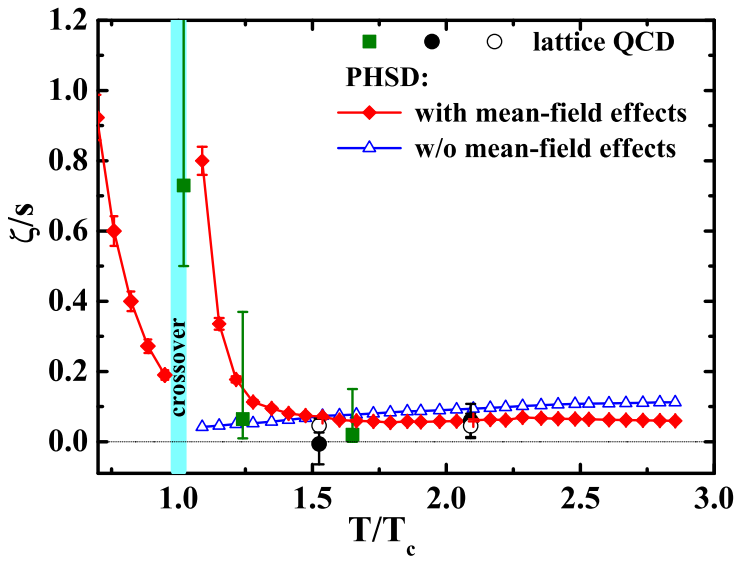

Figure 6.7: The bulk viscosity to entropy density ratio ζ/s as a function of temperature T extracted from the PHSD simulations in the box using the relaxation time approximation including mean-field effects (red line+diamonds) and without potential effects (blue line+open triangles). The available lQCD data from [229] are given by green squares and from [231] by black open and full circles, respectively.

6.1.5 Results for the bulk viscosity

In Fig. 6.7 we show the bulk viscosity to entropy density ratio ζ/s as a function of temperature T of the system obtained by the PHSD simulations in the box employing the relaxation time approximation including mean-field (or potential) effects (red line+diamonds) and without potential effects (blue line+open triangles) for the partons. For comparison, we show in the same figure the available lQCD data [229, 231]. Without mean-field effects we find an almost constant ratio $\zeta(T)/\eta(T)$ (see below) which is not in line with the findings from the lattice. Thus the dynamical mean fields (as incorporated in PHSD) play a decisive role for the temperature dependence of the bulk viscosity $\zeta(T)$ of the sQGP. The increase of the bulk viscosity per unit entropy at $T \approx T_c$ is generated by the collective interaction of partons via mean fields rather than by their scatterings. At high temperature the mean-field effects are less pronounced and the values for the bulk viscosity of partonic matter from PHSD are approaching those obtained in the scope of the SHMC-HQB model [239, 240, 254].

On the hadronic side, we observe that ζ/s falls with temperature, which is

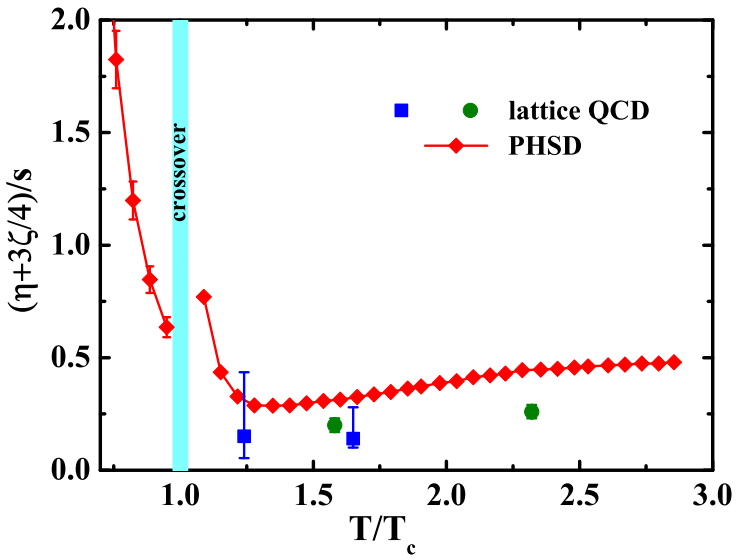

Figure 6.8: The specific sound channel $(\eta + 3\zeta/4)/s$ as a function of temperature T of the system obtained by the PHSD simulations in the box using the relaxation time approximation including mean-field effects (red line+diamonds). It is compared with lQCD data from [262] (green circles) and from combining results of [229] and [231] (blue squares).

in agreement with the results of the SHMC-HQB model [239, 240, 254] and of the chiral model for an interacting pion gas [260, 261]. However, we do not see a divergent behavior of the bulk viscosity to entropy density ratio for $T \to 0$ as predicted in Ref. [261].

Further related quantities are of interest, in particular the specific sound channel $(\eta + 3\zeta/4)/s$. A sound wave propagation in the z-direction with wavelength $\lambda = 2\pi/k$ is damped according to

$$T_{03}(t,k) \propto \exp\left[-\frac{\left(\frac{4}{3}\eta + \zeta\right)k^2 t}{2(\varepsilon + p)}\right], \tag{6.15}$$

where T_{03} is the momentum density in the z-direction, ε is the energy density and p is the pressure. Thus both the shear η and bulk ζ viscosities contribute to the damping of sound waves in the medium and provide a further constraint on the viscosities. In Fig. 6.8 we present the specific sound channel $(\eta+3\zeta/4)/s$ as a function of temperature T of the system obtained by the PHSD simulations in the box using the relaxation time approximation including mean-field effects (red line+diamonds). It is compared with lQCD results for pure $SU_c(3)$ gauge theory from Ref. [262] (green circles) and from combining results of Refs. [228]

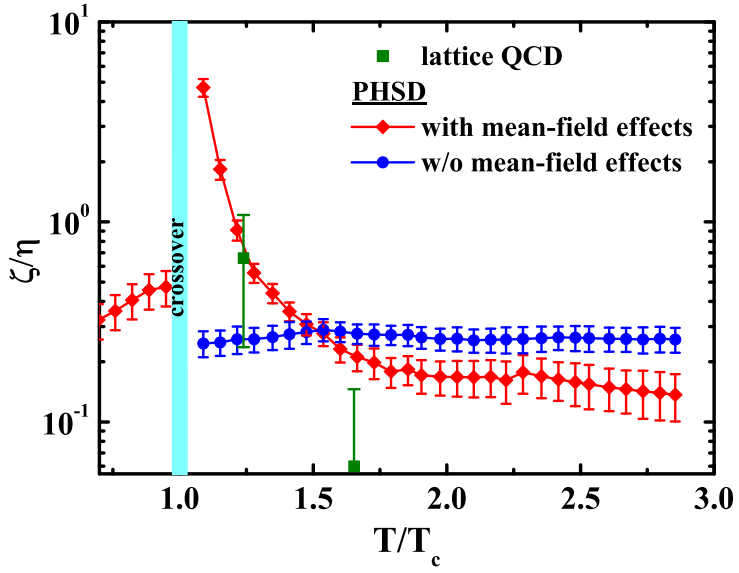

Figure 6.9: The bulk to shear viscosity ratio ζ/η as a function of temperature of the system obtained by the PHSD simulations in the box employing the relaxation time approximation including mean-field effects (red line+diamonds) and without potential effects (blue line+circles). It is compared with lQCD data from [228, 229] (green squares). Note the logarithmic scale in ζ/η.

and [229] (blue squares). Note that the PHSD calculations correspond to unquenched 3-flavor QCD and thus are not expected to match the results for the pure gauge theory exactly!

Finally, in Fig. 6.9, we show the bulk to shear viscosity ratio ζ/η as a function of temperature of the system extracted from the PHSD simulations in the box using the relaxation time approximation including mean-field (or potential) effects (red line+diamonds) and without potential effects (blue line+circles). Whereas an almost temperature independent result is obtained in the partonic phase when discarding mean-field effects, a strong increase close to T_c is found in the PHSD when including the mean fields for partons. The results for the shear to bulk viscosity ratio in the deconfined phase are in agreement with the lattice data [228,229] and with Ref. [263]. Since the PHSD gives a minimum in the shear viscosity η and a strong maximum in the bulk viscosity ζ close to T_c (note the logarithmic scale), the ratio ζ/η has a sizeable maximum in the region of the (crossover) phase transition.

6.2 Electric conductivity

Whereas shear and bulk viscosities of hot QCD matter at finite temperature T presently are roughly known (cf. Sec. 6.1), the electric conductivity σ_0 is a further macroscopic quantity of interest [264]. The basic question is: Is the "hot QCD matter" a good electric conductor? At first glance one might expect the deconfined QCD medium to be highly conductive, since color charges—and associated electric charges of the fermions—might move rather freely in the colored plasma. However, due to the actual high interaction rates in the plasma—reflected in a low ratio η/s (cf. Sec. 6.1)—this expectation is not so obvious. First results from quenched lattice calculation on the electromagnetic correlator provide results that vary by more than an order of magnitude [265–268]. Furthermore, the conductivity dependence on the temperature T (at $T > T_c$) is widely unknown, too. The electric conductivity σ_0 is also important for the creation of electromagnetic fields in ultrarelativistic nucleus-nucleus collisions from partonic degrees of freedom, since σ_0 specifies the imaginary part of the electromagnetic (retarded) propagator and leads to an exponential decay of the propagator in time $\sim \exp(-\sigma_0(t-t')/(\hbar c))$ [269]. High values of σ_0 would thus lead to the screening of external electromagnetic fields in the bulk of the highly-conducting QGP similar to the Meissner effect in superconductors as well as the "skin-effect" for the electric current. Accordingly, a sufficient knowledge of $\sigma_0(T)$ is mandatory to explore the possible generation of the Chiral-Magnetic-Effect (CME) in predominantly peripheral heavy-ion reactions [270–276].

In this Section we concentrate on calculating the electric conductivity for "infinite" QCD matter, which we simulate within a cubic box with periodic boundary conditions at various values for the energy density (or temperature) within PHSD. For more details on the simulation of equilibrated systems using PHSD in the box we refer the reader to Chapter 5.

6.2.1 External electric field

In order to include the effects from a constant external electric field E_z, the propagation of each testparticle (in $z-$direction) is performed with the additional force in the equation of motion:

$$\frac{d}{dt}p_z^j = q_j e E_z, \tag{6.16}$$

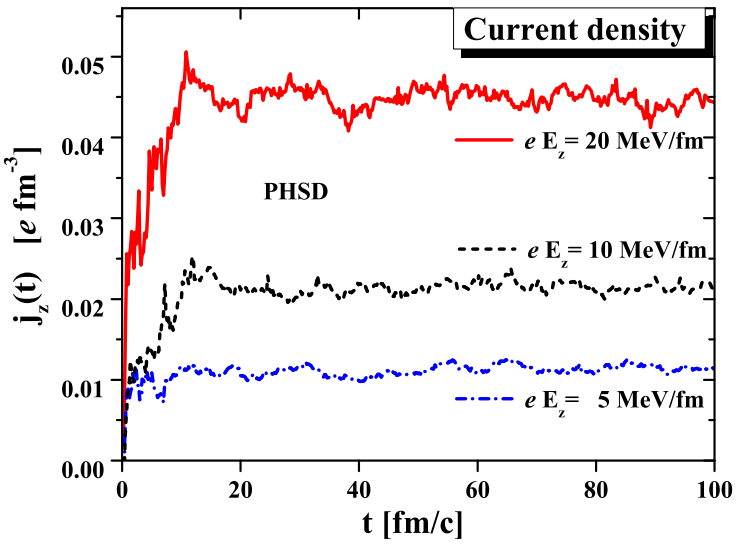

Figure 6.10: The electric current density $j_z(t)$ induced by an external (constant) electric field of strength eE_z as a function of time t. The calculations are performed for a system of partons at temperature $T = 190$ MeV in a box of volume 729 fm^3 within the PHSD approach.

where q_j denotes the fractional charges of the testparticles $(\pm 1/3, \pm 2/3)$.

The electric current density $j_z(t)$ then is given by

$$j_z(t) = \frac{1}{V} \sum_j eq_j \frac{p_z^j(t)}{M_j(t)}, \tag{6.17}$$

where $M_j(t)$ is the mass of the testparticle j at time t. A note of caution has to be given, since due to an external field we deal with an open system with increasing energy density (temperature) in time. Therefore we employ sufficiently small external fields, such that the energy increase during the computation time stays below 2% and the increase in temperature below 1 MeV.

Fig. 6.10 presents the time dependence of the electric current $j_z(t)$ induced by an external (constant) electromagnetic field of strengths $eE_z = 5$ MeV/fm, $eE_z = 10$ MeV/fm, and $eE_z = 20$ MeV/fm (for the temperature $T = 190$ MeV). It is seen that the current achieves an equilibrium value (denoted by j_{eq}) that is proportional to the external field. In fact, we obtain for the ratio of the current and the electric field strength[2]

$$\frac{\sigma_0}{T} = \frac{j_{eq}}{E_z T}, \tag{6.18}$$

[2]Note that one has to use the conversion constant ($\hbar c$) in order to translate the volume, electric field strength, etc to natural units (GeV) in the calculation of ratio.

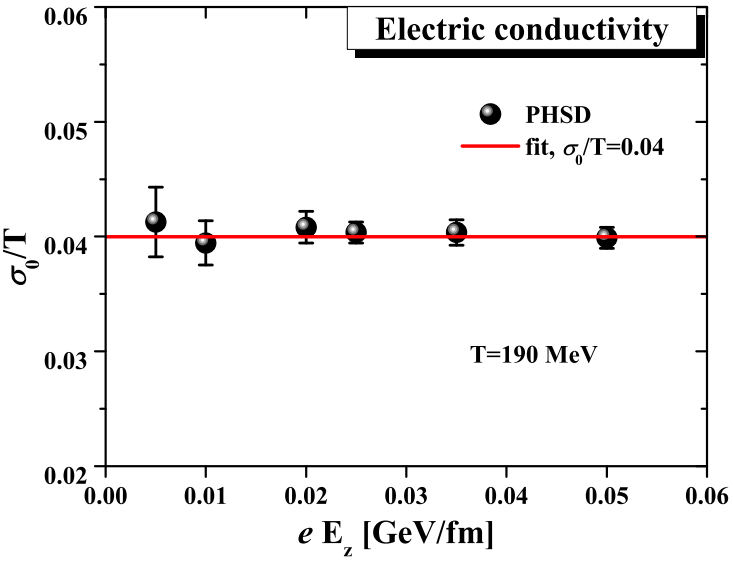

Figure 6.11: The dimensionless ratio of the conductivity to the temperature at $T = 190$ MeV as a function of the external electric field eE_z. The statistical accuracy of the calcualtions is reflected in the error bars. The straight line gives the best fit to the dimensionless ratio σ_0/T.

which is shown in Fig. 6.11 as a function of the external field eE_z. All results are compatible with a constant ratio (6.18) as indicated by the straight line. We note that our numerical results for σ_0 do not depend on the volume V of the box within reasonable variations by a factor of 8.

We have performed the PHSD studies for partonic/hadronic systems at various temperatures from $T = 100$ MeV up to $T = 350$ MeV. The respective results for the ratio σ_0/T versus the scaled temperature T/T_c are displayed in Fig. 6.12 by the full round symbols. We observe a decreasing ratio σ_0/T with T/T_c in the hadronic phase, a minimum close to T_c and an approximately linear rise with T/T_c above T_c (=158 MeV). Within the error bars of our calculations (which in Fig. 6.12 are indicated by the size of the symbols above T_c), the conductivity in the partonic phase is described by

$$\frac{\sigma_0}{T}(T) \approx 0.01 + 0.16\frac{T - T_c}{T_c} \tag{6.19}$$

for $T_c \leq T \leq 2.2T_c$. The lQCD numbers [265–268] are represented by symbols with error bars (using $C_{EM} = 8\pi\alpha_{EM}/3$, where $\alpha_{EM} = 1/137$). In view of the pQCD prediction of a constant asymptotic value for $\sigma_0/T \approx 5.9769/e^2 \approx 65$ in leading order of the coupling [224, 265, 277], such a linear rise of the dimen-

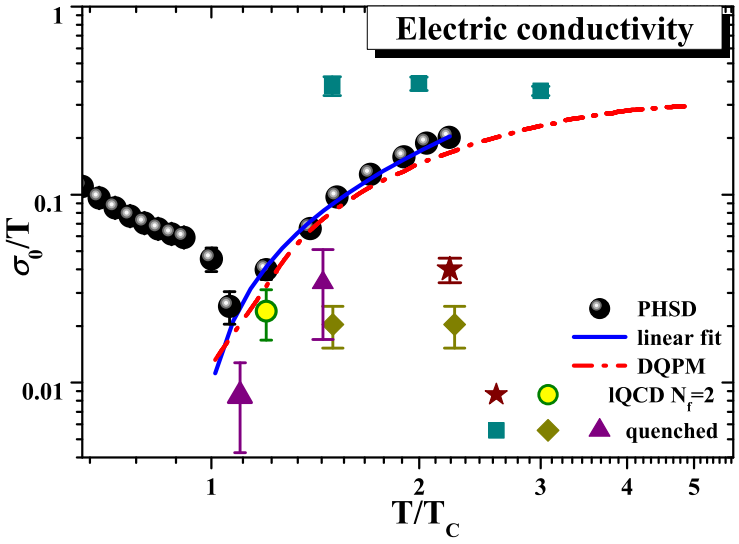

Figure 6.12: The ratio σ_0/T as a function of the scaled temperature T/T_c (T_c = 158 MeV). The round symbols show the PHSD results, the solid blue line is the linear fit to the PHSD results (above T_c), while the dash-dotted red line gives the corresponding ratio in the relaxation time approach (employing the DQPM parameters). The scattered symbols with error bars represent the results from lattice gauge calculations: the triangles – Ref. [265], the diamonds – Ref. [266], the squares – Ref. [267], the star – Ref. [268]. We used for the average charge squared $C_{EM} = 8\pi\alpha/3$ with $\alpha = 1/137$. Note that the pQCD result at leading order beyond leading log [224] is $\sigma_0/T \approx 5.97/e^2 \approx 65$.

sionless ratio with temperature might be surprising, but it can be understood in simple terms as demonstrated below. Only at the highest temperatures studied ($\sim 5T_c$) will we see a stabilization of the ratio.

6.2.2 The relaxation time approximation

The electric conductivity of gases, liquids and solid states is described in the relaxation time approach by

$$\sigma_0 = \frac{e^2 n_e \tau}{m_e^*}, \tag{6.20}$$

where n denotes the density of non-localized charges, τ is the relaxation time of the charge carriers in the medium and m_e^* their effective mass. This expression can be directly computed for partonic degrees of freedom within the DQPM, which was used to match in PHSD the quasiparticles properties to lQCD results in equilibrium for the equation of state (EoS) as well as various correlators (cf. Sec. 3.2). We note that the electromagnetic correlator

from lQCD calculations [265] appears to match rather well the back-to-back dilepton rate from PHSD at $T = 1.45T_c$ (cf. Fig. 2 in [277]), which suggests that the results of our calculations for σ_0 should also be close to the lQCD extrapolations from Ref. [265].

In the DQPM the relaxation time is given by:

$$\tau(T) = \Gamma_q^{-1}(T), \tag{6.21}$$

where $\Gamma_q(T)$ is the width of particles, which is defined by Eq. (3.14). Furthermore, the spectral distribution for the mass of the quasiparticle has a finite pole mass $M_q(T)$ that is also fixed in the DQPM, as well as the density of $(u, \bar{u}, d, \bar{d}, s, \bar{s})$ quarks/antiquarks as a function of temperature (cf. Sec. 3.2). Thus, we obtain for the dimensionless ratio (6.18) the expression

$$\frac{\sigma_0(T)}{T} \approx \frac{2}{9} \frac{e^2 n_q(T)}{M_q(T)\Gamma_q(T)T}, \tag{6.22}$$

where $n_q(T)$ denotes the total density of quarks and antiquarks and the prefactor 2/9 reflects the flavor averaged fractional quark charge squared $(\sum_f q_f^2)/3$. The result for the ratio (6.22) is displayed in Fig. 6.12 (dash-dotted line) and does not involve any new parameters. Apparently, the PHSD results in equilibrium and the relaxation time estimates match well up to $\sim 2\ T_c$ which demonstrates again that PHSD in equilibrium is a proper transport realization of the DQPM (cf. Chapter 5).

Our results from the DQPM suggest that above $T \sim 5T_c$ the dimensionless ratio (6.22) becomes approximately constant (≈ 0.3). This comes about as follows: At high temperature T, the parton density scales as $\sim T^3$, while $M_q(T) \sim T$ and $\Gamma_q(T) \sim T$. Accordingly the ratio (6.22) is approximately constant. Note, however, that energy densities corresponding to $T > 5T_c$ are not reached in present experiments with heavy-ions at RHIC or LHC! On the other hand, σ_0/T rises with decreasing temperature below T_c (in the dominantly hadronic phase), because at lower temperatures the system merges to a moderately interacting system of pions, which in view of Eq. (6.20) has a larger charge (squared) to mass ratio than in the partonic phase as well as a longer relaxation time.

6.3 Summary

In this Chapter we have employed the off-shell PHSD transport approach in a finite box with periodic boundary conditions for the study of the transport coefficients as a function of temperature (or energy density) for dynamical partonic and hadronic systems in equilibrium. We have used the Kubo formalism as well as relaxation time approximation to calculate the shear viscosity $\eta(T)$. We have found that both methods provide very similar results for the ratio $\eta(T)/s(T)$ with a minimum close to the critical temperature T_c, while approaching the pQCD limit at higher temperatures. For $T < T_c$, i.e., in the hadronic phase, the ratio $\eta(T)/s(T)$ rises fast with decreasing temperature due to a lower interaction rate of the hadronic system and a significantly smaller number of degrees of freedom (or entropy density). Our results are, furthermore, also in almost quantitative agreement with the ratio $\eta(T)/s(T)$ from the virial expansion approach in Ref. [70] as well as with lQCD data for the pure gauge sector.

We have evaluated the bulk viscosity $\zeta(T)$ in the relaxation time approach and focused on the effects of mean fields (or potentials) in the partonic phase. Here we have found a significant rise of the ratio $\zeta(T)/s(T)$ in the vicinity of the critical temperature T_c due to the scalar mean fields from PHSD. The result for this ratio is in line with that from lQCD calculations. Additionally, the specific sound $(\eta + 3\zeta/4)(T)/s(T)$ has been calculated and presents a non-trivial temperature dependence; the absolute value for this combination of the shear and bulk viscosities is in an approximate agreement with the lattice gauge theory. Furthermore, the ratio $\zeta(T)/\eta(T)$ within the PHSD calculations shows a strong maximum close to T_c, which has to be attributed to mean-field (or potential) effects that in PHSD are encoded in the infrared enhancement of the "resummed" coupling $g(T)$.

Finally, we have evaluated the electric conductivity $\sigma_0(T)$ of the QGP as well as the hadronic phase as a function of temperature T. We have found that the dimensionless ratio $\sigma_0(T)/T$ rises above T_c approximately linearly with T up to $T = 2.5T_c$, but approaches a constant (≈ 0.3) above $5T_c$, as expected from pQCD. This finding is naturally explained within the relaxation time approach using the DQPM spectral functions. Below T_c the ratio $\sigma_0(T)/T$ rises with decreasing temperature because the system merges to a moderately interacting gas of pions with a larger charge to mass ratio than in the partonic phase and a longer relaxation time.

Chapter 7

Summary and Discussion

It has been indicated in the Introduction (Chapter 1) that the deconfined state of matter (or QGP) can be created experimentally in relativistic heavy-ion collisions. The produced QGP shows features of a strongly interacting fluid unlike a weakly interacting parton gas. The current thesis has been dedicated to the study of the thermalization and equilibration as well as the transport coefficients, such as the shear viscosity, bulk viscosity, and electric conductivity of strongly interacting matter.

The nonequilibrium Green's function techniques, initiated by Schwinger as well as Kadanoff and Baym, were used to describe high-energy nuclear collisions. Based on the Schwinger-Keldysh formalism and on the two-particle irreducible (2PI) approach the Green's function techniques have been extended to relativistic systems for "resummed" propagators and couplings, as shown in Chapter 2. Furthermore, the Kadanoff-Baym equations and the generalized transport equations as well as testparticle solution to the resulting transport equation have been derived which are the formal basis for the PHSD transport approach.

The PHSD off-shell transport approach has been used as a method for our investigation. The main ingredients of the PHSD model have been presented in Chapter 3. This approach consistently describes the full evolution of a relativistic heavy-ion collision from the initial hard scatterings and string formation through the dynamical deconfinement phase transition to the strongly interacting QGP as well as hadronization and the subsequent interactions in the expanding hadronic phase.

To evaluate the self-energies for quarks and antiquarks as well as gluons—that enter the spectral functions and retarded Green's functions—the DQPM

has been introduced. This model is the basis for the partonic phase description in PHSD and describes QCD properties in terms of single-particle Green's functions (in sense of a 2PI approach). The DQPM has been matched to reproduce lQCD results—including the partonic equation of state—in thermodynamic equilibrium.

A further result of the DPQM has been achieved by separating timelike and spacelike quantities for particle densities, energy densities, etc. The mean-field potentials for quarks, antiquarks, and gluons have been obtained by taking derivatives of the potential energy densities with respect to the timelike fermion and gluon densities. Then second derivatives w.r.t. the gluon and/or fermion densities have defined effective interactions between partons. An extension of the DQPM to finite quark chemical potentials has been presented, too.

The PHSD transport approach is a powerful tool to study nucleus-nucleus collisions in a wide range of energies. The implementations of PHSD for heavy-ion collisions from SPS to RHIC energies have been presented in Chapter 4. It was found that even central collisions at the top SPS energy show a large fraction of non-partonic, i.e., hadronic or string-like matter, which can be viewed as a "hadronic corona". This finding implies that neither purely hadronic nor purely partonic models can be employed to extract physical conclusions in comparing model results with data. The PHSD results have been compared to the experimental data from the NA49 Collaboration for Pb+Pb collisions at SPS energies and it was found that the partonic phase has only a very low impact on the longitudinal rapidity distributions of hadrons, but a sizeable influence on the transverse-mass distribution of final kaons due to the partonic interactions. The most pronounced effect is seen on the production of multi-strange antibaryons due to a slightly enhanced $s\bar{s}$ pair production in the partonic phase from massive timelike gluon decay and a more abundant formation of strange antibaryons in the hadronization process. This enhanced formation of strange antibaryons in central Pb+Pb collisions at SPS energies by hadronization supports the early suggestion by Braun-Munzinger and Stachel [157, 278–280] in the statistical hadronization model, which describes well particle ratios from AGS to RHIC energies.

The PHSD results are in agreement with the experimental data for the hadron transverse mass and rapidity spectra at RHIC energies. The elliptic flow v_2 is well reproduced for Au+Au reactions at $\sqrt{s} = 200$ GeV as a function of centrality as well as of transverse momenta up to $p_T \simeq 1.5$ GeV. The PHSD

approach also gives an approximate quark number scaling of the elliptic flow as found experimentally by the STAR and PHENIX Collaborations. Furthermore, PHSD reproduces the results for the elliptic flow v_2 from the low Beam Energy Scan at RHIC.

The dilepton production in In+In collisions at 158A GeV has been studied within the PHSD off-shell transport approach including a collisional broadening of vector mesons, microscopic secondary multimeson channels and the strongly interacting QGP radiation, which is described by the interactions of dynamical quasiparticles in line with the degrees of freedom propagated in the transport approach. The dilepton yield is well described in comparison to the experimental data of the NA60 Collaboration by including the collisional broadening of vector mesons, while simultaneously accounting for the electromagnetic radiation of the strongly coupled QGP via off-shell quark-antiquark annihilation, quark annihilation with gluon Bremsstrahlung and the gluon-Compton scattering mechanisms. Furthermore, the spectra in the intermediate mass range ($1 \leq M \leq 2.5$ GeV) are found to be dominated by quark-antiquark annihilation in the nonperturbative QGP. Also, the observed softening of the transverse mass spectra at intermediate masses ($1 \leq M \leq 2.5$ GeV) was approximately reproduced.

Chapter 5 has been devoted to study systems slightly out of equilibrium as well as in equilibrium in a finite cubic box with periodic boundary conditions within the PHSD transport approach. The conclusions of this investigation are as follows:

- Partonic systems at energy densities ε above the critical energy density $\varepsilon_c \approx 0.5$ Gev/fm^3 achieve kinetic and chemical equilibrium in time.

- The energy density of the partonic system at fixed temperature and quark chemical potential for $\mu_q = 0$ is well in line with the DQPM or lQCD calculations in equilibrium.

- The strangeness degree of freedom equilibrates on time scales that are large compared to the reaction times in relativistic nucleus-nucleus collisions. These findings appear to be in contradiction; to experimental findings, however, the time scales from the box calculations cannot directly be applied to nucleus-nucleus collisions since the initial conditions are very different.

- For all observables the equilibration time $\tau_{\rm eq}$ is found to be shorter for the scaled variances than for the average values. This is most pronounced when considering all charged partons but less distinct for strange partons. Accordingly, scaled variances may achieve an equilibrium even if the average values of an observable are still out of equilibrium. This finding is reminiscent of strongly interacting quantum systems evaluated on the basis of Kadanoff-Baym equations, where quantum fluctuations stabilize early in time, i.e., long before a kinetic or chemical equilibrium is achieved.

- The scaled variances for the fluctuations in the numbers of different partons in the box show an influence of total energy conservation.

- A suppression of the parton number fluctuations in comparison to the fluctuations in the grand canonical ensemble is observed.

- After dividing the box into several cells it was found that the scaled variances for all observables approach the Poissonian limit with $\omega = 1$ when the cell volume is much smaller than that of the box. This observation indicates that global conservation laws (for energy-momentum and charges) are not important when one detects only a small fraction from all particle in the system.

- The scaled variances no longer depend on the size of the box when increasing it up to ≈ 5000 fm^3. Accordingly, the thermodynamic limit has approximately been reached in the calculations.

- Skewness and kurtosis practically vanished in time and especially in equilibrium for all observables. Within statistics our results are also compatible with lQCD results.

Finally, the PHSD transport approach has been used to extract the transport coefficients of the partonic and hadronic phases in Chapter 6. In this approach the transport coefficients do not enter as external parameters but are generic properties of the degrees of freedom under consideration and can be calculated for systems in equilibrium as a function of temperature explicitly without incorporating any additional parameters. The summary on transport coefficients reads as follows:

- The Kubo formalism and relaxation time approximation show about the same results within statistics for the ratio $\eta(T)/s(T)$ with a minimum close to the critical temperature T_c, while approaching the pQCD limit at higher temperatures. Our results are also in almost quantitative agreement with the ratio $\eta(T)/s(T)$ from the virial expansion approach as well as with lQCD data for the pure gauge sector.

- The QGP in PHSD behaves as a strongly interacting liquid.

- In the hadronic phase, the ratio $\eta(T)/s(T)$ rises fast with decreasing temperature due to a lower interaction rate of the hadronic system and a significantly smaller number of degrees of freedom (or entropy density).

- The ratio $\zeta(T)/s(T)$, which was calculated in the relaxation time approximation, shows a significant rise in the vicinity of the critical temperature T_c due to the scalar mean fields from PHSD. The result for this ratio is in line with that from lQCD calculations.

- The specific sound $(\eta + 3\zeta/4)(T)/s(T)$ has been calculated and presents a non-trivial temperature dependence; the absolute value for this combination of the shear and bulk viscosities is in an approximate agreement with the lattice gauge theory.

- The ratio $\zeta(T)/\eta(T)$ within the PHSD calculations shows a strong maximum close to T_c, which has to be attributed to mean-field (or potential) effects that in PHSD are encoded in the infrared enhancement of the "resummed" coupling $g(T)$.

- The dimensionless ratio $\sigma_0(T)/T$, which was calculated in the relaxation time approximation, rises above T_c approximately linearly with T up to $T = 2.5T_c$, but approaches a constant (≈ 0.3) above $5T_c$, as expected from pQCD.

- In the hadronic phase, the ratio $\sigma_0(T)/T$ rises with decreasing temperature because the system merges to a moderately interacting gas of pions with a larger charge to mass ratio than in the partonic phase and a longer relaxation time.

This study is expected shed some light of how and on what time scales thermodynamic equilibrium can be achieved in nucleus-nucleus collisions at

ultrarelativistic energies as well as on the transport properties of strongly interacting matter.

Appendix A

Multimeson channels of dilepton production

The dilepton excess yield in In+In collisions at 158A GeV incident energy for $M > 1$ GeV was found to be dominated by partonic sources within the dynamical studies of Renk and Ruppert [281,282] as well as Dusling and Zahed [283–285]. On the other hand, the model of van Hees and Rapp [286] suggests a dominance of hadronic sources dubbed "4π channels". To clarify this question, we have incorporated in PHSD the 4π channels for dilepton production on a microscopic level rather than assuming thermal dilepton production and incorporating a parametrization for the inverse reaction $\mu^+ + \mu^- \rightarrow 4\pi's$ by employing detailed balance as in Refs. [287, 288].

By studying the electromagnetic emissivity (in the dilepton channel) of the hot hadron gas, it was shown in Refs. [155, 289] that the dominating hadronic reactions contributing to the dilepton yield at the invariant masses above the ϕ peak are the two-body reactions, i.e., $\pi + \rho$, $\pi + \omega$, $\rho + \rho$, $\pi + a_1$. This conclusion was supported by the subsequent study in a hadronic relativistic transport model [290]. Therefore, we implement the above-listed two-meson dilepton production channels in the PHSD approach. In addition, some higher vector mesons (ρ', etc.) are tacitly included by using phenomenological form factors adjusted to data.

We determine the cross sections for the mesonic interactions with dileptons in the final state using an effective Lagrangian approach, following the works of Refs. [155, 290]. The dilepton production cross section is given by the product

of a form factor and the square of a scattering amplitude,

$$\frac{d\sigma}{dt} = \frac{1}{64\pi s}\frac{1}{|p_{\rm c.m.}|^2}|\bar{M}|^2|F(M)|^2, \tag{A.1}$$

where

$$p_{\rm c.m.} = \sqrt{(s-(m_1+m_2)^2)(s-(m_1-m_2)^2)}/2\sqrt{s} \tag{A.2}$$

is the center-of-mass momentum of the colliding hadrons with the masses m_1 and m_2, and $|\bar{\mathcal{M}}|^2$ can be written as

$$|\bar{\mathcal{M}}|^2 = 4\left(\frac{4\pi\alpha}{q^2}\right)^2 L_{\mu\nu}H^{\mu\nu}, \tag{A.3}$$

with $q = p_1 + p_2 = p_3 + p_4$ and the fine structure constant α. In Eq. (A.3), $L_{\mu\nu}$ is the leptonic tensor given by

$$L^{\mu\nu} = p_3^\mu p_4^\nu + p_4^\mu p_3^\nu - g^{\mu\nu}(p_3 p_4 + m_l^2), \tag{A.4}$$

while $H^{\mu\nu}$ is a hadronic tensor for the reaction.

The hadronic tensor $H^{\mu\nu}$ for the reaction $\pi^+ + \pi^- \to e^+ + e^-$ is given by

$$H^{\mu\nu} = (p_2^\mu - p_1^\mu)(p_2^\nu - p_1^\nu), \tag{A.5}$$

which leads to the well-known result for the $\pi\pi$ annihilation cross section,

$$\sigma_\pi(s) = \frac{4\pi\alpha^2}{3s}|F_\pi|^2\sqrt{1-\frac{4m_\pi^2}{s}}\left(1-\frac{4m_l^2}{M^2}\right)\left(1+\frac{2m_l^2}{M^2}\right), \tag{A.6}$$

where M is the mass of the lepton pair and m_l is the mass of the lepton. The electromagnetic form factor $|F_\pi(M)|^2$ plays an important role in this process, providing empirical support for the vector meson dominance: the pion electromagnetic form factor is dominated by the $\rho(770)$ meson. In Refs. [291, 292], Gale and Kapusta proposed the form

$$|F_\pi(M)|^2 = \frac{m_r^4}{(M^2-m_r'^2)^2 + (m_r\Gamma_r)^2}, \tag{A.7}$$

where $m_r = 0.775$ GeV, $m_r' = 0.761$ GeV, and $\Gamma_r = 0.118$ GeV.

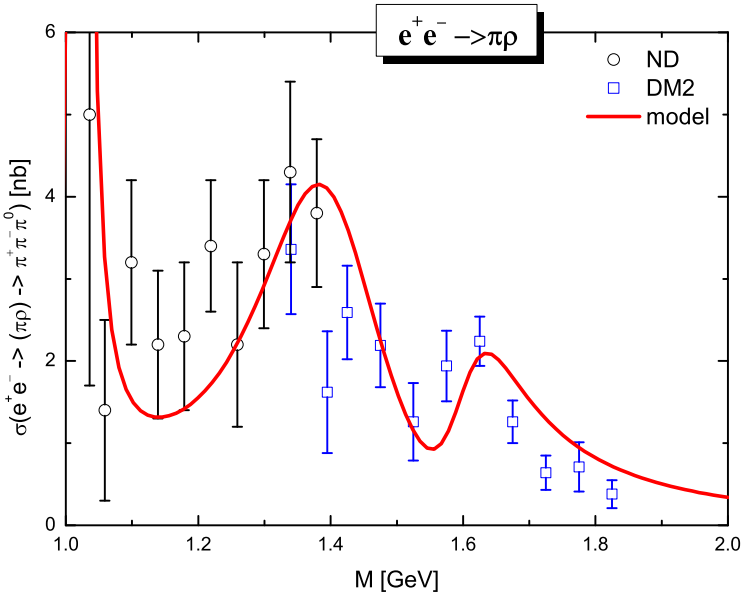

Figure A.1: Cross sections for the reactions $e^+e^- \to \pi + \rho$ in our model (solid red line) versus the experimental data from Refs. [294] (blue squares) and [295] (black circles).

According to Ref. [293], the cross section for $\pi\rho$ annihilation is given by

$$\sigma(\pi^+\rho^- \to l\bar{l}) = \frac{2\pi\alpha^2 p_{\rm c.m.}}{9M}|F_{\pi\rho}|^2\Big(1-\frac{4m_l^2}{M^2}\Big)\Big(1+\frac{2m_l^2}{M^2}\Big). \qquad \text{(A.8)}$$

Note that the cross section (A.8) is evaluated in the narrow-width approximation for illustration purposes only. This simplification is not used in the actual transport calculation. The electromagnetic form factor $|F_{\pi\rho}(M)|^2$ can then be determined by analyzing the experimental data for $e^+e^- \to \pi^+\pi^-\pi^0$. In Ref. [293], three isoscalar vector mesons, $\phi(1020)$, $\omega(1420)$, and $\omega(1670)$ were found to be important in order to fit the experimental data, i.e.,

$$F_{\pi\rho}(M) = \sum_V \left(\frac{g_{V\pi\rho}}{g_V}\right)\frac{e^{i\phi_V}m_V^2}{(m_V^2-M^2)-im_V\Gamma_V}. \qquad \text{(A.9)}$$

Here the summation runs over the three vector mesons listed above. While the coupling constants g_ϕ and $g_{\phi\pi\rho}$ can be determined from the measured widths, the coupling constants for two other mesons and the relative phases were determined by a fit to the experimental data of Refs. [296, 297]. These coupling constants were extracted from the latest data of the DM2 Collaboration [294] and the ND Collaboration [295]. The parameters are listed in Ref. [293]. The

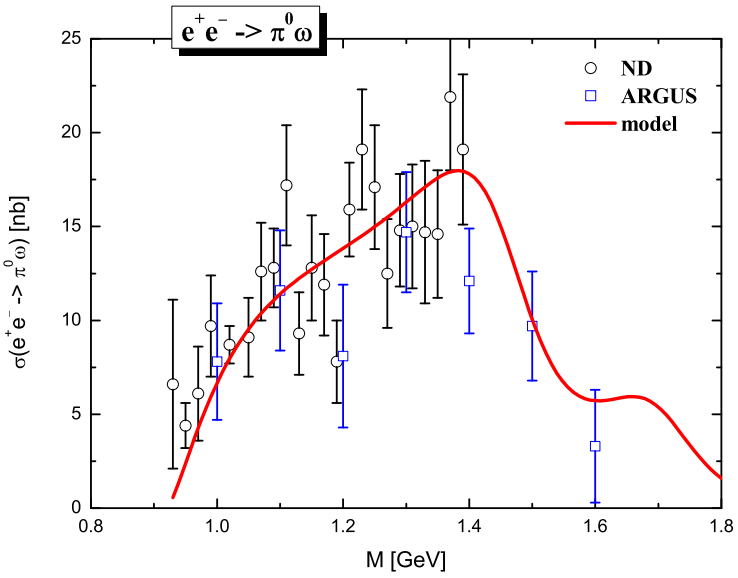

Figure A.2: Cross sections for the reactions $e^+e^- \to \pi + \omega$ in our model (solid red line) versus the experimental data from Refs. [298] (blue squares) and [295] (black circles).

comparison of the fit to the experimental data is shown in Fig. A.1.

The cross section for lepton pair production in pion-ω annihilation is given by [290]

$$\sigma(\pi^0\omega \to l\bar{l}) = \frac{4\pi\alpha^2 p_{\text{c.m.}}}{9M}|F_{\pi\omega}|^2\Big(1-\frac{4m_l^2}{M^2}\Big)\Big(1+\frac{2m_l^2}{M^2}\Big). \tag{A.10}$$

The form factor can be parametrized in terms of three isovector ρ-like vector mesons, $\rho(770)$, $\rho(1450)$, and $\rho(1700)$,

$$F_{\pi\omega}(M) = \sum_V \left(\frac{g_{V\pi\omega}}{g_V}\right)\frac{e^{i\phi_V}m_V^2}{(m_V^2-M^2)-im_V\Gamma_V}. \tag{A.11}$$

Here the summation runs over the three ρ-like resonances listed above. The parameters used are $m_{r1} = 0.77$ GeV, $m_{r2} = 1.45$ GeV, $m_{r3} = 1.7$ GeV, $\Gamma_{r1} = 0.118$ GeV, $\Gamma_{r2} = 0.25$ GeV, $\Gamma_{r3} = 0.22$ GeV, $A_{r1} = 0.85$, $A_{r2} = -0.077$, $A_{r3} = 0.034$, where $A_V = (g_{V\pi\omega}/g_V)\exp\{i\phi_V\}$. The comparison with the experimental data of the ND [295] and ARGUS Collaborations [298] is shown in Fig. A.2.

Additionally, we consider the reactions $\pi a_1 \to l\bar{l}$ and $\rho\rho \to l\bar{l}$, which are

effectively four-pion processes. Using the Lagrangian for the πa_1 interaction,

$$\mathcal{L}_{\pi a_1 \gamma *} = g e a^\mu [(\partial_\nu A_\mu)(\partial^\nu \pi) - (\partial_\mu A^\nu)(\partial_\nu \pi)], \tag{A.12}$$

one obtains for the cross section of the $\pi a_1 \to l\bar{l}$ process,

$$\begin{aligned}\sigma(\pi a_1 \to l\bar{l}) = \frac{\pi\alpha^2 g^2 M}{3p_{\rm c.m.}} \left(1 - \frac{4m_l^2}{M^2}\right)\left(1 + \frac{2m_l^2}{M^2}\right)\Bigg\{\frac{1}{4}\left(1 - \frac{m_{a1}^2}{M^2}\right) \\ \times\left[1 + \frac{2}{m_{a1}^2}\left(\frac{5p_{\rm c.m.}^2}{12} + \frac{m_{a1}^2}{2}\right)\right] + \left(1 - \frac{m_{a1}^2}{M^2}\right)\Bigg\{-\frac{1}{2}\left(1 - \frac{m_{a1}^2}{M^2}\right) \\ + \frac{\sqrt{p_{\rm c.m.}^2 + m_\pi^2}}{M} - \frac{M^2}{2m_{a1}^2}\left(1 + \frac{m_{a1}^2}{M^2}\right)\Bigg[\frac{p_{\rm c.m.}^2}{6M^2} - \frac{1}{2}\left(1 - \frac{m_{a1}^2}{M^2}\right) \\ + \frac{\sqrt{p_{\rm c.m.}^2 + m_{a1}^2}\sqrt{p_{\rm c.m.}^2 + m_\pi^2}}{M^2}\Bigg]\Bigg\} + \frac{5p_{\rm c.m.}^2}{6M^2}\left[\frac{(M^2 + m_{a1}^2)^2}{4m_{a1}^2 M^2} - 1\right]\Bigg\} \\ \times |F_{\pi a_1}|^2,\end{aligned} \tag{A.13}$$

where the value of the coupling constant $g = (g_\rho/f_\rho)$ is adjusted so that the experimentally measured radiative decay widths are reproduced.

We obtain the hadronic tensor $H^{\mu\nu}$ for the reaction $\rho^+\rho^- \to e^+e^-$ by generalizing the formula of Ref. [155] to explicitly take into account the broad spectral functions of the colliding ρ mesons:

$$\begin{aligned}H^{\mu\nu} = h_\rho^{\mu\alpha\beta} h^\nu_{\rho\,\alpha\beta} - h_\rho^{\mu\alpha\beta} p_{1\,\beta} h_{\rho\,\alpha}^{\nu\gamma} p_{1\,\gamma}/m_{\rho 1}^2 - h_\rho^{\mu\alpha\beta} p_{2\,\alpha} h_{\rho\,\beta}^{\nu\gamma} p_{2\,\gamma}/m_{\rho 2}^2 \\ + h_\rho^{\mu\alpha\beta} p_{1\,\beta} p_{2\,\alpha} h_\rho^{\nu\gamma\delta} p_{2\,\gamma} p_{1\,\delta}/(m_{\rho 1}^2 m_{\rho 2}^2)\end{aligned} \tag{A.14}$$

with

$$h_\rho^{\mu\alpha\beta} = (p_2^\mu - p_1^\mu) g^{\alpha\beta} + (q^\alpha - p_2^\alpha) g^{\beta\mu} + (p_1^\beta - q^\beta) g^{\mu\alpha}. \tag{A.15}$$

In this case, the hadronic tensor depends on (generally different) masses of the colliding particles $m_{\rho 1}$ and $m_{\rho 2}$. In the actual transport calculations, $m_{\rho i}$ are distributed according to the dynamical spectral functions. Using Eqs. (A.1)–(A.3) and (A.14) we obtain the following cross section as a function of M, $m_{\rho 1}$,

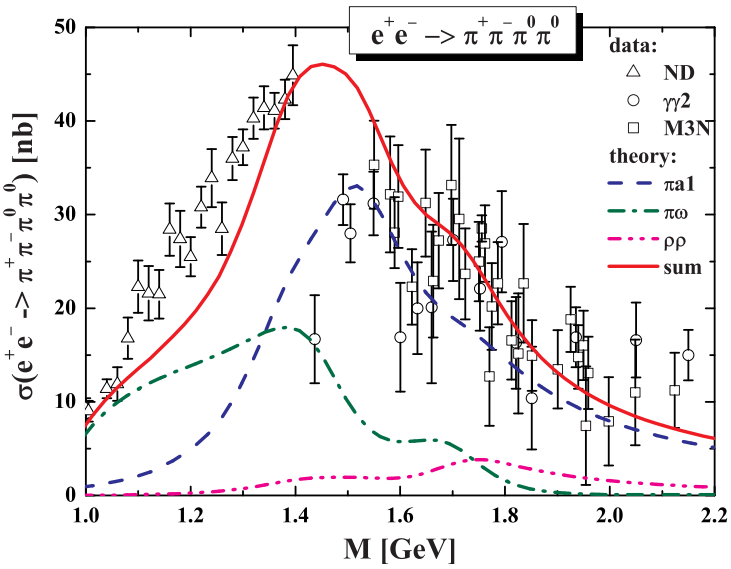

Figure A.3: The sum (solid red line) of the model cross sections for $e^+e^- \to \pi + \omega$ (green dash-dotted line), $e^+e^- \to \pi + a_1$ (blue dashed line), and $e^+e^- \to \rho + \rho$ (magenta dash-dot-dotted line) versus the measured cross section of the $e^+e^- \to \pi^+\pi^-\pi^0\pi^0$ reaction from Refs. [295] (black triangles), [299] (black circles), and [300] (black squares).

and $m_{\rho 2}$:

$$\begin{aligned}\sigma(\rho\rho \to l^+l^-) = \frac{\pi\alpha^2|F_{\rho\rho}|^2}{120 m_{\rho 1}^2 m_{\rho 2}^2 M^5 p_{\text{c.m.}}} \big[& 9m_{\rho 1}^8 + 18 m_{\rho 1}^6 \left(3m_{\rho 2}^2 - 2M^2\right) \\ & + \left(m_{\rho 2}^2 - M^2\right)^2 \left(819 m_{\rho 2}^4 + 632 m_{\rho 2}^2 M^2 - 11 M^4\right) \\ & - 2m_{\rho 1}^2 \left(363 m_{\rho 2}^6 + 32 m_{\rho 2}^4 M^2 + 327 m_{\rho 2}^2 M^4 - 2M^6\right) \\ & + m_{\rho 1}^4 \left(-156 m_{\rho 2}^4 + 266 m_{\rho 2}^2 M^2 + 34 M^4\right)\big], \end{aligned} \tag{A.16}$$

which reduces in the narrow width approximation to

$$\begin{aligned}\sigma(\rho\rho \to l^+l^-) = & \frac{\pi\alpha^2|F_{\rho\rho}|^2}{60 m_\rho^4 M^3 \sqrt{M^2 - 4m_\rho^2}} \\ & \times \left(840 m_\rho^6 + 1076 m_\rho^4 M^2 - 658 m_\rho^2 M^4 + 11 M^6\right). \end{aligned} \tag{A.17}$$

The form factors $|F_{\pi a_1}|^2$ and $|F_{\rho\rho}|^2$ can be determined by analyzing the $e^+e^- \to \pi^+\pi^-\pi^+\pi^-$ and $e^+e^- \to \pi^+\pi^-\pi^0\pi^0$ data. We determine $|F_{\pi a_1}(M)|^2$ from experimental data for $e^+e^- \to \pi^+\pi^-\pi^+\pi^-$ from the $\gamma\gamma 2$ Collaboration [299], the M3N Collaboration [300], and the ND Collaboration [295]. Further constraints on $|F_{\pi a_1}|^2$ and the determination of $|F_{\rho\rho}|^2$ were provided by the

experimental data for $e^+e^- \to \pi^+\pi^-\pi^0\pi^0$, which can come from $\pi\omega$, πa_1, and $\rho\rho$ intermediate states. Our form factors are

$$F_{\pi a_1}(M) = \sum_V \left(\frac{g_{V\pi a_1}}{g_V}\right) \frac{e^{i\phi_V} m_V^2}{(m_V^2 - M^2) - i m_V \Gamma_V} \tag{A.18}$$

with $m_{r1} = 0.77$ GeV, $m_{r2} = 1.45$ GeV, $m_{r3} = 1.7$ GeV, $\Gamma_{r1} = 0.118$ GeV, $\Gamma_{r2} = 0.25$ GeV, $\Gamma_{r3} = 0.235$ GeV, $A_{r1} = 0.05$, $A_{r2} = 0.58$, $A_{r3} = 0.027$, and

$$F_{\rho\rho}(M) = \sum_V \left(\frac{g_{V\rho\rho}}{g_V}\right) \frac{e^{i\phi_V} m_V^2}{(m_V^2 - M^2) - i m_V \Gamma_V} \tag{A.19}$$

with $m_{r1} = 0.77$ GeV, $m_{r2} = 1.45$ GeV, $m_{r3} = 1.7$ GeV, $\Gamma_{r1} = 0.118$ GeV, $\Gamma_{r2} = 0.237$ GeV, $\Gamma_{r3} = 0.235$ GeV, $A_{r1} = 0.05$, $A_{r2} = 0.05$, $A_{r3} = 0.02$. The comparison to the data is shown in Fig. A.3.

Let us summarize that to fix the form factors in the cross sections for dilepton production by the interaction of $\pi + \rho$, $\pi + \omega$, $\rho + \rho$, and πa_1, we use the measurements in the detailed-balance-related channels: $e^+e^- \to \pi + \rho$, $e^+e^- \to \pi + \omega$, $e^+e^- \to \rho + \rho$, and $e^+e^- \to \pi + a_1$. Note that we fitted the form factors while taking into account the widths of the ρ and a_1 mesons in the final state by convoluting the cross sections with the (vacuum) spectral functions of these mesons in line with Ref. [301] (using the parametrizations of the spectral functions as implemented in HSD and described in [302]). In Figs. A.1–A.3 we present the resulting cross sections, which are related by detailed balance to the ones implemented into PHSD.

Bibliography

[1] K. G. Wilson, Phys. Rev. D **10**, 2445 (1974).

[2] A. M. Polyakov, Nucl. Phys. B **120**, 429 (1977).

[3] T. Kugo and I. Ojima, Prog. Theor. Phys. Suppl. **66**, 1 (1979).

[4] V. N. Gribov, Eur. Phys. J. C **10**, 91 (1999).

[5] G. S. Bali, Phys. Rept. **343**, 1 (2001).

[6] G. S. Bali, H. Neff, T. Duessel, T. Lippert, and K. Schilling, Phys. Rev. D **71**, 114513 (2005).

[7] M. E. Peskin and D. V. Schroeder, *An Introduction to Quantum Field Theory* (Addison-Wesley, 1995).

[8] S. Weinberg, *The Quantum theory of fields. Vol. 1: Foundations* (Cambridge: Univ. Pr., 1995).

[9] M. Gell-Mann, Phys. Lett. **8**, 214 (1964).

[10] O. Linnyk, *Quark off-shelness effect on parton distributions* (PhD thesis, Giessen, 2006).

[11] M. Guidal, H. Moutarde, and M. Vanderhaeghen, arxiV:1303.6600[hep-ph].

[12] F. Karsch, J. Phys. G **31**, S633 (2005).

[13] E. Laermann and O. Philipsen, Ann. Rev. Nucl. Part. Sci. **53**, 163 (2003).

[14] Z. Fodor and S. D. Katz, JHEP **0404**, 050 (2004).

[15] P. Petreczky, J. Phys. G **39**, 093002 (2012).

[16] W. Cassing, Nucl. Phys. A **795**, 70 (2007).

[17] W. Cassing, Nucl. Phys. A **791**, 365 (2007).

[18] A. Peshier and W. Cassing, Phys. Rev. Lett. **94**, 172301 (2005).

[19] A. Peshier, B. Kämpfer, O. P. Pavlenko, and G. Soff, Phys. Rev. D **54**, 2399 (1996).

[20] A. Peshier, B. Kämpfer, and G. Soff, Phys. Rev. C **61**, 045203 (2000).

[21] A. Peshier, B. Kämpfer, and G. Soff, Phys. Rev. D **66**, 094003 (2002).

[22] M. Bluhm, B. Kämpfer, R. Schulze, D. Seipt, and U. Heinz, Phys. Rev. C **76**, 034901 (2007).

[23] W. Cassing and E. L. Bratkovskaya, Phys. Rev. C **78**, 034919 (2008).

[24] W. Cassing and E. L. Bratkovskaya, Nucl. Phys. A **831**, 215 (2009).

[25] E. L. Bratkovskaya, W. Cassing, V. P. Konchakovski, and O. Linnyk, Nucl. Phys. A **856**, 162 (2011).

[26] S. A. Bass *et al.*, Prog. Part. Nucl. Phys. **41**, 225 (1998).

[27] M. Bleicher *et al.*, J. Phys. G: Nucl. Part. Phys. **25**, 1859 (1999).

[28] Z. Xu and C. Greiner, Phys. Rev. C **71**, 064901 (2005).

[29] Z.-W. Lin, C. M. Ko, B. Zhang, and S. Pal, Phys. Rev. C **72**, 064901 (2005).

[30] STAR Collaboration, J. Adams *et al.*, Phys. Rev. Lett. **92**, 112301 (2004).

[31] PHENIX Collaboration, S. S. Adler *et al.*, Phys. Rev. C **69**, 034909 (2004).

[32] BRAHMS Collaboration, I. G. Bearden *et al.*, Phys. Rev. Lett. **94**, 162301 (2005).

[33] PHOBOS Collaboration, B. B. Back *et al.*, Phys. Rev. C **72**, 051901 (2005).

[34] CMS Collaboration, S. Chatrchyan *et al.*, Phys. Rev. Lett. **107**, 052302 (2011).

[35] ALICE Collaboration, B. Abelev *et al.*, Phys. Lett. B (2013).

[36] CMS Collaboration, S. Chatrchyan *et al.*, Eur. Phys. J. C **72**, 1945 (2012).

[37] ATLAS Collaboration, G. Aad *et al.*, Phys. Lett. B **697**, 294 (2011).

[38] NA60 Collaboration, A. Arnaldi *et al.*, Eur. Phys. J. C **61**, 711 (2009).

[39] NA60 Collaboration, S. Damjanovic, R. Shahoyan, and H. J. Specht, CERN Cour. **49N9**, 31 (2009).

[40] M. Gyulassy and L. D. McLerran, Nucl. Phys. A **750**, 30 (2005).

[41] E. V. Shuryak, Nucl. Phys. A **750**, 64 (2005).

[42] L. P. Kadanoff and G. Baym, *Quantum Statistical Mechanics* (New York: Benjamin, 1962).

[43] S. Juchem, W. Cassing, and C. Greiner, Phys. Rev. D **69**, 025006 (2004).

[44] S. Juchem, W. Cassing, and C. Greiner, Nucl. Phys. A **743**, 92 (2004).

[45] J. Schwinger, J. Math. Phys. **2**, 407 (1961).

[46] P. Danielewicz, Ann. Phys. (N.Y.) **152**, 305 (1984).

[47] W. Cassing and S. Juchem, Nucl. Phys. A **672**, 417 (2000).

[48] L. V. Keldysh, Zh. Eks. Teor. Fiz. **47**, 1515 (1964).

[49] L. V. Keldysh, Sov. Phys. JETP **20**, 1018 (1965).

[50] W. Cassing, Eur. Phys. J. ST **168**, 3 (2009).

[51] S. Mrowczynski and P. Danielewicz, Nucl. Phys. B **342**, 345 (1990).

[52] J. Berges and J. Cox, Phys. Lett. B **517**, 369 (2001).

[53] W. Cassing and S. Juchem, Nucl. Phys. A **665**, 377 (2000).

[54] C. Greiner and S. Leupold, Ann. Phys. **270**, 328 (1998).

[55] W. Botermans and R. Malfliet, Phys. Rep. **198**, 115 (1900).

[56] S. Leupold, Nucl. Phys. A **672**, 475 (2000).

[57] S. Leupold, Nucl. Phys. A **695**, 377 (2001).

[58] Y. B. Ivanov, J. Knoll, and D. N. Voskresensky, Nucl. Phys. A **672**, 313 (2000).

[59] M. Bonitz, *Quantum Kinetic Theory* (Stuttgart-Leipzig: Teubner, 1998).

[60] W. Cassing, V. Metag, U. Mosel, and K. Niita, Phys. Rep. **188**, 363 (1990).

[61] C. M. Ko and G. Q. Li, J. Phys. G: Nucl. Part. Phys. **22**, 1673 (1996).

[62] J. Aichelin, Phys. Rep. **202**, 233 (1991).

[63] W. Cassing and E. L. Bratkovskaya, Phys. Rep. **308**, 65 (1999).

[64] W. Cassing and S. J. Wang, Z Phys. A **337**, 1 (1990).

[65] E. L. Bratkovskaya and W. Cassing, Nucl. Phys. A **619**, 413 (1997).

[66] E. L. Bratkovskaya and W. Cassing, Nucl. Phys. A **807**, 214 (2008).

[67] A. Peshier, Phys. Rev. D **70**, 034016 (2004).

[68] A. Peshier, J. Phys. G **31**, S371 (2005).

[69] P. Levai and U. Heinz, Phys. Rev. C **57**, 1879 (1998).

[70] S. Mattiello and W. Cassing, Eur. Phys. J. C **70**, 243 (2010).

[71] E. Riedel, Z. Phys. **210**, 403 (1968).

[72] B. Vanderheyden and G. Baym, J. Stat. Phys. **93**, 843 (1998).

[73] J.-P. Blaizot, E. Iancu, and A. Rebhan, Phys. Rev. Lett. **83**, 2906 (1999).

[74] J.-P. Blaizot, E. Iancu, and A. Rebhan, Phys. Rev. D **63**, 065003 (2001).

[75] S. Borsanyi and *et al.*, J. High Energy Phys. **09**, 073 (2010).

[76] S. Borsanyi and *et al.*, J. High Energy Phys. **11**, 077 (2010).

[77] O. Kaczmarek, F. Karsch, F. Zantow, and P. Petreczky, Phys. Rev. D **70**, 074505 (2004).

[78] B. D. Serot and J. D. Walecka, Adv. Nucl. Phys. **16**, 1 (1986).

[79] B. D. Serot, Rep. Prog. Phys. **55**, 1855 (1992).

[80] P. G. Reinhard, Rep. Prog. Phys. **52**, 439 (1989).

[81] E. Braten and R. D. Pisarski, Phys. Rev. D **45**, 1827 (1992).

[82] J.-P. Blaizot and E. Iancu, Nucl. Phys. B **417**, 608 (1994).

[83] H. Vija and M. H. Thoma, Phys. Lett. B **342**, 212 (1995).

[84] Z. Fodor, S. D. Katz, and K. K. Szabo, Phys. Lett. B **568**, 73 (2003).

[85] C. R. Allton *et al.*, Phys. Rev. D **66**, 074507 (2002).

[86] F. Csikor *et al.*, Prog. Theor. Phys. Suppl. **153**, 93 (2004).

[87] V. P. Konchakovski *et al.*, Phys. Rev. C **85**, 044922 (2012).

[88] NA49 Collaboration, C. Alt *et al.*, Phys. Rev. C **66**, 054902 (2002).

[89] NA49 Collaboration, C. Alt *et al.*, Phys. Rev. C **77**, 024903 (2008).

[90] E. L. Bratkovskaya *et al.*, J. Phys. Conf. Ser. **316**, 012027 (2011).

[91] E. L. Bratkovskaya, S. Soff, H. Stöcker, M. van Leeuwen, and W. Cassing, Phys. Rev. Lett. **92**, 032302 (2004).

[92] J. Geiss, W. Cassing, and C. Greiner, Nucl. Phys. A **644**, 107 (1998).

[93] NA49 Collaboration, T. Anticic *et al.*, Phys. Rev. C **80**, 034906 (2009).

[94] NA57 Collaboration, C. Antinori *et al.*, Phys. Lett. B **595**, 68 (2004).

[95] NA57 Collaboration, C. Antinori *et al.*, J. Phys. G: Nucl. Phys. **32**, 427 (2006).

[96] W. Ehehalt and W. Cassing, Nucl. Phys. A **602**, 449 (1996).

[97] E. L. Bratkovskaya, W. Cassing, and H. Stöcker, Phys. Rev. C **67**, 054905 (2003).

[98] STAR Collaboration, J. Adams *et al.*, Phys. Rev. Lett. **92**, 052302 (2004).

[99] STAR Collaboration, J. Adams *et al.*, Phys. Rev. Lett. **95**, 122301 (2005).

[100] PHENIX Collaboration, A. Adare *et al.*, Phys. Rev. Lett. **98**, 162301 (2007).

[101] PHENIX Collaboration, S. Afanasiev *et al.*, Phys. Rev. C **80**, 024909 (2009).

[102] M. Nasim, L. Kumar, P. K. Netrakanti, and B. Mohanty, Phys. Rev. C **82**, 054908 (2010).

[103] E. L. Bratkovskaya *et al.*, to be published in J. Phys. Conf. Ser. , arXiv:1304.4115[nucl-th].

[104] O. Linnyk, J. Phys. G **38**, 025105 (2011).

[105] O. Linnyk, S. Leupold, and U. Mosel, Phys. Rev. D **71**, 034009 (2005).

[106] O. Linnyk, S. Leupold, and U. Mosel, Phys. Rev. D **75**, 059901(E) (2007).

[107] E. L. Bratkovskaya, W. Cassing, and O. Linnyk, Phys. Lett. B **670**, 428 (2009).

[108] J. Manninen, E. L. Bratkovskaya, W. Cassing, and O. Linnyk, Eur. Phys. J. C **71**, 1615 (2011).

[109] O. Linnyk, E. L. Bratkovskaya, and W. Cassing, Int. J. Mod. Phys. E **17**, 1367 (2008).

[110] O. Linnyk, E. L. Bratkovskaya, W. Cassing, and H. Stöcker, Phys. Rev. C **76**, 041901 (2007).

[111] O. Linnyk, E. L. Bratkovskaya, **V. Ozvenchuk**, W. Cassing, and C. M. Ko, Phys. Rev. C **84**, 054917 (2011).

[112] G. E. Brown and M. Rho, Phys. Rev. Lett. **66**, 2720 (1991).

[113] G. E. Brown and M. Rho, Phys. Rep. **363**, 85 (2002).

[114] T. Hatsuda and S. H. Lee, Phys. Rev. C **46**, R34 (1992).

[115] M. Akasawa and C. M. Ko, Phys. Rev. C **48**, R526 (1993).

[116] C. M. Shakin and W.-D. Sun, Phys. Rev. C **49**, 1185 (1994).

[117] F. Klingl and W. Weise, Nucl. Phys. A **606**, 329 (1996).

[118] F. Klingl, N. Kaiser, and W. Weise, Nucl. Phys. A **624**, 527 (1997).

[119] S. Leupold, W. Peters, and U. Mosel, Nucl. Phys. A **628**, 311 (1998).

[120] G. Chanfray, R. Rapp, and J. Wambach, Phys. Rev. Lett. **76**, 368 (1996).

[121] R. Rapp, G. Chanfray, and J. Wambach, Nucl. Phys. A **617**, 472 (1997).

[122] W. Peters, M. Post, H. Lenske, S. Leupold, and U. Mosel, Nucl. Phys. A **632**, 109 (1998).

[123] M. Post, S. Leupold, and U. Mosel, Nucl. Phys. A **689**, 753 (2001).

[124] R. Rapp and J. Wambach, Adv. Nucl. Phys. **25**, 1 (2000).

[125] C. Song, S. H. Lee, and C. M. Ko, Phys. Rev. C **52**, 476 (1995).

[126] C. Song, V. Koch, S. H. Lee, and C. M. Ko, Phys. Lett. B **366**, 379 (1996).

[127] CERES Collaboration, G. Agakichiev *et al.*, Phys. Rev. Lett. **75**, 1272 (1995).

[128] T. Ullrich *et al.*, Nucl. Phys. A **610**, 317 (1996).

[129] A. Drees *et al.*, Nucl. Phys. A **610**, 536 (1996).

[130] HELIOS/3 Collaboration, M. A. Mazzoni *et al.*, Nucl. Phys. A **566**, 95 (1994).

[131] HELIOS/3 Collaboration, M. Masera *et al.*, Nucl. Phys. A **590**, 93 (1995).

[132] T. Åkesson *et al.*, Z. Phys. C **68**, 47 (1995).

[133] G. Q. Li, C. M. Ko, and G. E. Brown, Phys. Rev. Lett. **75**, 4007 (1995).

[134] C. M. Ko, G. Q. Li, G. E. Brown, and H. Sorge, Nucl. Phys. A **610**, 342c (1996).

[135] W. Cassing, W. Ehehalt, and C. M. Ko, Phys. Lett. B **363**, 35 (1995).

[136] C. Ernst, S. A. Bass, M. Belkacem, H. Stöcker, and W. Greiner, Phys. Rev. C **58**, 447 (1998).

[137] W. Cassing, E. L. Bratkovskaya, R. Rapp, and J. Wambach, Phys. Rev. C **57**, 916 (1998).

[138] I. Tserruya, Nucl. Phys. A **681**, 133c (2001).

[139] I. Tserruya, Eur. Phys. J. C **43**, 399 (2005).

[140] NA60 Collaboration, A. Arnaldi *et al.*, Phys. Rev. Lett. **96**, 162302 (2006).

[141] NA60 Collaboration, J. Seixas *et al.*, J. Phys. G **34**, S1023 (2007).

[142] NA60 Collaboration, S. Damjanovic *et al.*, Nucl. Phys. A **783**, 327 (2007).

[143] CERES Collaboration, D. Adamova *et al.*, Nucl. Phys. A **715**, 262 (2003).

[144] CERES Collaboration, D. Adamova *et al.*, Phys. Rev. Lett. **91**, 042301 (2003).

[145] CERES Collaboration, G. Agakichiev *et al.*, Eur. Phys. J. C **41**, 475 (2005).

[146] CERES Collaboration, D. Adamova *et al.*, Phys. Lett. B **666**, 425 (2008).

[147] J. Ruppert, T. Renk, and B. Müller, Phys. Rev. C **73**, 034907 (2006).

[148] E. L. Bratkovskaya and C. M. Ko, Phys. Lett. B **445**, 265 (1999).

[149] W. Cassing, Y. S. Golubeva, A. S. Iljinov, and L. A. Kondratyuk, Phys. Lett. B **396**, 26 (1997).

[150] Y. S. Golubeva, L. A. Kondratyuk, and W. Cassing, Nucl. Phys. A **625**, 832 (1997).

[151] V. Metag, Prog. Part. Nucl. Phys. **61**, 245 (2008).

[152] R. Rapp, arXiv:nucl-th/0204003 .

[153] NA60 Collaboration, R. Arnaldi *et al.*, Eur. Phys. J. C **59**, 607 (2009).

[154] J. Alam, T. Hirano, J. K. Nayak, and B. Sinha, arXiv:0902.0446 .

[155] C. Song, C. M. Ko, and C. Gale, Phys. Rev. D **50**, 1827 (1994).

[156] J. Aichelin and K. Werner, Phys. Rev. C **79**, 064907 (2009).

[157] P. Braun-Munzinger, J. Stachel, J. P. Wessels, and N. Xu, Phys. Lett. B **365**, 1 (1996).

[158] P. Braun-Munzinger, J. Stachel, J. P. Wessels, and N. Xu, Phys. Lett. B **344**, 43 (1995).

[159] J. Stachel, Nucl. Phys. A **654**, 199c (1999).

[160] J. Cleymans and H. Satz, Z. Phys. C **57**, 135 (1993).

[161] J. Sollfank, M. Gazdzicki, U. Heinz, and J. Rafelski, Z. Phys. C **61**, 659 (1994).

[162] F. Becattini, M. Gazdzicki, and J. Sollfank, Eur. Phys. J. C **5**, 143 (1998).

[163] C. Spieles, H. Stöcker, and C. Greiner, Eur. Phys. J. C **2**, 351 (1998).

[164] J. Cleymans, H. Oeschler, and K. Redlich, J. Phys. G **25**, 281 (1999).

[165] W. Broniowski and W. Florkowski, Phys. Rev. C **65**, 064905 (2002).

[166] H. Stöcker and W. Greiner, Phys. Rep. **137**, 277 (1986).

[167] U. Ornik, M. Plumer, B. R. Schlei, D. Strottman, and R. M. Weiner, Phys. Rev. C **54**, 1381 (1996).

[168] S. Bernard, J. A. Maruhn, W. Greiner, and D. H. Rischke, Nucl. Phys. A **605**, 566 (1996).

[169] J. Sollfank *et al.*, Phys. Rev. C **55**, 392 (1997).

[170] P. Koch, B. Müller, and J. Rafelski, Phys. Rep. **142**, 167 (1986).

[171] A. Lang *et al.*, Z. Phys. A **340**, 287 (1991).

[172] B. Blättel, V. Koch, and U. Mosel, Rep. Prog. Phys. **56**, 1 (1993).

[173] M. Belkacem *et al.*, Phys. Rev. C **58**, 1727 (1998).

[174] L. V. Bravina *et al.*, Phys. Lett. B **434**, 379 (1998).

[175] L. V. Bravina *et al.*, J. Phys. G **25**, 351 (1999).

[176] L. V. Bravina *et al.*, Phys. Rev. C **60**, 024904 (1999).

[177] L. V. Bravina *et al.*, Phys. Rev. C **62**, 064906 (2000).

[178] J. Sollfrank, U. Heinz, H. Sorge, and N. Xu, Phys. Rev. C **59**, 1637 (1999).

[179] E. L. Bratkovskaya, W. Cassing, M. Greiner, C. Effenberger, U. Mosel, and A. Sibirtsev, Nucl. Phys. A **675**, 661 (2000).

[180] **V. Ozvenchuk**, O. Linnyk, M. I. Gorenstein, E. L. Bratkovskaya, and W. Cassing, Phys. Rev. C **87**, 024901 (2013).

[181] **V. Ozvenchuk**, O. Linnyk, E. L. Bratkovskaya, M. I. Gorenstein, and W. Cassing, Phys. Atom. Nucl. **75**, 903 (2012).

[182] **V. Ozvenchuk**, E. L. Bratkovskaya, O. Linnyk, M. I. Gorenstein, and W. Cassing, EPJ Web Conf. **13**, 06006 (2011).

[183] W. Cassing, Nucl. Phys. A **700**, 618 (2002).

[184] R. Gavai and S. Gupta, Phys. Lett. B **696**, 459 (2011).

[185] S. Borsanyi *et al.*, Nucl. Phys. A **855**, 253 (2011).

[186] S. Ejiri, F. Karsch, and K. Redlich, Phys. Lett. B **633**, 275 (2006).

[187] M. Cheng *et al.*, Phys. Rev. D **79**, 074505 (2009).

[188] S. Plumari, W. M. Alberico, V. Greco, and C. Ratti, Phys. Rev. D **84**, 094004 (2011).

[189] V. Skokov, B. Friman, and K. Redlich, Phys. Lett. B **708**, 179 (2012).

[190] B. Friman, F. Karsch, K. Redlich, and V. Skokov, Eur. Phys. J. C **71**, 1694 (2011).

[191] N. Strodthoff, B.-J. Schaefer, and L. von Smekal, Phys. Rev. D **85**, 074007 (2012).

[192] B.-J. Schaefer and M. Wagner, Phys. Rev. D **85**, 034027 (2012).

[193] M. Nahrgang, T. Schuster, M. Mitrovski, R. Stock, and M. Bleicher, J. Phys. G **38**, 124150 (2011).

[194] V. P. Konchakovski, M. I. Gorenstein, E. L. Bratkovskaya, and W. Greiner, J. Phys. G **37**, 073101 (2010).

[195] V. V. Begun, M. I. Gorenstein, A. P. Kostyuk, and O. S. Zozulya, Phys. Rev. C **71**, 054904 (2005).

[196] V. V. Begun, M. I. Gorenstein, A. P. Kostyuk, and O. S. Zozulya, J. Phys. G **32**, 935 (2006).

[197] V. V. Begun *et al.*, Phys. Rev. C **76**, 024902 (2007).

[198] M. Hauer, V. V. Begun, and M. I. Gorenstein, Eur. Phys. J. C **58**, 83 (2008).

[199] K. Aamodt *et al.*, Phys. Rev. Lett. **105**, 252302 (2010).

[200] P. Huovinen, P. F. Kolb, U. Heinz, P. V. Ruuskanen, and S. A. Voloshin, Phys. Lett. B **503**, 58 (2001).

[201] P. F. Kolb, P. Huovinen, U. Heinz, and H. Heiselberg, Phys. Lett. B **500**, 232 (2001).

[202] D. Teaney, J. Lauret, and E. V. Shuryak, Phys. Rev. Lett. **86**, 4783 (2001).

[203] T. Hirano and K. Tsuda, Phys. Rev. C **66**, 054905 (2002).

[204] P. F. Kolb and R. Rapp, Phys. Rev. C **67**, 044903 (2003).

[205] P. Danielewicz and M. Gyulassy, Phys. Rev. D **31**, 53 (1985).

[206] G. Policastro, D. T. Son, and A. O. Starinets, Phys. Rev. Lett. **87**, 081601 (2001).

[207] P. K. Kovtun, D. T. Son, and A. O. Starinets, Phys. Rev. Lett. **94**, 111601 (2005).

[208] A. Buchel, Phys. Lett. B **663**, 286 (2008).

[209] P. Romatschke and U. Romatschke, Phys. Rev. Lett. **99**, 172301 (2007).

[210] H. Song and U. Heinz, Phys. Rev. C **77**, 064901 (2008).

[211] M. Luzum and P. Romatschke, Phys. Rev. C **78**, 034915 (2008).

[212] B. Schenke, S. Jeon, and C. Gale, Phys. Rev. C **82**, 014903 (2010).

[213] L. P. Csernai, J. I. Kapusta, and L. D. McLerran, Phys. Rev. Lett. **97**, 152303 (2006).

[214] A. S. Khvorostukhin, V. D. Toneev, and D. N. Voskresensky, Phys. Rev. C **83**, 035204 (2011).

[215] D. Kharzeev and K. Tuchin, JHEP **09**, 093 (2008).

[216] F. Karsch, D. Kharzeev, and K. Tuchin, Phys. Lett. B **663**, 217 (2008).

[217] P. Romatschke and D. T. Son, Phys. Rev. D **80**, 065021 (2009).

[218] O. Moore, G. D.and Saremi, JHEP **09**, 015 (2008).

[219] C. Sasaki and K. Redlich, Phys. Rev. C **79**, 055207 (2009).

[220] C. Sasaki and K. Redlich, Nucl. Phys. A **832**, 62 (2010).

[221] K. Paech and S. Pratt, Phys. Rev. C **74**, 014901 (2006).

[222] G. Torrieri and I. Mishustin, Phys. Rev. C **78**, 021901 (2008).

[223] P. B. Arnold, G. D. Moore, and L. G. Yaffe, JHEP **11**, 001 (2010).

[224] P. B. Arnold, G. D. Moore, and L. G. Yaffe, JHEP **05**, 051 (2003).

[225] P. B. Arnold, C. Dogan, and G. D. Moore, Phys. Rev. D **74**, 085021 (2006).

[226] M. Prakash, M. Prakash, R. Venugopalan, and G. Welke, Phys. Rep. **227**, 321 (1993).

[227] J. W. Chen and J. Wang, Phys. Rev. C **79**, 044913 (2009).

[228] H. B. Meyer, Phys. Rev. D **76**, 101701 (2007).

[229] H. B. Meyer, Phys. Rev. Lett. **100**, 162001 (2008).

[230] A. Nakamura and S. Sakai, Phys. Rev. Lett. **94**, 072305 (2005).

[231] S. Sakai and A. Nakamura, Pos **LAT2007**, 221 (2007).

[232] F. Reif, *Fundamentals of Statistical and Thermal Physics* (New York: McGraw-Hill Book Company, 1965).

[233] S. R. de Groot, W. A. van Leeuwen, and C. Weert, *Relativistic Kinetic Theory, Principles and Applications* (Amsterdam: North-Holland Company, 1980).

[234] M. S. Green, J. of Chem. Phys. **22**, 398 (1954).

[235] R. Kubo, J. Phys. Soc. Japan **12**, 570 (1957).

[236] R. Kubo, Rep. Prog. Phys. **29**, 255 (1966).

[237] M. Bluhm, B. Kämpfer, and K. Redlich, Phys. Rev. C **84**, 025201 (2011).

[238] M. H. Thoma, Phys. Lett. B **269**, 144 (1991).

[239] A. S. Khvorostukhin, V. D. Toneev, and D. N. Voskresensky, Phys. Rev. C **84**, 035202 (2011).

[240] A. S. Khvorostukhin, V. D. Toneev, and D. N. Voskresensky, Nucl. Phys. A **845**, 106 (2010).

[241] A. Muronga, Phys. Rev. C **69**, 044901 (2004).

[242] N. S. Demir and S. A. Bass, Eur. Phys. J. C **62**, 63 (2009).

[243] S. Pal, Phys. Lett. B **684**, 211 (2010).

[244] C. Wesp *et al.*, Phys. Rev. C **84**, 054911 (2011).

[245] J. Fuini III, N. S. Demir, D. K. Srivastava, and S. A. Bass, J. Phys. G **38**, 015004 (2011).

[246] **V. Ozvenchuk**, O. Linnyk, M. I. Gorenstein, E. L. Bratkovskaya, and W. Cassing, to be published in Phys. Rev. C , arXiv:1212.5393[hep-ph].

[247] W. Cassing, O. Linnyk, T. Steinert, and **V. Ozvenchuk**, to be published in Phys. Rev. Lett. , arXiv:1302.0906[hep-ph].

[248] E. L. Bratkovskaya, **V. Ozvenchuk**, W. Cassing, V. P. Konchakovski, and O. Linnyk, to be published in J. Phys. Conf. Ser. , arXiv:1304.7154[nucl-th].

[249] R. Zubarev, O. Morozov, and G. Röpke, *Statistical Mechanics of Nonequilibrium Processes Volume 2: Relaxation and Hydrodynamic Processes* (Akademie Verlag GmbH, 1996).

[250] A. Hosoya and K. Kajantie, Nucl. Phys. B **250**, 666 (1985).

[251] S. Gavin, Nucl. Phys. A **435**, 826 (1985).

[252] P. Chakraborty and J. I. Kapusta, Phys. Rev. C **83**, 014906 (2011).

[253] Y. Aoki *et al.*, Phys. Lett. B **643**, 46 (2006).

[254] A. S. Khvorostukhin, V. D. Toneev, and D. N. Voskresensky, arXiv:1240.5855 [nucl-th] .

[255] V. P. Konchakovski *et al.*, J. Phys. Conf. Ser. **389**, 012015 (2012).

[256] J.-W. Chen and E. Nakano, Phys. Lett. B **647**, 371 (2007).

[257] M. I. Gorenstein, M. Hauer, and O. N. Moroz, Phys. Rev. C **77**, 024911 (2008).

[258] R. Lang, N. Kaiser, and W. Weise, Eur. Phys. J. A **48**, 109 (2012).

[259] J. Noronha-Hostler, J. Noronha, and C. Greiner, Phys. Rev. C **86**, 024913 (2012).

[260] A. Dobado, F. J. Llanes-Estrada, and J. M. Torres-Rincon, Phys. Lett. B **702**, 43 (2011).

[261] E. Lu and G. D. Moore, Phys. Rev. C **83**, 044901 (2011).

[262] H. B. Meyer, Nucl. Phys. A **830**, 641c (2009).

[263] M. Bluhm, B. Kämpfer, and K. Redlich, Phys. Lett. B **709**, 77 (2012).

[264] Y. Hirono, M. Hongo, and T. Hirano, arXiv:1211.1114 .

[265] H.-T. Ding *et al.*, Phys. Rev. D **83**, 034504 (2011).

[266] G. Aarts *et al.*, Phys. Rev. Lett. **99**, 022002 (2007).

[267] S. Gupta, Phys. Lett. B **597**, 57 (2004).

[268] P. V. Buividovich *et al.*, Phys. Rev. Lett. **105**, 132001 (2010).

[269] K. Tuchin, arXiv:1301.0099 .

[270] D. E. Kharzeev, L. D. McLerran, and H. J. Warringa, Nucl. Phys. A **803**, 227 (2008).

[271] D. E. Kharzeev, Ann. Phys. (NY) **325**, 205 (2010).

[272] K. Fukushima, D. E. Kharzeev, and H. J. Warringa, Phys. Rev. D **78**, 074033 (2008).

[273] D. E. Kharzeev and A. Zhitnitsky, Nucl. Phys. A **797**, 67 (2007).

[274] D. E. Kharzeev and H. J. Warringa, Phys. Rev. D **80**, 034028 (2009).

[275] V. Skokov, A. Illarionov, and V. D. Toneev, Int. J. Mod. Phys. A **24**, 5925 (2009).

[276] V. Voronyuk *et al.*, Phys. Rev. C **83**, 054911 (2011).

[277] O. Linnyk *et al.*, Phys. Rev. C **87**, 014905 (2013).

[278] P. Braun-Munzinger, I. Heppe, and J. Stachel, Phys. Lett. B **465**, 15 (1999).

[279] P. Braun-Munzinger, D. Magestro, K. Redlich, and J. Stachel, Phys. Lett. B **518**, 41 (2001).

[280] A. Andronic, P. Braun-Munzinger, and J. Stachel, Nucl. Phys. A **772**, 167 (2006).

[281] T. Renk and J. Ruppert, Phys. Rev. C **77**, 024907 (2008).

[282] J. Ruppert, C. Gale, T. Renk, P. Lichard, and J. I. Kapusta, Phys. Rev. Lett. **100**, 162301 (2008).

[283] K. Dusling, D. Teaney, and I. Zahed, Phys. Rev. C **75**, 024908 (2007).

[284] Dusling and I. Zahed, Phys. Rev. C **80**, 014902 (2009).

[285] Dusling and I. Zahed, Nucl. Phys. A **825**, 212 (2009).

[286] H. van Hees and R. Rapp, Phys. Rev. Lett. **97**, 102301 (2006).

[287] H. van Hees and R. Rapp, Nucl. Phys. A **806**, 339 (2008).

[288] E. Santini, J. Steinheimer, M. Bleicher, and S. Schramm, Phys. Rev. C **84**, 014901 (2011).

[289] C. Gale and P. Lichard, Phys. Rev. D **49**, 3338 (1994).

[290] G.-Q. Li and C. Gale, Phys. Rev. C **58**, 2914 (1998).

[291] C. Gale and J. Kapusta, Phys. Rev. C **35**, 2107 (1987).

[292] C. Gale and J. Kapusta, Phys. Rev. C **38**, 2659 (1988).

[293] K. Haglin and C. Gale, Phys. Rev. D **52**, 6297 (1995).

[294] DM2 Collaboration, A. Antonelli *et al.*, Z. Phys. C **56**, 15 (1992).

[295] ND Collaboration, S. Dolinsky *et al.*, Phys. Rep. **202**, 99 (1991).

[296] V. Aulchenko *et al.*, Novosibirsk Report No. , 86 (1986).

[297] R. Baldini-Ferroli, *Hadronic Physics at Intermediate Energy: 2nd: Winter School Proceedings* (Amsterdam/New York: Elsevier, 1987).

[298] ARGUS Collaboration, N. Albrecht *et al.*, Phys. Lett. B **185**, 223 (1987).

[299] $\gamma\gamma 2$ Collaboration, C. Bacci *et al.*, Nucl. Phys. B **184**, 31 (1981).

[300] M3N Collaboration, A. Cordier *et al.*, Phys. Lett. B **109**, 129 (1982).

[301] C. Song and C. M. Ko, Phys. Rev. C **53**, 2371 (1996).

[302] E. L. Bratkovskaya, S. M. Kiselev, and G. B. Sharkov, Phys. Rev. C **78**, 034905 (2008).

Acknowledgments

I would like to thank my friends and colleagues, without whom this work would not be possible. First of all, I am grateful to my supervisor Prof. Dr. E. Bratkovskaya for her kind support and help during my study. It is a big pleasure and I am very happy to work with her. I am extremely grateful to Dr. O. Linnyk for the encyclopedic knowledge, scientific enthusiasm, and great motivation, which helped me a lot. Her contribution to the thesis hardly can be overestimated. I greatly appreciate collaboration with Prof. Dr. W. Cassing for his excellent pedagogical skills as well as for original ideas and deep physical intuition, which provided a groundwork for the dissertation. Let me also express my appreciation to Prof. M. Gorenstein for his contribution to this work. I am also thankful to Dr. V. Konchakovski for the answers to my numerous questions.

Countless thanks go to the friends for creating a welcoming atmosphere in a foreign country, in particular, to V. Pauk, Iu. Sorokin, A. Yakubovich, and A. Merdeev.

I acknowledge financial support through the HIC for FAIR framework of the LOEWE program and Helmholtz Research School for Quark Matter Studies in Heavy Ion Collisions. I am very glad to be a member of the H-QM School and I thank all of the participants of the School for the communication and support during my study.

I especially thank my whole family for sharing every day of my live, despite the spatial distance.

Vitalii Ozvenchuk

Curriculum Vitae

Helmholtz Research School
University of Frankfurt
+49-176-985-21343
+49-69-798-47522
ozvenchuk@fias.uni-frankfurt.de

General information

Date of birth	May 27, 1987
Place of birth	Vinnytsya, Ukraine
Nationality	Ukrainian
Sex	Male
Address	Frankfurt Institute for Advanced Studies Ruth-Moufang-Str. 1 60438 Frankfurt am Main, Germany

Field of scientific interests

Relativistic nuclear physics, heavy-ion physics, transport models for relativistic nuclear collisions, dynamical equilibration and transport properties of strongly interacting matter.

Education

2010–present	**PhD. Student**, *Helmholtz Research School*, University of Frankfurt, Germany.
2004-2009	**Student**, *Physics Department*, Taras Shevchenko National University of Kyiv, Kyiv, Ukraine.
1998-2004	**Pupil**, *Physics and Mathematics Gymnasium #17*, Vinnytsya, Ukraine.
1994-1997	**Pupil**, *Secondary School #1*, Vinnytsya, Ukraine.

Grades

July 2013 (planned)	**PhD**, *Institut für Theoretische Physik*, University of Frankfurt, Germany, Advisor – Prof. Dr. E. L. Bratkovskaya (ITP). Title – 'Dynamical equilibration and transport coefficients of strongly interacting matter'.
2009	**MS**, *Physics Department, Chair of Quantum Field Theory*, Taras Shevchenko National University of Kyiv, Kyiv, Ukraine, Advisor – Prof. O. Ya. Dzyublik (INR, Kyiv, Ukraine). Title – 'Influence of laser radiation on the disintegration of nuclear isomers'.
2008	**Bachelor**, *Physics Department, Chair of Quantum Field Theory*, Taras Shevchenko National University of Kyiv, Kyiv, Ukraine, Advisor – Prof. I. S. Dotsenko (TSNUK, Kyiv, Ukraine). Title – 'Calculation of correlation function of Bell's inequalities'.
2004	**School Certificate**, *Physics and Mathematics Gymnasium #17*, Vinnytsya, Ukraine.

Presentations at International Conferences

November 2012 **International Workshop on Hot and Dense Nuclear and Astrophysical Matter**, *Invited lecturer "Introduction to transport theory" (2x45 min)*, Johannesburg, South Africa.

November 2012 **International Workshop on Hot and Dense Nuclear and Astrophysical Matter**, *Talk*, Johannesburg, South Africa.

October 2012 **Young Scientists Conference on Modern Problems in Theoretical Physics**, *Talk*, Kyiv, Ukraine.

June 2012 **Second International Symposium on Non-equilibrium Dynamics and Network Workshop 'TURIC'**, *Talk*, Hersonissos, Crete, Greece.

November 2011 **Critical Point and Onset of Deconfinement 2011**, *Talk*, Wuhan, China.

September 2011 **International Symposium on Non-equilibrium Dynamics and Network Workshop 'TORIC'**, *Talk*, Heraklion, Crete, Greece.

May 2011 **Quark Matter 2011**, *Poster*, Annecy, France.

August 2010 **Critical Point and Onset of Deconfinement 2010**, *Poster*, Dubna, Russia.

August 2010 **Hot and Cold Baryonic Matter 2010**, *Poster*, Budapest, Hungary.

Seminar talks

January 2013 **Seminar of the Institute for Theoretical Physics**, *Justus-Liebig-University of Giessen*, Giessen, Germany.

January 2013 **Seminar of the Institute for Theoretical Physics**, *University of Frankfurt*, Frankfurt am Main, Germany.

December 2012 **Meeting of the Transport theory working groups of FIAS and University of Frankfurt**, *Frankfurt Institute for Advanced Studies*, Frankfurt am Main, Germany.

December 2012 **Seminar of the Frankfurt International Graduate School for Science (FIGSS)**, *Frankfurt Institute for Advanced Studies*, Frankfurt am Main, Germany.

May 2012 **Seminar of the Institute for Theoretical Physics**, *University of Frankfurt*, Frankfurt am Main, Germany.

January 2011 **Seminar of the Institute for Theoretical Physics**, *University of Frankfurt*, Frankfurt am Main, Germany.

Talks given at graduate Lecture Weeks

October 2012 **Heavy Ion Collisions: The Big Picture II**, *Talk: "How to measure centrality in heavy-ion collisions"*, Eutin, Germany.

April 2012 **Electromagnetic Probes**, *Talk: "How to measure dimuons with ALICE"*, Strasbourg, France.

October 2011 **Hydrodynamics and Flow**, *Talk: "The HBT puzzle"*, Kloster Marienburg/Mosel, Germany.

March 2011 **Heavy Probes in Heavy Ion Collisions**, *Talk: "Basics of calorimetry"*, Manigod, France.

March 2010 **Heavy Ion Collisions: The Big Picture**, *Talk: "Event-by-event fluctuations: What can they signal, how are they connected to lQCD susceptibilities"*, Rolandseck/Rhine, Germany.

Additional Education

June 2012 **2012 Jet Summer School**, Montreal, Canada.

February 2012 **Second Joint Helmholtz-Rosatom School**, Bekasovo, Russia.

November 2011 **International School for High-Energy Collisions**, Wuhan, China.

September 2011 **Career Development and Leadership**, *Soft skills training*, Osterholtz-Scharmbeck, Germany.

February 2011 **First Joint Helmholtz-Rosatom School**, Hirschegg, Austria.

September 2010 **International School "Dense QCD Phases in Heavy-Ion Collisions"**, Dubna, Russia.

June 2010 **Presentation Skills and Scientific Writing**, *Soft skills training*, Lohmar, Germany.

February 2010 **Initial training: "Starting the PhD"**, *Soft skills training*, Castle Buchenau, Germany.

Awards

2010-2013 **Scholarship** of the Helmholtz Research School "Quark Matter Studies" (H-QM).

Winner Diplomas of regional (Vinnitsya oblast, Ukraine) olympiads in Physics:

2003 second place,

2002 third place.

Winner Diplomas of city (Vinnitsya, Ukraine) olympiads in Physics:

2000, 2002 first place,

2001, 2003 third place.

2004-2009 Elected as the **speaker** of the Quantum Field Theory group at the Taras Shevchenko National University of Kyiv.

Computer Skills

very good FORTRAN, LaTeX, Origin, Pascal;

good Mathematica, C++, MS Power Point, MS Word.

Language Skills

native speaker Ukrainian

fluently Russian, English

basic knowledge German

Publication List

1. E. L. Bratkovskaya, **V. Ozvenchuk**, W. Cassing, V. P. Konchakovski, and O. Linnyk, *Parton-hadron matter in- and out-off equilibrium*, to be published in J. Phys. Conf. Ser., arXiv:1304.7154[nucl-th].
2. E. L. Bratkovskaya, W. Cassing, V. P. Konchakovski, O. Linnyk, **V. Ozvenchuk**, V. D. Toneev, and V. Voronyuk, *The QGP dynamics in relativistic heavy-ion collisions*, to be published in J. Phys. Conf. Ser., arXiv:1304.4115[nucl-th].
3. W. Cassing, O. Linnyk, T. Steinert, and **V. Ozvenchuk**, *On the electric conductivity of hot QCD matter*, Phys. Rev. Lett. **110**, 182301 (2013).
4. **V. Ozvenchuk**, O. Linnyk, M. I. Gorenstein, E. L. Bratkovskaya, and W. Cassing, *Shear and bulk viscosities of strongly interacting "infinite" parton-hadron matter within parton-hadron-string dynamics transport approach*, to be published in Phys. Rev. C, arXiv:1212.5393[hep-ph].
5. **V. Ozvenchuk**, O. Linnyk, E. L. Bratkovskaya, M. I. Gorenstein, and W. Cassing, *Strongly interacting parton matter equilibration*, Phys. Atom. Nucl. **75**, 903 (2012).
6. E. L. Bratkovskaya, O. Linnyk, V. P. Konchakovski, W. Cassing, **V. Ozvenchuk**, J. Manninen, and C. M. Ko, *Dilepton production from SIS to LHC energies*, J. Phys. Conf. Ser. **389**, 012016 (2012).
7. E. L. Bratkovskaya, W. Cassing, O. Linnyk, V. P. Konchakovski, V. Voronyuk, and **V. Ozvenchuk**, *Dynamics of hot and dense nuclear and partonic matter*, Phys. Atom. Nucl. **75**, 679 (2012).
8. **V. Ozvenchuk**, O. Linnyk, M. I. Gorenstein, E. L. Bratkovskaya, and W. Cassing, *Dynamical equilibration of strongly interacting "infinite" parton matter within the parton-hadron-string transport approach*, Phys. Rev. C **87**, 024901 (2013).
9. O. Linnyk, E. L. Bratkovskaya, **V. Ozvenchuk**, W. Cassing, and C. M. Ko, *Dilepton production in nucleus-nucleus collisions at top CERN Super Proton Synchrotron energy of* $158A$ *GeV within the parton-hadron-string transport approach*, Phys. Rev. C **84**, 054917 (2011).
10. E. L. Bratkovskaya, W. Cassing, V. P. Konchakovski, O. Linnyk, **V. Ozvenchuk**, and V. Voronyuk, *Properties of the partonic phase at RHIC within PHSD*, J. Phys. Conf. Ser. **316**, 012027 (2011).
11. **V. Ozvenchuk**, E. L. Bratkovskaya, O. Linnyk, M. I. Gorenstein, and W. Cassing, *Dynamical equilibration in strongly interacting parton-hadron matter*, EPJ Web Conf. **13**, 06006 (2011).